Hydrogen Bonded Nanostructures on Surfaces: STM, XPS and Electrospray Deposition

by Janine Cathy Swarbrick, MSci (Hons)

Thesis submitted to The University of Nottingham
for the degree of Doctor of Philosophy, September 2006

Abstract

Molecules adsorbed on surfaces can show fascinating characteristics and properties. In particular the assembly of molecules into ordered arrays on surfaces is of great interest, whether one considers possible commercial applications or fundamental physical interactions. Specifically, the mediation of ordered molecular arrangements via hydrogen bonding yields many interesting structures.

This thesis focusses primarily on the importance of hydrogen bonding between molecules on surfaces in ultra high vacuum (UHV), and how these interactions govern ordered phase formation. Scanning tunnelling microscopy is used to investigate the planar perylene derivative PTCDA on the hexagonal Ag-Si(111) $\sqrt{3} \times \sqrt{3}$R30° surface alone, with C_{60}, and with melamine. Interesting molecular architectures are observed including a square PTCDA arrangement, and a PTCDA-melamine hexagonal network which contains both stabilising hydrogen bonds and potentially repulsive interactions. Hydrogen bonding systems of pyridinecarboxylic acids on rutile TiO_2 have been studied using photoemission spectroscopy. Ordered films of isonicotinic acid were investigated using valence band photoemission, and an angular dependence is observed in valence band spectra as the angle between the sample and the incoming light is changed. Biisonicotinic acid was also studied on TiO_2 and on gold using core level photoemission to determine how it bonds to these surfaces; it is thought to chemisorb to both TiO_2 and gold through its carboxylic acid groups in an upright orientation.

Some large or fragile molecules cannot be sublimed in vacuum for deposition as they fragment. Another research focus has been the development of a technique for depositing non-volatile molecules in vacuum directly from solution. Concepts of electrospray ionisation have been used in the development of a vacuum electrospray deposition system. The molecule is dissolved or suspended in solution and electrosprayed directly into a vacuum environment, with the result that molecules of interest are deposited on a sample without fragmentation or corruption. The samples may then be investigated with vacuum based techniques such as scanning tunnelling microscopy and photoemission spectroscopy.

Acknowledgements

I am lucky enough to have worked with many people during my PhD who have shown me various experimental techniques and shared their expertise. Firstly I would like to thank my two supervisors, Peter Beton and James O'Shea, who have spent a lot of their time sharing their knowledge and enthusiasm to help me produce all of the work written here.

The nanoscience group at Nottingham is a great place to be based for a PhD, and the help and company of all the members over the years have made my studies a great experience. There are too many people to mention them all but I particularly want to thank Phil Moriarty, James Sharp, Karina Schulte, James Theobald, Rich Woolley, Martin Humphry, Luís Perdigão, Rich Fawcett, Chris Martin, Jin Ma, Ben Rogers and Giselle Fontes. A huge thankyou has to go to Ben Taylor and Louise Mayor for their work with the electrospray system, and for their company on the many beamtimes we spent together.

From the School of Chemistry, thanks to Neil Oxtoby and Neil Champness for their help and guidance with the PTCDA work and to David Ring for chemical synthesis. During beamtimes, I want to thank Vin Dhanak and George Miller from beamline 4.1 at Daresbury, and Lissy Kjeldgaard and Sven Stoltz from Maxlab, for their advice and support.

It was great to work with Katharina Nilson and Carla Puglia from Uppsala University, and Barbara Brena and Yi Luo from KTH, Stockholm, in the isonicotinic acid collaboration, which became my first publication.

Closer to home, I want to thank my Nan and Mick for their constant support and love, who, since the day I was born, have encouraged me to always enjoy what I'm doing.

Finally I want to thank my wonderful husband Jon, for everything.

Nature goes her own way and all that to us seems an exception is really according to order.

Johann Wolfgang von Goethe (1749-1832)

Contents

Chapter 1

Hydrogen bonded molecular systems

This chapter aims to give an overview of recent research into ordered molecular arrangements on surfaces, in particular those whose behaviour is mediated by hydrogen bonding. Much of the work presented here is based on scanning tunnelling microscopy (STM) studies, but other techniques can be used to investigate these molecular arrays. Examples of hydrogen bonded multilayer structures (of isonicotinic acid) investigated using synchrotron radiation based techniques are discussed in Chapter 6.

1.1 Molecular adsorption on surfaces

The study of surfaces and molecular adsorbates on the nanoscale is currently of wide interest [1, 2]. Recent advances in technology such as the invention of the scanning tunnelling microscope (STM, see Section 2.1) allow visualisation of surfaces on the nanoscale. There is also an ever increasing demand for understanding how matter behaves on the scale of a few atoms or molecules. Future electronics are likely to be based on nanoscale devices on surfaces, thus templating surfaces is important for new device and array fabrication. Self-assembling molecules, which arrange themselves into ordered architectures through intermolecular interactions, are an attractive possibility for building regular nanoscale molecular arrays, on a much smaller scale than that possible with modern lithographic techniques ($\sim$ 20nm for electron beam lithography, 1μm for conventional lithography). Directional interactions such as hydrogen bonds allow further scope for molecular control in order to design and construct specific arrangements.

There has been much effort recently employed in the study of ordered molecular adsorbates, with many impressive and interesting results published. This chapter aims

to highlight recent important developments which demonstrate the factors affecting the formation of ordered surface molecular systems, with the emphasis placed on hydrogen bonded nanostructures.

1.2 Hydrogen bonding

Hydrogen bonding is an attractive interaction between molecules involving a hydrogen atom in one molecule essentially acting as a bonding species. Hydrogen bonding is also a directional interaction, which must be considered when determining how molecules may order themselves. Generally hydrogen bonding occurs when a hydrogen atom is bonded in a molecule to an atom with high electronegativity such as oxygen or nitrogen. The electronegative species attracts the electron from the hydrogen atom rendering it partially positively charged, and the electronegative species becomes slightly negatively charged. The partially positively charged hydrogen atom can then interact with a neighbouring species with negative character, such as a lone pair of electrons on an atom, thus forming a bond between the two molecules. Stronger hydrogen bonds can form when the hydrogen atom involved is bonded to an atom with more electronegative character, though the bond length and angle also determine the strength of the interaction. A simple example of hydrogen bonding is that present in water, schematically shown in Figure 1.1. Many of the physical properties of water are due to its hydrogen bonded nature, such as its relatively high melting and boiling points.

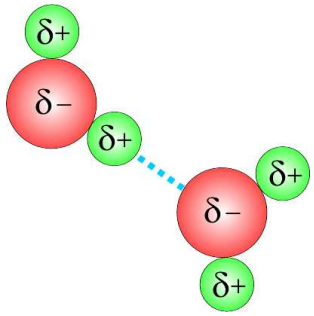

FIGURE 1.1: Schematic hydrogen bonding between two water molecules. The large circles are oxygen atoms and the smaller circles are hydrogen atoms.

Hydrogen bonding can act to arrange molecules in energetically favourable orientations with respect to each other, and in some cases can be present as a cooperative interaction. In water, a hydrogen bond exists between two water molecules and causes a

redistribution of electrons on those molecules which in turn affects the possibility of further hydrogen bonding occurring. The water molecule which has donated a hydrogen atom to the interaction (the top molecule in Figure 1.1) has an increased electron density around its lone pair region on the oxygen atom [3], which encourages hydrogen bond acceptance. An accepting water molecule then has reduced electron density present around its hydrogen atoms, encouraging donation but discouraging further acceptance. This cooperative behaviour enables water to bond in an favourable way for all molecules.

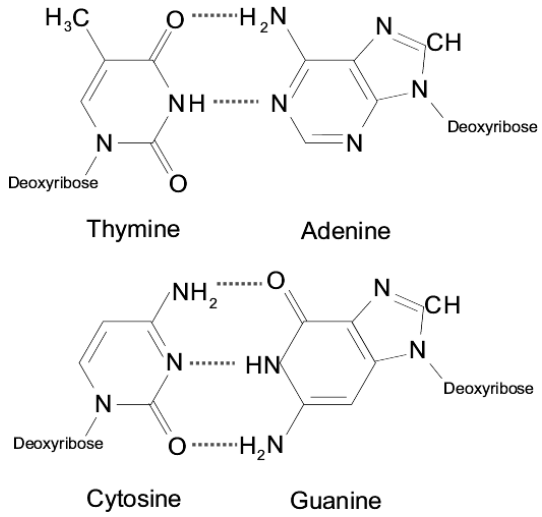

FIGURE 1.2: Schematic of DNA base pairs which hydrogen bonds as shown to hold two strands together to form a double helix. The deoxyribose species is a sugar attached to the base, which in turn is bonded to a phosphate ester; these esters polymerise to form the DNA strands.

Hydrogen bonding is present in many different molecular arrangements in solutions, crystals and surface structures. The base pair bonding in DNA is another well known example [4] (Figure 1.2). Before the double helix structure of DNA was fully understood, it was known that equal amounts of the bases adenine and thymine, and of cytosine and guanine, were present. The double helix structure demonstrates why this is the case. The two helix chains are bound together by hydrogen bonding between adenine:thymine and cytosine:guanine residues. These bases pair up as shown in Figure 1.2; adenine and thymine share two hydrogen bonds, while cytosine and guanine have three.

Molecules can be designed with possible hydrogen bond formation in mind for the construction of ordered surface nanostructures. The following examples show how hydrogen bonding in different molecule-surface systems can lead to the formation of novel structures.

It is important to realise that it is not only hydrogen bonding which determines molecular ordering. Adsorbate-substrate interactions, surface defect densities, steric factors, temperature, adsorbate abundance, and many other factors also contribute to the resulting surface morphology. Other bonding interactions may also be present such as metal-coordination bonding, but these interactions are not considered in detail here.

1.3 Molecular structures

Hydrogen bonding is not necessarily the deciding factor in the formation of molecular arrays, and directionally ordered phases can form without hydrogen bonding interaction being significant. Bai *et al* [5] have studied pyrene and perylene, both flat aromatic molecules, in $HClO_4$ on Cu(111), and found one dimensional linear ordered molecular arrays form which follow the surface crystallographic directions. No hydrogen bonding effects are determined to be present between molecules, and the directionality of the molecular structures is concluded to be due to adsorbate-surface interactions. They determine also that the larger perylene molecules have a stronger interaction with the surface.

However, hydrogen bonds can be present in molecular structures and these may consequently be highly ordered with specific directionality. Barth *et al* [6–8] studied the molecule PVBA (4-[trans-2-(pyrid-4-vinyl)]benzoic acid), which becomes chiral upon adsorption on a surface as it is confined to a 2-D plane; the two resulting enantiomers being labelled λ and δ. The achiral equivalent PEBA(4-[(pyrid-4-yl-ethynyl)]benzoic acid) was also studied which has no chirality when adsorbed. At 150K both species form irregular networks over the Ag(111) surface (Figure 1.3) with end-to-end molecular interactions present as expected. After annealing, the PVBA molecules rearrange themselves to form straight ordered rows two molecules wide as shown in Figure 1.3, which extend in a remarkably straight fashion for very long lengthscales (μm), forming a "nanograting". The achiral PEBA molecules form 2-D hydrogen bonded close packed islands after annealing with enantiomorphic properties due to the molecular packing. This research demonstrates that annealing molecular structures can change their ordering, and the regularity of the PVBA nanograting shows that hydrogen bonding can mediate the formation of very regular highly directional molecular surface phases.

Cooperative hydrogen bonding can be present in ordered molecular surface structures. An example is demonstrated by Otero *et al* [9], who present STM images of guanine,

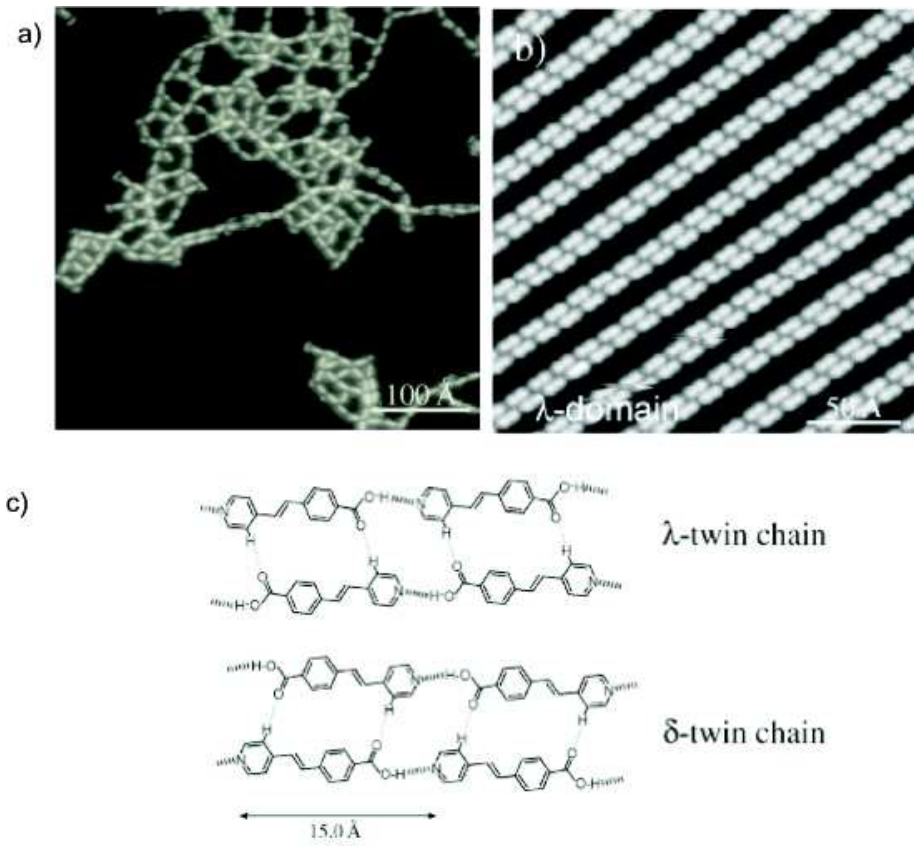

FIGURE 1.3: a) PVBA on Ag(111) at 125K. b)λ PVBA 'nanograting' on Ag(111) formed at 300K. b) schematic showing the two enantiomers of PVBA, λ and δ, and the two resulting chiral double chains, with OH$\cdots$N and weak lateral CH$\cdots$OC hydrogen bonds (after Barth *et al*) [6].

one of the four base pairs of DNA, deposited at room temperature on Au(111) in UHV conditions. Guanine molecules are found to group into quartets of four molecules in a square arrangement, which the authors model computationally using density functional theory (DFT) and confirm that the quartet arrangement is more stable than a molecular dimer through stabilisation by cooperative hydrogen bonding. One may expect at first that a dimer structure would form as nucleic acids do in DNA. The guanine quartets pattern the surface to give a network structure. Figure 1.4 shows the quartet arrangement observed. After annealing the sample, the guanine molecules rearrange to form a self assembled monolayer with a 30% increase in packing density, though hydrogen bonding is still present.

Tanaka *et al* [10, 11] have also studied DNA base pair interactions on the Cu(111) surface, and here base-base hydrogen bonding interactions play a role in determining the

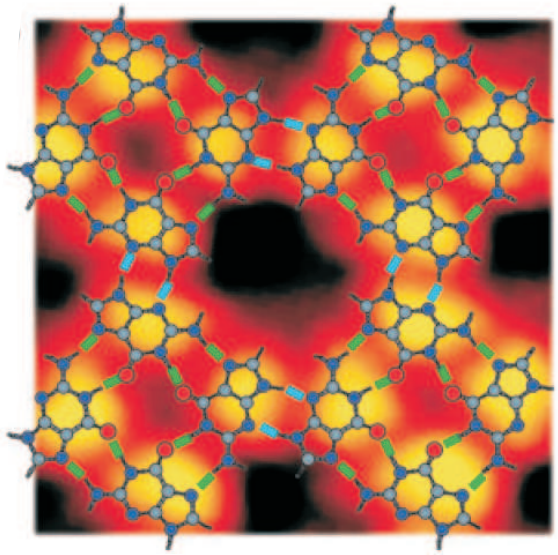

FIGURE 1.4: Cooperative hydrogen bonds (shown in green) stabilise quartets of guanine on Au(111); these quartets hydrogen bond (shown in blue) to form a network over the surface (after Otero *et al*) [9].

phases formed. It was determined that adenine forms 1-D chains, thymine forms 2-D islands, guanine arranges in 2-D square lattices and cytosine forms 1-D zig-zag networks of clusters.

Hydrogen bonded clusters of molecules have been observed which appear self terminating in size, and do not extend to give larger arrays. Böhringer *et al* [12–14] investigated the phases formed by 1-nitronaphthalene on Au(111). 1-D chains and both chiralities of 10-molecule clusters were observed using STM. The molecules became pseudochiral on adsorption, though the molecules are not geometrically enantiomeric when not restricted to a plane as with PVBA [7]. The 1-D rows form at ~ 0.1ML coverage with clusters forming at ~ 0.2ML coverage. High-resolution STM images and local density calculations reveal the orientations of individual molecules.

Hydrogen bonded molecular structures can be engineered through careful choice of functional groups, and can be considered as single entities as demonstrated by Keeling *et al* [15] who found that diimide interactions in naphthalene tetracarboxylic diimide (NTCDI) on Ag:Si(111)$\sqrt{3}\times\sqrt{3}$R30° mediate the formation of 1-D rows and close packed islands. The similar molecule NTCDA (dianhydride) was also deposited on Ag:Si(111)$\sqrt{3}\times\sqrt{3}$R30° and was not observed to form any hydrogen bonded structures. Thus the functional groups of adsorbate molecules can control, to some extent, the possibility of hydrogen bonded array

formation. The researchers demonstrate the manipulation of a row of hydrogen bonded NTCDI molecules across the surface as a single object using the STM tip.

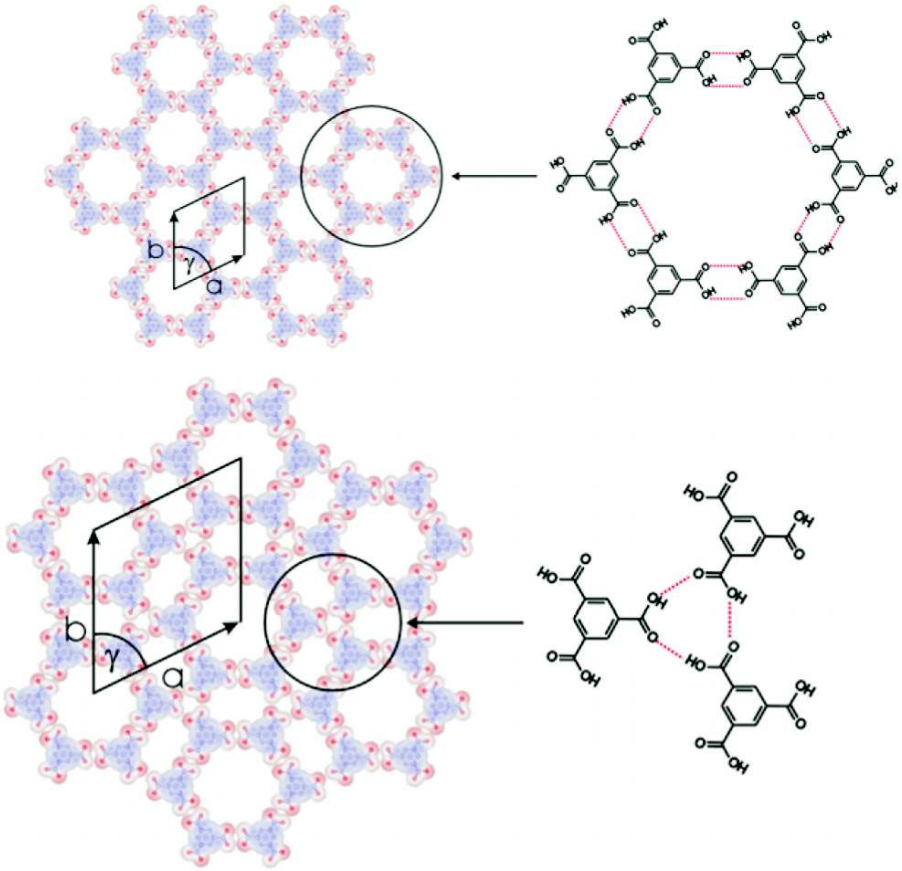

FIGURE 1.5: Trimesic acid molecules can arrange in different hydrogen bonding configurations to give these two structures on graphite (after Griessl *et al*) [16]

Hydrogen bonding between molecules need not necessarily lead to the formation of a single phase under a set of growth conditions, and different ordered phases can form together. The substrate on which the molecules are deposited also plays a crucial role in the possible ordering of the molecules, as does the temperature of the surface. Trimesic acid deposited in vacuum onto Cu(100) by Dmitriev *et al* [17] was found at low temperatures ($\sim$ 200K) to form two dimensional hexagonal networks stabilised by carboxylic acid hydrogen bonding interactions between neighbouring molecules. Increasing the temperature to room temperature allows the molecules to rearrange themselves, forming a stripe motif with molecules oriented such that they no longer lie flat, but the plane of the molecules is

oriented perpendicular to the surface. The molecules are bonded to the surface through the carboxylic acid groups. Griessl *et al* [16] deposited trimesic acid in vacuum onto naturally grown graphite (0001), and imaged two coexisting phases as shown in Figure 1.5. These two phases are labelled as a hexagonal phase and a flower phase, and they can coexist due to different possible bonding geometries in which the molecules arrange to form hydrogen bond stabilised networks. In the hexagonal configuration, each carboxylic acid group is hydrogen bonded to another carboxylic acid group on a neighbouring molecule, thus each trimesic acid molecule acts as a trigonal vertex. In the flower structure, each carboxylic acid group bonds to two neighbouring carboxylic acid groups, giving rise to units of three trimesic acid molecules which bond together in a different way. The open pores in the hexagonal networks were used to house further host trimesic acid molecules in various orientations.

Lackinger *et al* [18] investigated the adsorption of trimesic acid on highly ordered pyrolytic graphite (HOPG) using a liquid deposition method, and subsequently used STM to image the molecules at the liquid-solid interface. Both the hexagonal and flower phases were observed under ambient conditions but the yield of each phase was found to be dependent on the solvent used in its deposition. A range of alkanoic acids from butyric to nonanoic were used, and it was observed that the longer chain acids allowed the preferential formation of the hexagonal phase over the flower phase. Much pioneering work of molecular ordering at the liquid-solid interface has been achieved by de Feyter and de Schryver [1,19,20]. They have studied the arrangements of many long chain organic molecules including alcohols, fatty acids and amines, amongst others. The liquid-solid interface provides a different environment for a rich array of molecular adsorbate studies. This environment will not be discussed in detail in thesis, which looks only at molecular arrangements on surfaces in vacuum.

1.4 Bimolecular structures

Much research has focussed on the ordering of a single molecular species on a surface. Recently there has been interest in depositing two different species to investigate intermixed hydrogen bonded molecular structures. Two molecular species can interact to form interesting structures, relying on the properties of both species to form the arrangements observed. Early work involving the behaviour of two different molecular species and the resulting structures which formed in solution was performed by Whitesides *et al*. They

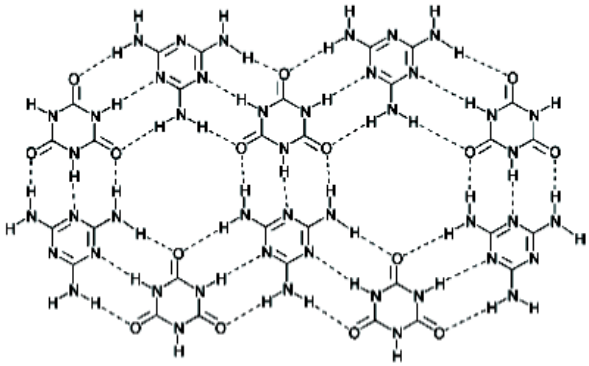

FIGURE 1.6: The triple melamine-cyanuric acid hydrogen bonding junction occurs as shown to form hexagonal arrays, both in solution and on surfaces. (after Perdigão *et al* [21])

investigated the formation of regular hexagonal arrays stabilised by N-H$\cdots$N hydrogen bonds by combining 1,3,5-triazine-2,4,6-triamine (melamine) and 1,3,5-triazine-2,4,6-triol (cyanuric acid) [22, 23]. This work has recently been extended by Perdigão *et al*, who studied two dimensional melamine-cyanuric networks on the silver terminated silicon surface Ag:Si(111)$\sqrt{3} \times \sqrt{3}$R30° [21]. These two species can hydrogen bond together to form an intermixed hexagonal network as shown in Figure 1.6.

However, two molecules on a surface need not necessarily intermix. A hexagonal hydrogen bonded network was formed on the HOPG surface using a tricarboxylic acid derivative, 1,3,5-tris(10-carboxydecyloxy)benzene (TCDB), by Lu *et al*, who then subsequently deposited a second species as a guest molecule to sit in the pores of the TCDB network [24]. Copper phthalocyanine (CuPc) and coronene were demonstrated to be suitable guest molecules, and a single guest molecule per pore is observed. This research demonstrates that careful molecular engineering, in this case the use of a triangular molecule with three $(CH_2)_{10}$COOH carboxylic acid terminated branches can be used to fabricate an open network with tunable pore size determined by the length of the molecular branches.

Theobald *et al* [25] studied the perylene derivative perylene3,4,9,10tetracarboxylic-3,4,9,10diimide (PTCDI) and melamine on Ag:Si(111)$\sqrt{3}\times\sqrt{3}$R30°, and found them to form a supramolecular hexagonal hydrogen bonded network (see Figure 1.7). At the vertex of each hexagonal pore a triangular melamine molecule is bonded to three PTCDI molecules by means of a triple hydrogen bond consisting of two O$\cdots$H-N bonds and a central N$\cdots$H-N bond. This triple hydrogen bonding configuration provides network stability. The network

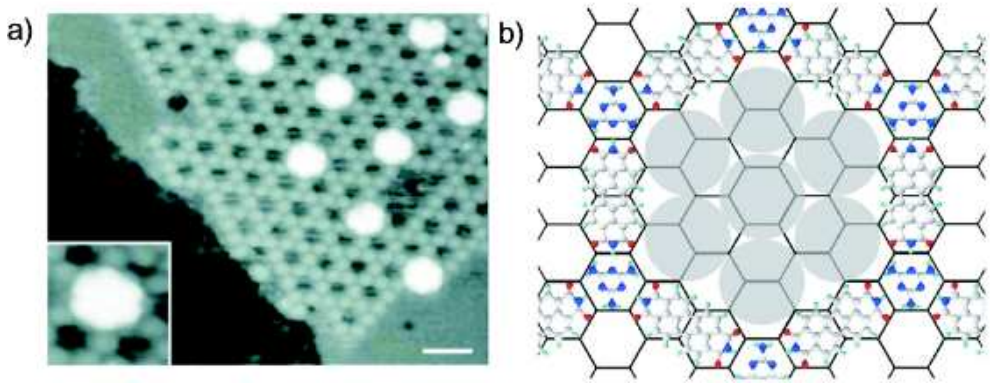

FIGURE 1.7: a) C_{60} heptamers captured in a PTCDI-melamine supramolecular network. Scale bar is 5nm, b) schematic of the supramolecular bonding and placement of the C_{60} heptamers in the network pores ((after Theobald *et al*) [25])

was then used as a template in which to house clusters of guest molecules. Heptameric clusters of C_{60} molecules (Figure 1.7) and different sized clusters of C_{84} [26] were observed to rest inside the network pores, and these clusters could then be manipulated using the STM tip and were manually placed in different pores in the network [27]. A similar network was formed, again using PTCDI and melamine, on the Au(111) surface by Perdigão *et al* [28] who observed it alongside a chiral intermixed arrangement. The molecular networks were used in a similar manner to that described by Theobald *et al*, to trap clusters of fullerene molecules, thus demonstrating that these networks can form on different substrates.

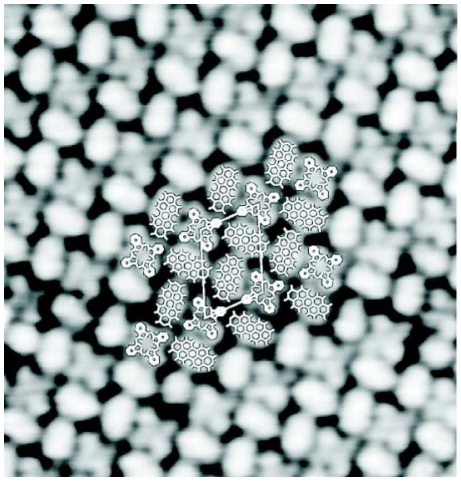

FIGURE 1.8: Cu-Pc and PTCDA molecules on Cu(111) forming an intermixed phase (after Bobisch *et al*) [29]

Aside from open networks, two molecular species can form close packed ordered structures on a surface. Bobisch *et al* [29] investigated PTCDA and copper phthalocyanine (Cu-Pc) on Cu(111). These two molecules interact on the surface to form domains of molecules comprised of 3-molecule chevrons; one Cu-Pc is bound to two PTCDA molecules and this unit is repeated to build up an ordered close packed phase. Another phase was observed consisting of rows of Cu-Pc molecules alternating with zig-zag rows of PTCDA, forming a second close packed structure (Figure 1.8).

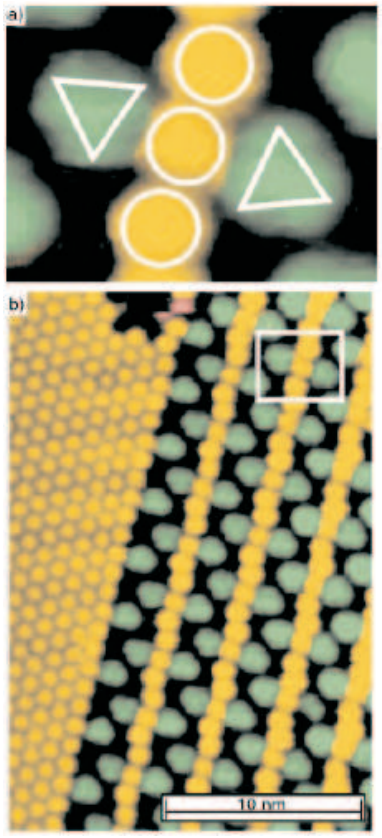

FIGURE 1.9: SubPc and C_{60} form coverage dependent intermixed phases on Ag(111). This image shows how two triangular SubPc molecules bond to a C_{60} molecule to form staggered chains, next to a region of close packed C_{60} (after de Wild *et al* [30])

The phases observed involving two molecular species can depend on the relative concentrations of each species. de Wild *et al* [30] investigated the phases formed by depositing chloro[subphthalocyaninato]boron(III) (SubPc) and C_{60} on Ag(111). The intermixed phases formed were found to be coverage dependent, and by changing the ratio of SubPc:C_{60} on the surface several different motifs were observed (Figure 1.9) including 1-D C_{60} chains

and star motifs.

1.5 Summary

A great deal of effort has been spent in understanding ordered molecular adsorbate systems. From single species to bimolecular arrangements, including host-guest networks and intermixed phases, both in vacuum and at the solid-liquid interface, there are many possibilities for the formation of self assembled surface nanostructures with controllable feature size and directionality. This research area of molecular adsorbates is growing rapidly, with related areas of interest including metal-coordination bonded systems, which involve stronger bond strengths. Future work is likely to concentrate on careful molecular design to produce species which will form specific molecular structures. It may be possible to build into the molecular structure some chemical functionalisation which is active in network pore sites. There is much still to be learned about how different molecules interact with the surface and each other, which will lead to a greater understanding overall of surface architectures and how we can tune molecular properties to our specific requirements. There are potential applications in biophysics, semiconductor physics, quantum computing and many other areas of research. Future challenges also include contacting nanoscale structures to the macroscopic world, and incorporating more complex functionality for specific tasks.

This chapter outlines the importance of hydrogen bonding, and provides an overview of recent work in which hydrogen bonding between molecules facilitates the formation of interesting nanostructures, whose morphology depend on temperature, coverage, surface chemistry, and relative molecular proportions.

Chapter 2

Scanning probe microscopy

This chapter introduces the nanoscale surface imaging technique of scanning tunnelling microscopy (STM), including electron tunnelling and instrumentation, and provides a brief overview of atomic force microscopy (AFM).

2.1 Scanning tunnelling microscopy (STM)

Scanning tunnelling microscopy (STM) was pioneered as an imaging technique by Binnig and Rohrer in 1982 [31]. It is a real space, high-resolution imaging method exploiting quantum-mechanical electron tunnelling between a sharp tip and the sample whose surface is imaged. The tip is raster scanned over the surface and a topographic image is obtained. Though quantum theory in the 1920's postulated the tunnelling of electrons through vacuum, several advances in vacuum technology, electronics and quantum theory were required before STM became a laboratory technique. This chapter explains the nature of electron tunnelling through vacuum, discusses the STM instrumentation used in this thesis, and how STM allows images of surfaces to be obtained on the nanoscale.

2.2 Electron tunnelling

Electron tunnelling is a quantum mechanical phenomenon forbidden in classical mechanics, and involves electrons travelling between two electrodes. In STM the electrodes are the tip and the sample; these must both be conductors. In the simplest case, the electron tunnelling may be mathematically represented by a 1-D rectangular potential barrier, where the barrier represents the vacuum between the tip and sample. There is a finite probability of electrons travelling through the classically impenetrable barrier due to their wave-like nature. The

electron wavefunctions either side of the barrier decay into it. A narrow enough barrier allows the wavefunctions to overlap and electron tunnelling is then possible. Application of a bias voltage results in the flow of a quantum mechanical tunnel current.

Figure 2.1 shows a schematic 1-D rectangular barrier which we can consider using Schrödinger's equation.

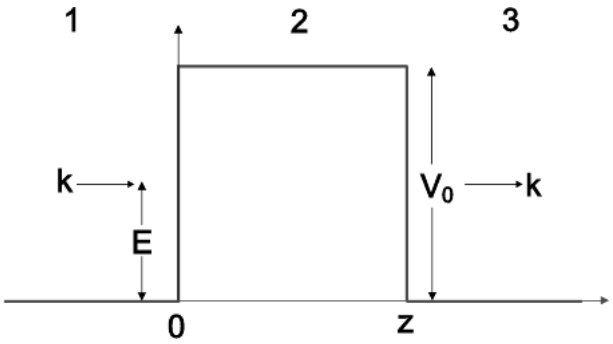

FIGURE 2.1: A rectangular barrier in a one dimensional quantum mechanical system. Electrons (wavevector k) can tunnel from the left through the barrier to the right with a finite probability dependent on the height and width of the barrier.

Assuming a rectangular barrier of width z and height V_0, and considering an electron with energy E, wavevector k and mass m, we can solve the time independent Schrödinger wave equation in the three regions marked in Figure 2.1.

For region 1,

$$\frac{-\hbar^2}{2m}\frac{d^2\Psi}{dz^2} = E\Psi$$

$$\Psi = Ae^{ikz} + Be^{-ikz} = e^{ikz} + Be^{-ikz} \qquad \text{as} \qquad A = 1$$

$$\text{with} \qquad k^2 = \frac{2mE}{\hbar^2}$$

For region 3,

$$\frac{-\hbar^2}{2m}\frac{d^2\Psi}{dz^2} = E\Psi$$

$$\Psi = Fe^{ikz} + Ge^{-ikz} = Fe^{ikz} \qquad \text{as} \qquad G = 0$$

For region 2,

$$\frac{-\hbar^2}{2m}\frac{d^2\Psi}{dz^2} + V_0\Psi = E\Psi$$

$$\Psi = C'e^{ik'z} + D'e^{-ik'z} = Ce^{iKz} + De^{-iKz}$$

where $K = -k' = \sqrt{\frac{2m(V_0 - E)}{\hbar^2}}$ is known as the inverse decay length.

From a consideration of the continuity of Ψ and $\frac{d\Psi}{dx}$ at $x = 0$ and $x = z$, the coefficients B, C, D and F may be determined (Ref. [32] pp105-107). $A = 1$ since the term Ae^{ikx} refers to an incident plane wave travelling from left to right on the left of the barrier. Similarly $G = 0$ since the term Ge^{-ikx} refers to the wave propagating from right to left on the right of the barrier. We are interested in the transmission of the electron through the barrier so the transmission current density j_t is such that

$$j_t = \frac{-i\hbar}{2m}(\Psi^* \frac{d\Psi}{dx} - \Psi \frac{d\Psi^*}{dx})$$

$$j_t = \frac{-i\hbar}{2m}|F|^2$$

Similarly for the incident current density

$$j_i = \frac{-i\hbar}{2m}$$

Thus the transmission coefficient $T = \frac{j_t}{j_i} = |F|^2$

T is found to be a continuous finite function of barrier width and height dominated by the term e^{-2Kz}, thus the tunnel current $I \propto e^{-2Kz}$. In an STM, the barrier, with a typical width of 5Å and height of 4eV, is the vacuum gap between the tip and the sample. Thus the separation z between them must be of the order of a few Ångstroms in order for tunnelling to be significant. Since most work functions are of the order 4eV, typically $2K \sim 2\text{Å}^{-1}$, and thus a 1Å change in the separation between the tip and sample z has an order of magnitude effect on the current, due to the exponential relationship. This exponential relationship ultimately accounts for the high spatial resolution of the STM technique.

A more realistic theoretical treatment of the 1-D rectangular energy barrier includes rounded barrier edges which are present due to image charges existing in the two electrodes [32]. An alternative to considering a rectangular barrier is to examine electron tunnelling through an arbitrary shaped barrier using the WKB approximation (after

Wentzel, Kramers and Brillouin in 1926). This is a one dimensional model, though a three dimensional generalisation has been studied by Das and Mahanty [33] who show that the maximum tunnel current is found directly under the tip. A 1Å separation of the electrodes changes the measured tunnel current by an order of magnitude, and thus a macroscopically blunt tip may be able to image atoms, as it is the very end of the tip which provides the major contribution to the tunnel current. A blunt tip will, however, give poor resolution images of surface corrugations (see Figure 2.11c)).

A more thorough theoretical treatment of the tunnelling phenomenon for a small electron transmission barrier may be applied using time dependent perturbation theory [34]. Instead of using exact solutions to the equations, which is not realistic for this problem, Bardeen proposed an approximation to give an expression for the transmitted tunnel current j_t, which relies on a tunnelling matrix element $|M_{rl}|$ and the density of states in the final state $\frac{dN}{dE_r}$ [35]. This solution may be written as:

$$j_t = \frac{2\pi}{\hbar}|M_{rl}|^2 \frac{dN}{dE_r}$$

From this treatment it can be seen that the local density of states is detected and contributes to the measured tunnel current in STM. This time dependent solution and the simpler time independent solution given earlier are actually equivalent in this case, though the time dependent treatment is more generally applicable.

2.3 Imaging using tip-sample tunnelling

In the experiments presented in this thesis we are normally concerned with a semiconducting surface. Figure 2.2 is an energy level diagram for a metal-semiconductor junction separated by a vacuum energy barrier. The metal tip represented on the left of the figure has electrons in energy states up to the Fermi level E_F^{Tip} (strictly this occurs at 0K). In the semiconducting sample on the right of the figure electrons exist in the valence band, which lies below the Fermi level E_F^{Sample} for a lightly doped p-type semiconductor such as the Si samples used in this thesis. The empty electronic states of the semiconductor lie in the conduction band above the Fermi level. In Figure 2.2a), the Fermi levels of the tip and the sample are aligned and there are no free states into which electrons can tunnel. In Figure 2.2b) the tip has a positive voltage bias applied and electrons can tunnel from the occupied states of the sample into the unoccupied states in the tip. Conversely, in Figure 2.2c) the sample is

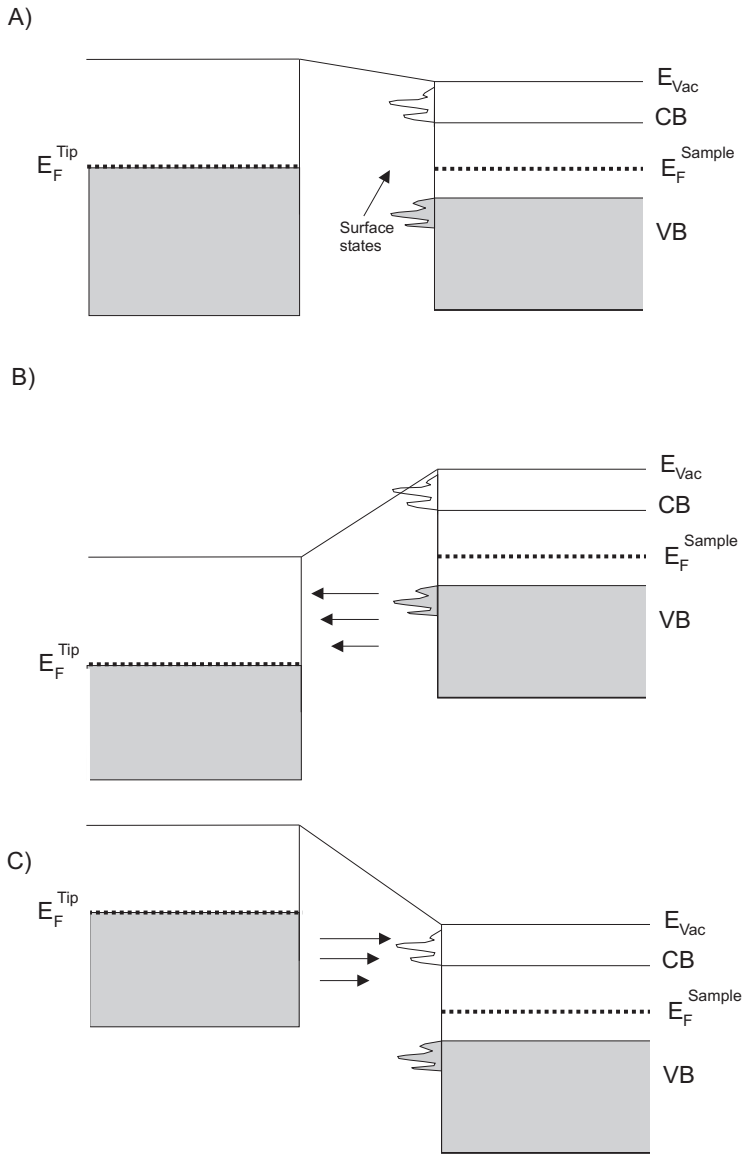

FIGURE 2.2: This energy level diagram shows a metallic tip on the left with continuous occupation to the Fermi level, and a semiconducting surface on the right with surface states, separated by an energy gap, with idealised band structures [36][2]. VB - valence band, CB - conduction band, E_F - Fermi level, E_{vac} - Vacuum level. a) No bias is applied, and there are no states available for electrons to tunnel into. b) Here the tip has a positive bias applied. Electrons can tunnel from the valence band of the sample into the empty states of the metal tip. c) The sample is biased positively, thus the electrons can tunnel into the conduction band of the sample from the tip.

positively biased with respect to the tip and so electrons from the tip can tunnel into the empty states of the sample. To create an image of a surface using STM, the tunnel current

must be measured in many places over the sample surface, by raster scanning the tip over the region of interest. The tunnel currents measured provide a representation of the local density of states of the surface.

With a semiconducting sample, the polarity and magnitude of the bias applied can have a significant effect on the images obtained, as different electronic states of the sample are accessed. A famous example is that of the semiconductor GaAs (Figure 2.3), where the valence band states are localised on the As atoms in filled dangling bonds, and the conduction band states are localised on the Ga atoms as empty dangling bonds. As such, imaging clean crystalline GaAs biased positively and negatively results in selective imaging of the Ga and As atoms respectively. It is important to obtain the positive and negative bias images simultaneously as each atom, Ga or As, appears roughly as a round bright feature and their relative positions must be known in order to fully understand how the surface atoms are arranged.

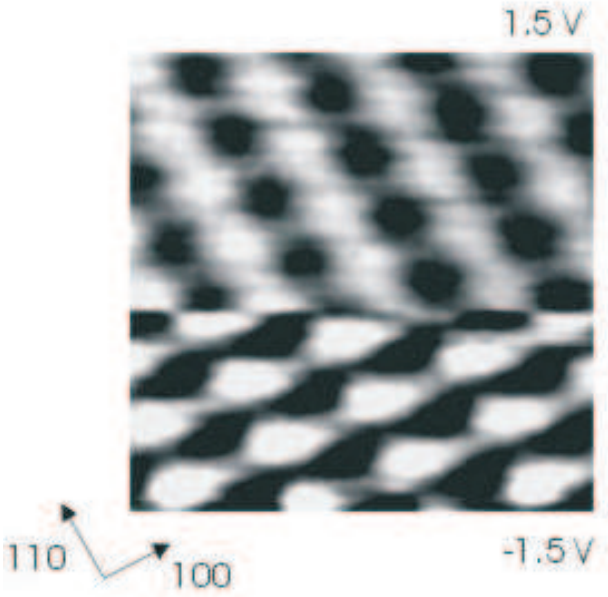

FIGURE 2.3: This is an STM image of the GaAs (110) surface. At positive sample bias (top of image), only tunnelling into the Ga atoms empty states is observed. At negative sample bias (bottom of image), only the filled As dangling bonds are imaged (after Gebauer *et al* [37])

When imaging organic adsorbate molecules, the electron tunnelling occurs between the tip and the occupied or unoccupied molecular orbitals. One can determine the orien-

tation of individual molecules by examining their representation in an STM image as STM provides a representation of the local density of states of a surface. In Chapter 5 it is demonstrated by comparison of the appearance of a PTCDA molecule in STM images to the shape of the calculated highest occupied molecular orbital (HOMO), that the position of a single molecule may be deduced. However, the appearance of a single molecule may also vary due to its adsorption site on the surface and on the arrangement of neighbouring molecules. A particularly high resolution STM study of PTCDA on Ag(111) by Eremtchenko *et al* [38] reveals that the detailed molecular orbital structure of a single PTCDA molecule can be resolved, as shown in Figure 2.4. Here the researchers compare the calculated lowest unoccupied molecular orbital (LUMO) shape to the appearance of PTCDA molecules observed in STM images.

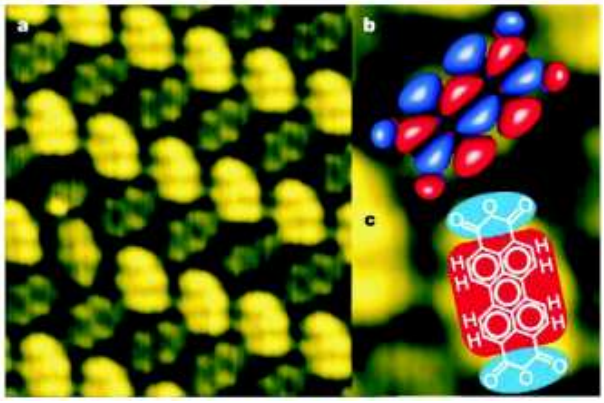

FIGURE 2.4: PTCDA on the Ag(111) surface. a) STM image of PTCDA herringbone phase (7nm^2, current 0.46 nA, sample bias -2.3 V); b) Calculated probability density of the LUMO of PTCDA; c) Chemical structure of PTCDA, with schematic indication of intramolecular charge distribution (red shows positive, and blue shows negative, partial charges) [38].

2.4 Moving the STM tip

It is necessary to position the STM tip accurately over the surface in order to construct an image. The tip is mounted on a piezoelectric crystal device which can accurately move (sub-Ångstrom increments) the tip over the sample surface by raster scanning in the $x-y$ plane, and perpendicularly to the surface in the z direction. This device can be a piezoelectric scan tube, or three individual crystals for movement in the three orthogonal directions x, y and z. The tip can ideally move with sub-Ångstrom precision, and a good STM scanning

mechanism must also have high resolution, linearity, orthogonality, mechanical rigidity and a large range [34]. The STM used in this thesis employs a scan tube for tip positioning, as shown in Figure 2.5. The tube is made of a piezoelectric material and is split into four quadrants which are contacted on the outside, whilst the inside of the scan tube is attached to a ground connection. The tube in Figure 2.5b) has a voltage δV applied to all four quadrants resulting in a movement in the z direction. Voltages of $\pm$V applied to the quadrants as shown cause an overall lateral movement.

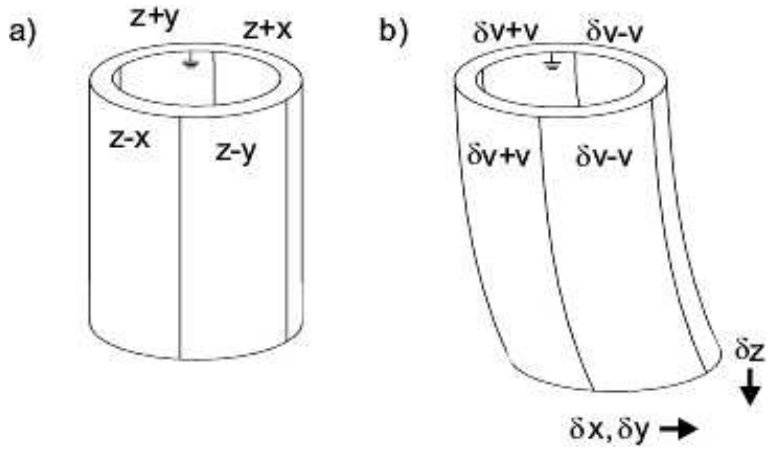

FIGURE 2.5: a) Piezoelectric scan tube with no potential applied. b) A potential δV applied to all quadrants extends the crystal in the Z direction, whilst $\pm$V applied as shown causes a lateral movement.

Two scanning modes are commonly used in STM. The mode used in this thesis is called constant current mode. Here the tip is allowed to move in the z direction during scanning in order to maintain the constant tunnel current as the tip scans across the surface. The detected tunnel current is exponentially dependent on the tip-sample separation (Section 2.2), and in order to maintain a constant current the z-position of the tip is adjusted using a feedback system. At each point on the surface the tip height is adjusted such that the detected tunnel current equals a pre-defined setpoint current. The changes in height required to maintain this setpoint current during the scan are converted into an image of the surface. The setpoint is usually of the order 0.1nA. The other scanning method used is called constant height mode. In this mode the tip is raster scanned over the surface at a constant height, thus the scan tube does not extend in the z direction. As the tip-sample separation changes during the scan due to surface corrugations, so the measured tunnel current changes accordingly. These current changes are recorded and converted into a to-

pographic surface image. The disadvantage of constant height mode is that if the surface is particularly rough, the height differences of the surface can be large enough to cause the tip to crash into the surface. For this reason constant height mode is not used in this thesis. Constant height mode, however, is much faster than constant current mode, since the height of the tip is not constantly changing to meet a pre-defined setpoint. Constant height mode also has the advantage of not suffering from low frequency noise, which is not detected due to the fast scan rate.

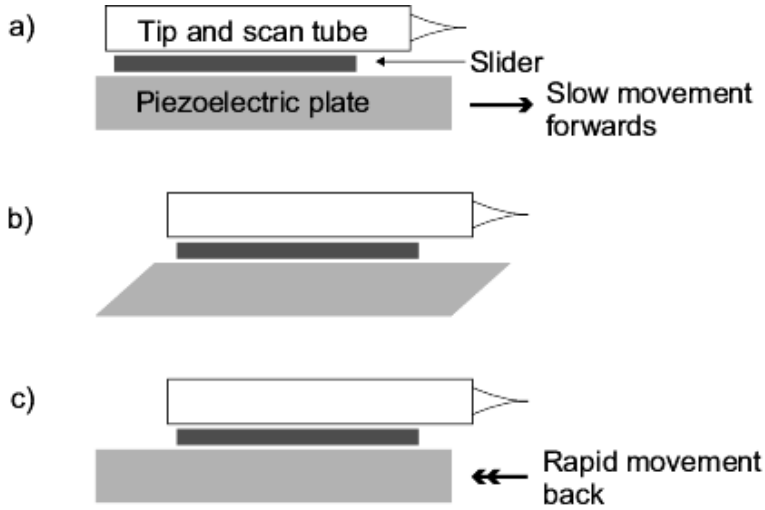

FIGURE 2.6: Slip-stick movement of the tip. a) and b) A voltage is slowly applied to the piezoelectric plate causing a shear movement and the tip and scan tube move forwards. c) The piezoelectric plate is grounded causing a rapid movement back to its original state. The tip and scan tube remain forwards of their initial position as the slider slips on the surface of the piezoelectric plate.

In order to manoeuvre the tip over larger distances than is possible with the scan tube alone (to perform tip or sample transfers, or look at a different area on the surface), a coarser movement device is used. A schematic of the apparatus and movement process is shown in Figure 2.6. The scan tube is attached to a slider on slip stick motors (shear mode piezoelectric plates) which can position the tip over the sample in the x and y directions and away from the sample in the z direction.The slip stick motors are connected to a high voltage waveform generator ($\pm$150V). Initially an exponential waveform is applied to the piezoelectric plate, which causes it to slowly distort in a shear movement, thus moving the slider forwards on which the scan tube is held by friction. The piezoelectric plate is then very quickly (a few μs) snapped back into its rest position by the application of a ground

connection. The crystal moves back to its rest position so quickly that friction cannot hold the slider on the plate's surface and it maintains its position forwards of where it started. Thus the tip is moved forwards. This process is repeated to move the sliders and therefore the scan tube and tip in the required direction.

During image acquisition in constant current mode, the tip is raster scanned across the surface by the scan tube and the tunnel current between the tip and the sample surface is detected by a preamplifier. The current is converted to a voltage using an I to V converter and then input to a controller. This voltage is then converted to a digital signal using an analog-to-digital converter (ADC) and is compared to a pre-defined setpoint (the user defined tunnel current setpoint). The z position of the tip is then adjusted to equalise the detected and pre-defined voltage values. The necessary z alteration is calculated using a proportional-integral (PI) feedback algorithm. This feedback voltage is then superimposed on the waveform controlling the tip movement, and output to the scan tube which moves the tip. The changes in z required to maintain a constant current are recorded and used to create a topographic image of the surface.

2.5 Nottingham STM

The STM apparatus used in this thesis is housed in a three chamber ultra high vacuum (UHV) system, as shown in Figure 2.7. The base pressure is maintained at $\sim 1 \times 10^{-10}$ torr by an ion pump at the base of each chamber (B, C, D). The sample entry chamber (A) is pumped by a scroll backing pump and a turbomolecular pump, and is used for changing the tip or sample. Each chamber B, C, D has a titanium sublimation pump (TSP), used for maintaining the low pressure. An UHV environment is important to ensure that samples are not contaminated. Samples such as clean Si (111) are very reactive and vacuum is required for an atomically clean surface to be maintained. Chamber D is used for the deposition of well characterised organic molecules and silver, and is used for cleaning silicon. Chamber C houses the STM head, and chamber B is used for sample annealing and deposition of less well characterised organic materials.

A schematic diagram of the STM head is shown in Figure 2.8. The main features are: the slip stick motors, which allow for a coarse positioning of the tip; the spring suspension, which provides vibrational isolation; and the tip, which is mounted on the piezoelectric scan tube. The clamp holds the head firm when tip or sample transfers are

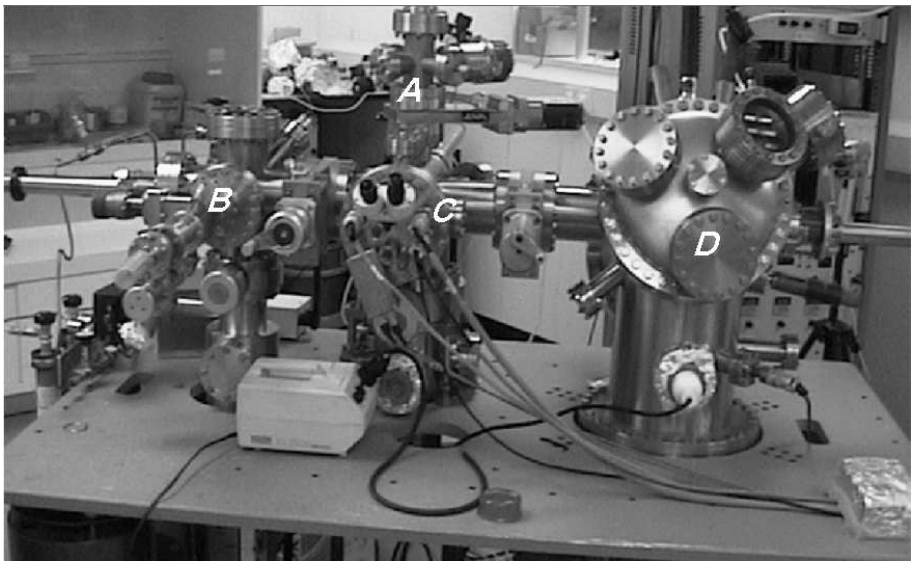

FIGURE 2.7: The STM system used. Chamber A is the load lock, Chamber B is used for indirect sample heating and for deposition of unfamiliar organic molecules. Chamber C houses the STM, and Chamber D is the main deposition chamber and is also used to prepare silicon.

being performed to avoid damaging the mounting springs. The viewport is used to monitor coarse tip positioning.

Samples are mounted in sample holders (Figure 2.9) which allow both direct and indirect heating. The samples used are $\sim 3 \times 7\text{mm}^2$ in size and a sample is held on a sapphire (insulating) disc by two tantalum clips. The sapphire disc sits on a Macor ceramic unit which in turn rests on two halves of a phosphor bronze disc. The tantalum screws fasten the clips each to one half of the phosphor bronze disc, allowing a current to be passed directly through the sample. Passing a current through a silicon sample cleans it via direct resistive heating; this is known as flashing the silicon as it glows bright orange during this high temperature ($\sim 1200°\text{C}$) heating. Indirect heating can be used for low temperature annealing of samples, and is achieved in Chamber B using the yoke in which the sample holder is held, which has a fine tungsten filament in ceramic housing around it. This filament may have a current passed through it to heat the sample surroundings, which heats the sample up to 150°C. The steel pins hold the sample holder in the yoke, STM head, or other holder in the system.

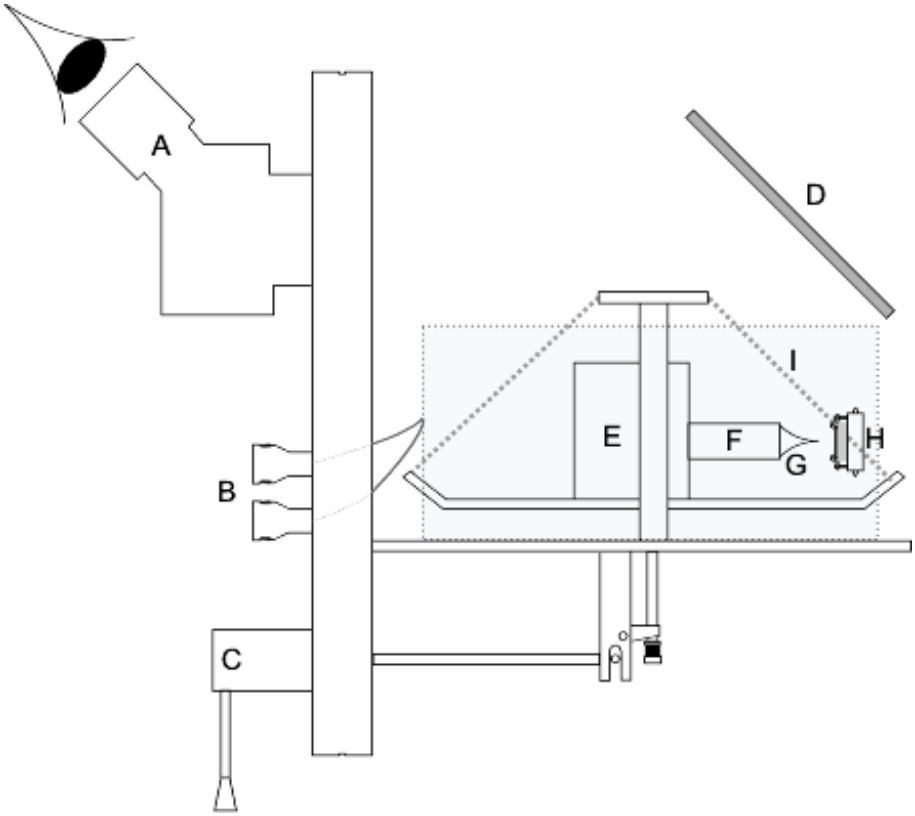

FIGURE 2.8: The STM head features. A - Microscope viewport, B - Electrical feedthroughs, C - Clamp, D - Mirror, E - Sliders on slip-stick motors, F - Scan tube, G - Tip, H - Sample holder and sample, I - Springs.

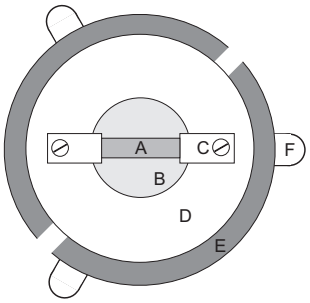

FIGURE 2.9: Schematic of the sample holders used in STM work. A - Sample, B - Sapphire disc, C - Tantalum clip and screw, D - Macor housing, E - Phosphor bronze plates, F - Steel bayonet.

2.6 STM tip preparation

The arrangement used for preparing STM tips is shown in Figure 2.10. Tungsten wire is held in a tip nut which is later attached to the scan tube. Tungsten is a popular choice

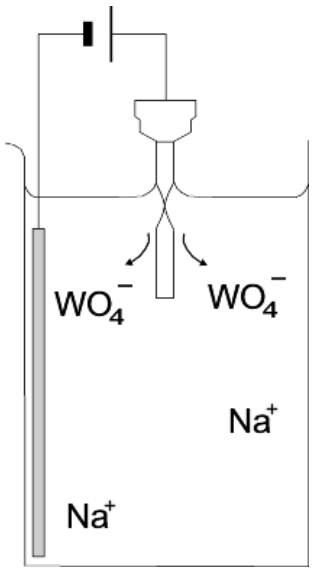

FIGURE 2.10: The STM tip is made by chemically etching a tungsten wire in NaOH solution. The cathode is a plate inside the beaker; the anode is the wire itself.

for UHV STM as it is relatively cheap and easily etched. A $\sim$ 1cm piece of wire is left to protrude from the tip nut and this protrusion of wire is held in a beaker of strong NaOH solution (see Figure 2.10). The tip nut is attached in the electrolysis circuit as the anode, and a cathode plate is present in the beaker of solution. Negative hydroxide ions are formed during electrolysis and react with the tungsten wire to form tungsten oxide ($WO_4{}^{2-}$) ions. The wire is etched preferentially at the solution meniscus. A sharp tip is formed when the excess wire in the solution can no longer remain attached at the etch point and falls off under its own weight. It is important to clean the tip nut and wire before etching in (sequentially) acetone, methanol and isopropyl alcohol (IPA) in a sonic bath, as the wire is not clean enough for UHV use otherwise. After loading a new tip into the UHV system via the load lock chamber A, it is cleaned by electron beam heating before being positioned on the end of the scan tube.

An ideal tip is one which terminates in a single atom, shown schematically in Figure 2.11a). As the measured tunnel current depends exponentially on the tip-sample separation, atoms further away from the surface than the terminal tip atom will contribute negligibly to the overall tunnel current. The macroscopic geometry of the tip also has a direct effect on the images obtained. A sharp tip is desirable in order to clearly resolve surface corrugations, as shown in Figure 2.11b). A sharp tip can be moved across the surface and can accurately

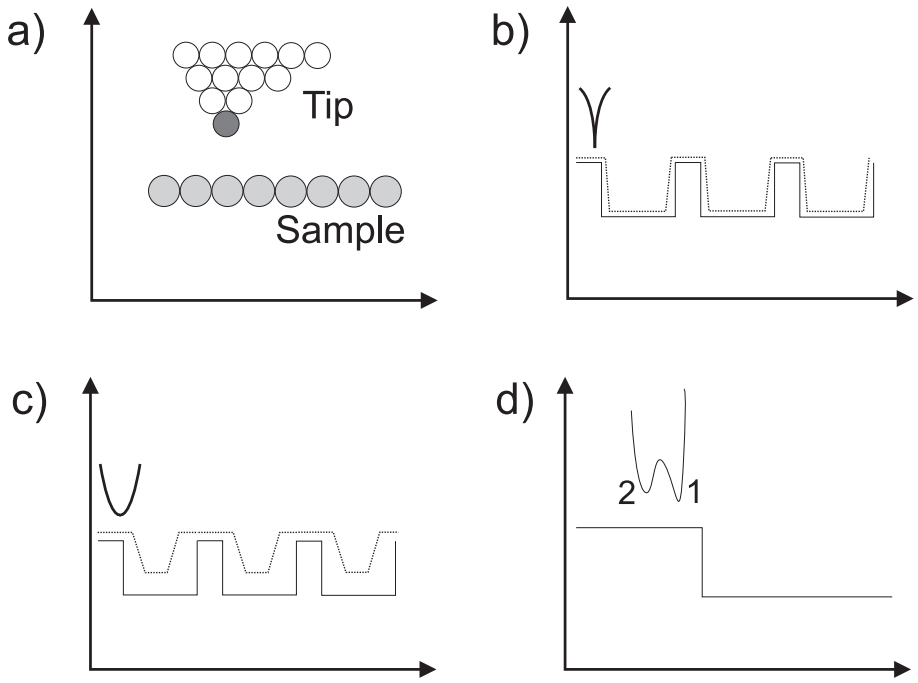

FIGURE 2.11: a) An ideal STM tip is one which terminates in a single atom, so atomic features may be resolved. b) A sharp tip can move across the surface and pick out small features in the surface giving a high resolution image. c) A blunt tip cannot accurately trace the surface topography so the images will appear blurred and any fine detail will be smeared out. d) A double tip effectively images the sample twice (firstly tip 1 moves over the step edge then tip 2 will copy the image) giving 'ghost' features.

trace the peaks and troughs in the surface topography. STM image resolution is lower if the tip has a low aspect ratio (Figure 2.11c)), as the tip cannot accurately trace the surface corrugations and images appear blurred. If images of the surface contain lots of identical 'ghost' features, and large surface features such as step edges and adsorbates appear to have a twin shadow, the tip may have a double point (Figure 2.11d)). In this case tunnelling occurs first through tip 1, then when the tip position has been adjusted, tunnelling occurs again through tip 2.

Tips can become contaminated by attracting loosely bound adatoms which are then dragged across the surface. The tip may be cleaned by passing a voltage pulse through it to remove any adhered adatoms. This voltage pulsing also usually changes the profile of the tip end and can remove a double tip, or cause the tip to become sharper. Streaking in images can also be due to loosely bound adatoms diffusing over the surface.

Noise in images also reduces resolution. Switching off the ion gauges during scan-

ning can reduce vibrational noise. Noise in images may also be caused by coupling between the STM chamber and the surrounding environment via trailing wires, and from external vibrations such as a nearby door slamming. A tip which is not held firmly in the tip nut or scan tube may also cause vibrational noise. Vibrational isolation of the STM head is achieved by decoupling the head from the chamber by mounting it on springs, which in turn are attached to posts held with Viton (UHV rubber) to the chamber; the Viton provides vibrational damping. The STM chamber itself rests on a pneumatic air table.

2.7 Atomic force microscopy (AFM)

Atomic force microscopy (AFM) is a scanning probe microscopy technique which can be used to obtains images of surfaces on the nanometre scale, including both conducting and insulating surfaces. In this thesis AFM was used to image carbon nanotubes and polymers on SiO_2 which were deposited by electrospray deposition (see Chapter 7).

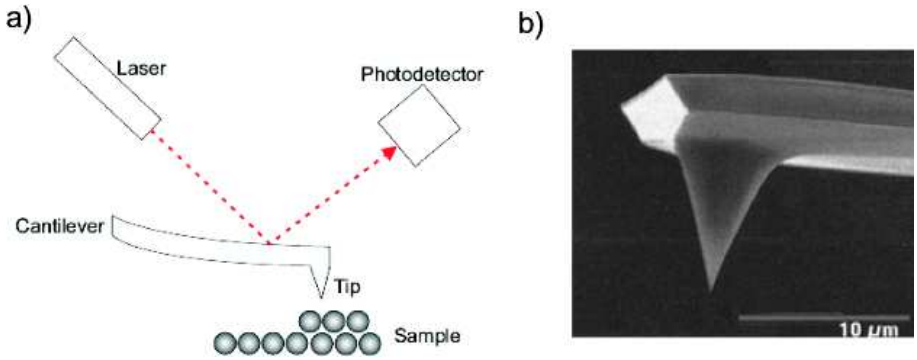

FIGURE 2.12: a)The AFM tip on the end of a cantilever moves across the sample surface. Deflections of the cantilever due to forces on the tip from the surface are detected using the reflection of a laser beam, the position of which is detected using a photodiode device. b) Image of a typical AFM tip on the end of a cantilever [39]

AFM employs an atomically sharp tip on the end of a cantilever. The tip is raster scanned over the region of interest on a surface and by monitoring the behaviour of the tip during scanning a topographic image may be obtained. The sample topography is detected by measuring the force, or force gradient, experienced by the tip, which depends on the tip-sample separation. The displacement of the cantilever due to forces from the surface may be detected in different ways, but commonly optical detection is used. A laser beam is reflected from the rear side of the cantilever (shown in Figure 2.12.) The position of

the laser beam is detected using a photodiode device, so that a change in the deflection of the cantilever during scanning changes the position on the diode where the reflected beam strikes. The AFM used in this thesis is a Dimension Multimode which makes use of a photodiode detector which is split into four quadrants to detect the reflected laser beam position.

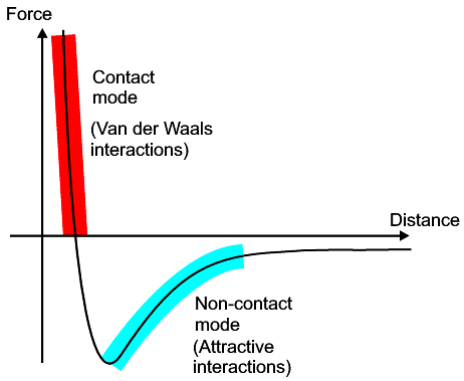

FIGURE 2.13: The van der Waals forces which exist between atoms determine the imaging regime used in atomic force microscopy. At small distances we image in contact mode with repulsive forces, and in non-contact AFM the tip-sample distance is much larger giving rise to attractive forces between the tip and the sample. Tapping mode is a combination of the two imaging modes and is used in this thesis.

Unlike STM, the dependence on the forces present between tip and sample is used to create the image, rather than detection of a tunnel current. This makes AFM a lower resolution technique than STM but one capable of imaging insulating surfaces and imaging larger regions than STM. A force-distance relation is shown in Figure 2.13 to illustrate the different types of interactions possible which give rise to the different imaging modes used in AFM. There are three such imaging modes: contact mode, non-contact mode, and tapping mode. Contact mode is concerned with repulsive van der Waals interactions at small separations, and non-contact mode uses attractive interactions at larger tip-sample separations. Tapping mode is a combination of these two modes.

In contact mode the tip is brought into close proximity to the surface such that the forces present between the tip and the sample are repulsive interactions. The resulting cantilever deformation obeys Hooke's law. The tip is raster scanned over the sample and the cantilever responds to changes in the interaction force experienced by the tip due to the contours of the sample surface. This cantilever deformation is detected by either using a feedback loop to measure the experienced force and move the tip in the z direction to

maintain a constant deformation, or by keeping the z height constant and measuring the deflection of the cantilever due to the surface corrugations. The changes in height required, or the deformation measured, at each sampled position on the surface are converted into a topographic image. A drawback of this scanning mode is that soft surfaces can easily become damaged as the tip is dragged across them. Also the tip lifetime can be relatively short due to prolonged contact with the sample.

In non-contact mode the separation between the tip and sample is kept at a few tens of nm and thus the force interaction between the two is attractive. The magnitude of the forces present between tip and sample is much smaller than that in contact mode. In non-contact mode the cantilever is driven into oscillation close to its resonant frequency using a piezoelectric crystal. As the separation changes between the tip and sample during scanning due to the presence of surface features, so do the force gradients present as detected by the oscillating tip. Thus the spring constant and hence the resonant frequency of the cantilever changes, which alters the size of the oscillation as measured using a laser probe. A feedback loop acts to maintain a constant oscillation amplitude by adjusting the tip-sample spacing during scanning. An image of the force gradients detected over the surface can be formed. This method can be difficult to operate in ambient conditions as atmospheric water vapour can cause the tip and sample to be attracted to one another through capillary effects; the attraction due to this contaminant fluid layer is larger than the effect from van der Waals. However, a surface roughness of as little as 5nm may be detected when scanning is possible.

In tapping mode, which is the mode used in this thesis, a combination of contact and non-contact mode is employed. The cantilever is driven into oscillation close to its resonant frequency at relatively high amplitude (higher than that used in non-contact mode, at > 20nm), in close enough proximity to the surface that the tip intermittently taps the sample for a fraction of its oscillation period. The surface is detected by changes in the magnitude of oscillation of the cantilever. During scanning the amplitude of the cantilever oscillation is maintained by using a feedback loop. As the tip moves over a protrusion on the surface its amplitude of oscillation decreases. Similarly when the tip moves over a surface depression the magnitude of oscillation increases. The oscillation is monitored by a reflected laser beam and input to the microscope electronics. The feedback adjusts the tip-sample separation to maintain a constant oscillation amplitude and these adjustments are translated into a surface topography. When the tip makes contact with the surface, the

high frequency cantilever oscillations reduce possible adhesion forces, making tapping mode less susceptible to problems than non-contact mode due to the tip sticking to the surface. The brief contact between tip and surface can be measured and translated into a map of the surface showing adhesion characteristics. Tapping mode can also be used to scan relatively large areas and the tip lifetime is much longer than that found using contact mode.

Cantilever designs vary widely and are constructed with different spring constants, in different materials and with various tip sharpness and morphology available for different imaging techniques. In this thesis AFM was used to image samples which do not require any specialised care or handling, so standard cantilevers were used with a resonant frequency of about 75kHz.

2.8 Summary

STM is an imaging technique ideally suited to visualising nanoscale surface structures of conducting samples. A quantum mechanical tunnel current between a sharp tip and the surface of interest is monitored and used to build up an image of the surface by probing the local density of states of the sample. STM has a high spatial resolution, depending on the quality of the tip, and by varying the bias applied to a semiconducting sample different images of the surface are recorded. Similarly when imaging molecules on surfaces, varying the sample bias results in different molecular orbitals being probed.

AFM is another imaging technique used in this thesis for examining electrosprayed samples of insulating materials, including polymers and carbon nanotubes. In tapping mode a resonating cantilever with a sharp tip at the end oscillates close to the sample surface, and changes in sample height result in a change of the force experienced by the tip, which in turn affect the resonant frequency of the cantilever. A topography can thus be obtained of the surface.

Chapter 3

Synchrotron radiation

This chapter explains what a synchrotron is, why they are useful facilities for the study of surfaces, and how a synchrotron operates. The techniques of core level photoemission and valence band photoemission are explained along with a description of the information which may be obtained from them. The process of data calibration is also discussed.

3.1 Why use synchrotron radiation?

Photons (light quanta) are a useful tool with which to study matter through a myriad of techniques. Photons of different wavelengths are suited to probing different samples. For example, infra-red radiation is of a similar energy to atomic and molecular vibrations, while hard x-rays are of the required wavelength for probing the crystal structure of materials. Synchrotrons can be used for a wide variety of experiments in many scientific disciplines. In this thesis the synchrotron based investigations focus on using ultra violet (UV) and soft x-rays in valence band and core level photoemission studies of molecular adsorbates on surfaces.

Light, as an electromagnetic wave, has wavelength and frequency linked by $\nu = c/\lambda$, where ν is the frequency of the light, c is the speed of light and λ is the wavelength. Also, light as a photon has an energy, E, which can be expressed as $E = h\nu$ where h is the Planck constant. In this thesis, for photoemission studies, photons are required with energies comparable to the typical energy required to remove either a valence or core level electron from an atom. These energies lie in the ultra violet and soft x-rays range with energies between $\sim 20 - 700$ eV. Figure 3.1 shows the electromagnetic spectrum, with the range of photon energies accessible at a synchrotron shown on the left of the figure in yellow.

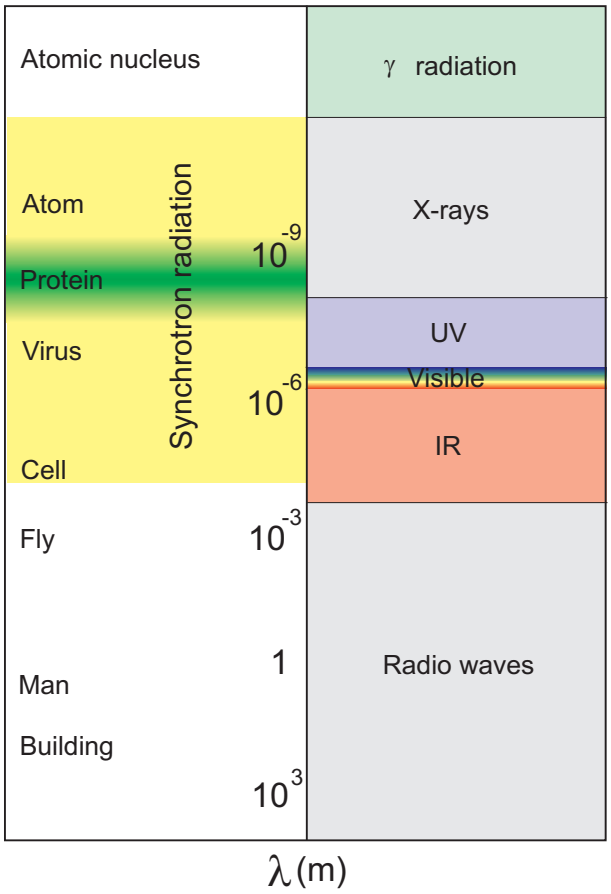

FIGURE 3.1: The electromagnetic spectrum. Wavelengths are indicated alongside objects of similar dimensions. The yellow region on the left indicates the range of photon wavelengths available in synchrotron radiation, and the green region is the approximate range used for core level and valence band spectroscopy investigations used in this thesis.

The range of energies used in this thesis is highlighted in green. Also given is an indication of objects of similar dimension to the different wavelengths of electromagnetic radiation.

In laboratory based photoemission experiments, one can use monochromatic sources such as a helium lamp with spectral emission lines at E=21.2eV and 40.8eV. These photon energies can excite electrons from the valence band of many elements (see Section 3.3.2). There are also higher energy monochromatic x-ray sources available for accessing core electrons, such as Mg-kα ($E = 1.254$ keV) and Al-kα ($E = 1.487$ keV). These sources, however, can only provide photons of a single energy. Ideally one would like a tunable source of photons, which a synchrotron facility can provide, in order to perform studies using techniques such as near edge x-ray absorption fine structure spectroscopy (NEXAFS, see Section 3.7),

which is dependent on measuring the electron (or photon) emission from a sample over a range of incoming photon excitation energies. The cross section for photoionisation, or the likelihood of a particular electron being removed from an atom through photoemission, is dependent on the energy of the incident radiation. Thus very small amounts of an element may be detected by using a photon energy which correlates with the highest cross section of the element of interest. As well as being a tunable energy photon source, synchrotron light is very intense, linearly polarised and coherent, which are all desirable properties for various investigative techniques. Synchrotrons are complicated facilities so an explanation of the key features is instructive in understanding the importance of synchrotron radiation and why it is so well suited for use in surface science experiments.

Synchrotron radiation was discovered in the 1960's and was originally an unwanted by-product from particle physics experiments. It was observed that electrons circulating around a path at close to the speed of light emitted electromagnetic radiation due to the acceleration of the charged particles as they changed direction. The radiation emitted ranged in energy from the infra red (IR) region up to high energy x-rays, and other scientists saw the potential applications of this radiation for different experiments. There was not at the time any advanced sources of IR and x-ray radiation. The first generation synchrotrons were therefore based on these particle physics facilities, with radiation emitted and subsequently detected and used in parasite chambers attached to the main accelerator ring. Second generation light sources were developed in the 60's and 70's with electron rings specifically designed for the emission of synchrotron radiation. The potential applications of this radiation gained the interest not only of physicists but also of chemists, materials scientists, biologists and other researchers. Third generation sources are now available which make use of devices which increase the emitted radiation intensity, and the synchrotron main storage ring around which the electrons travel can have up to 30 specialised beamlines. All third generation sources have several key features which are outlined in Section 3.2.

3.2 How a synchrotron works

Figure 3.2 shows a schematic diagram of a third generation synchrotron alongside a photograph of a real synchrotron, the new Diamond facility based at Oxford. Photons are created from electrons travelling around the storage ring, which experience an acceleration as they change direction. These electrons are initially created by a hot filament, and travel

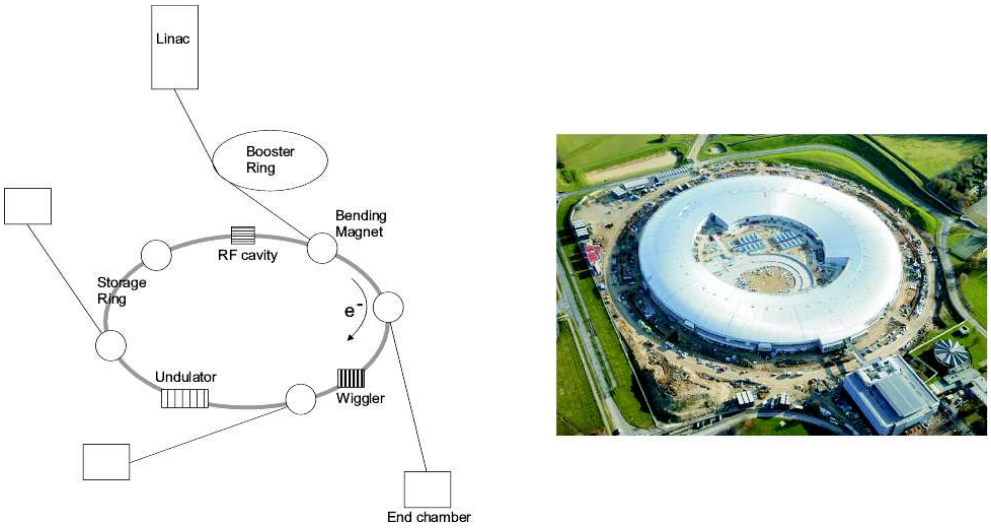

FIGURE 3.2: Left: a schematic diagram of a synchrotron, showing the linear accelerator (linac), booster ring, bending magnets, and an undulator and a wiggler (adapted from [40]). Right: The new Diamond synchrotron facility being built at Oxford.

through to a linear accelerator (or linac). Here, high energy radio waves create a pulsed electron beam and the electrons are accelerated close to the speed of light before exiting. The electrons then travel to a booster ring, which uses magnetic fields to force the electrons into a circular path. The electrons are also boosted to an energy of a few GeV before travelling into the main storage ring. This storage ring is actually made up of several straight sections, and there are devices called bending magnets situated around the ring which force the electrons to turn a corner to carry on travelling around the ring. As an electron is forced to change direction at the bending magnets it experiences an acceleration towards the centre of the ring, and this causes the emission of a photon in order to conserve the electron's momentum.

Insertion devices are also positioned in the storage ring to cause the electrons' path to change, and subsequently synchrotron radiation to be emitted. Undulators and wigglers are two insertion devices designed to produce synchrotron radiation with specific characteristics. An undulator is a device consisting of an array of closely spaced vertically oriented dipole magnets of alternating polarity, which cause the electrons to undergo oscillations as they travel through it. The electrons emit a cone of radiation at each bend in their path and these cones overlap to give a highly collimated intense beam of radiation at a fundamental frequency and a few higher harmonics due to constructive interference of

the radiation cones. Wigglers are another type of insertion device, similar to an undulator but which generally have a higher magnetic flux. These devices produce a continuous radiation spectrum of higher flux than an undulator. Detailed explanations of undulators and wigglers can be found in Ref. [41].

As the electrons are constantly losing energy through radiation emission, extra devices are required so the electrons' energy is maintained. Radio frequency (RF) cavities are present in the storage ring and on passing through them electrons receive an energy boost. These RF cavities switch off when high energy electrons pass through and are active when electrons pass through which have lost energy through radiative emission. In this way the electrons actually move around the storage ring in bunches so they all remain as high energy electrons. Synchrotron radiation is actually pulsed and some techniques make use of this property, such as pulsed field ionisation photoelectron (PFI-PE) measurements [42] and monitoring the dynamics of chemical and biological processes [43].

3.2.1 Polarised light

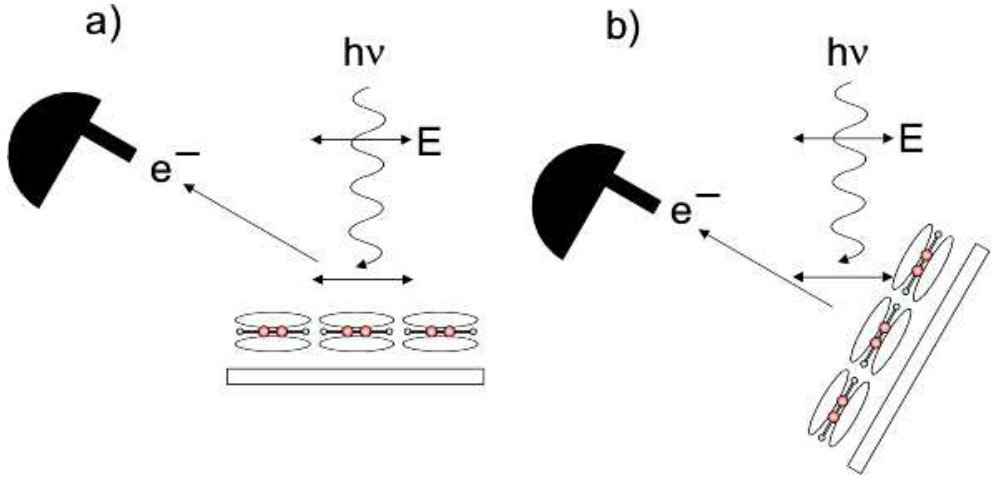

FIGURE 3.3: Making use of polarised light to investigate ordered molecular structures. The benzene molecules illustrated have extended π orbitals above and below the plane of the molecule. a) In this normal incidence geometry the incoming E-field vector of the polarised light is parallel to the molecular plane and will interact mainly with σ orbitals, b) With the sample at grazing incidence/normal emission (the plane of the sample is perpendicular to the direction to the analyser) the E-vector probes predominantly π orbitals.

A desirable property of synchrotron radiation for the studies presented here is the high degree of polarisation. Some undulator beamlines can provide light with tunable

polarisation (circular, elliptical and linear polarisation) but generally synchrotron radiation is linearly polarised. Synchrotron radiation is an electromagnetic wave with perpendicular electric and magnetic field (**E** and **B** field) transverse waves. Linearly polarised light has its direction of propagation of the waves in a fixed orientation. In the storage ring electrons are rotating around the ring and as viewed from the side the electrons appear to be oscillating back and forth. As the radiation is emitted at a bending magnet, it does so as linearly polarised light, with the **E** vector parallel to the plane of the ring. This polarisation is useful when considering how the radiation interacts with ordered molecular adsorbates on surfaces.

We can consider an example of benzene molecules which are ordered with their plane parallel to the surface. The molecules have a delocalised π orbital in the plane of the molecule above and below the ring structure. In Figure 3.3a), the **E** vector is parallel to the surface in this normal incidence configuration, and is also parallel to the plane of the molecules. It will thus excite electrons in orbitals with predominantly σ character. In Figure 3.3b) the sample is at the normal emission position, with the plane of the surface perpendicular to the direction of the analyser, and thus at grazing incidence to the direction of the incoming radiation. Here the incoming radiation is such that the **E** vector cuts across the molecular plane, thus interacting with electrons in predominantly π type molecular orbitals. The polarisation of synchrotron radiation is used extensively in NEXAFS spectroscopy and is considered in this thesis as a useful property of synchrotron light used in valence band photoemission measurements to probe the molecular ordering of monolayer and multilayer films of pyridinecarboxylic acid molecules.

3.2.2 Photon energy selection

Synchrotron radiation is emitted over a large range of photon energies, and after emission it travels along a beamline towards an experimental end station for use in experiments. Along the beamline are several devices used to focus the radiation and to filter out all but the photon energy required in the experiment. Curved mirrors are often used to focus the synchrotron light into a tightly focussed beam. In order to select the photon energy required for experiments, a monochromator is used. For the experiments in this thesis a diffraction grating monochromator is used. A diffraction grating is essentially a surface with a periodic array of lines on it; for use with x-rays it is designed such that the incident radiation is

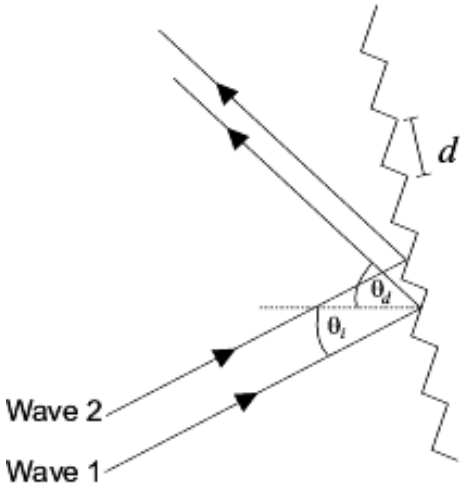

FIGURE 3.4: A diffraction grating in a monochromator. Two waves are incident at similar points on the surface. d is the distance between slits, θ_i is the incident angle and θ_d is the diffracted (reflected) angle

reflected from the surface. Figure 3.4 shows a schematic diagram of a sawtooth diffraction grating.

Two waves, 1 and 2, are reflected by equivalent points from two lines of the grating. The path difference is given by $dsin\theta_d + dsin\theta_i$ For use with soft x-rays, d is typically $\sim$ 800nm. If the path difference is equal to one wavelength then the two reflected waves are in phase and interfere constructively. Any reflections which are not in phase interfere destructively. If an incoming beam contains multiple wavelengths, then the maximum reflected intensity occurs at a particular reflection angle for different photon wavelengths (and therefore photon energies). The condition for maximum intensity is that the path difference is an integer multiple of the wavelength, $d(sin\theta_i + sin\theta_d) = m\lambda$ where λ is the wavelength and m is the order of the diffracted beam.

By using a slit after the reflection, all unwanted photon energies can be blocked from transmission. In reality the monochromator does not select a single photon energy, but filters out a small continuous range of energies. The energy spread of the selected photons is called the absolute resolution of the monochromator. There are many types of monochromators, and a summary of these may be found in Ref. [40].

3.2.3 End chambers

After the required photon energy has been selected, the light travels through to the experimental end chamber where the measurements are taken. In photoemission experiments the synchrotron light probes the sample by causing electrons to be ejected, and these are subsequently analysed. These photoelectrons need to be detected and so an electron analyser is used to collect the electrons and measure their kinetic energies. In the experiments in this thesis a hemispherical analyser was used.

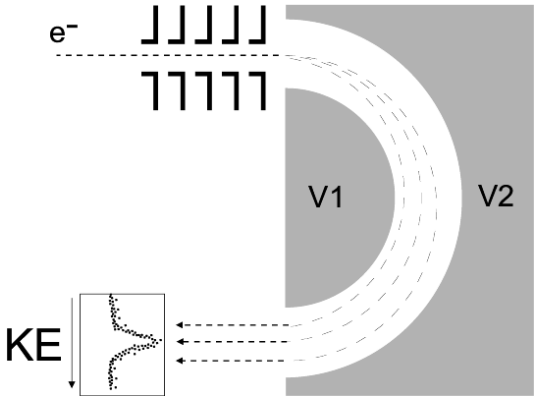

FIGURE 3.5: A schematic of a hemispherical electron energy analyser operating in fixed mode. The photoelectrons are channelled into the analyser via a lens system. Only if they are inside the selected kinetic energy window, determined by the voltages V1 and V2, can the electrons travel along the paths shown and be detected (diagram adapted from [40] p69).

A hemispherical analyser is shown schematically in Figure 3.5. The analyser lenses retard the incoming electrons to a small energy window, known as the pass energy, which is typically between 10 - 200 eV. The electrons which pass through the hemispheres are dispersed onto the detector according to their kinetic energies. In the case of a Scienta SES-200 used in these studies, the detector is a 2-D multichannel plate and CCD camera. The pass energy determines the spread of energies dispersed onto the detector and hence the resolution of the spectrum.

An experimental end chamber can typically perform several functions. A manipulator is a precise positioning device on which the sample is mounted during measurements. The low pressure in the chamber is maintained with different pumps. For synchrotron work the chamber pressure should be lower than 1×10^{-9} Torr, otherwise gaseous contaminants may be present in the beamline which can contaminate the optical devices. There may be

a low energy electron diffraction (LEED) device present for investigations of the surface integrity and crystal structure (see Section 6.4.1). A preparation chamber is often attached to the main experimental chamber for evaporating chemicals and cleaning samples without risking contamination of the main chamber. For more information on specific synchrotron beamlines, the various facility websites provide relevant information. Also each beamline is described in a published article, including the layout and capabilities (beamline 4.1, Daresbury laboratories [44, 45], beamline I311, MaxLab [46] and I511 MaxLab [47]). The two beamlines which have been used in experiments presented in this thesis are described next.

Beamline 4.1, Daresbury Laboratories

Ultra violet photons are of the ideal energy for studying the valence band photoemission characteristics of molecular films, as in the pyridinecarboxylic acid experiments performed on beamline 4.1 at Daresbury Laboratories [44, 45]. This beamline is the branchline from a bending magnet, and is suitable for experiments which require photons in the energy range 15-220eV, thus being well suited to access valence band states and shallow core levels. The chamber is equipped with LEED, a manipulator capable of sample rotation about the azimuthal axis as well as the tilt axis, which can be used to heat the sample with electron beam heating and cool the sample with a nitrogen gas flow cooled to -100°C. The chamber is kept at ultra high vacuum (UHV) using a magnetically levitated turbomolecular pump to achieve a base pressure of about 5×10^{-10} Torr. Valence band photoemission data was obtained using photon energies in the range of 21.2 to 55 eV using a Scienta SES-200 hemispherical electron analyser with an acceptance angle of $\pm 5°$. An overall spectral resolution of 200 meV can be achieved.

The experimental geometry of the photoemission measurements is shown in Figure 3.6. The angle between the incoming radiation and the analyser is fixed at 54.7° and variation of the polarisation of the light with respect to the sample surface is achieved by tilting the sample (changing θ) or rotating the sample (changing ω) to change its azimuthal angle. The emission angle ϕ is also changed when the tilt angle in changed.

Beamlines I311 at MaxLab, Sweden

Higher energy photons up to 600 eV are used to access the core levels of carbon, nitrogen and oxygen atoms in molecular films at the Beamline I311, MaxLab. I311 is an undulator

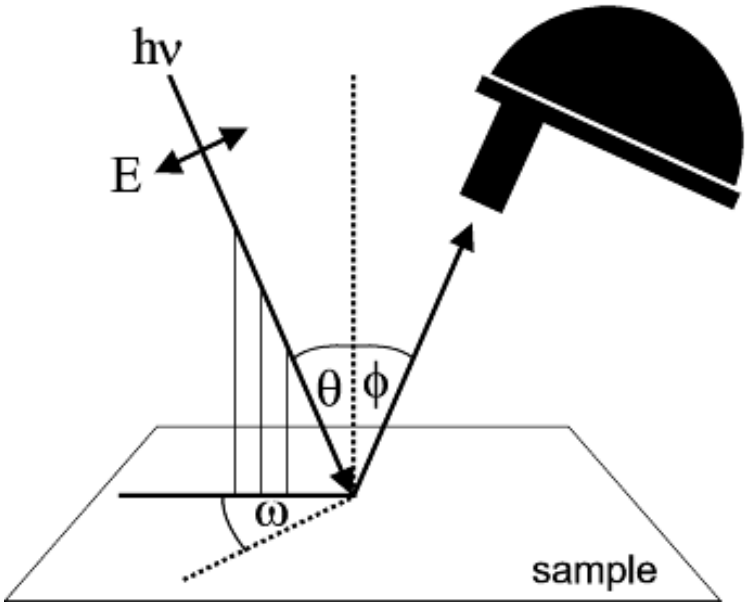

FIGURE 3.6: Experimental geometry used in valence band photoemission experiments. θ is the incident radiation angle with respect to the surface normal. ϕ is the photoelectron emission angle with respect to the surface normal, ω is the azimuthal rotation angle of the surface. The sum of θ and ϕ is fixed by the geometry of the analysis chamber at 54.7°.

based vacuum ultra-violet/soft X-ray beamline designed for high resolution x-ray photoemission spectroscopy (XPS) and x-ray absorption spectroscopy (XAS) with a photon energy range of 30 - 1500 eV [46]. Beamline I311 is equipped with a Scienta SES-200 hemispherical analyser and a LEED system. The monochromator is designed specifically for high resolution measurements. The main chamber is kept at a base pressure of around 2×10^{-10} Torr

3.3 Photoemission spectroscopy

3.3.1 Core-level photoemission (XPS)

Core level photoemission spectroscopy, sometimes called x-ray photoemission spectroscopy (XPS) is a technique based on the photoelectric effect [48] and uses photons to eject core level electrons from atoms. It has undergone much development as a technique to become a powerful tool for surface scientists. XPS can reveal information on the relative abundance of specific atoms and their chemical environments, and as such is an ideal technique with which to study the chemical environment of organic molecular adsorbates. Photoemission

spectroscopy can be performed with any x-ray source but a synchrotron is an excellent facility for surface science XPS as detailed above.

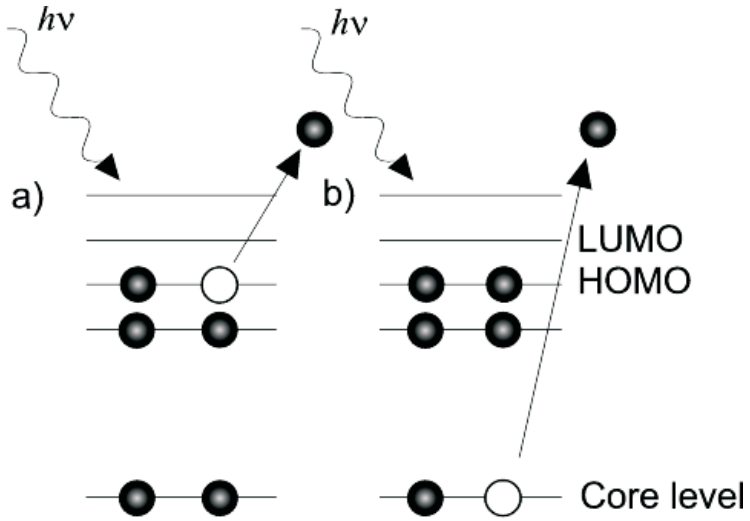

FIGURE 3.7: Overview of electron movement in photoemission. a) Valence band photoemission (Section 3.3.2) and b) Core level photoemission

A photon of a specific energy $h\nu$ is absorbed by an atom and the energy from the photon is transferred to an electron which is then promoted to a higher energy level. If the energy transferred is sufficiently high, the photoelectron is ejected with a specific amount of kinetic energy E_{KE}. Figure 3.7 shows an energy level diagram of the process occurring in both valence band (Section 3.3.2) and core level photoemission. Figure 3.8 shows diagrammatically valence band and core level photoemission occurring in the context of a real molecule, in this case benzene. The core level electron comes from an energy level associated with a particular atom in the molecule as shown.

By collecting the ejected photoelectrons in a suitable analyser (see Section 3.2.3), deductions may be made about the atom from the resulting photoemission spectrum. This spectrum is composed of different peaks originating from different electronic states in the sample. We can say

$$h\nu = E_{BE} + E_{KE} + \phi \tag{3.1}$$

where $h\nu$ is the energy of the photon which has frequency ν, E_{KE} is the kinetic energy of the emitted electron, E_{BE} is the binding energy of the electron, and ϕ is the work

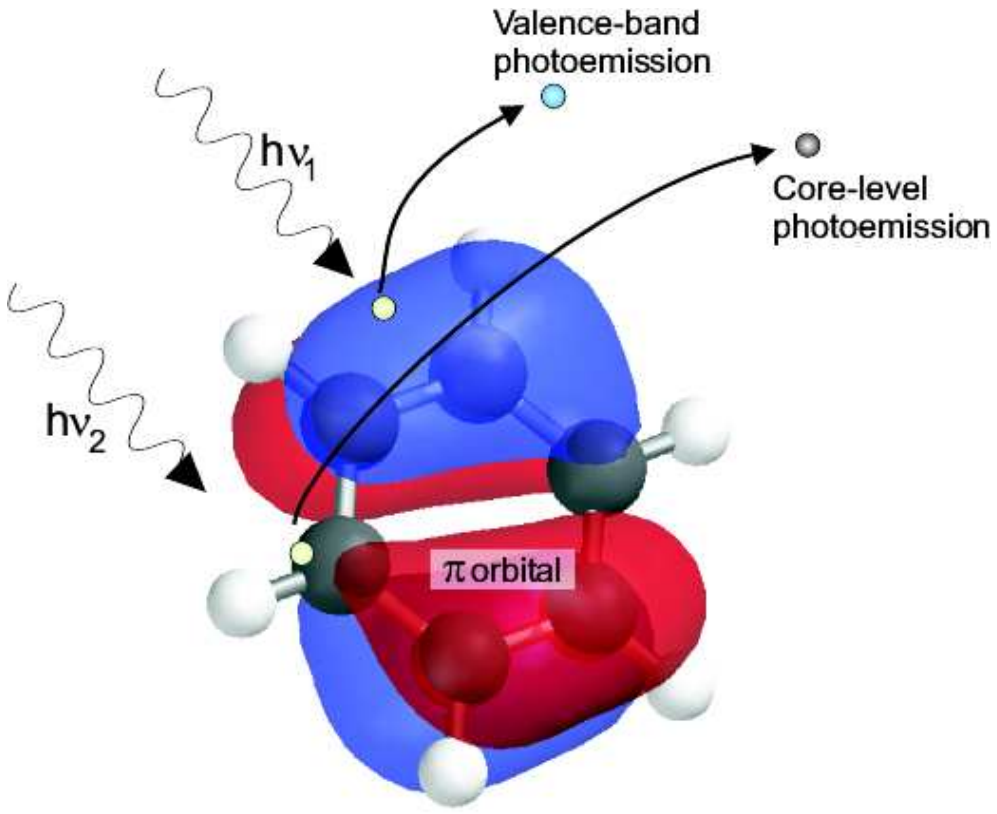

FIGURE 3.8: a) A benzene ring with its calculated HOMO shown. A valence electron is ejected from the HOMO by a photon of energy hν_1, and a core level electron is ejected from a carbon atom by a photon hν_2. The molecular orbitals were calculated using DFT theory in the B3LYP model with a 6-31G* basis set in Spartan'02. The red and blue regions denote regions of positive and negative probability amplitude.

function of the spectrometer. If we know the incoming photon energy, which is selected with the monochromator (Section 3.2.2), and the kinetic energy of the photoelectrons, as measured by the detector (Section 3.2.3), and the work function of the analyser, then the binding energy of the electron can be calculated. The binding energy is dependent on the chemical environment of the atom from which the electron was ejected (see Section 3.4.1). Influences from neighbouring molecules, the bonding within a molecule, and the adsorbate-substrate coupling, amongst other factors can all influence the emitted electron binding energy. To ensure that surface atoms are being investigated in these systems we can use the tunable nature of synchrotron light to look selectively at the uppermost layers of the sample (Section 3.3.3).

3.3.2 Valence band photoemission spectroscopy

Valence band photoemission (sometimes called ultraviolet photoemission spectroscopy, UPS) follows the same principles as core-level photoemission but the ejected electron originates from the valence energy levels rather than the core levels, shown in Figure 3.7a). Whereas a core level photoemission spectrum can, in simpler cases, be broken down into a series of individual peaks, valence band spectra are usually more complicated and it is not a trivial matter to calculate the individual spectral components. Valence band photoemission is useful for the study of organic molecules because it can provide information about the molecular orbitals in a molecule. The highest occupied molecular orbital (HOMO) of a molecule is the orbital in which the electrons with the lowest binding energies reside. Subsequent higher binding energy molecular orbitals are labelled HOMO-1, HOMO-2 etc. Valence band spectra of molecular films consist of a series of peaks at low binding energies, showing electrons excited from the HOMO, HOMO-1, HOMO-2 and so on.

The shapes of the molecular orbitals can be simulated using a computational chemistry package such as Spartan'02 [49], Gaussian 98 [50] or Siesta [51]. Figure 3.8 shows the calculated HOMO for a benzene molecule, which is a relatively simple molecule with its molecular orbitals formed from hybridisation of the carbon atom p orbitals lying out of the plane of the ring structure. The calculation was performed in Spartan'02 using DFT at the B3LYP level with a 6-31G* basis set. Figure 3.8a) shows schematically where core level photoelectrons and valence band electrons originate from in a molecular adsorbate. Valence band electrons come from lower energy states in the delocalised molecular orbitals.

By using a suitable model the molecular orbital shapes can be predicted as shown, and also the occupied and unoccupied energy levels of the molecule may be calculated. By plotting a feature on an energy scale corresponding to each calculated energy level and convolving these theoretical energy levels with a theoretical peakshape (usually a Gaussian function with a full-width at half-maximum (FWHM) of 1eV), we can obtain a theoretical approximation of the valence band. More factors can be taken into account to make the calculation more accurate, such as the relative cross sections of the elements in the molecule (how likely the electron from a particular energy level in an atom will be ejected) and the geometry of the system. Detailed calculations like this were performed for the isonicotinic acid work in Chapter 6 by B. Brena and Y. Luo from KTH, Stockholm University.

3.3.3 Surface sensitivity

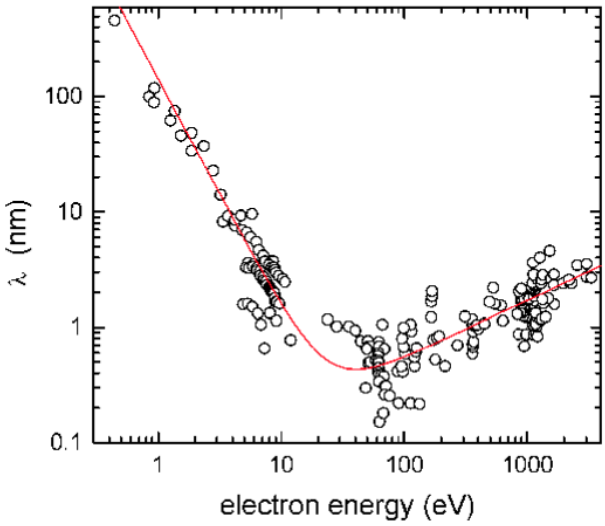

FIGURE 3.9: The escape depth λ (nm) vs. kinetic energy of photoelectrons (eV) follows this universal curve ([52], adapted from Ref. [53]). The red curve is a best fit with the experimental points. Thus electrons with a kinetic energy of around 35 eV are from the sample surface.

In surface science experiments the important region for study is the uppermost few monolayers of a sample, thus we need to tune the energy of our synchrotron light to probe this region only. Electrons cannot travel very far through matter without energy losses through interacting with the sample, and if they lose too much energy they will never exit the sample, and thus are not detected. Even if these scattered electrons do leave the sample they will have lost the energetic information required to make deductions about the sample. These scattered electrons contribute to the background count, which is why at very low kinetic energies there is a very large background intensity (See Section 3.8.2 which explains how to calibrate photoemission spectra). The distance electrons can travel through matter and still have enough energy to leave the sample is called the escape depth. Investigations on many different elements have been plotted together in a graph (Figure 3.9) showing the escape depth of electrons as a function of the kinetic energy of the photoelectrons; it is evident that the points from different elements all lie on one universal curve.

Hence for photoemission experiments which are very surface sensitive, the photon energy required should be large enough to allow the electrons to escape, but not so large as

to excite deeper lying bulk electrons. If the kinetic energy of the electron is too low then the photoelectrons do not excite any lattice processes such as plasmons which act to lower the electron escape depth and bulk electrons can escape from the surface. The optimum kinetic energy for photoelectrons to leave with in order to only probe the surface layers, from the minimum in the universal curve, is around 35eV. By having a synchrotron as a tunable source of photons one can vary the surface sensitivity of a spectrum.

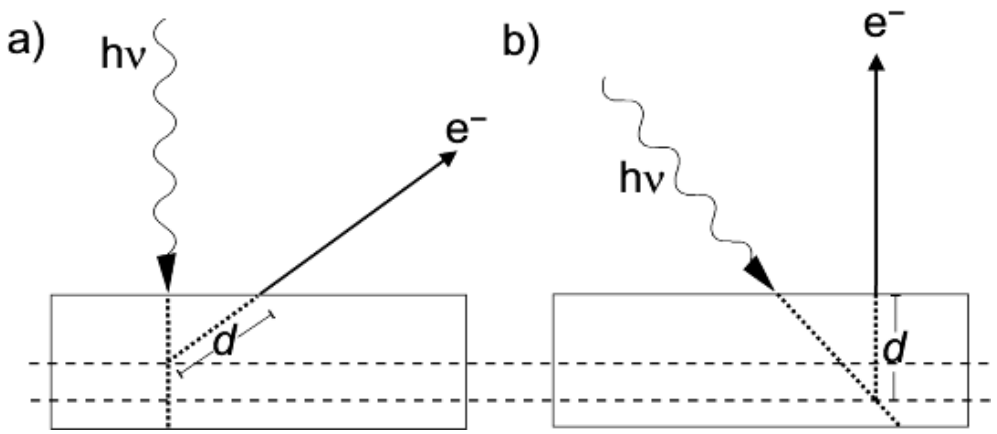

FIGURE 3.10: The geometry of the experiment can determine the surface sensitivity. a) The grazing emission angle only allows surface photoelectrons to escape; b) The normal emission angle allows more bulk electrons to escape but the detected intensity will be higher. The escape depth for photoelectrons from a specific energy level is fixed for fixed photon energy.

The surface sensitivity in an experiment is dramatically increased by changing the experimental geometry. The escape depth of the photoelectrons is fixed for a particular photon energy. Thus if the detected electrons are ejected at a grazing emission angle (Figure 3.10a)) then a much higher surface sensitivity is achieved than if the detected photoelectrons are emitted at normal emission (though a higher count rate is achieved in this geometry, see Figure 3.10b)).

3.4 Initial state effects

Initial state effects are factors which determine the binding energy of the detected photoelectron before any excitation has taken place. These include chemical shifts, arising from the arrangement of atoms in the molecule. Also surface core level shifts (SCLS) can change the binding energy of electrons. SCLS occur as surface atoms experience a different chemical environment to bulk atoms, either due to having less neighbouring atoms in the surface

than in the bulk, or surface atoms may also arrange into a surface reconstruction, providing the atoms involved with a different bonding environment.

3.4.1 Chemical shifts

Core level photoemission is a powerful technique for determining the chemical environment of atoms in a sample. Photoelectrons are detected using an electron analyser which measures their kinetic energies, thus we can determine their binding energy. If we then say that the binding energy is the difference in energy between the final $(N-1)$ and initial (N) states of the ionised atom, and we assume that there is no effect (final state relaxation) from the photoelectron leaving the sample, either to the atom from which it is removed, or on surrounding atoms, then the binding energy of the electron can be taken to be the negative of the atomic core level energy. This approximation is called Koopman's theorem and a great simplification. However, it is accurate, as factors not taken into account such as the atom's relaxation and the effect the positive core hole has on the ejected photoelectron tend to balance one another out. Thus the binding energy of the detected electrons tells us about the atomic energy levels in the sample.

The binding energy of a photoelectron is influenced by the chemical environment of the atom from which the electron was ejected. The atom's position in a molecule affects the ejected electron's peak positions. This movement of a peak due to the chemical environment of an atom is called the chemical shift. An example of chemical shift effects, or the difference in binding energy of an electron from its expected position due to atomic bonding, is found in the C $1s$ core level photoemission spectrum of ethyl trifluoroacetate, shown in Figure 3.11. The lowest binding energy peak originates from the methyl carbon atoms. The carbon atoms bound to oxygen atoms have a slightly higher binding energy due to the oxygen atoms' electronegativity, which exert an extra attractive force on the C $1s$ electrons (see Section 1.2). At higher binding energy are the C $1s$ electrons from the carbon atom bound to two oxygen atoms, then the highest binding energy peak arises from the C $1s$ electrons ejected from the carbon atoms bound to three fluorine atoms (fluorine has a higher electronegativity than oxygen.)

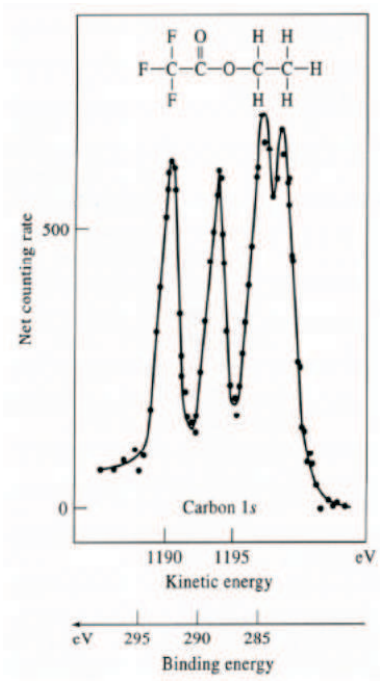

FIGURE 3.11: Ethyl trifluoroacetate C 1*s* core level photoemission spectrum. This example demonstrates that the chemical environment of an atom in a molecule has a pronounced effect on the photoemission peaks measured due to chemical shifts (from Ref. [54]).

3.4.2 Surface core-level shifts (SCLS) and surface states

Core level photoemission can also be used to give information about substrate surfaces, such as the quality of the surface reconstruction and the cleanliness of the sample. The atoms situated at the top surface of a sample will be in a different chemical environment to atoms in the bulk because they have fewer nearest neighbours to bond to. The change in peak position of the surface atoms relative to the peaks from bulk atoms is called the surface core level shift (SCLS). If the surface has reconstructed the surface atoms will be in a different bonding configuration specific to the surface reconstruction, and the characteristic shapes of the core level peaks due to the reconstruction can be used to show if the surface has been prepared as required. Synchrotron radiation facilities can measure spectra with a high enough resolution that these small binding energy shifts can be measured.

The quality of the surface being investigated can be characterised to some extent using XPS. A surface may contain crystal defects, perhaps from being sputtered. For TiO_2 surface defects occur by oxygen atoms being removed selectively during the sputtering

process, leaving surface Ti atoms in different bonding states to Ti atoms in the main reconstruction. This is shown in the Ti $2p$ spectrum of a sputtered surface in Figure 3.14 later in this chapter. The peaks at higher binding energy to the main peaks are from titanium in a environment where oxygen has been removed. The surface quality can be affected by annealing at too low a temperature for the surface to reconstruct fully, which is the case with Si(111) (7×7). One can observe defect states, or the absence of certain surface states related to the correct reconstruction, in the XPS spectrum from these imperfect surfaces.

A simple way of measuring the cleanliness of a sample is to take a C 1s XPS spectrum (unless the surface inherently contains carbon, such as graphite). The most common contaminants in vacuum chambers are carbon based, such as carbon, CO and CO_2. A clean sample should show a very small, or ideally no C $1s$ peak.

3.5 Final state effects

XPS peaks are influenced not only by the properties of the atom before photoionisation, but also after the excitation has occurred. Satellite features can often be observed at a higher binding energy to the main core-level photoemission peak due to emitted photoelectrons exerting an effect on the other electrons in the atom. These effects are known as shake-up and shake-off (Section 3.5.1). Quantum effects can change the appearance of core level peaks dramatically, causing the less energetic core level peaks for some heavier elements to split through spin orbit (l-s) coupling (Section 3.5.2). Other molecular effects can also change the appearance of the spectrum peaks, such as vibrational excitations. The appearance of peaks in a spectrum is also related to the overall resolution possible.

3.5.1 Shake-up and shake-off

As the photoelectron exits the atom, it can excite subsequent processes which produce satellite features in the XPS spectrum. Figure 3.12a) shows an energy level diagram of a shake up effect. As the photoelectron is leaving the atom it excites another high-lying electron into an unoccupied state, losing energy in the process and thus being of the appearance of originating from a more strongly bound state. Thus a peak appears at higher binding energy relative to the main peak. This is a shake-up event. Another satellite feature can occur at still higher binding energy if the second electron is not just promoted but is actually ejected from the atom (Figure 3.12b). This is known as a shake-off feature and does not

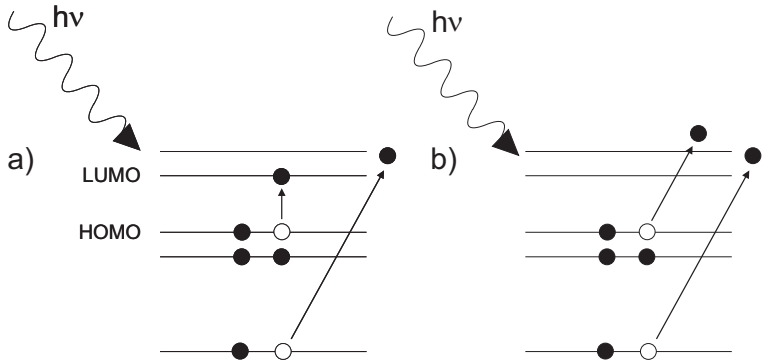

FIGURE 3.12: The two predominant satellite peak mechanisms are a) Shake up and b) Shake off.

give rise to a distinct peak but to a broad background as the second electron is promoted to a quasi-bound state above the vacuum level.

3.5.2 *l-s* coupling

The energy level from which photoelectrons are ejected has a significant effect on the appearance of the XPS peaks. Spin-orbit coupling, or *l-s* coupling (from the associated quantum numbers l, orbital angular momentum and s, the electron spin) leads to peak splitting. After an electron has been ejected from an atomic energy level with $l > 0$ the remaining electron in that energy level can adopt a spin up or spin down configuration. Spin orbit coupling determines the total angular momentum quantum number $j = l + s$ and thus the extent to which the remaining electron becomes a spin up or spin down electron. For a p orbital, $j = \frac{1}{2}$ or $\frac{3}{2}$. The degeneracy, or likelihood that the remaining electron will fall into an up or down state, is given by $2j + 1$, and thus two peaks appear in the XPS spectrum in the ratio $2(\frac{1}{2}) + 1 : 2(\frac{3}{2}) + 1$ or $1 : 2$ with the higher energy peak being the lower angular momentum state.

Figures 3.13 and 3.14 show a Ti $2p$ XPS peak taken using 520eV photons. The clean TiO_2 spectrum in Figure 3.13 shows the $2p_{\frac{1}{2}}$ and $2p_{\frac{3}{2}}$ peaks at 463.9eV and 458.2eV respectively. Two peaks have been fitted to the spectrum; the difference between the data and the fitted peaks is the residual peak above, which gives an indication as to how accurate the peak fit is. The peak areas are in the ratio $0.68 : 0.31 \simeq 2 : 1$ as expected for a p type energy level. The Ti $2p$ XPS spectrum for a sputtered sample in Figure 3.14, which has not been annealed, has two extra peaks in the trace, which arise from defect states in the

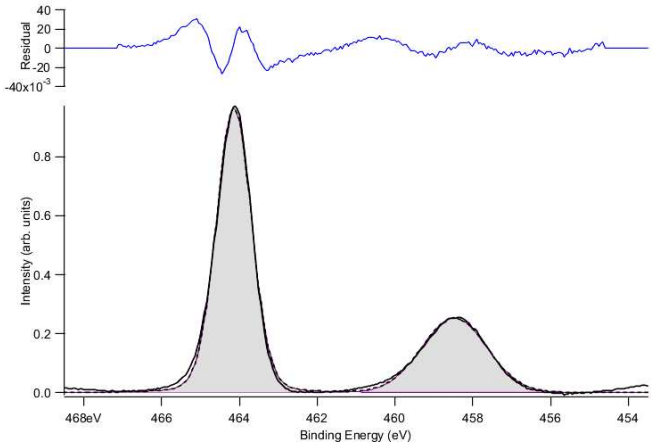

FIGURE 3.13: Ti $2p$ XPS spectra for clean TiO_2 with peaks fitted. The fitted peak areas are in the ratio $0.68 : 0.31 \simeq 2 : 1$, as expected for a p type orbital. The trace at the top is the residual, the data minus the fitted peaks, to show the accuracy of the fit.

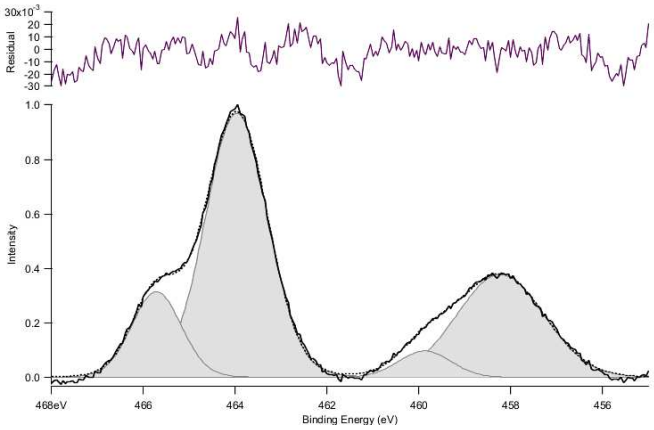

FIGURE 3.14: Ti $2p$ XPS spectra for sputtered TiO_2 with peaks fitted. The expected peaks appear at 463.9eV and 458.2eV with shoulder peaks at higher binding energy, due to defects on the surface from the sputtering process. These extra peaks are still in the 2:1 ratio.

surface. The defect states originate from Ti atoms which are not in the same oxidation state as the other Ti atoms in the surface reconstruction, because oxygen atoms have been sputtered away. This spectrum is an example of using XPS to determine the quality of a prepared surface. Again the difference between the fitted peaks and the experimental data is shown at the top of each spectrum.

3.6 Instrumentation effects

The physical equipment used in synchrotron experiments is not perfect and devices such as the monochromator and analyser have a finite resolution. This is discussed in Section 3.6.1.

3.6.1 Peak broadening

Real photoemission peaks are not simply narrow peaks, and peak broadening occurs due to different effects. The ejected photoelectron leaves behind a positive core hole which decays when another electron relaxes to fill it according to an associated lifetime. This effect causes Lorentzian broadening of the photoemission peak. Gaussian peak broadening occurs because the monochromator has a finite resolution (Section 3.2.2), and the electron detector measuring kinetic energies has an associated error (Section 3.2.3). Thermodynamic processes such as the presence of phonons can lead to Gaussian broadening also (a phonon is a quantised lattice vibration). The surface being probed will inevitably contain local defects which also affect the photoelectron emission, and the photoexcitation process itself causes vibrational broadening.

3.6.2 Background subtraction

All photoemission spectra contain an overall underlying contribution from secondary electron events (scattering and vibrational processes) which cause the spectrum to sit on a background count rather than an ideally flat background. To remove this background one can use different shaped spectra and subtract the appropriate one from the data. A Shirley background [55] is a smoothed step function which is a good approximation to the background that a single photoemission peak sits on. Its shape accounts for inelastically scattered electrons from the processes which are involved in producing the peak. Other backgrounds used for subtraction from photoemission spectra include a linear function, and a Tougaard background (a more complicated smooth step background used to account for inelastic processes [56]). All core level photoemission spectra in this thesis, and valence band spectra where appropriate, have a Shirley background removed.

3.6.3 Peak fitting in XPS

After measuring a core level photoemission spectrum it is desirable to know the individual peak components which compose the trace. Curve fitting software can be used to determine the individual peaks in a spectrum. In this thesis a curve fitting extension macro for the data analysis package IGOR Pro was used for peak fitting, which was developed in house [1]. The number of peaks thought to be present in the spectrum can be specified, along with their intensities, the estimated Gaussian and Lorentzian broadening (see Section 3.6.1), and peak positions. Limits may then be specified within which these parameters may change in order to produce an overall spectrum which provides the closest match to the original data. The resulting peaks are known as Voigt functions (a convolution of Gaussian and Lorentzian). There must be great care taken when choosing the initial fit paraments in order to obtain physically reasonable results. For example, including more peak components will inevitably produce a more accurate theoretical spectrum but it may not necessarily correspond to any physical process. Similarly the ranges within which the broadening parameters are allowed must be reasonable otherwise falsely broad peaks may fit well to the spectrum but not be physically meaningful.

3.7 X-ray absorption spectroscopy (XAS)

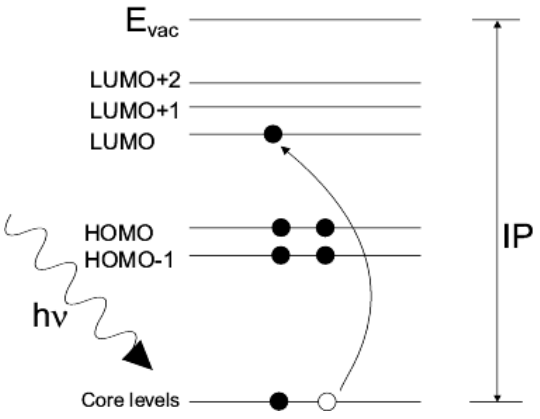

FIGURE 3.15: A molecular core electron is promoted to the unoccupied molecular orbitals (LUMO, LUMO+1 etc.). When an adsorption takes place a peak appears in the spectrum due to the electron relaxing back to its core state and releasing either a photon (fluorescence yield) or an electron (electron yield).

[1] by Michael Phillips, PhD student 2001-2004

Another useful technique for determining molecular orientations on surfaces is x-ray absorption spectroscopy (XAS). This technique requires a range of photon energies to be used to excite core level electrons into previously unoccupied energy levels. Thus spectra are acquired by sweeping the excitation photon energy while measuring the decay processes occurring in the sample. Rather than measuring the occupied energy levels in a system, XAS probes the unoccupied states above the Fermi level in a sample. Taking an x-ray absorption spectrum using photon energies which can just promote a core level electron into a previously unoccupied energy level (this region is called the absorption edge) is called near edge x-ray absorption fine structure, or NEXAFS. Absorption spectra involving higher energy unoccupied stated are extended x-ray absorption fine structure spectra, or EXAFS; these are not covered here.

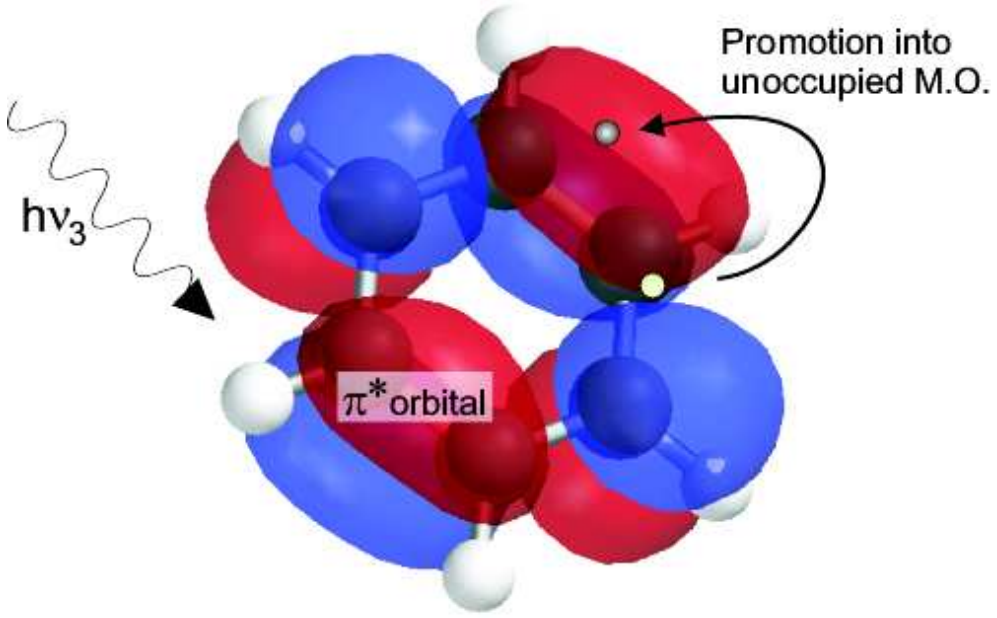

FIGURE 3.16: A benzene ring with its LUMO shown. In NEXAFS spectroscopy a core level electron is promoted into the unoccupied molecular orbitals as shown. Its relaxation provides information on the unoccupied molecular orbitals. The molecular orbitals were calculated using DFT theory in the B3LYP model with a 6-31G* basis set. The red and blue orbitals denote regions of positive and negative probability amplitude.

In NEXAFS, photons are used to probe the sample in order to promote a core level electron. As the photon energy is gradually increased it reaches the energy required for a core electron to just be promoted into the lowest unoccupied molecular orbital, or LUMO. This

produces a spectral feature in the form of a sharp signal increase in the NEXAFS spectrum, known as the absorption edge. This transition is shown in an energy level diagram in Figure 3.15. Figure 3.16 shows the calculated LUMO for a benzene molecule and the transition from a core level to the LUMO is shown.

The first feature (occurring at the lowest photon energy) in the NEXAFS spectrum appears when electrons are provided with enough energy to just be promoted into the LUMO. As the photon energy continues to increase, so core level electrons can be promoted into the higher energy LUMO+1, LUMO+2 etc. In this way the density of unoccupied states are accessed and plotted in a spectrum. There are different ways of detecting the transition. As the promoted electron subsequently relaxes, it can cause the release of another electron from that atom, which is called an Auger electron. The initially excited electron can also relax by releasing a photon, which is detected in fluorescence yield NEXAFS. Alternatively the drain current from the sample can be measured. NEXAFS is a powerful technique which can be used to great effect in determining the orientation of molecules on ordered films following the sample principle as that outlined in Section 3.3. An example of NEXAFS used to determine molecular ordering is given in Section 6.1.1.

3.8 Spectra calibration

It is very important that all spectra are calibrated carefully in order to draw valid conclusions concerning binding energies and relative energy shifts. At a synchrotron facility the electrons are reinjected periodically into the storage ring (usually once a day) as the electron current in the storage ring gradually decreases with time. After an injection the position of the beam in the ring may change slightly, which can affect the energy calibration. The photon energy is selected using the monochromator (Section 3.2.2), but the value chosen to pass through and the actual photon energy of the light used to probe the sample may not correspond exactly, since the monochromator and control software are not perfect. Spectra may either be calibrated relative to a known feature, such as a bulk peak or Fermi level, or they may be calibrated to an absolute energy scale, the ionisation potential. both these calibration methods are described next.

3.8.1 Relative energy calibration

Often for calibration purposes a relative energy calibration is sufficient. In this process a spectral feature is chosen, such as the Fermi edge (occurring at zero binding energy) or a bulk substrate peak. The Fermi edge actually occurs at $h\nu - \phi$, where $h\nu$ is the photon energy and ϕ is the work function of the spectrometer (usually $\sim$ 5eV). The Fermi level of a semiconductor may be estimated even though there is no density of states at the Fermi level to probe. To measure the Fermi level for a semiconductor sample we measure the Fermi level of a metal in contact with it, which is usually a sample clip holding the sample to a mounting plate. The Fermi edges of the metal clip and semiconductor sample align as they are in contact, and should occur at zero binding energy, so all spectra can be aligned to this reference point. Other reference energies may be used too. If the position of a bulk sample peak, such as Si $2p$, is well known then this may also be used as a reference. Each time the monochromator is moved to change the photon energy, or when the beam is reinjected into the storage ring, it is important to take a spectrum of the 'known feature' as well as spectra of the energy levels being measured for reliable calibration.

3.8.2 Absolute energy calibration

Photoemission spectra

It is possible to calibrate photoemission spectra (core level and valence band) and NEXAFS data on the same absolute energy scale to build up a complete picture of the electronic structure of the occupied and unoccupied electronic states in a sample. A convenient reference point for all the spectra is the vacuum level. For semiconducting samples, other reference levels such as the Fermi level can be used (Section 3.8.1) but also can be difficult to measure reliably. The Fermi level of a semiconductor lies in the bandgap, where there is no density of states, and as such its position cannot be known as accurately as the vacuum level. It may be estimated by taking a spectrum of a metal in contact with it, the Fermi level of which should be the same as that of the semiconductor due to band bending. However, if chemicals are deposited onto the sample by evaporation, they will also adsorb onto the metal clips and surrounding sample holder, thus the metal will not be accessible to measure the Fermi edge from. One can calibrate to a core level of well known binding energy, but this is not always possible. The vacuum level of any sample can be measured relatively straightforwardly.

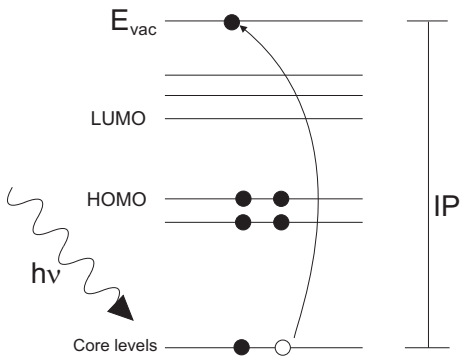

FIGURE 3.17: A molecular core electron is promoted to the vacuum level. The amount of energy required for this is the ionisation potential (IP) which is equal to the photon energy $h\nu$. The electron has zero kinetic energy.

To measure the vacuum level (Figure 3.17) electrons are promoted from the core level (or valence band) of interest to the vacuum level with no extra kinetic energy after the excitation. Thus the vacuum level is accessed when the photon energy used for the excitation is equal to the ionisation potential.

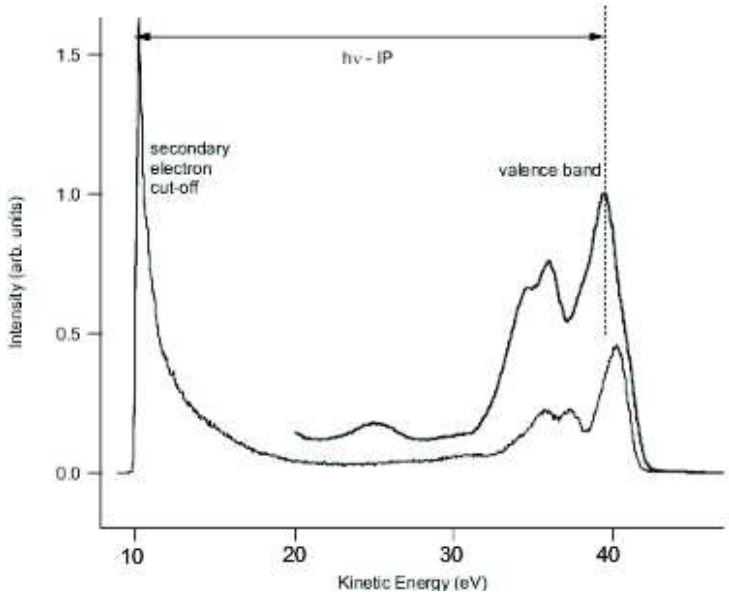

FIGURE 3.18: The vacuum level is shown at the secondary electron cut off on the left, at zero kinetic energy. The photoemission feature shown is the valence band of a multilayer of isonicotinic acid on TiO_2 taken at normal emission with 40eV photons. The difference between the valence band peak indicated and the vacuum level is the photon energy minus the ionisation potential for that valence band peak.

To measure the vacuum level and hence determine the ionisation potential, we measure a photoemission spectrum which covers the zero kinetic energy point on the kinetic energy scale as shown in Figure 3.18. This spectrum shows the valence band of a multilayer of isonicotinic acid on TiO_2 taken at normal emission with 40eV photons (see Section 6.5). The secondary electron cut-off on the left is the point at which the photoelectrons have zero kinetic energy and cannot reach the detector anymore (as the signal falls sharply to zero). The zero kinetic energy point is taken to be half way up the cut-off slope. The photoemission peak requiring calibration is plotted on the same kinetic energy scale as the electron cut-off. The difference between the valence band peak kinetic energy and the vacuum level is therefore the photon energy minus the ionisation potential for the valence band peak. Since the photon energy and the kinetic energy scale are known, the ionisation potential of the valence band peak may be calculated.

In fact the secondary electron cut off graph in Figure 3.18 appears shifted up in kinetic energy by 9.8V, as the cut off region is at 9.8eV rather than 0eV kinetic energy. In order that the excited electrons can reach the analyser, despite their low kinetic energy (close to zero), the sample is biased with a ~ -10 V potential (9.8V in this case). Thus the kinetic energy scale shows all features to be at an energy higher than their true value by an amount equal to the bias applied to the sample. Subtracting the 9.8eV potential from the kinetic energy scale would give the actual kinetic energy scale of the cut off and photoemission peaks. The important measurement from this spectrum is the separation from the secondary electron cut-off and the photoemission peak.

Photon energy calibration is also important as the monochromator is not ideal. To calibrate the photon energy the first and second order light from the monochromator is used to measure the spectrum. The monochromator works using a diffraction grating, which allows through integer multiples of the chosen photon wavelength of synchrotron light (Section 3.2.2). Taking a spectrum with first and (much weaker) second order light allows us to calculate the difference in energy between them, which is the true photon energy used. The order is given by m in the equation in Section 3.2.2 for the diffracted light in a monochromator. Figure 3.19 shows the first and second order photoemission peaks for the valence band of the same isonicotinic acid multilayer sample as before, taken using 40eV photons. The difference between the first and second order peaks is actually 39.75eV showing that the true photon energy is actually 0.25eV less than that expected. The deviation between the photon energy chosen and the energy of the photons actually

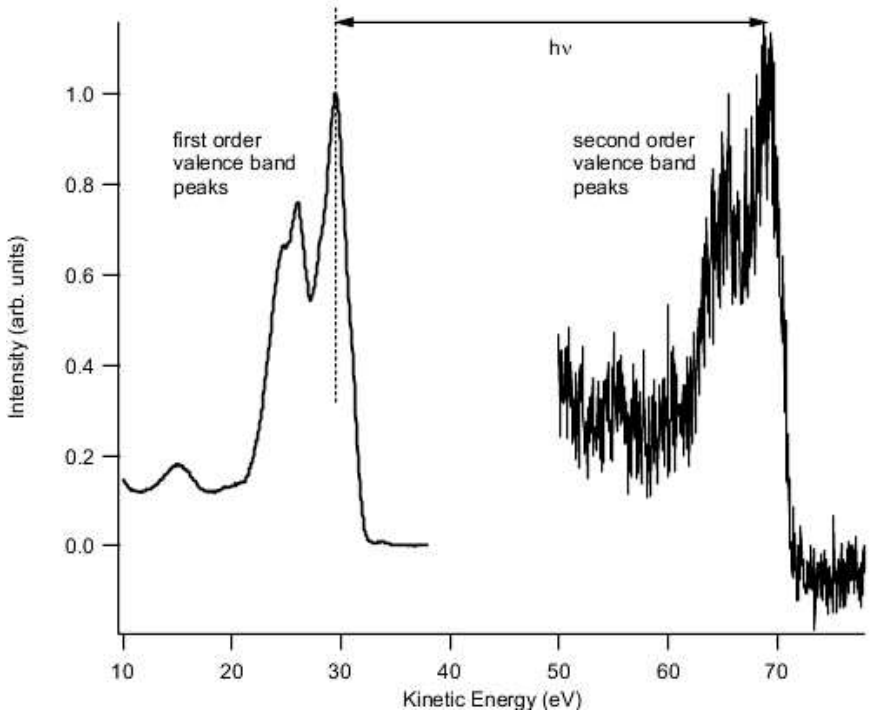

FIGURE 3.19: These valence band spectra are taken from a multilayer isonicotinic acid sample in TiO_2. The first order valence band peak is at 29.4 eV kinetic energy, and the second order peak, which is much weaker in intensity, is at 69.15 eV. Both spectra have been normalised to the highest feature for comparison. The difference between them is 39.75 eV, the true photon energy used. The photon energy was set to 40eV for these measurements.

transmitted tends to be larger as the photon energy increases. Hence there is not a large deviation from the expected and true values for this relatively low photon energy.

All photoemission peaks can be calibrated using the method described above. Alternatively, one photoemission peak can be calibrated in this way and all other peaks can be calibrated to that peak. This can be achieved by taking a photoemission spectrum at the photon energy required for a surface sensitive scan of the as yet uncalibrated peak over a kinetic energy range which covers both the calibrated peak and the peak being measured. All the photon energies used for measuring the various spectra must be calibrated using first and second order light for complete calibration.

X-ray absorption spectra

Alongside the calibrated photoemission spectra, one can also plot an x-ray absorption (NEXAFS) spectrum for the sample to examine the unoccupied states and occupied states to-

gether and obtain a complete picture of the electronic levels of the sample. The first calibration required is that of the photon energies used in taking the NEXAFS scan. This is again done by using first and second order light again to measure a photoemission feature, using a photon energy included in the photon energy scale of the NEXAFS scan. For completeness the photon energy can be calibrated for the photon energies used at the start and the end of the range over which the NEXAFS spectrum is measured, in case the deviation from the measured value and the true value changes over the range of the NEXAFS scan. For example, for an N 1s NEXAFS spectrum, a photon energy range of 395-440 eV may be chosen to cover the absorption edge at $\sim$ 398 eV, and the π^* and σ^* resonances up to 440 eV. Thus the calibration of 395 eV and 440 eV photons may be performed.

The photon energy in the NEXAFS energy scale which numerically equals the ionisation potential for the corresponding core level excitation is the vacuum level, and the NEXAFS spectrum may be plotted on the same ionisation potential energy scale as the photoemission data to give a complete picture of the density of states of the sample. By considering the molecular orbital diagram in Figure 3.16 it can be seen that the LUMO states are delocalised electronic orbitals formed from hybridisation of atomic orbitals. If the molecule has C, N and O atoms present the delocalisation of orbitals can occur over different atom types. Thus the unoccupied states are derived from all contributing atoms. The energy required for a core-level to LUMO transition depends on the energy of the core level rather than on the final energy level the electron is excited into.

Figure 3.20 (from Ref. [57]) shows the entire calibration process for a monolayer of biisonicotinic acid on TiO_2 (Ref. [57] is used here as no NEXAFS data is presented for the samples examined in this thesis). Figure 3.20 a1) shows the secondary electron cut off in relation to the C 1s peak, thus placing this feature on the ionisation potential scale. Figure 3.20 a2) shows the calibration of the N 1s peak by comparison to the calibrated C 1s peak. Figure 3.20 b) is the N 1s NEXAFS spectrum and indicates where the photon energy equals the ionisation potential. This is set to zero on the ionisation potential energy scale in Figure 3.20 c) which shows the complete density of states for the sample (both the biisonicotinic acid monolayer on TiO_2 and clean TiO_2 with an estimated conduction band are shown). The data in Figure 3.20 show the electronic structure of the core excited (rather than the ground) state since all the measurements were taken of an atom with a core electron removed.

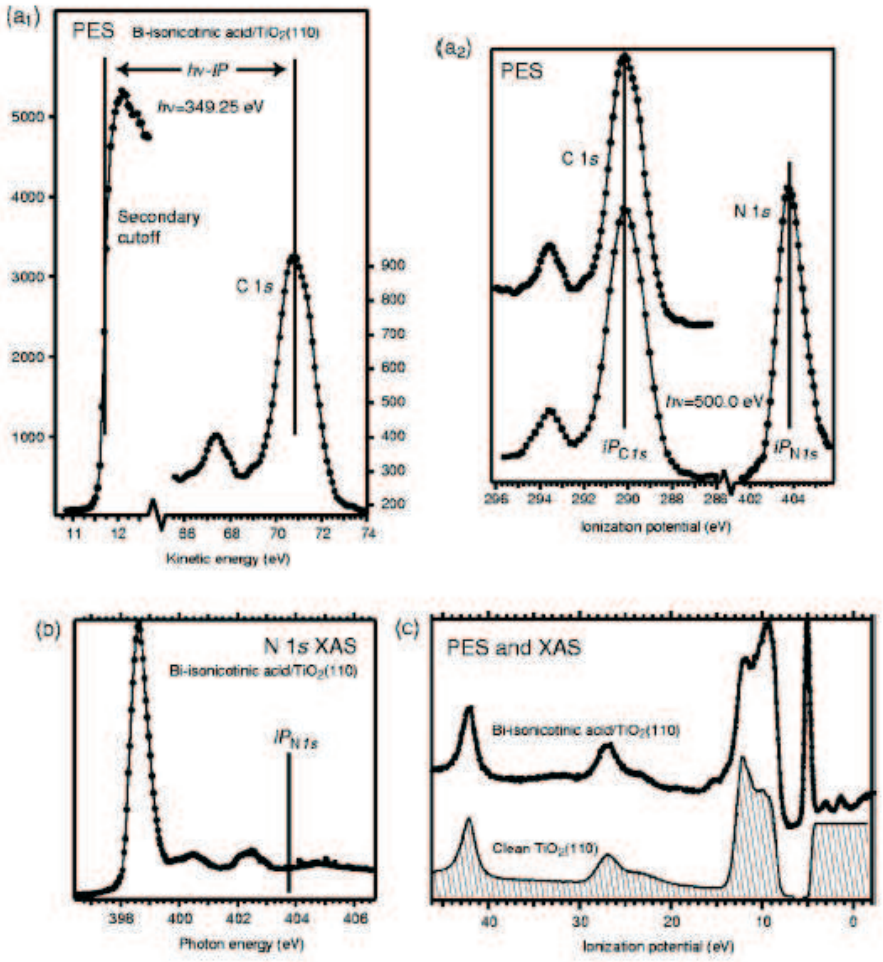

FIGURE 3.20: This figure from Ref. [57] shows the complete calibration of XPS and NEXAFS data for a monolayer of biisonicotinic acid on TiO_2. a1) the secondary electron cut off is used to determine the IP of the C 1*s* peak, a2) The calibrated C 1*s* peak is used to calibrate the N 1*s* peak. b) The N 1*s* NEXAFS data has the energy marked on the energy scale where the photon energy is equal to the ionisation potential, and this point is set at zero on the ionisation potential scale. c) The complete calibrated data set for both the biisonicotinic acid monolayer and for clean TiO_2 showing the valence band and the unoccupied states. The unoccupied states for the TiO_2 have been modelled as a continuum.

3.9 Summary

Synchrotron radiation can be used as a source of tunable, intense, monochromatic photons with which to probe the electronic properties of matter. Synchrotrons are complex experimental systems consisting of electrons travelling round a storage ring. As the electrons

change direction, synchrotron radiation is emitted by the electrons and this radiation can be manipulated for use in many different types of experiment. For surface science we make use of photons in the ultra violet and soft x-ray range, in valence band and core level photoemission, to provide information about the chemical environment of atoms in a sample. When interpreting photoemission spectra, there are both initial and final state effects which must be considered, and for meaningful comparisons between spectra a reliable calibration method must also be employed. In Chapter 6 synchrotron radiation is used to better understand ordered hydrogen bonded films of isonicotinic acid, and the bonding of biisonicotinic acid to TiO_2 and to gold.

Chapter 4

Surface preparation

It is important to prepare samples carefully to obtain the desired surface reconstruction. The sample surfaces used in Chapters 5 and 6 are required to be atomically clean and defect free in order to study molecular adsorption. To prepare the surfaces much of the sample preparation is performed in ultra high vacuum (UHV) to avoid contamination.

4.1 Si(111)(7×7)

Silicon (Si) is a commonly used substrate in surface science experiments. It is an important material due to its relevance in modern semiconductor technology and it is a relatively easy surface to prepare for surface science investigations. The Si(111) surface may be prepared so that a (7×7) surface reconstruction is formed. The widely accepted model for the surface reconstruction of Si(111)(7×7) is the dimer-adatom-stacking model. This model was proposed by Takayanagi *et al* in 1985, and is shown in Figure 4.1 [58]. The uppermost atomic layer contains 12 adatoms per unit cell, which are the bright round features observed in the STM images. Each of these adatoms is bonded to three Si atoms in the layer below and the fourth valence electron is involved in a dangling bond. The second layer has 48 atoms per unit cell, six of which triple-coordinate with neighbouring atoms. These atoms also each have a dangling bond. The other atoms in this layer form dimers around the triangular atom sub-units. The layer below this is the bilayer between the surface atoms and the bulk crystal. The four corners of the unit cell each have a dangling bond from the bilayer. Each unit cell contains 19 dangling bonds, and these contribute to the high reactivity of the surface. The unreconstructed surface has 49 dangling bonds per 7×7 unit cell, providing the driving force for the reconstruction to occur One half of the unit cell is

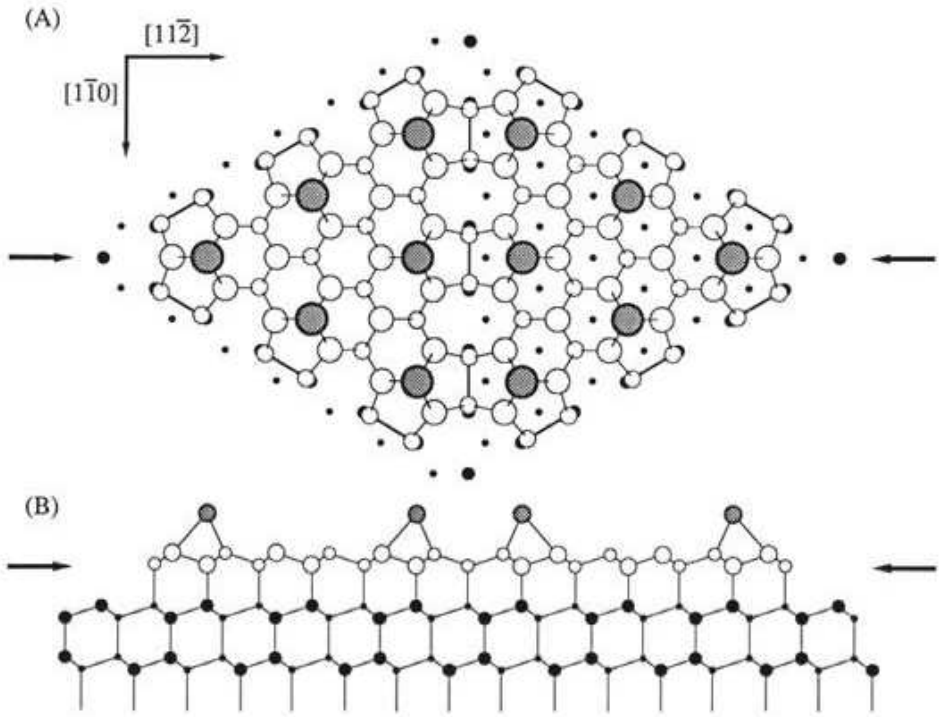

FIGURE 4.1: The Dimer-Adatom-Stacking (DAS) model for the Si(111) 7×7 surface. (after Takayanagi et al [58]). The right side of the unit cell is the faulted half.

lower than the other from bonding considerations, which gives rise to a faulted half and an unfaulted half in the unit cell. The faulted unit cell is apparent in Figure 4.2 a).

The clean reconstructed Si (111)7×7 surface is prepared in vacuum by degassing a piece of p-type Si(111) wafer to remove any carbon contamination present due to exposure of the sample to air. The sample is then heated by direct current ("flashing") to 1173°C until no significant pressure burst occurs. The surface forms the reconstruction upon cooling to 860°C. The reconstruction is quite easy to observe using STM; the uppermost surface atoms (grey circles in Figure 4.1) are imaged as shown in Figure 4.2 in positive and negative bias. It was one of the first surfaces to be imaged using STM in 1983 [59]. Si(111)(7×7) is a reactive surface and adatoms and molecules tend to "hit and stick", with structures mediated by adsorbate-substrate interactions.

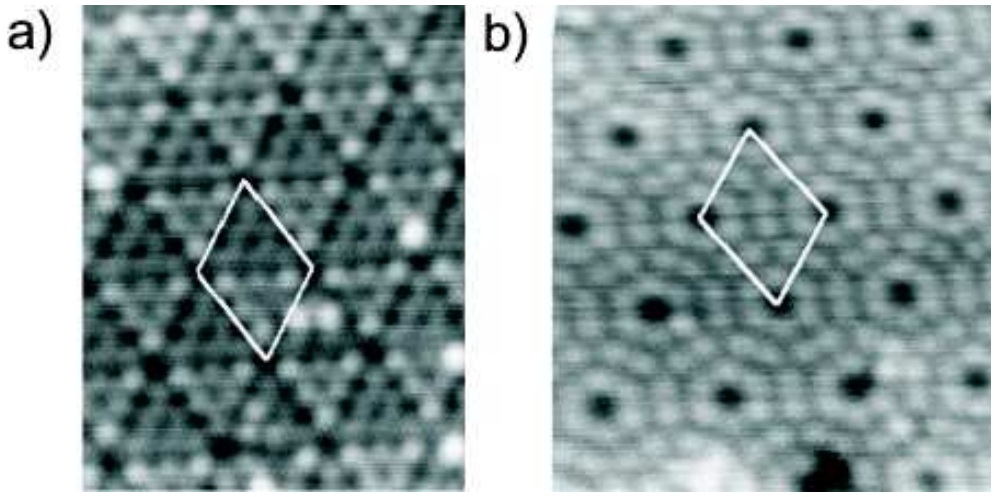

FIGURE 4.2: Close up of the Si(111) 7×7 reconstruction taken at a) -3.0V, showing the occupied states. The faulted halves of the unit cell are clear, and the primitive unit cell is indicated. b) Image taken at +3V showing the unoccupied states of the surface.

4.2 Ag:Si(111)$\sqrt{3} \times \sqrt{3}$R30°

The Si(111) surface is very reactive and in order to deposit molecules on it which can then diffuse freely over the surface, the surface can be passivated. Passivating the surface reduces the number of reactive dangling bonds present. In this thesis a silver termination is used, which gives a well characterised surface which has been used previously to study molecular adsorbates [60]. Silicon (111) is an inherently reactive surface due to the number of dangling bonds per unit cell (Section 4.1). By terminating the surface using silver atoms, the dangling bonds are rendered passive by bonding with silver atoms deposited on the surface. Under the required conditions described below, a Ag:Si(111)$\sqrt{3} \times \sqrt{3}$R30° reconstruction forms which can be imaged using STM. The surface is not simply a monolayer of silver atoms siting on top of the silicon atoms, but rather it is a new surface compound of silver and silicon (see Figure 4.4). The surface also has semiconducting characteristics; the electrons in the surface reconstruction atoms are involved in bonding between the silicon and silver atoms.

To prepare a silver terminated silicon (Ag:Si(111)$\sqrt{3} \times \sqrt{3}$R30°) surface, silver metal is deposited onto clean Si(111)(7×7) at 830°C by heating a silver nugget in a Knudsen cell, while the sample is heated to 550°C. Heating the surface to 550°C prevents the formation of clusters of silver, which occurs at lower surface temperatures, and allows

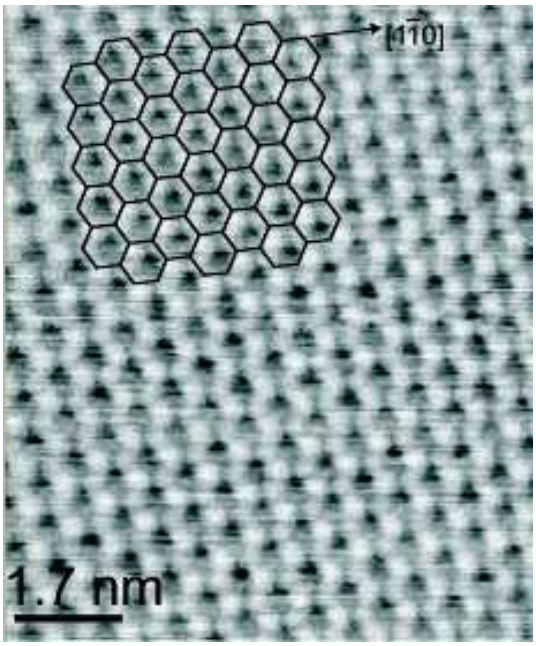

FIGURE 4.3: Image of the $\sqrt{3} \times \sqrt{3}$ R30° Ag reconstruction, taken using a bias = -3.0V. The overlay is the schematic model used when determining molecular adsorption sites on this surface. Each hexagonal unit has a silver trimer at each vertex. The [1$\bar{1}$0] direction is that of the underlying silicon substrate.

the $\sqrt{3} \times \sqrt{3}$R30° reconstruction to form rather than another reconstruction which can occur at higher surface temperatures, such as the 3×1 reconstruction.

The Ag-Si(111)$\sqrt{3}\times\sqrt{3}$R30° reconstruction is shown in Figure 4.3. It is important to monitor the temperature of the substrate carefully during silver deposition as there are other surface reconstructions which can form [61]. This $\sqrt{3}\times\sqrt{3}$R30° reconstructed surface is commonly described using the honeycomb-chain trimer model proposed by Takahashi *et al* [62] and can be represented schematically by a hexagonal lattice, with the network vertices corresponding to Ag trimers and a Si trimer positioned at the centre of each hexagonal repeat unit, as shown in Figure 4.4. Each Ag trimer is located above a second layer Si atom. so that all Si dangling bonds are saturated. This Ag:Si(111)$\sqrt{3} \times \sqrt{3}$R30° surface is relatively passive as all dangling bonds are saturated, so adatoms and adsorbed molecules can readily diffuse across the surface. These adsorbates can form ordered structures which may be mediated by molecule-molecule interactions (see Chapter 5).

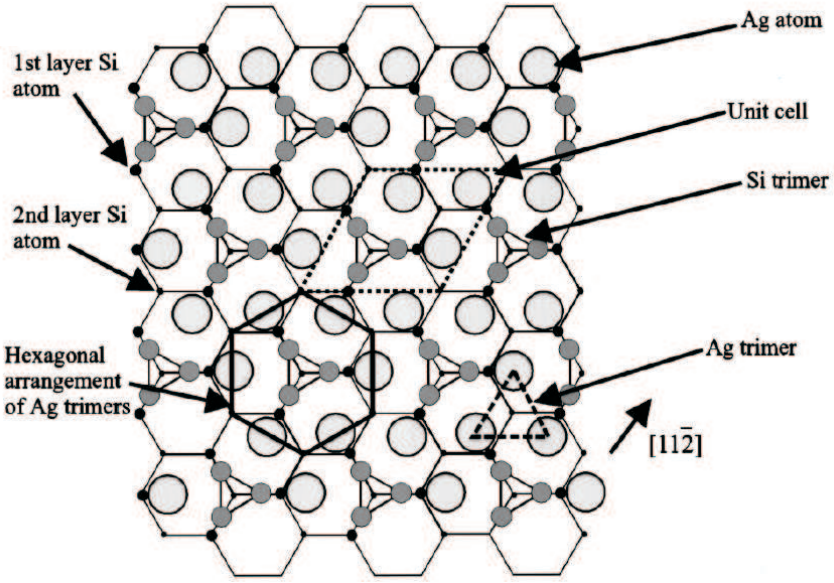

FIGURE 4.4: The Honeycomb Chain Trimer (HCT) model for the Ag:Si$\sqrt{3} \times \sqrt{3}$ R30° surface (after Butcher et al [60]).

4.3 Rutile TiO_2

Titanium dioxide (TiO_2) is a comprehensively studied semiconducting material, and an excellent review of recent research based on TiO_2 can be found in Ref [63]. TiO_2 is used in catalysis with a metal coating as a model metal/oxide interface, it has interesting photoelectric properties, and much research is focussed on TiO_2 being a good choice of material for photo-assisted decomposition of organic molecules.

The interest in this thesis in TiO_2 is as a substrate in molecular solar cell development. Grätzel cells (after Michael Grätzel) contain a mesoporous layer of anatase TiO_2 nanoparticles with a monolayer of dye molecules adsorbed. A commonly used dye molecule used is N3 (Ru(4,4dicarboxy-2,2-bipyridine)$_2$*cis*(NCS)$_2$), an octahedral complex with a central Ru atom, two biisonicotinic acid groups and two nitrogen-carbon-sulphur (NCS) branch groups. The biisonicotinic acid groups act as bonding ligands. Light incident on the dye molecules causes electrons to be excited from the dye into the conduction band of the TiO_2 over a rapid timescale (fs). The dye molecules are replenished with electrons from an electrolyte solution over a longer timescale (ns), and thus electrical energy is obtained, but at a relatively low efficiency ($\sim 10\%$). [64–68]. The study of the bonding ligand components of

these dye molecules such as isonicotinic acid and biisonicotinic acid on single crystal TiO_2 provides a useful insight into the geometry and charge transfer dynamics of molecular solar cells [69].

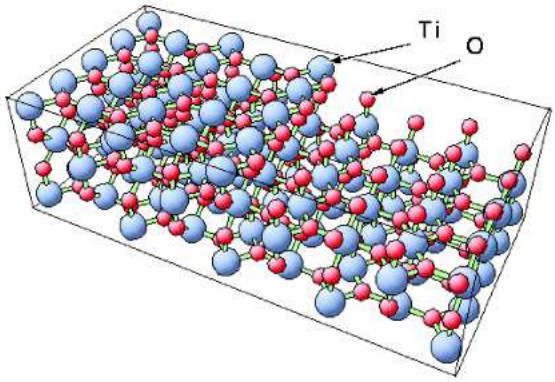

FIGURE 4.5: Schematic of the rutile $TiO_2(110)$ surface. The Ti cations are octahedrally surrounded by O anions. Each O anion has a planar triangle of Ti cations around it (from [70]).

$TiO_2(110)$ single crystal substrates are used in these studies (obtained from Pi-Kem, UK). In order to make the crystal non-insulating (so that XPS spectra are not affected by the sample charging), N-type semiconduction is first induced in the TiO_2 crystal by annealing to 700°C in 1×10^6 Torr O_2 to create bulk defects such as oxygen vacancies and titanium interstitial atoms. The surface is then cleaned by sputtering with Ar^+ ions for 10 minutes. The sputtering process, along with removing surface contaminants, also preferentially removes oxygen atoms from the surface. The sputtering process is thus followed by annealing of the sample in 1×10^{-6} Torr oxygen gas (99.999% pure) for 10 minutes at 600°C to minimise surface defects. The sputtering process also leads to the formation of bulk defects [71] and sputter-anneal cycles change the colour of the crystal from white to a green/blue colour.

A schematic of the rutile $TiO_2(110)$ surface is shown in Figure 4.5. An STM image of $TiO_2(110)$ taken at a sample bias of +1.6V is shown in Figure 4.6 (from [63, 72]). Currently imaging the TiO_2 surface with a negative bias is impossible [73]. Much evidence points towards the contrast differences showing bright and dark rows being electronic effects rather than topographic differences. The bright rows are believed to be due to Ti atoms,

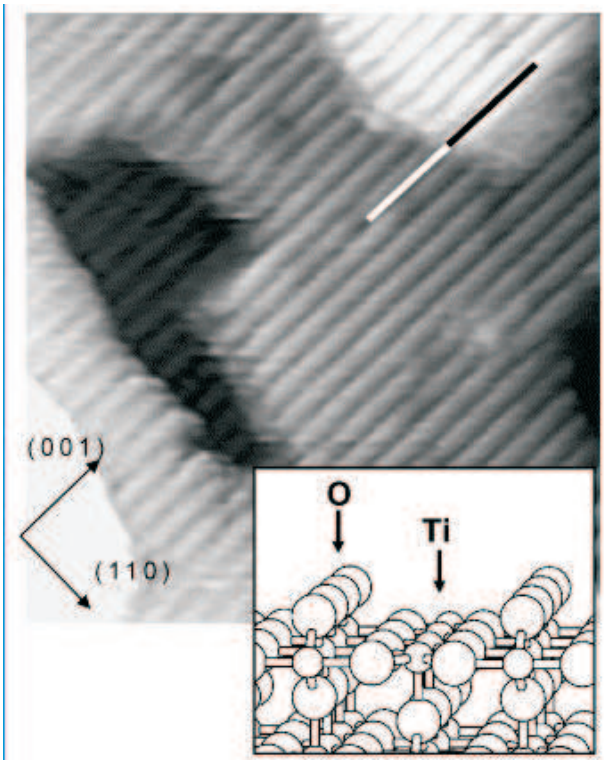

FIGURE 4.6: STM of TiO_2(110) 140Å×140Å. Sample bias +1.6 V, tunnelling current 0.38 nA. The inset shows a schematic of the surface (after Diebold *et al* [72]).

though from the schematic inset one can see the bridging oxygen atoms are topographically higher on the surface.

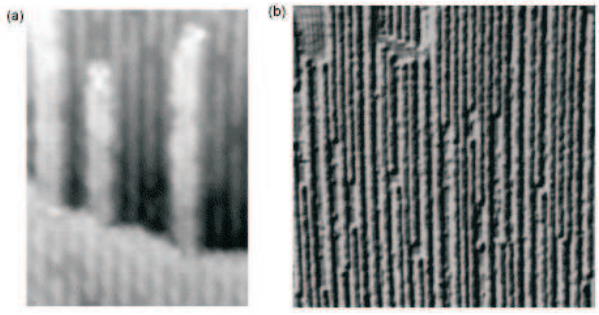

FIGURE 4.7: STM of TiO_2 (110) showing the formation of line structures growing from step edges. (a) Strings of atoms are centered at the fivefold coordinated Ti rows of the lower terrace (8.5 nm×12.3 nm, sample bias +0.7 V, tunnel current: 0.3 nA). (b) Variable current scan of (1×2) ordered strings on the surface annealed at 1150 K. (70 nm × 70 nm, sample bias +2.0 V, tunnel current 0.3 nA). The vertical axis in both images is parallel to the [0 0 1] direction (after Onishi *et al* [74])

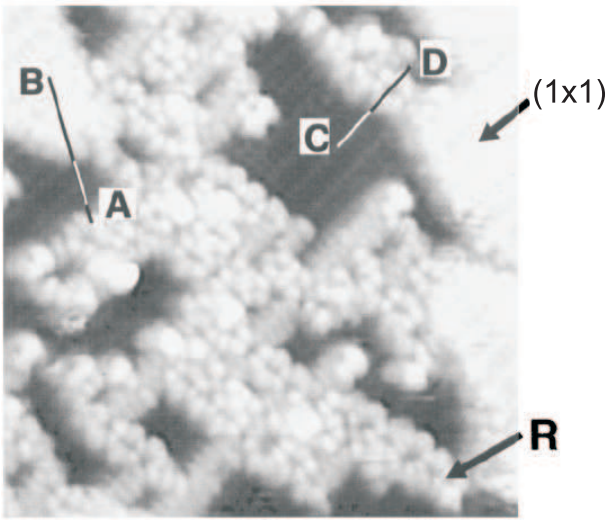

FIGURE 4.8: STM of TiO_2 (110) taken using a sample bias of between +0.5V and +2.0V. The line profiles A-B and C-D show a step height of 6Å. The area labelled R is a networked series of rosette structures (after Li *et al* [75]).

The surface of rutile TiO_2, though well characterised, requires careful preparation in order to avoid the formation of patterned surface structures. The sputter-anneal cleaning process also introduces bulk defects into the sample which make it conducting; this is required for synchrotron studies to prevent sample charging. Annealing also allows the formation of larger terraces and "heals" the surface after sputtering by minimising defects. Repeated sputter-anneal cycles, or annealing at a higher temperature than required can change the surface morphology and produce patterned surfaces which have an effect on subsequent molecular depositions. Surface features which are likely to affect molecular adsorption include the formation of lines at step edges. These are shown in Figure 4.7 and are believed to be a precursor to the formation of the (1×2) reconstruction [72, 74]. This surface was prepared by annealing at 1020 K for 1 min. Crystallographic shear planes can also form after annealing which change the surface structure. Rosette structures (Figure 4.8) can form through oxidation and annealing the crystal at 550K. [75]. Generally, the surface reconstruction, surface features and therefore surface chemistry are highly dependent on preparation conditions and surface history. It is believed that pale blue crystals are the best for a good (1×1) surface, whilst annealing many times in oxygen can give rise to more complex surface features.

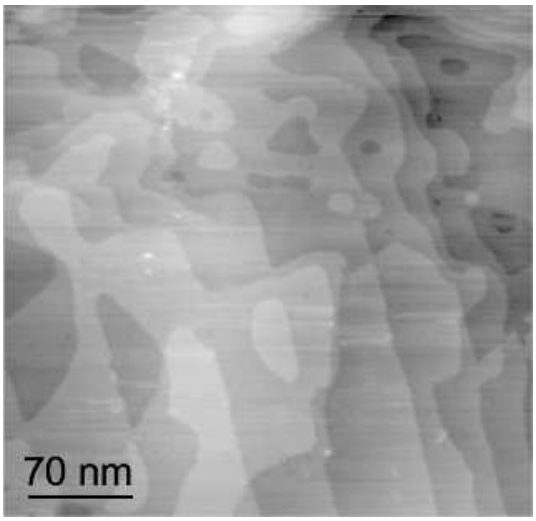

FIGURE 4.9: Large scale image of clean Au(111) surface. Bias = -2V, current = 0.05nA

4.4 Au(111)

Au(111) substrates were used in this thesis in the STM based study of biisonicotinic acid (Section 6.9.3). Gold was chosen as a comparison to photoemission studies described in chapter 6 of biisonicotinic acid on gold deposited on TiO_2(110).

The gold Au(111) surface is the only face-centered-cubic metal surface which undergoes a reconstruction [76] to a $22 \times \sqrt{3}$ arrangement. There is a transition between face centered cubic packing and hexagonal-close-packed stacking of the upper atoms on the surface, and because of this an atomic corrugation can be observed. A further superstructure exists due to a correlated bending of 120° of the corrugation lines every $\sim$ 250Å, indicating the surface undergoes long range strain relief. The ends of the corrugation lines, which tend to exist in pairs, are characterised by well defined "u-turns" and no corrugation line ends abruptly. Since the reconstruction occurs over a large scale, step edges and defects can affect the reconstruction by allowing the formation of more irregular corrugations on the surface, but corrugation lines can continue over step edges. Figures 4.9 and 4.10 show the overall morphology of an Au(111) surface and a close up showing the corrugation lines, prepared in the studies described in Section 6.9.3. Here smaller irregular areas of corrugations were imaged rather than larger terraces showing the uninterrupted $22\times\sqrt{3}$ reconstruction.

The samples used in this thesis were mica substrates with a 150nm gold layer on top, which have been flame annealed by the manufacturers using a hydrogen flame in a

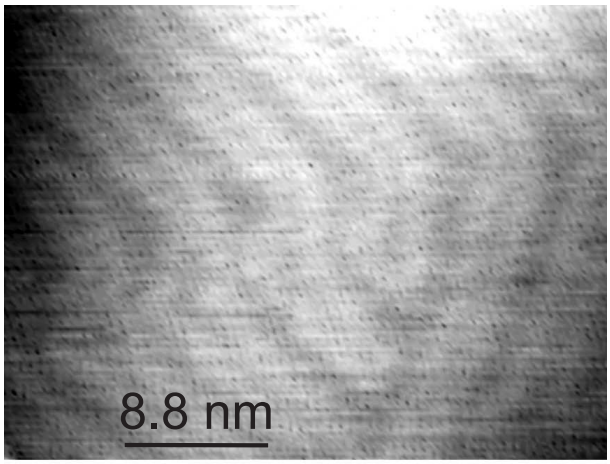

FIGURE 4.10: Zoomed in STM image of clean Au(111) surface showing the herringbone features. Bias = -2V, current = 0.05nA

clean environment, which allows the $22\times\sqrt{3}$ to form and which cleans the surface. They are prepared in these studies after introduction to the UHV environment by first sputtering with 1kV Ar^+ ions in 1×10^{-6} Torr Ar for 20 minutes to clean the surface. The sample is then annealed at 600°C for several hours (between 2 and 12 hours). It was found that longer anneal times tended to give surfaces which were easier to image with larger domains. These gold samples were used in STM studies of biisonicotinic acid on gold (Section 6.9.3), complementary to synchrotron studies of biisonicotinic acid on gold on TiO_2(110) (Chapter 6).

4.5 Summary

In this thesis different surfaces have been used. Si(111) can be prepared to form the 7×7 reconstruction, and this reactive surface can be terminated using silver to form the Ag:Si(111)$\sqrt{3} \times \sqrt{3}$R30° surface. The Au(111) surface, which shows a $22 \times \sqrt{3}$ reconstruction, is also used here for STM studies of biisonicotinic acid. TiO_2 is used in research based upon many practical applications including molecular solar cell manufacture. Rutile TiO_2 is an interesting surface and is used here in photoemission studies of pyridinecarboxylic acids.

Chapter 5

PTCDA and bimolecular PTCDA arrays

Perylene-3,4,9,10-tetracarboxylic-3,4,9,10-dianhydride (PTCDA) is a planar organic molecule which exhibits many different ordered phases when adsorbed on different surfaces, and which has applications in organic electronic devices. This chapter describes the ordered phases formed by PTCDA on the Ag-Si(111)$\sqrt{3} \times \sqrt{3}$R30° surface using scanning tunnelling microscopy (STM). The observed molecular ordering in these studies is different to that which has been previously reported on other surfaces, particularly a square phase which is observed here. Models for the different observed phases are presented and simple theoretical calculations have been performed to indicate the stability of the models.

Following the study of PTCDA molecules alone on the Ag-Si(111)$\sqrt{3}\times\sqrt{3}$R30° surface, bimolecular systems were studied, again using STM, of PTCDA and C_{60}, and PTCDA and melamine. PTCDA and C_{60} do not form any intermixed supramolecular structures, but the two species form separate ordered regions. The combination of PTCDA and melamine forms a hexagonal intermixed network and a double row phase. The hexagonal phase appears to be stabilised by a previously unseen hydrogen bonding junction.

5.1 Previous research

PTCDA is a widely studied molecule in terms of molecular interactions and its suitability for organic device fabrication. A schematic diagram of PTCDA is shown in Figure 5.1 along with a calculated representation on the highest occupied molecular orbital, calculated in Spartan'02 [49]. The semi-empirical AM1 model used here to calculate the shape of the highest occupied molecular orbital (HOMO) is a simple model but satisfactory for molecular orbital shape estimations. The AM1 model is a molecular mechanics method

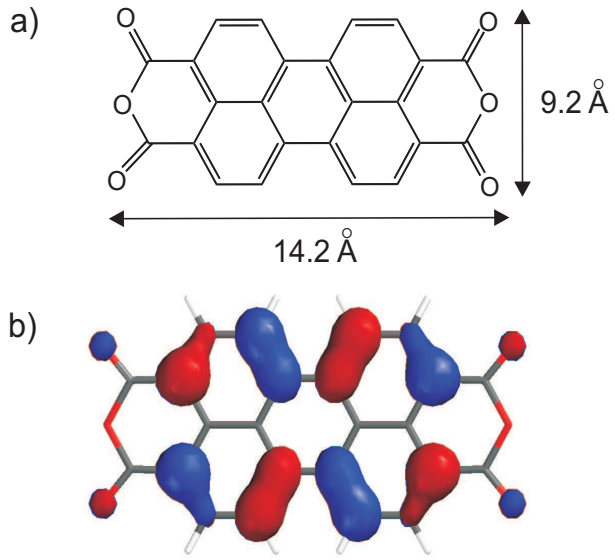

FIGURE 5.1: a) PTCDA schematic and b) HOMO calculated using the AM1 model in Spartan '02. the red and blue lobes show the positive and negative signs of the probability amplitude.

which describes molecules in terms of connected atoms and ideal bond angles and lengths, like a 'ball and spring' model. By calculating electron distribution over the molecule it can predict the shape of the molecular orbitals. These models are a useful indicator of how a molecule may appear in STM images, though it should be considered as a guideline only. Here it appears that the electron density has a minimum along the central long axis of the molecule - this is in fact apparent is most of the STM images of the square and hexagonal phases. An extensive study of the appearance in high resolution STM images of planar aromatic organic adsorbates on graphite, MoS_2 and Ag(111), compared to the calculated molecular orbitals using the semi empirical MNDO model, was performed by Strohmaier *et al* [77].

The structure and behaviour of PTCDA thin films is an active research area for many groups worldwide, and the growth of PTCDA layers and crystallites has been studied on many surfaces. Examples include the growth of PTCDA films on noble metal surfaces by Glöckler *et al* [78], who investigated PTCDA and dimethyl-perylene-3,4,9,10-tetracarboxylic-3,4,9,10-diimide (dM-PTCDI) on Ag(111) and Ag(110), and observed the formation of different commensurate structures with high submolecular resolution. Schmitz-Hübsch *et al* [79] also studied PTCDA on different gold reconstructions and found herring-

bone and rod structures formed, with influence from the substrate. Chizhov *et al* [80] observe PTCDA arranged in the herringbone phase alongside another phase with PTCDA molecules forming a near perpendicular junction with one another on Au(111). Tiba *et al* [81] studied PTCDA on the ferromagnetic oxygen passivated nickel surface (O-p(2 x 2)-Ni(111)) and found epitaxial PTCDA layer growth, then proceeded with further depositions which were observed to form ordered crystallites. Sazaki *et al* [82] studied the crystallographic behaviour of PTCDA on hydrogen passivated Si(111). Kendrick *et al* [83] found that PTCDA on highly ordered pyrolytic graphite (HOPG) forms a quasi-epitaxial herringbone structure where crystallographic strain in the PTCDA overlayers can be observed in STM images as contrast differences.

The growth of PTCDA on organic monolayers has also been investigated by Schmitz-Hübsch *et al* [79] who observed PTCDA on hexa-peri-benzocoronene (HBC) on highly ordered pyrolytic graphite (HOPG), and that it formed large flat, defect free plains, with Moiré patterns indicating the heteroepitaxy present. Staub *et al* [84] also observed a square-type phase of PTCDA on an organic decanethiol layer on an Au(111)-mica substrate. They found the PTCDA disrupted the decanethiol layer to produce a herringbone phase as well as square arrangements in 2-D islands and rows.

A herringbone pattern is the most commonly observed motif observed in molecular layers of PTCDA, similar to the alpha and beta bulk phases of PTCDA which exist as monoclinic stacked herringbone crystals. Figure 5.2 shows some of these PTCDA herringbone structures which were observed under various conditions.

PTCDA is also a candidate material for organic electronic devices, demonstrated by Wagner *et al* [87] who show the suitability of PTCDA for device preparation in growing well defined crystallites of PTCDA on copper and gold surfaces. The epitaxy of grown PTCDA films is an important consideration in device fabrication and is widely studied [38, 82, 88–91].

5.2 Experimental method

The initial aim of the investigation presented here was to deposit a submonolayer coverage of PTCDA onto a clean Ag-Si(111)$\sqrt{3} \times \sqrt{3}$R30° surface, in order to observe if the molecules arranged into an ordered structure. The surface was imaged using room temperature scanning tunnelling microscopy (STM) using the STM described in Section 2.4. The

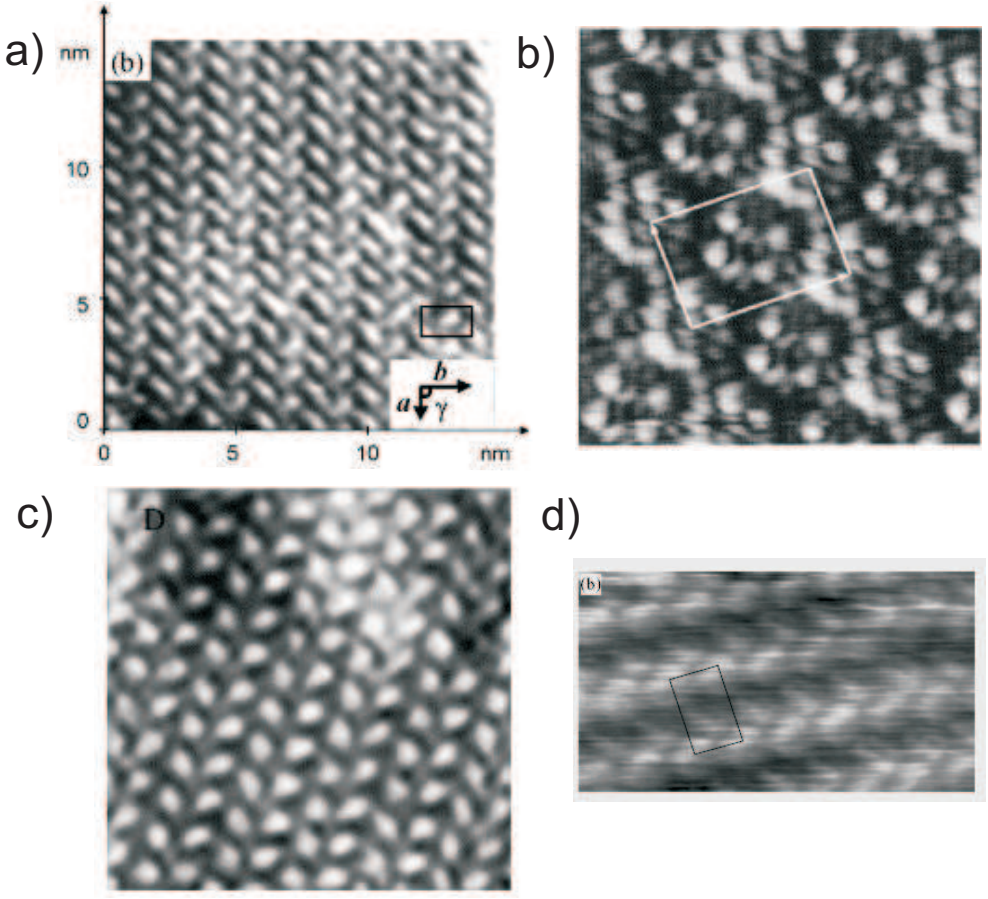

FIGURE 5.2: PTCDA forms herringbone phases on various surfaces. a) Tiba *et al* studied PTCDA on O-p(2 x 2)-Ni(111) [81]; b) Glockler *et al* obtained a high resolution 45 × 45Å scan of PTCDA in the herringbone phase on Ag(111) [78]; c) 12 × 12 nm image of a PTCDA crystallite on H:Si(111) by Chen *et al* [85]; d) 10nm×5.8nm image of PTCDA on S passivated GaAs(100) by Nicoara *et al* [86].

STM operates in constant current mode in an ultra-high vacuum (UHV) system, with a base pressure of 1×10^{-10} Torr. Electrochemically etched tungsten tips were used (Section 2.6) for imaging. The Ag-Si(111)$\sqrt{3} \times \sqrt{3}$R30° surface was prepared as described in Section 4.1.

PTCDA was obtained from Sigma Aldrich (99.9% pure) and was thoroughly degassed prior to deposition. PTCDA was deposited at 330°C for 10 minutes onto the sample, to give a submonolayer coverage (<0.1ML). The substrate was held at room temperature during deposition. Several samples were prepared and imaged to ensure reproducibility of the phases observed. The imaging parameters used were a -3.0V bias and 0.1nA tunnel current. When imaging the square phase, contrast variations were observed using a bias of -2.5V. It was not possible to image in positive bias in these experiments.

5.3 PTCDA phases

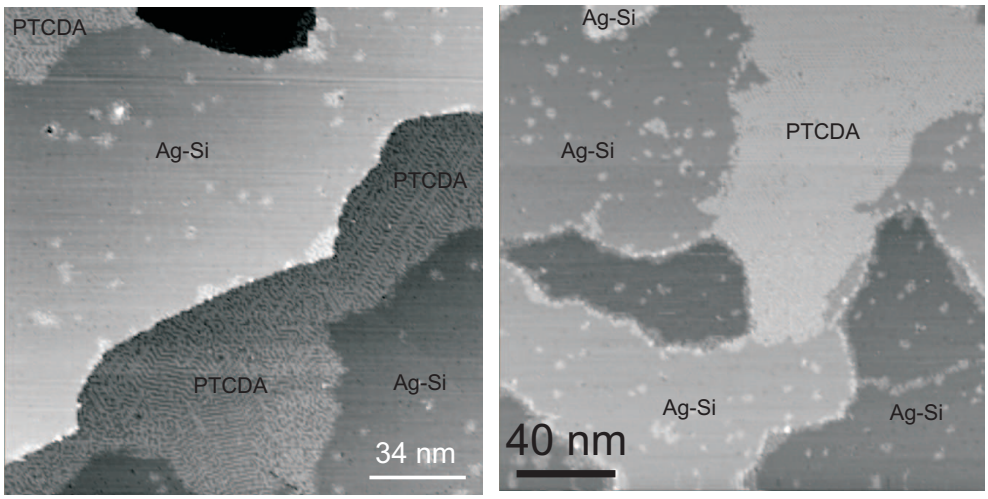

FIGURE 5.3: Larger scale images of PTCDA islands on the Ag-Si$\sqrt{3} \times \sqrt{3}$ R30° surface. For both images, bias = -3.0 V, current = 0.1nA

STM images of the surface after the deposition of $\sim$ 0.1ML of PTCDA are shown in Figure 5.3. Islands of close packed PTCDA molecules with lateral dimensions of up to 300nm were observed, often growing from step edges or between steps on the Ag-Si(111)$\sqrt{3}\times$ $\sqrt{3}$R30° surface. Three distinct phases were observed within these islands, which can coexist in a single island, as shown in Figure 5.4. The three phases present are: the herringbone phase, which is commonly observed; a square phase, which is also abundant over the surface;

with a third hexagonal phase present, which we believe is a combination of the herringbone and square phases. The three phases were all observed under the same growth conditions on the same sample. Some islands consisted of all three phases, others of only two of the three phases, and others of only a single phase. There were also other small regions of irregularly arranged molecules. The islands have a topographic height of 2.4 ± 0.5Å, consistent with a single layer of molecules lying flat on the surface, as expected for a large π-conjugated molecule.

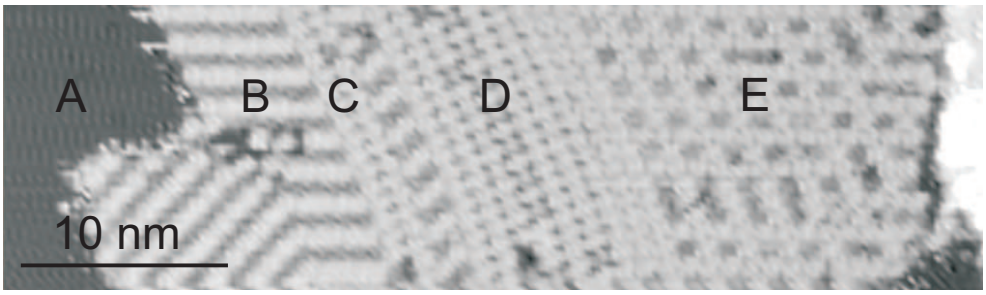

FIGURE 5.4: This region shows all three main phases present. A - Ag-Si surface, B - Herringbone phase, C - A boundary row, D - Square phase, E - Hexagonal phase. Bias = -3.0 V, current = 0.1nA

5.3.1 Herringbone phase

The commonly observed herringbone phase is shown in Figure 5.5: The herringbone phase in this case is composed of alternating rows of canted molecules, which run along the major axes of the Ag-Si(111)$\sqrt{3} \times \sqrt{3}$R30° termination. Each molecule appears as a single bright topographic feature with an apparent height which alternates from row to row. The silver termination is shown in the inset to Figure 5.5b), and is represented in the models as a hexagonal network describing the honeycomb-chain-trimer model which is commonly accepted, and illustrated in Figure 4.2. The underlying silicon lattice vector $[1\bar{1}0]$ is indicated on all models in this chapter as a reference direction.

The separation between equivalent rows of this herringbone phase can be determined from images in which the silver termination and the molecular overlayer are both resolved. The separation is $3a$, where $a = 6.65$Å is the lattice constant of the Ag-Si(111)$\sqrt{3} \times \sqrt{3}$R30° surface, or the distance between the centres of two adjacent hexagonal units in the model. From studying similar images, the molecular separation within a row

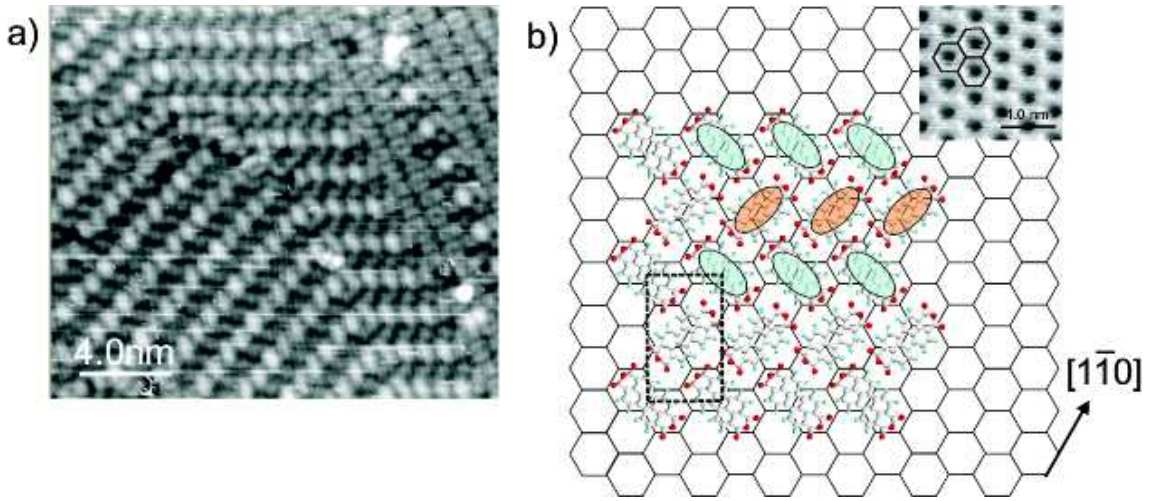

FIGURE 5.5: a) Two domains of the herringbone phase are shown. The square phase appears in the top left of the image (section 5.3.2). Bias = -2.5V, current = 0.1 nA. b) This model shows the molecules sitting in inequivalent sites in alternate horizontal rows on the Ag-Si(111)$\sqrt{3} \times \sqrt{3}$R30° surface, which would account for the contrast variation seen in the images. [1$\bar{1}$0] is the underlying Si lattice vector. The inset in part b) shows an STM image of the Ag-Si(111)$\sqrt{3} \times \sqrt{3}$R30° reconstruction (see text). Bias = 2.0V, current = 0.1 nA

has been determined to be $\sqrt{3}a$. These dimensions form the basis for the model shown in Figure 5.5b. The unit cell of the molecular packing is shown as $3a \times \sqrt{3}a$, or 20.01Å×11.55Å.

A similar herringbone phase has been reported on many other surfaces (Section 5.1) and is very similar to the stacked planes of molecules in the bulk monoclinic α phase of PTCDA. The unit cell dimensions are 19.91Å×11.96Å for the bulk herringbone unit cell [78]. These values are close to the unit cell dimensions observed in this work, and, within experimental error, the molecular angles are the same for this phase and in the bulk α phase. There also exists a bulk β phase which has a 'squashed' unit cell compared with the α phase, but the surface herringbone phase observed here resembles the α phase much more closely. Semi empirical modelling using the AM1 model of a planar cluster of six PTCDA molecules gives optimum unit cell dimensions of 19.5Å×12.1Å, in reasonable agreement with observed dimensions. This and the following semi empirical calculations do not include the surface.

The difference in contrast of adjacent rows indicates that molecules are sitting at inequivalent binding sites on the surface. In Figure 5.5b, a possible registry with the surface in which alternate rows are adsorbed on inequivalent sites, which is consistent with

the observed contrast variation, is shown. Similar contrast variations have previously been reported in herringbone phases of PTCDA on HOPG [83], on Ag(111) [38], and of NTCDA on Au(111) [92]

5.3.2 Square phase

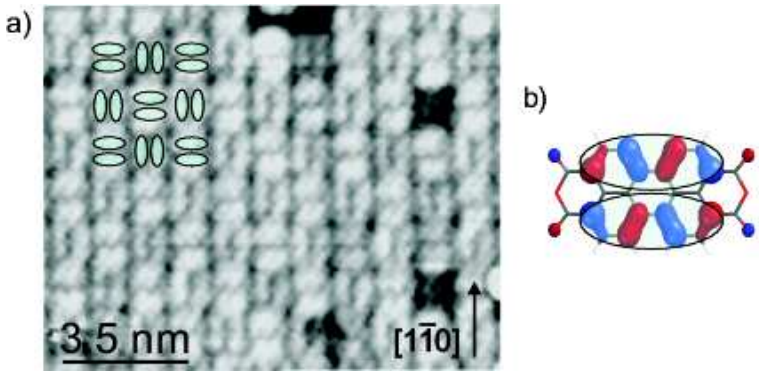

FIGURE 5.6: STM images of the square phase. a) In this image intermolecular contrast is resolved showing that adjacent molecules are perpendicular to each other. This is illustrated by the schematic overlay of the lobes of the HOMO over the intramolecular features. (Bias = -3.0V, current = 0.1nA), b) This schematic shows the calculated HOMO for a PTCDA molecule with an overlay of the orbital shape visible in STM images, to indicate how a molecule appears in this phase.

In addition to the commonly observed herringbone phase, two other close packed molecular phases were observed. The second principal phase is shown in Figures 5.3a), 5.6, 5.7 and 5.8. The apparent square arrangement of these molecules is very unusual; the molecules are adsorbed on a hexagonal substrate, which would perhaps not be expected to support an overlayer with square symmetry. Staub *et al* [84] report a square phase but do not elucidate the structure, giving two possibilities. Also Chizhov *et al* [80] note a square-type arrangement but this is more open than the one observed here with a molecule/molecule angle of 83° rather than 90° for a truly square packing.

In images such as Figure 5.6a), it is possible to resolve intramolecular contrast in the form of two lobes running along the length of each molecule. We associate these lobes with the HOMO calculated using a semi empirical model (see Figure 5.6b)) and these images show that nearest neighbours are perpendicular to each other and form a square arrangement. This arrangement is very close to a candidate structure proposed by Staub *et al* [84]. It is clear that this phase is stable, as extended, well ordered regions are observed

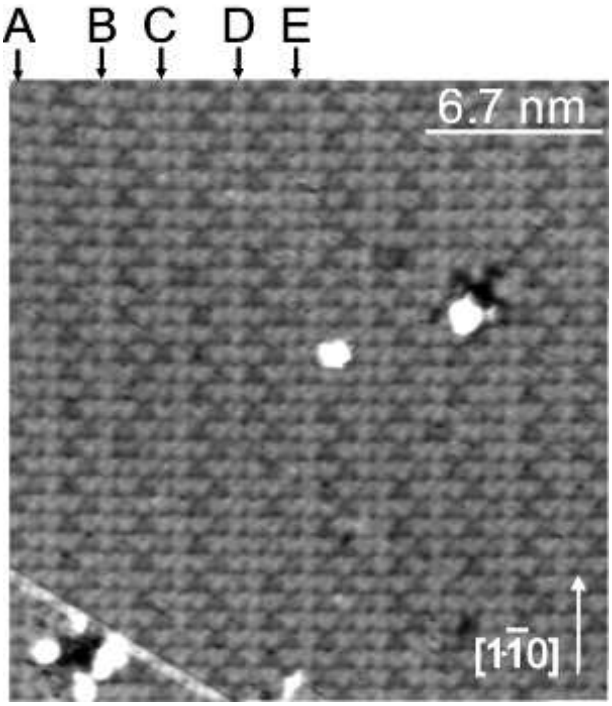

FIGURE 5.7: b) A larger square packed region showing contrast variation between different molecules - the arrows marked A-E indicate "equivalent" bright rows and are explained in the text. (Bias = -2.5V, current = 0.1nA)

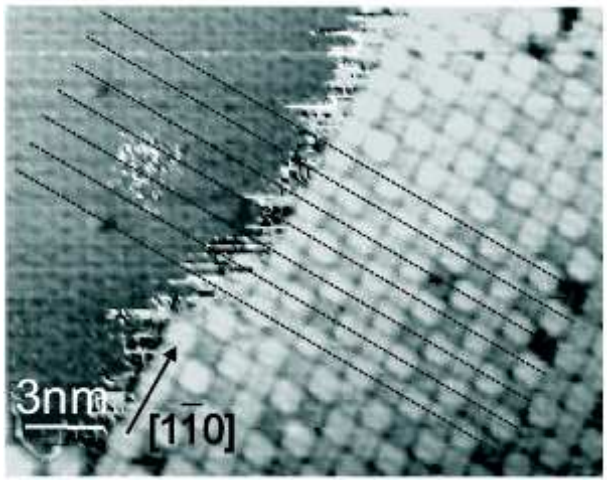

FIGURE 5.8: This image shows the initial steps in determining the registry of PTCDA molecules in the square phase. The silver termination is resolved in the upper left of the image, and the dotted lines show the separation of molecules with respect to the silver termination. (Bias = -2.5V, current = 0.1nA)

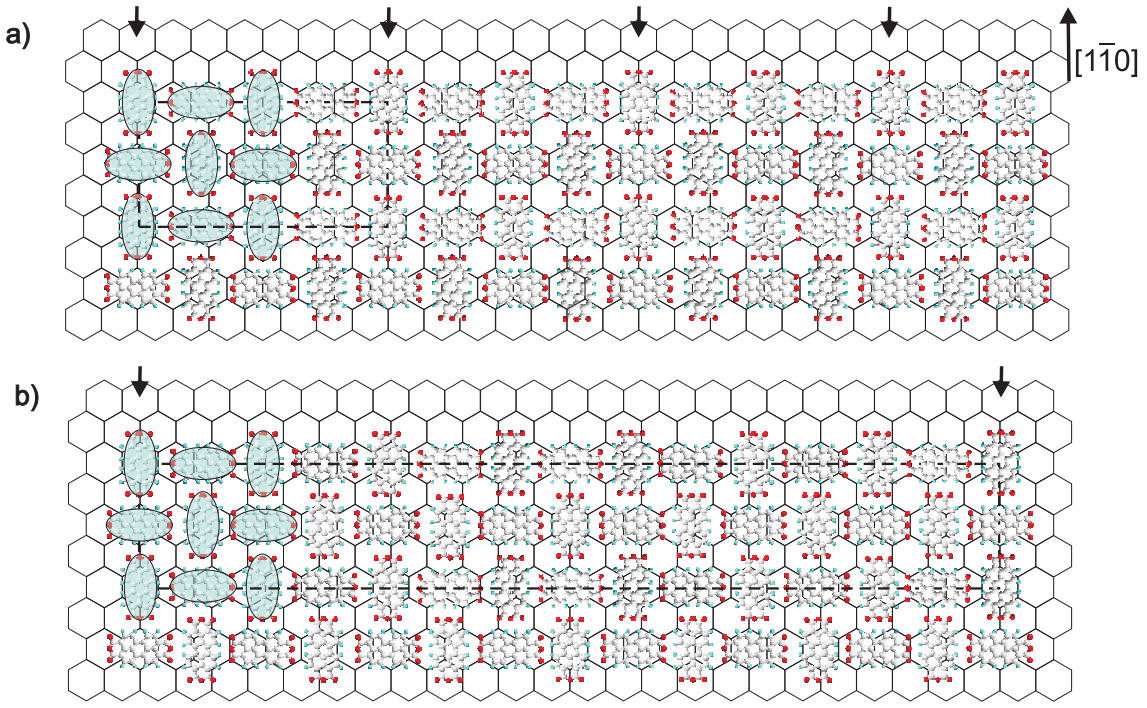

FIGURE 5.9: The two molecular models considered for this phase. Figure (a) shows a model with unit cell dimensions of $2\sqrt{3}a \times 7a$; Figure b) shows an alternative model with a larger unit cell of $2\sqrt{3}a \times 24a$. The unit cells are shown with dotted lines and the arrows indicate molecular rows in equivalent positions on the surface. The [1$\bar{1}$0] direction of the underlying silicon substrate is also indicated as a reference.

(Figure 5.3).

Images where both the hexagonal Ag-Si(111)$\sqrt{3} \times \sqrt{3}$R30° surface reconstruction and square packed molecular islands are well resolved, such as Figure 5.8, show that one axis of the square phase is parallel to the [1$\bar{1}$0] direction of the underlying silicon surface. Also the separation of the centres of two equivalent molecules in this direction may be accurately measured as $2\sqrt{3}a$, or 23.1Å, from the construction in Figure 5.8. Alternate molecules aligned in rows running in the [1$\bar{1}$0] direction are in equivalent surface adsorption sites shown in the models in Figure 5.9.

It is much more difficult to identify the separation of the adsorption sites in the rows running perpendicular to the [1$\bar{1}$0] direction. Within experimental error the molecular spacing in the two orthogonal directions is equal. Possible models for commensurate arrangements were considered in which n molecular repeat units (consisting of two orthogonal molecules) are placed over m lattice constants. For n repeat units the unit cell dimension

Table 1: Summary of two possible square phase dimensions

n, m	$2n\sqrt{3}$	ma/n	$1-(2m/\sqrt{3})$
$n=2$, $m=7$	6.93	23.3Å	-1.0%
$n=7$, $m=24$	24.25	22.8Å	+1.0%

This table summarises the dimensions of two possible commensurate arrangements of molecules in rows perpendicular to the $[1\bar{1}0]$ direction of the Si substrate. The commensurability corresponds to n orthogonal molecular pairs over m lattice constants. The integers n and m are given in Column 1. Column 2 gives the dimension of the unit cell perpendicular to the $[1\bar{1}0]$ direction in units of the surface lattice constant - this value should be close to m. Column 3 gives the average length occupied by an orthogonal molecular pair and Column 4 gives the % difference between the molecular spacing parallel and perpendicular to the $[1\bar{1}0]$ direction - a positive value indicates that rows perpendicular to the $[1\bar{1}0]$ are compressed.

in the $[1\bar{1}0]$ direction is $2n\sqrt{3}a$. From a simple consideration of the geometry of square and hexagonal lattices it is clear that we must identify a pair of integers n and m which satisfy the relationship $2n\sqrt{3}a = ma$, i.e give a molecular repeat unit with sides of equal length. Although this equality cannot be satisfied exactly since $\sqrt{3}$ is an irrational number, there are two pairs of integers (n, m) for which this condition holds to within 1%. These integer pairs are (2,7) and (7,24) and the resulting values for the molecular separation are shown in Table 1. Note that the molecular repeat unit length is given by ma/n, which is equal to 23.3Å and 22.8Å respectively for the (2,7) and (7,24) models. These values correspond to a 1% extension and compression compared with the spacing in the $[1\bar{1}0]$ direction, and both these models are shown in Figure 5.9.

The stability of the proposed arrangements has been investigated using semi empirical modelling. The AM1 model has been used to minimise the total energy of the planar cluster of nine PTCDA molecules (and also smaller clusters) shown in Figure 5.10. First a single PTCDA molecule was modelled using the AM1 model, which calculated the optimum geometry of the molecule in terms of bond lengths and angles. This model was copied and repeated to form a 3×3 pattern of nine molecules in square phase as in Figure 5.10, then this cluster was modelled within the AM1 model to check its stability. These simulations confirm that this arrangement is stable with a calculated separation between equivalent molecules of 22.8Å. The perpendicular orientation of neighbouring molecules is stabilised by weak C-H$\cdots$O hydrogen bonding between the dianhydride groups and the hydrogen atoms bonded to the perylene core of PTCDA as discussed in Ref [85] in combination with the quadrupolar interaction between PTCDA molecules. The calculated spacing, 22.8Å, is very close to the molecular repeat unit in the proposed models both parallel and

perpendicular to the $[1\bar{1}0]$ direction.

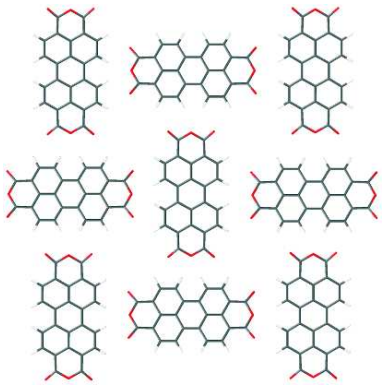

FIGURE 5.10: The semi empirical model of a nine-molecule cluster in the square phase as calculated by Spartan gives a distance between equivalent molecules of 22.8Å.

It is possible to distinguish experimentally between the (2,7) and (7,24) models of molecular packing by acquiring images with the sample bias in the range -2.0V to -2.5V. Over this bias range we observe a contrast variation between molecules adsorbed at different surface sites. Figure 5.7 shows an STM image of a region of the square packed phase acquired in this bias range. The resulting contrast variation has the appearance of stripes running in the $[1\bar{1}0]$ direction, since molecules in the rows running in this direction are adsorbed in equivalent sites (although note that neighbouring molecules are orthogonal resulting in a contrast difference between alternate molecules giving some of the rows in this direction a two-fold periodicity).

There is a more complex contrast variation perpendicular to the $[1\bar{1}0]$ direction which arises from the occupancy of many non-equivalent surface sites in the rows running in this direction. However, a variation in apparent brightness is observed only for one of the two possible orthogonal molecular orientations. Specifically, molecules oriented with their long axis perpendicular to the $[1\bar{1}0]$ direction show strong variations in molecular contrast for different adsorption sites along the rows running perpendicular to the $[1\bar{1}0]$ direction. However, for molecules with their long axis along the $[1\bar{1}0]$ direction the variation in contrast is much weaker. The formation of one of the commensurate structures discussed above would give rise to a regular sequence of stripes (parallel to $[1\bar{1}0]$) with a period (in the direction perpendicular to $[1\bar{1}0]$) corresponding to n molecular repeat units. For the (2,7) proposed array the contrast would be periodic with a period corresponding to 2 pairs of orthogonal molecules, i.e. every fourth row running along the $[1\bar{1}0]$ axis would be equivalent. Similarly

for the (7,24) array every 14th row would be equivalent.

In most of the STM images it is difficult to pick out a clear repeating sequence. There is some evidence for the (7,24) ordering as shown in Figure 5.6b). As marked on this figure (A - E), double and single bright rows run along $[1\bar{1}0]$ which are alternately separated by 3 or 4 molecules (e.g. the separation of A and B is 4 molecules, the separation of B and C is 3 molecules, etc.). This ordering is consistent with an overall periodicity of 7 molecular repeat units, although, unsurprisingly for such a large unit cell, this sequence is not seen to repeat over multiple unit cells. Although some local order is present with a repeat unit of 4 molecules there is no evidence for extended regions showing the (2,7) ordering, which, for this smaller unit cell, would be expected if it were the preferred configuration.

Overall it is most likely that the (7,24) ordering is more stable, while noting that the combination of a large unit cell, many possible (7) non-equivalent adsorption sites and the presence of defects on the surface limits the formation of domains displaying this order over many unit cells. Indeed, even for surfaces with relatively low defect densities as prepared for these studies, it is difficult to distinguish experimentally the formation of commensurate packing with such a large unit cell from an incommensurate arrangement.

5.3.3 Hexagonal phase

STM images of the third major phase of PTCDA, the hexagonal phase, are shown in Figure 5.11. Figures 5.11a) and b) show extended regions of this hexagonal phase adjacent to the herringbone and square phases respectively. Figures 5.11c) and d) show a higher magnification of the hexagonal region in which intramolecular features may be resolved, but each image shows a different chirality of the hexagonal phase. PTCDA molecules are not inherently chiral, but the hexagonal arrangements seen here are pseudochiral due to the molecules being confined to a plane (as they are adsorbed onto the surface). The lobe features in c) and d) are very similar to those observed for molecules in the square phase (see Section 5.3.2) and are again thought to be the two lobes of the HOMO. Analysis of profiles across the phase shows that the darkest features are not empty pores, since they do not have the same apparent height as the silver termination. These low contrast features inside the hexagons correspond to molecules which have a low apparent brightness, similar to the dark rows in the herringbone phase (Section 5.3.1). The separation between low contrast molecules is equal to $2\sqrt{3}a$.

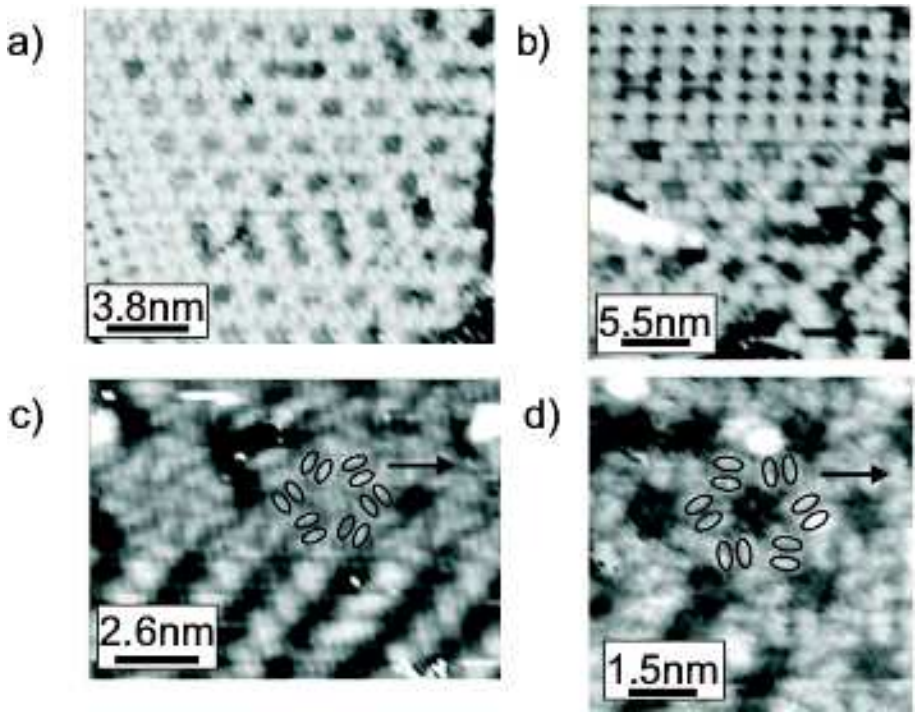

FIGURE 5.11: a) Extended region of the hexagonal phase. Bias=-3.0V, current=0.1 nA, b) The hexagonal phase neighbouring a square phase region. Bias=-3.0V, current=0.1 nA, c) and d) show the resolved lobes of the molecules (see Figure 5.6a), indicating their individual orientations. A group of six molecules representing one hexagonal unit is highlighted in c) and d), showing the two different pseudochiralities present, and the arrows show the $[1\bar{1}0]$ direction. For (c) and (d) bias = -3.0V, current = 0.1 nA.

Hexagonal and square phases can coexist in the same island with no disordered boundary where they meet, as shown in Figure 5.11b). The horizontal rows of the square phase are parallel to rows in the hexagonal phase and, in fact, the bright rows of the hexagonal phase have a nearly equivalent appearance to the rows of the square phase. Hexagonal and herringbone phases also coexist in the same island with no disordered boundary between them, as shown in Figure 5.11a). In this case the horizontal rows in the hexagonal phase which appear alternately bright and dark are parallel, and very similar to, rows of the herringbone phase (with alternate bright and dark contrast molecules) which run along $[1\bar{1}0]$ direction.

By examining images of multi-phase islands, it is possible to determine, to a first approximation, that the hexagonal phase is composed of alternating rows of molecules in the square and herringbone configurations. The model for this arrangement is shown in Figure

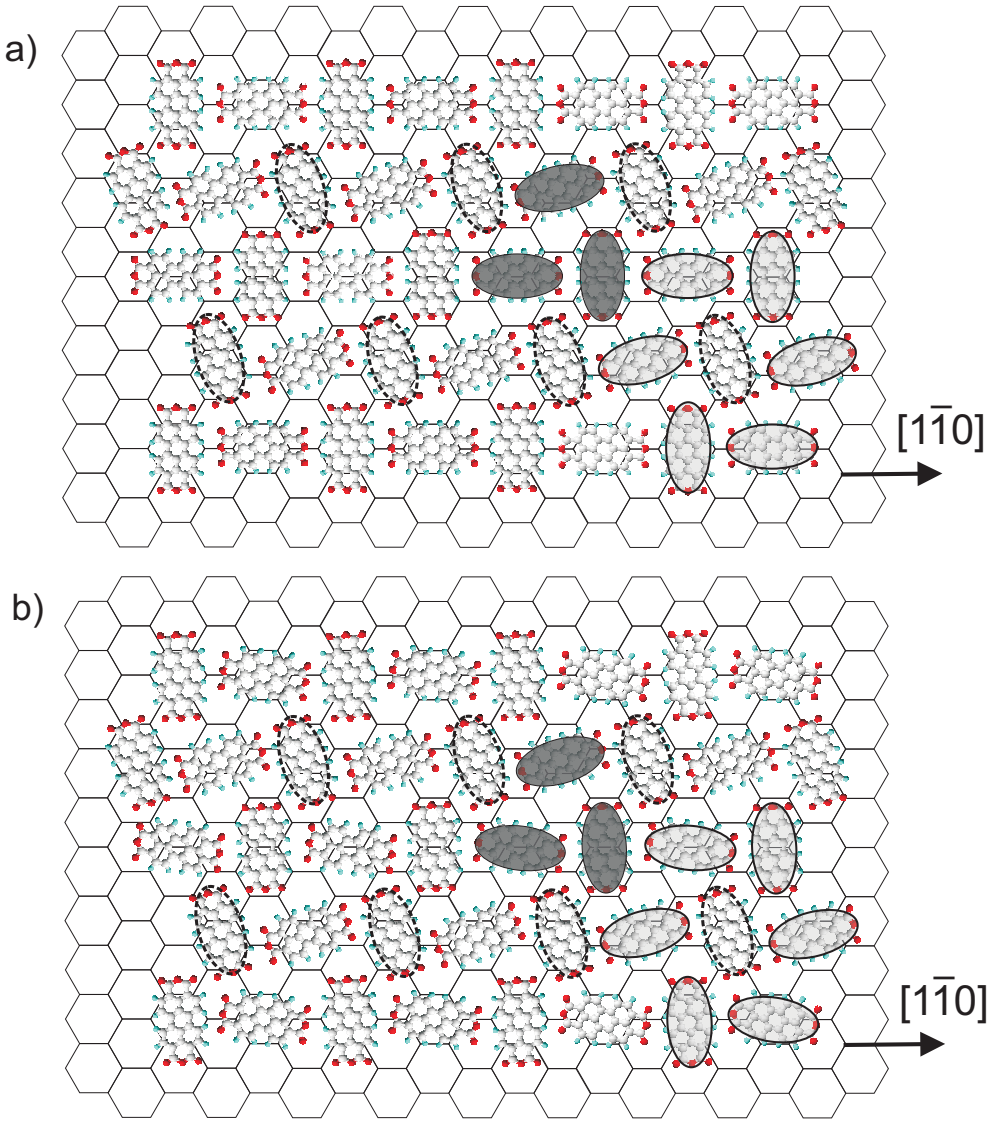

FIGURE 5.12: a) This initial model shows the combination of square and herringbone phase rows which comprise the hexagonal phase. b) This model shows the relaxed form, with the molecules oriented to give a hydrogen bonding configuration. A triangular repeat unit is shown by dark ovals, and a hexagonal unit like those in Figure 5.11 is highlighted by pale outlined ovals. The molecules of low contrast in the images are shown with dotted oval outlines. The mirror image of this model is valid for the opposite chirality version observed for this phase. The chirality shown is that in Figure 5.11d)

5.12. We have analysed the proposed molecular arrangement using numerical modelling. The AM1 semi empirical model was used to minimise the energy of the cluster shown in Figure 5.13 and our results confirm that this arrangement of molecules is stable. However,

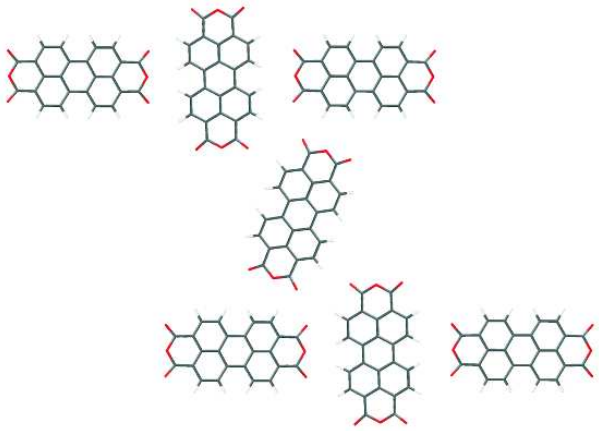

FIGURE 5.13: The semi empirical model of a seven-molecule cluster in the hexagonal phase, made of two three-molecule square phase rows and a central herringbone molecule as calculated by Spartan. The angle of the long axis of the central molecule from the vertical is 22°.

Table 2: Packing Fractions of PTCDA Phases

Phase	Packing fraction ($Å^2$per molecule)
Herringbone	114.9
Bulk α	119.1
Square (2,7)	134.1
Square (7,24)	131.3
Hexagonal	134.1

This table gives the packing fractions of the observed phases of PTCDA in terms of area per molecule as well as the packing fraction for the bulk α phase to compare with the herringbone phase. Note the packing fractions for the two proposed models for the square phase are given. The herringbone phase is the most close-packed phase.

the molecular configurations relax slightly from those shown in Figure 5.12a which correspond exactly to alternate rows of square and hexagonal phases. The relaxed configuration is shown in Figure 5.12b. Note that within the square phase rows the molecules are rotated through approximately 5° to relax the molecular arrangement and allow optimum hydrogen bonding geometries. This model is consistent with the observed orientation of the molecules (see highlighted intramolecular structure in Figure 5.11c) and d)).

The packing fraction of the three observed phases along with the packing fraction of molecules in the bulk α phase are in Table 2 as a summary. The herringbone phase has the highest packing density, while the symmetrical square and hexagonal surface phases have a lower packing density to the bulk α phase. This implies the new 2-D phases we have

observed are stabilised by interactions with the surface.

5.4 PTCDA and C_{60}

C_{60} is the third allotrope of carbon (after diamond and graphite) and is a spherical cage molecule consisting of 60 carbon atoms arranged in 12 pentagons and 20 hexagons as shown in Figure 5.14. It belongs to a family of carbon-cage molecules called buckminsterfullerenes and was discovered in 1985 after experiments to determine the origin of certain chemical species found in interstellar gas [93]. C_{60} was originally produced using laser ablation of graphite targets in an inert gas atmosphere. Further developments have allowed larger quantities to be produced, by heating two graphite plates in an helium atmosphere, creating a cloud of C_{60} particles which condense and may be collected and purified [94]. C_{60} and related fullerenes are of great interest, and related research is active in many fields, including novel material engineering, drug delivery and quantum computer fabrication, amongst others.

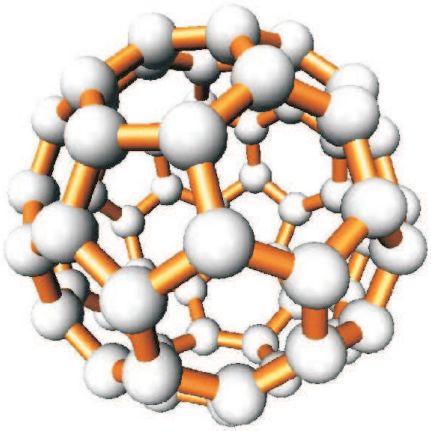

FIGURE 5.14: Schematic of C_{60} molecule.

Particularly relevant to the study of C_{60} and another molecular species on a surface is research on the behaviour of C_{60} and chloro[subphthalocyaninato]boron(III) (SubPc), performed by de Wild et al [30]. The two species were co-deposited in different relative amounts onto Ag(111) and found to self organise into different phases dependent on the amount of material deposited of each species. It was therefore thought that similar intermixing may be observed using PTCDA and C_{60}, as described in the rest of this section.

5.4.1 Method and Results

Ag-Si(111)$\sqrt{3} \times \sqrt{3}$R30° was again chosen as a suitable substrate on which to deposit the two species. PTCDA and C_{60} were codeposited onto a clean Ag-Si(111)$\sqrt{3}\times\sqrt{3}$R30° surface by heating the molecules simultaneously, each in a Knudsen cell, for 10 minutes, to achieve a submonolayer coverage. C_{60} sublimes at 300°C and PTCDA sublimes at 330°C. The resulting samples were again studied using STM.

A typical image of the resulting surface structures observed is shown in Figure 5.15. In fact after the deposition there was roughly three times more PTCDA than C_{60}. The two species form separate islands, with no supramolecular phases forming. The square PTCDA phase can clearly be observed in this figure, and is outlined in C_{60} molecules. This outline actually appears to be a step edge on the Ag-Si(111)$\sqrt{3} \times \sqrt{3}$R30° surface which may explain its apparent behaviour as a set of nucleation sites for the C_{60} molecules on the edge of the PTCDA island. C_{60} has been shown previously to bond more strongly to the step edges of this surface than on the terraces [95].

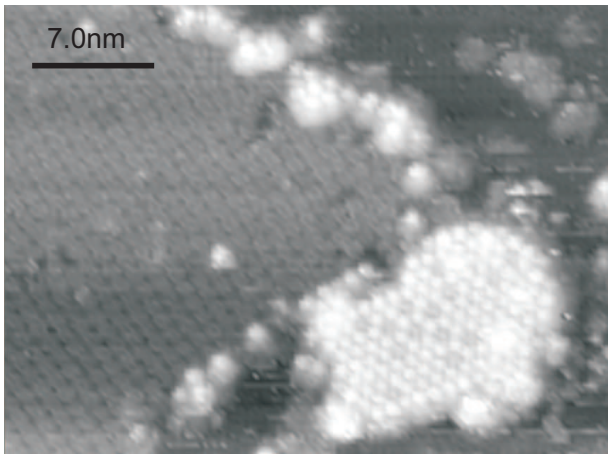

FIGURE 5.15: Co-depositing PTCDA and C_{60} results in separate islands. The PTCDA is on the left in the square phase, and the C_{60} is in the bright island. Its hexagonal appearance is characteristic, with some molecules showing a lower contrast. Bias = -3.0V, current = 0.1nA

The C_{60} islands appear to have the same arrangement as those observed by Upward *et al* [96] who observe similarly hexagonally ordered domains on the Ag-Si(111)$\sqrt{3}\times\sqrt{3}$R30° surface. It may be interesting as a future experiment to anneal these samples and observe whether the increased temperature allows the molecules to diffuse and possibly form an

intermixed phase, and also to perform more calibrated depositions to carefully control the amount of each species on the surface.

5.5 PTCDA and melamine

PTCDA is an interesting molecule for study in its own right (see Section 5.1), and was found to form three ordered phases on the Ag-Si(111)$\sqrt{3} \times \sqrt{3}$R30° surface, a herringbone phase, square phase, and a hexagonal phase. Preliminary experiments with co-deposition of PTCDA and C_{60} produces isolated islands of either species with no intermixing.

However, it was found by Theobald *et al* that PTCDI (the imide analogue to PTCDA) and melamine form extended supramolecular hexagonal networks [25]. Thus PTCDA and melamine were considered as a potentially interesting combination for study. The two molecules, PTCDA and melamine, are shown schematically in Figure 5.16. The junction present in PTCDI-melamine networks is a stable threefold hydrogen bond between the imide and melamine giving two N-H···O bonds flanking a N···H-N bond. Therefore, a combination of PTCDA and melamine on the Ag-Si(111)$\sqrt{3} \times \sqrt{3}$R30° surface was considered as a possible candidate for supramolecular structure formation. The analogous PTCDA-melamine bonding junction involves the two N-H···O bonds flanking a potentially repulsive N-O interaction, which is a junction not previously observed in surface or solution chemistry. In fact hexagonal networks do form with PTCDA and melamine mediated by this new bonding junction, alongside a more abundant complex double row structure.

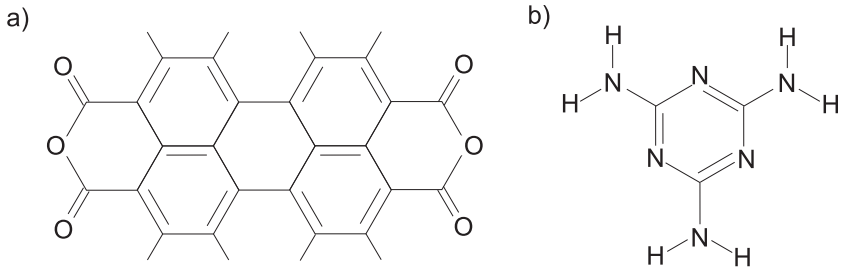

FIGURE 5.16: Molecules studied: a) PTCDA, with a perylene core and dianhydride end groups and b) melamine, a triazine ring with three amine groups.

5.5.1 Experimental method

Images were acquired using an STM as described previously (see Section 2.5). The hexagonal Ag-Si(111)$\sqrt{3}\times\sqrt{3}$R30° surface reconstruction was prepared as detailed before (Section 4.2.

The molecules were degassed thoroughly prior to deposition. PTCDA (99.9% pure, Sigma Aldrich) was deposited at 330°C for 15-20 minutes to achieve $\sim$ 0.15 ML coverage. To investigate the PTCDA-melamine bimolecular system, melamine (99% pure, Sigma-Aldrich) was subsequently sublimed from a home built evaporator at 90°C for 15 minutes onto a sample with PTCDA adsorbed. The sample was kept at room temperature throughout and no further annealing took place after the melamine deposition. The entire experiment was performed in the same three-chamber UHV system.

5.5.2 PTCDA and melamine

Immediately after the deposition of PTCDA on the Ag-Si(111)$\sqrt{3}\times\sqrt{3}$R30° surface, three close packed phases formed: a herringbone phase, a square phase, and a combination of these which form a hexagonal structure. These are discussed in detail elsewhere (see Section 5.3 and Ref. [97]). Deposition of melamine onto these samples completely changes the surface morphology, suggesting the PTCDA phases, though stable enough to be imaged many times, are easily broken up by the addition of melamine on the surface. The introduction of C_{60}, rather than melamine, does not change the PTCDA phases, and PTCDA and C_{60} simply segregate into islands with no mixed molecular phases forming (Figure 5.15). Melamine is not observed to form close packed islands on the PTCDA and melamine samples prepared in this work. This perhaps indicates that melamine is only stable enough on the surface to be imaged when interacting with PTCDA molecules. Melamine islands have however previously been imaged on the Au(111) surface by Perdigão *et al* [28].

Figure 5.17 shows the overall surface morphology, with PTCDA and melamine supramolecular structures covering the surface. In this image the bright features which are clearly resolved are PTCDA molecules. Two distinct phases are present in small regions ($\sim$ 20nm across). The short rows two PTCDA molecules wide constitute the double row phase. The other phase, which appears less abundantly, is the hexagonal network.

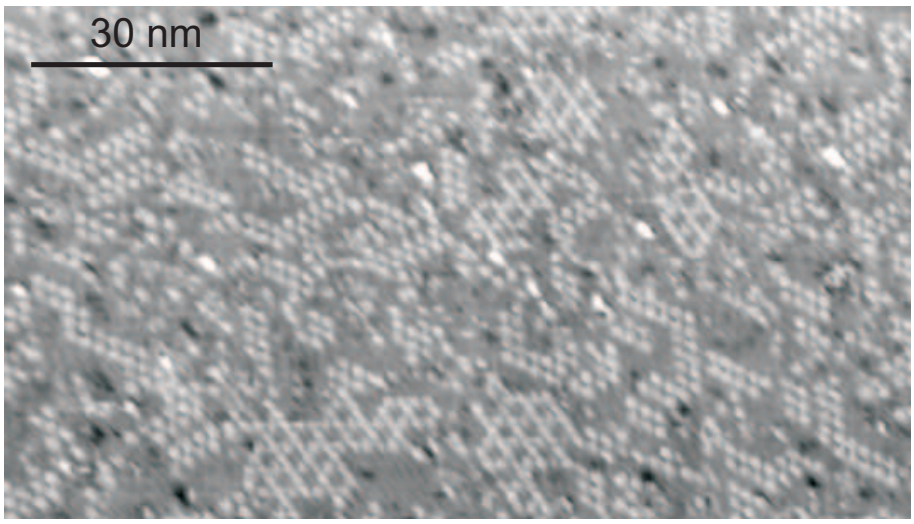

FIGURE 5.17: Overall surface morphology of PTCDA and melamine combined on the Ag-Si(111)$\sqrt{3} \times \sqrt{3}$R30° surface (bias = -3V, current = 0.1nA). The entire surface is covered in these hexagonal and double row structures.

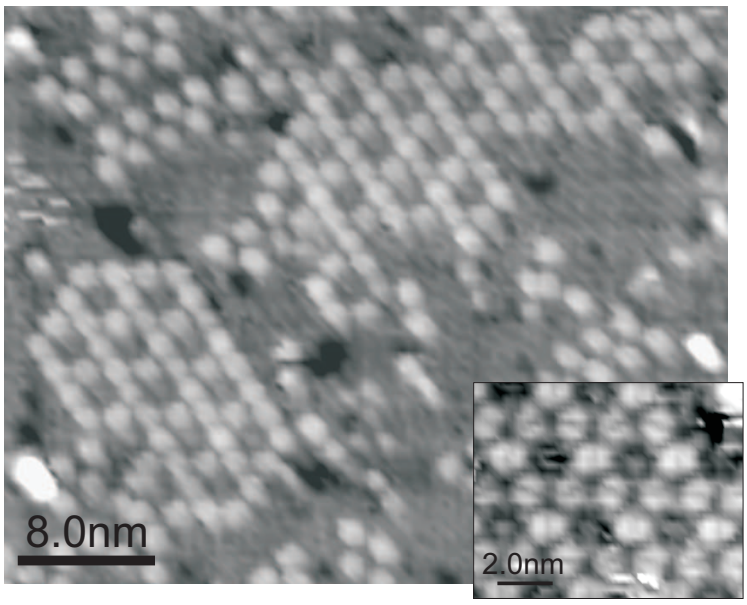

FIGURE 5.18: This image shows two regions of PTCDA-melamine hexagonal network on the Ag-Si(111)$\sqrt{3} \times \sqrt{3}$R30° surface. Areas of the double row phase each of ∼10 PTCDA molecules can also be seen in the top left corner of the image. Insert: This high-resolution section of a hexagonal network shows the two halves of the HOMO of each PTCDA molecule, as illustrated by the overlayer on one hexagonal unit. For both images, bias is -3V, current is 0.1nA.

5.5.3 Hexagonal networks

The PTCDA-melamine hexagonal network is shown in Figure 5.18. Each bright round feature is a PTCDA molecule. The hexagonal networks were observed to have a maximum size of about 30 hexagonal units. The insert in Figure 5.18 shows intramolecular features resolved within the PTCDA molecules. Each molecule has two bright lobes with a darker contrast line along the centre, corresponding to the shape of HOMO, calculated using the AM1 model for an isolated molecule (see Figure 5.1). This intramolecular contrast, with the molecule appearing as two halves, allows for the easy identification of the alignment of each PTCDA molecule in the array. The period of the network is 34.6Å, or $3\sqrt{3}a_0$, where $a_0 = 6.65$Å is the lattice constant of the Ag-Si(111)$\sqrt{3} \times \sqrt{3}$R30° surface. Both the period and the molecular orientations are the same as those observed by Theobald *et al* [25, 26] in previous studies of PTCDI-melamine networks. A model is proposed for this molecular arrangement in Figure 5.19. The hexagonal background illustrated in the models is a representation of the Ag-Si(111)$\sqrt{3} \times \sqrt{3}$R30° surface as before (see Figure 5.5).

In images of this phase, PTCDA molecules are visible, but melamine molecules cannot readily be resolved. From a comparison with previous studies of PTCDI-melamine networks, the vertices of the network can be identified as melamine molecules [25]. Figure 5.19a) shows a schematic of the molecular network on the Ag-Si(111)$\sqrt{3} \times \sqrt{3}$R30° surface. As well as the stabilising N-H$\cdots$O bonds, there is also in this arrangement a potentially repulsive electrostatic interaction, between the central anhydride oxygen atoms and the triazine ring nitrogen in the melamine, which both carry negative character (Figure 5.19b)). The competition of energetics allows the phase to form; thus the possible repulsive interactions are overcome by the hydrogen bonds which are strong enough to hold the network together. One may also consider the surface commensurability of this phase; from the model the molecules are all positioned in equivalent binding sites on the surface. This binding site homogeneity may contribute to the stability of the phase. To our knowledge no analogous molecular networks with equivalent hydrogen bonded junctions have previously been observed in assembled structures or solution chemistry. This may not only reflect any instability of the anhydride:diaminopyridine interaction but also the observation that in solution, anhydrides, including PTCDA, readily react with amines to afford imide moieties. [98]

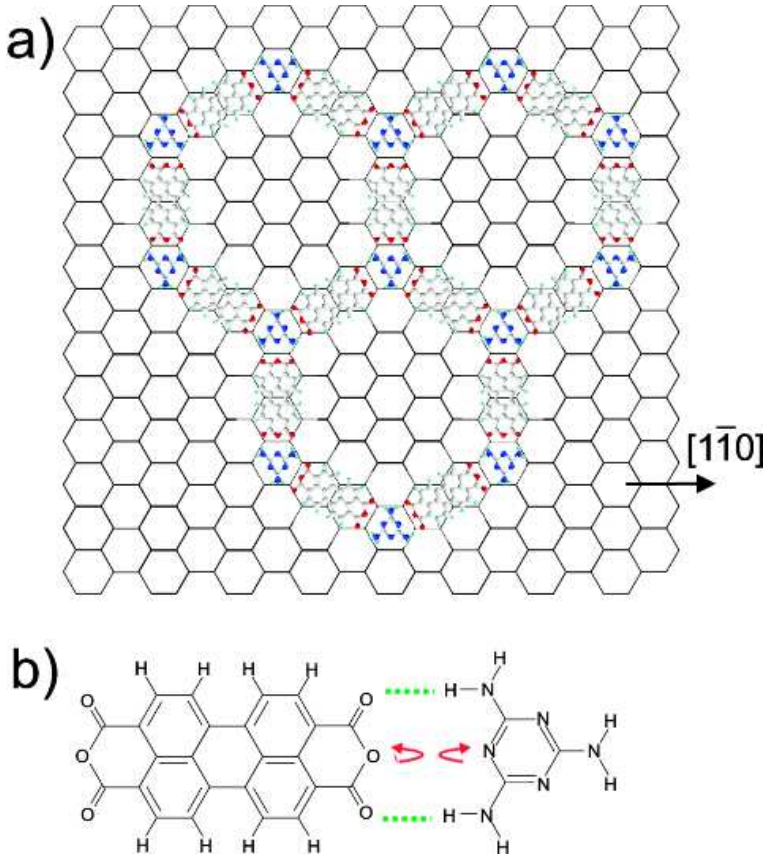

FIGURE 5.19: a) This model shows the molecules in the PTCDA-melamine network on the Ag-Si(111)$\sqrt{3} \times \sqrt{3}$R30° surface. All molecules are in equivalent positions. b) The hexagonal network is stabilised partially by melamine molecules at the hexagon vertices hydrogen bonding via N-H—O interactions to the PTCDA anhydride groups, though there is an expected repulsion between the melamine ring nitrogen and the central dianhydride oxygen of PTCDA.

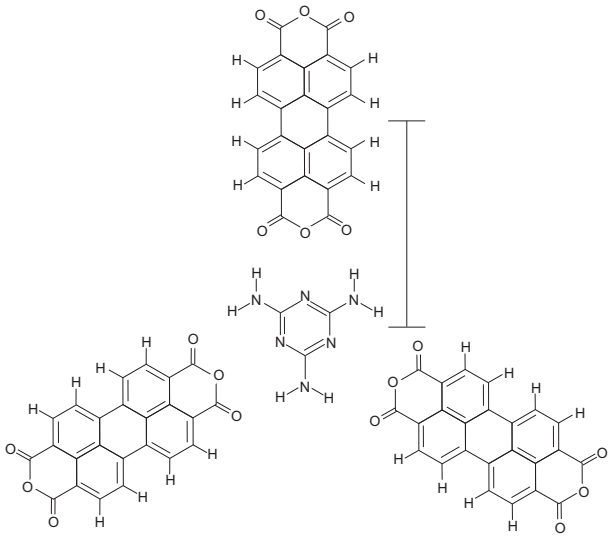

FIGURE 5.20: Diagram showing the calculated arrangement of a single junction of the hexagonal PTCDA-melamine arrangement. The distance between the centre of the PTCDA and melamine molecules (indicated) in the relaxed geometry is 10.3Å

Chemical modelling

In order to confirm the stability of the hydrogen bonding junction present in these PTCDA-melamine networks, calculations were performed using density functional theory with the SIESTA package [51,99] by Dr. Ben Rogers [1]. Details of the calculations can be found in Ref [100]. Calculations performed on an arrangement of a single melamine molecule with three PTCDA molecules (Figure5.20) indicate an interaction energy of -0.40eV per threefold-junction. This equates to an interaction energy of -0.13eV per individual PTCDA-melamine junction, confirming that the proposed network is stable through weak but favourable interactions. The calculated spacing between the centres of PTCDA and melamine in the network is 10.3Å, compared with the measured value from images of 9.98 ± 0.10Å. The model takes no account of the surface involved and as such the commensurability with the surface, which may be why the separations indicated in the theory and experiments are slightly different.

[1] University of Nottingham 2005

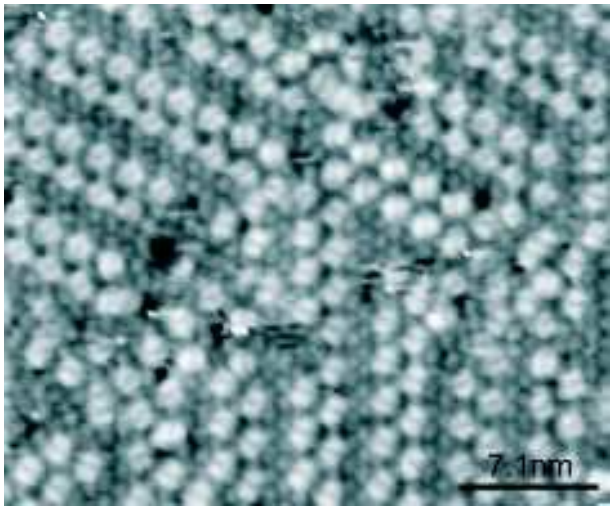

FIGURE 5.21: This image shows the molecules in the PTCDA-melamine double row phase on the Ag-Si(111)$\sqrt{3} \times \sqrt{3}$R30° surface. Both molecular species can be resolved in this image (bias is -3.0V, current is 0.1nA).

5.5.4 PTCDA and melamine: double rows

As shown in Figure 5.18 another phase co-exists with the hexagonal network. Figure 5.21 shows an STM image of this phase highlighting the presence of PTCDA-melamine double rows, which are the dominant motif observed in these PTCDA-melamine samples. This phase consists of alternating double rows of PTCDA and melamine which lie along the $\langle 11\overline{2} \rangle$ directions of the silicon lattice (indicated in Figure 5.23). The dimensions of the hexagonal network phase were used to measure dimensions in the double row phase, as the underlying substrate could not always be resolved clearly in the images of the double rows. The spacing of adjacent PTCDA molecules in the direction parallel to the double rows was measured to be $3a_0$. Similarly the separation of two PTCDA molecules across a double row, parallel to the molecular long axis, is $3a_0$. The distance between two adjacent double rows of PTCDA molecules was found to be $8a_0$. These dimensions, along with the observed orientations of the PTCDA molecules, allow us to accurately extract their relative positions on the surface, as shown in Figure 5.23. The angular orientation of the PTCDA molecules can be deduced from the direction of the HOMO lobes which run along the length of the molecule. Their separation and alignment is not consistent with close packed PTCDA islands (see Section 5.1).

Rows of melamine molecules form between the double rows of PTCDA molecules

and may be clearly resolved in Figure 5.21. There are two melamine molecules in each of the $3a_0$ repeat units separating PTCDA molecules in the direction parallel to the rows. Consequently every other melamine molecule is associated with an anhydride group. In the absence of defects, the melamine rows have a width corresponding to two molecules. At the junctions of rows we also observe small areas of melamine with a local hexagonal order, similar to that observed for melamine islands by Perdigão *et al* on Au(111). The fixed width of the rows suggests that there is a symmetry in the molecular packing that does not allow these structures to be extended in a regular fashion.

Pairs of PTCDA molecules within a double row are aligned end to end such that their anhydride groups point toward each other. Neighbouring PTCDA molecules parallel to the row direction are too far apart, at $3a_0$, for a direct interaction between them to have a significant effect. Accordingly, built into the proposed model for the arrangement of molecules in this phase (Figure 5.23), is a structure in which melamine molecules are coadsorbed between the PTCDA molecules, stabilising the double row arrangement. There is evidence for these melamine molecules bound between PTCDA along the rows as bright regions. Figure 5.22 shows these particularly clearly but images with this resolution are the exception rather than the rule. Therefore the stabilising melamine molecules in-between PTCDA molecules have been placed in estimated positions in the model according to bright features in the images, and such that stabilising hydrogen bonds may be present.

The model in Figure 5.23 is the best estimate of all molecular positions in this complicated double row phase. The positions and angular orientations of PTCDA molecules in this model have been accurately determined, though the positions and angular orientations of the melamine molecules comprising double rows is approximate., since they are not well resolved in the images. Melamine molecules have been positioned in the model such that they might stabilise the PTCDA molecules through N-H$\cdots$O interactions, and may give rise to an axis of symmetry for the formation of PTCDA double rows only two molecules wide. It is not currently realistic to perform any computation modelling to determine the stability of the proposed model, since a unit cell is very large.

5.5.5 Other motifs

Some interesting isolated PTCDA-melamine arrangements were also observed, including the rosette shown in Figure 5.24. These isolated structures were observed in images taken imme-

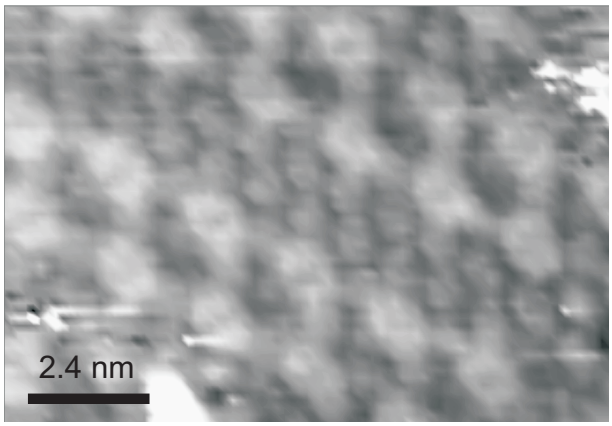

FIGURE 5.22: This image shows the molecules in the PTCDA-melamine double row phase on the Ag-Si(111)$\sqrt{3} \times \sqrt{3}$R30° surface with particularly clear melamine molecules (bias is -3V, current is 0.1nA).

diately after preparation, with little long range ordering present in the adsorbed molecules. Six PTCDA molecules are arranged in a hexagon with seven melamine molecules trapped in the centre. One suggestion for their presence is that these structures are locally stable but are broken up as surrounding molecules arrange in to the other two more commonly observed phases.

5.6 Conclusions

PTCDA forms many interesting phases on the Ag-Si(111)$\sqrt{3} \times \sqrt{3}$R30° surface. A square phase was observed, which contains contrast variations due to the number of inequivalent adsorption sites and orientations. The formation of the square phase may be due in part to a commensurability between molecular dimensions and the surface lattice constant, although in one direction the resulting coincidence lattice extends over many molecular repeat units. A herringbone phase was observed which is similar to a molecular layer in the bulk packing of monoclinic PTCDA crystals. A third hexagonal phase was also observed which is thought to be a combination of both the herringbone and square phases. The formation of a square phase on a hexagonal surface is an important observation and may give rise to the formation of new heteroepitaxial interfaces between materials with quite different crystal symmetries. The molecular ordering present is different to that which has been previously reported on different surfaces, particularly the square phase observed here.

Following the PTCDA studies, bimolecular systems were studied using STM again,

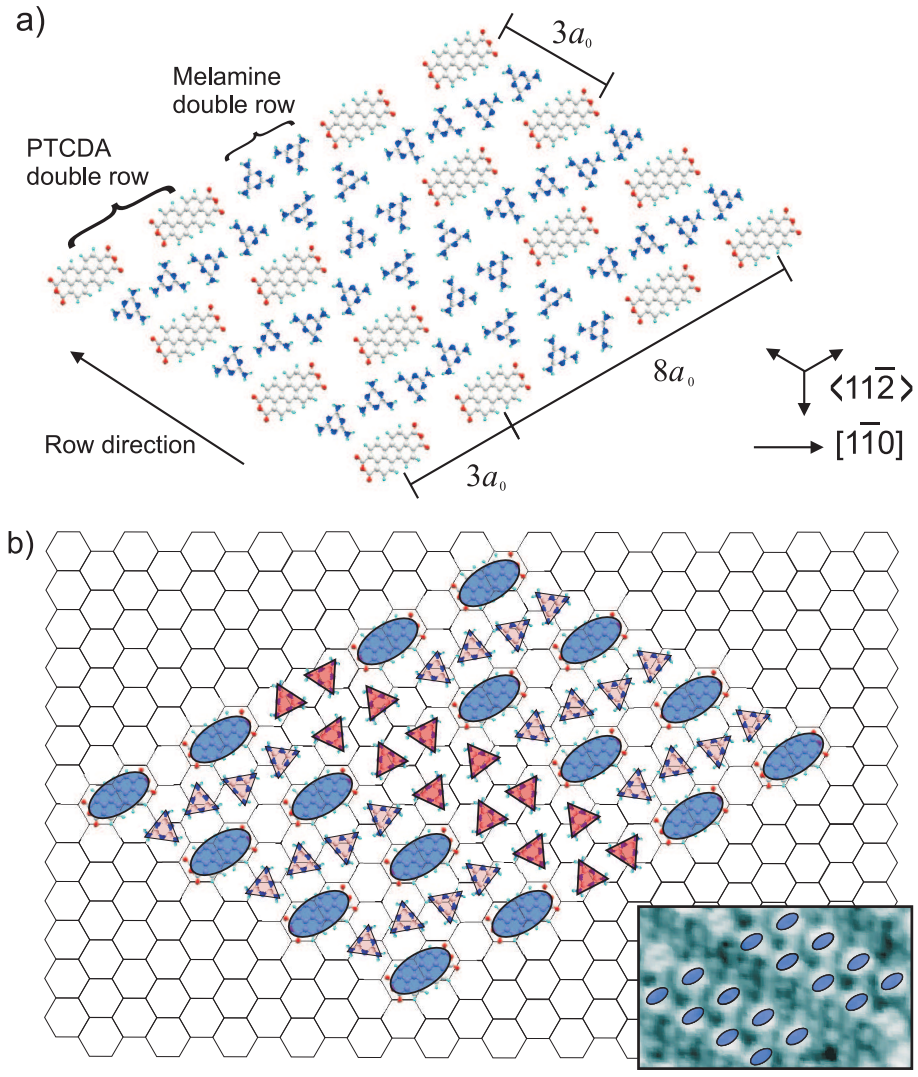

FIGURE 5.23: a) Schematic model showing the molecular position in the PTCDA-melamine double row structure. The PTCDA and melamine double row molecules are indicated along with crystallographic directions of the underlying Si surface. b) A copy of part (a) including a lattice representing the Ag-Si(111)$\sqrt{3} \times \sqrt{3}$R30° surface. PTCDA molecules are highlighted with blue ovals, and melamine molecules are shown as red triangles, shaded darker for the melamine double row, which is more easily resolved in the images. Insert: Section of image shown in Figure 5.21 with PTCDA molecules highlighted as in part (b).

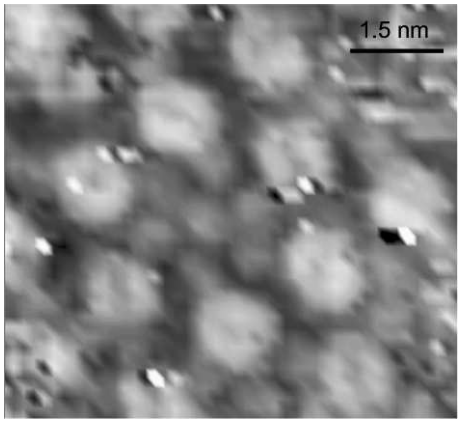

FIGURE 5.24: STM image showing a rosette-like structure of PTCDA and melamine. Current = 0.05nA, bias = -3.0V

including PTCDA and C_{60}, and PTCDA and melamine combinations. PTCDA and C_{60} do not form any supramolecular structures but the two species form separate regions, with the C_{60} molecules arranging in a previously observed hexagonal close packed scheme [60].

A combination of PTCDA and melamine on the Ag-Si(111)$\sqrt{3} \times \sqrt{3}$R30° surface forms a hexagonal network motif and a double row phase, stabilised by a previously unseen hydrogen bonding junction. Both phases form under the same growth conditions. Rosette structures also form though these are only observed directly after melamine deposition. The formation of the network is analogous to previous work by Theobald *et al*, yet rather than the triple hydrogen bonded junction present with PTCDI and melamine, PTCDA and melamine bond through a double hydrogen bond flanking a potentially repulsive interaction between oxygen and nitrogen atoms. However, the network is stable and can be imaged several times over a period of days. Density functional calculations also showing the arrangement is stable through weak but favourable interactions. The double row phase is more abundant than the hexagonal lattice, but is rather complicated and involves many different adsorption sites and orientations.

Chapter 6

Isonicotinic acid and Biisonicotinic acid on TiO_2

6.1 Introduction

Pyridinecarboxylic acids are a class of molecules which contain a pyridine ring (5 carbon atoms and one nitrogen atom) with a carboxylic acid group. They are shown schematically in Figure 6.1. Of these, isonicotinic acid, and the related molecule biisonicotinic acid, represent the fundamental building blocks and bonding ligands of dye molecules such as those used in dye-sensitised solar cells [65–67,101]. Pyridinecarboxylic acids are also studied in relation to many medical applications. Nicotinic acid is niacin (Vitamin B3) and is used for reducing cholesterol [102]. Isonicotinic acid derivatives (isonicotinic acid hydrazine) are of widespread medical interest, e.g. in the treatment of tuberculosis [103]. The metal coordination chemistry of pyridinecarboxylic acids is also of interest for the synthesis of interesting macrocyclic materials and novel bonding junctions [104].

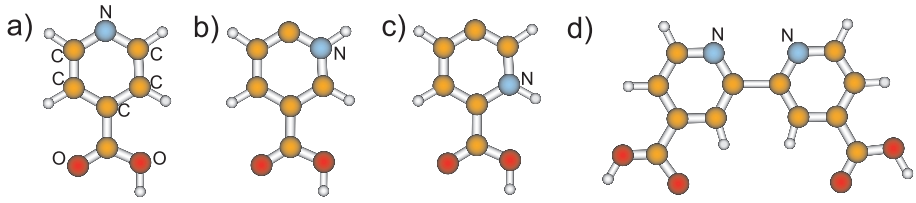

Figure 6.1: Schematic diagram of pyridinecarboxylic acid molecules - a) Isonicotinic acid, b) Nicotinic acid, c) Picolinic acid and d) Biisonicotinic acid.

The research presented in this chapter is an example of a molecular hydrogen bonded structure with the directional hydrogen bonding directed out of the plane of the surface. Isonicotinic acid, and its larger cousin, biisonicotinic acid, have been investigated on rutile TiO_2 using synchrotron based techniques to probe the structure and geometry

of monolayer and multilayer films. Valence band spectroscopy is used to show to presence of order in isonicotinic acid monolayer and multilayer samples, and comparisons are made with calculated valence band spectra. Core level photoemission is used to determine how biisonicotinic acid bonds to TiO_2 and to gold on TiO_2, and some preliminary valence band studies are presented. STM studies of biisonicotinic acid have also been performed to study bonding geometries on Ag-Si(111)$\sqrt{3} \times \sqrt{3}$R30° and Au(111) $22 \times \sqrt{3}$.

6.1.1 Previous research

There have been many studies to determine the geometric and electronic properties of pyridinecarboxylic acids adsorbed on rutile TiO_2, [69, 105, 106]. Recent studies [107–109] have focussed on understanding the properties of biisonicotinic acid on anatase TiO_2, the second commonest crystal structure of TiO_2. These studies are of interest in part due to their relevance with molecular solar cell research.

There are several types of molecular solar cell devices, arguably the most famous of which are called Grätzel cells [67, 101]. These are composed of a dye molecule (usually a Ru dye with biisonicotinic acid bonding ligands) which is chemisorbed to a nanoparticulate anatase TiO_2 layer on conducting glass. The glass-TiO_2-dye arrangement is housed in an electrolytic solution. The absorption of sunlight by a dye molecule excites an electron from the dye molecule which tunnels away into the substrate over a very fast (fs) timescale. The hole left on the dye molecule becomes filled by an electron from the electrolytic solution but this occurs over a slower timescale (ns) which accounts for the relatively low efficiency ($\sim 10\%$) of these devices [68].

Photoemission spectroscopy (Chapter 3) is a common technique used for the investigation of adsorbed molecular layers, as it can clearly show the chemical environment of an element through peak positions and relative intensities in a spectrum. Figure 6.2 shows the O $1s$ core level photoemission spectra of biisonicotinic acid in a multilayer and a submonolayer on rutile TiO_2 [106]. In the submonolayer spectrum, the two peaks arise from the deprotonated oxygen atoms in the carboxylic acid group bonded to the substrate at 536.6eV, and from oxygen in the TiO_2 substrate at 535.0 eV. These peaks reveal that the molecule is bonded to the surface via its carboxylic acid groups as all four oxygen atoms from one biisonicotinic acid molecule are in the same chemical environment; there is only one molecular peak present. The calculated optimum geometry of a biisonicotinic acid

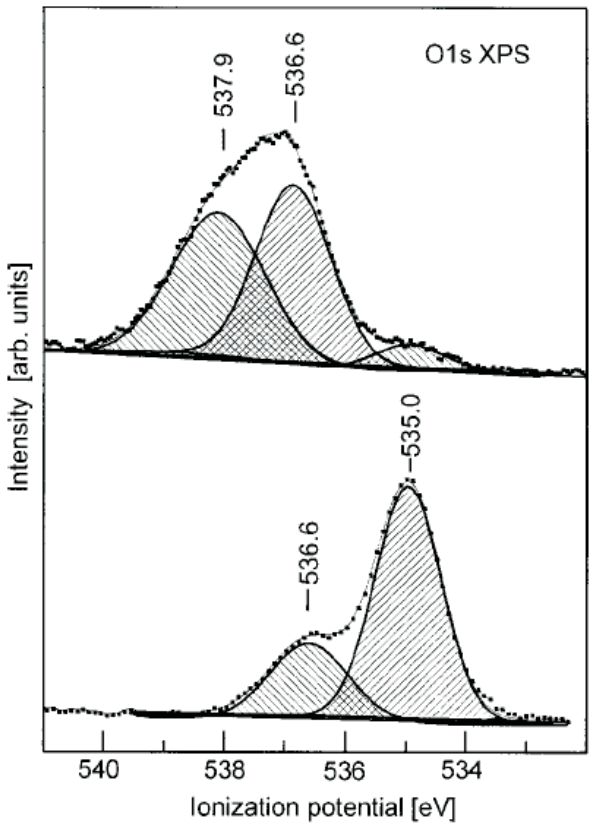

FIGURE 6.2: O 1*s* XPS spectra recorded with 600eV photons for (bottom) a submonolayer and (top) a multilayer of biisonicotinic acid on a TiO_2 cluster. The peak position are explained in the text (after Patthey *et al* [106]).

molecule adsorbed on a rutile TiO_2 surface is shown in Figure 6.3 from Persson *et al* [71]. The multilayer spectrum in Figure 6.2 shows three oxygen peaks. These arise from the substrate (again at 535.0 eV but heavily attenuated), from carbonyl oxygen atoms at 536.6 eV, and at 537.9 eV from hydroxyl oxygen atoms, which are possibly involved in hydrogen bonding to neighbouring nitrogen atoms.

Patthey *et al* also show using near-edge X-ray adsorption fine structure (NEXAFS) measurements (Section 3.7), shown in Figure 6.4, that the orientation of a biisonicotinic acid molecule bonded to rutile $TiO_2(110)$ is such that the plane of the pyridine rings is roughly perpendicular to the plane of the surface. In Figure 6.4, the peaks in the spectrum associated with π^* unoccupied molecular orbitals, mainly situated either side of the pyridine ring, are more intense as the direction of polarisation moves from being perpendicular to parallel with the surface. In agreement, those peaks associated with σ^* orbitals in the

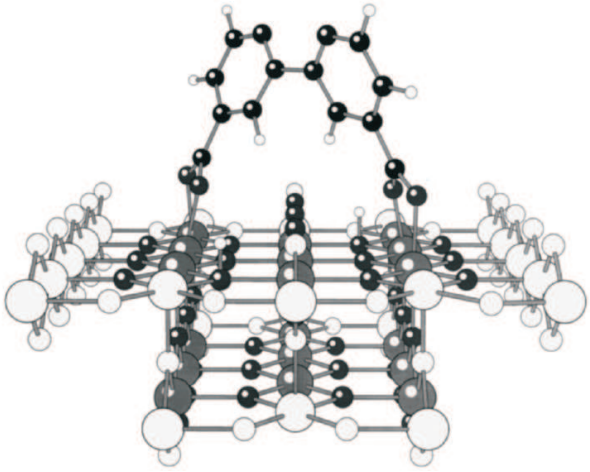

FIGURE 6.3: Calculated optimum geometry of biisonicotinic acid chemisorbed to a rutile TiO_2 surface (after Persson *et al* [71]).

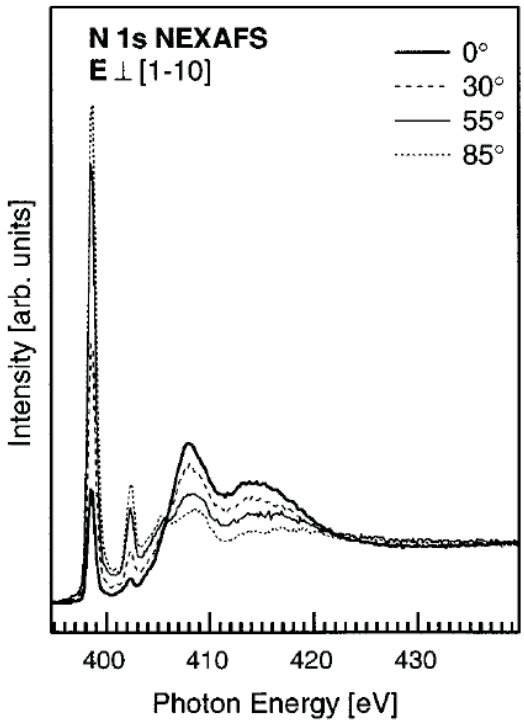

FIGURE 6.4: N 1*s* NEXAFS of a biisonicotinic acid monolayer bound to a rutile TiO_2 surface. Changes in the relative intensity of the peaks suggest a geometry with the plane of the pyridine rings perpendicular to the surface (after Patthey *et al* [106]).

molecule become relatively weaker as the same polarisation angle change is made. This suggests the plane of the pyridine rings is perpendicular to the surface plane. Interestingly, Thomas *et al* [107] find biisonicotinic acid on anatase TiO_2 bonds at different angles to the plane of the surface depending on the crystallographic plane of the surface. NEXAFS studies reveal the pyridine rings bond at $20° \pm 3°$ on the (101) surface and at $53° \pm 5°$ on the (001) surface.

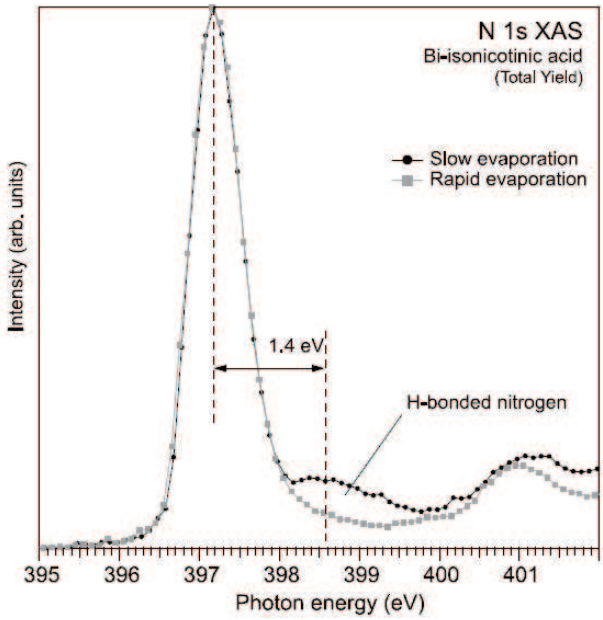

FIGURE 6.5: N $1s$ XAS of biisonicotinic acid in both ordered and disordered multilayer films. The ordered film exhibits an addition peak due to hydrogen bonding between nitrogen and a neighbouring carboxylic acid group (after O'Shea *et al* [110]).

O'Shea *et al* demonstrate the presence of hydrogen bonding in ordered biisonicotinic acid multilayers (Figure 6.5) using X-ray absorption spectra (XAS) of hydrogen-bonded ordered multilayers and non-hydrogen bonded disordered films of biisonicotinic acid on $TiO_2(110)$ [110]. The ordered multilayers exhibit an additional peak in the N $1s$ XAS spectrum due to nitrogen atoms hydrogen bonded to a neighbouring carboxylic group in an N$\cdots$H-O configuration. The two NEXAFS spectra here are measured from two films prepared in different ways. The disordered film, with no hydrogen bonding present, was prepared via a fast deposition of biisonicotinic acid (a chamber pressure of $\sim 1 \times 10^{-6}$); the film showing ordering with possible hydrogen bonding between molecules was prepared through a slow deposition (a chamber pressure of $\sim 1 \times 10^{-8}$), thus the molecules have time

to arrange into the most stable arrangement, including intermolecular hydrogen bonding.

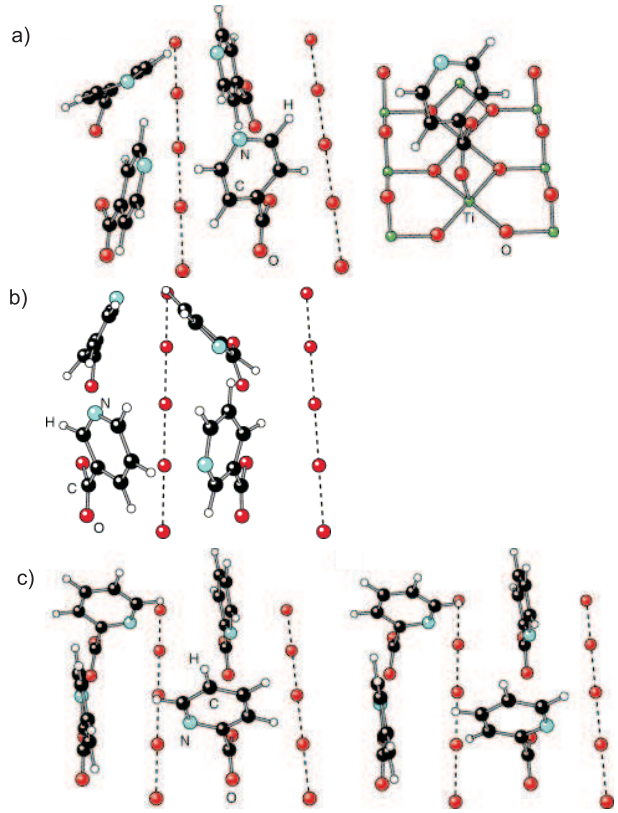

FIGURE 6.6: This figure shows the geometries of a) isonicotinic, b) nicotinic and c) picolinic acid molecules in a monolayer. The surface is represented only by the bridging oxygen atoms along the [0 1] surface direction, apart from the right hand part of a). (After Schnadt *et al* [111]).

The geometries of isonicotinic acid, nicotinic acid and picolinic acid monomers bound to rutile $TiO_2(110)$ were determined using XAS, XPS and STM, and was found by Schnadt *et al* to be broadly upright [73, 111]. Core level photoemission spectra were collected from monolayers of each isomer, which were all found to bond to the surface of $TiO_2(110)$ through the oxygen atoms in the deprotonated carboxylic group to titanium atoms in the surface. In this bidentate bonding configuration the molecules stand upright on the surface, with the ring directed into vacuum. Figure 6.6, taken from Ref. [111], shows the geometry of isonicotinic, nicotinic and picolinic acid molecules in a monolayer on the rutile TiO_2 surface. XPS core level shifts were been used to determine the angular positions of the pyridine rings in relation to one another.

It was found by Schnadt and O'Shea *et al* that isonicotinic and picolinic acids

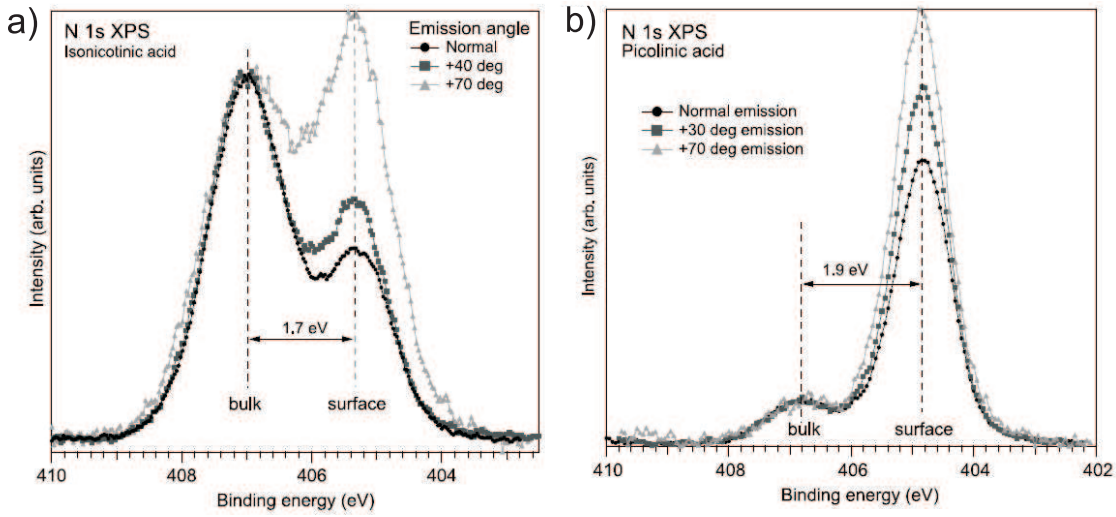

FIGURE 6.7: XPS results from Ref [110] showing the effect of hydrogen bonding on multilayers of a) isonicotinic acid and b) picolinic acid. There are two N $1s$ peaks, one from nitrogen atoms shifted to higher binding energy due to the presence of hydrogen bonding, and another from surface nitrogen atoms not involved in bonding. The relative enhancement of the lower binding energy peak at increased surface sensitivity (more grazing emission) shows it to arise from the surface atoms.

both form hydrogen bonded multilayers if prepared under the necessary growth conditions. In investigations of ordered isonicotinic acid multilayers, the observed ordering arises when the molecules are deposited slowly enough to allow hydrogen bonding interactions to form between molecules. The ordered multilayer film represents the bulk crystallographic structure [112]. Using XPS as a probe of the chemical bonding in the films, it was observed that surface core level shifts in the XPS spectra of these molecules arise due to the non-hydrogen-bonded nitrogen atoms in the surface molecular layer of an ordered multilayer. Figure 6.7 shows XPS results from Ref. [110] highlighting the presence of hydrogen bonding in ordered multilayers of isonicotinic and picolinic acids. The 1.7eV shift between hydrogen bonded and non-hydrogen bonded nitrogen atoms in the sample agrees with values calculated using density functional theory (DFT) calculations. Figure 6.8 shows a schematic of three hydrogen bonded isonicotinic acid molecules bonded to a substrate in the bidentate fashion. This orientation has been calculated using DFT with a B3LYP model and the 6-31G* basis set [1].

[1]Calculations by B. Brena and Y. Luo, of KTH, Stockholm

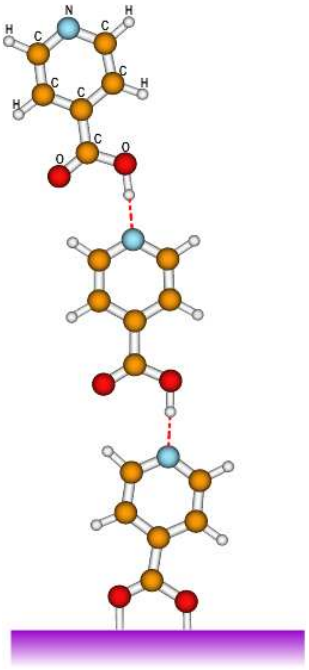

FIGURE 6.8: Calculated (using DFT) bonding between three isonicotinic acid molecules linked via head-to-tail intermolecular hydrogen bonds (shown in red). The bottom molecule is schematically shown (but not calculated) to be chemisorbed to a rutile TiO_2 surface via its deprotonated carboxylic group.

6.2 Experimental outline

This chapter describes experiments in which monolayers and multilayers of isonicotinic acid and biisonicotinic acid on rutile $TiO_2(110)$ were investigated to try and find an indicative signature, using valence band spectroscopy, for the presence of hydrogen bonding. The methods used for sample preparation are first discussed here, as the study of isonicotinic acid multilayers requires careful sample preparation to obtain either an ordered or disordered film. Then a characterisation of the clean TiO_2 is presented as the valence band spectra vary with both tilt and azimuthal angle orientation with respect to the polarisation of the incoming synchrotron light.

Studies of isonicotinic acid are then presented, showing that an ordered film has valence band characteristics which are dependent on the tilt angle of the sample, whereas a disordered film shows no angular dependence. This is due to the molecular orbitals being probed to different extents by the polarised synchrotron light as the angle of the sample is changed. Initial DFT calculations of an isolated isonicotinic acid molecule show

peak position agreement with experimental data of a multilayer sample. More detailed calculations by Brena and Luo, accounting for possible hydrogen bonding interactions and geometric components of the valence band, show that an angular dependence in valence band spectra can be theoretically modelled. Changes in the azimuthal angular orientation of an ordered multilayer show negligible changes in the valence band, which may not be expected, and reasons for this are discussed.

Preliminary valence band studies of biisonicotinic acid were performed. A monolayer of biisonicotinic acid was deposited and valence band spectra were taken at normal emission. These measurements are compared with DFT calculations and are in close agreement. Core level photoemission investigations of biisonicotinic acid on TiO_2 confirm that it is bonded upright on the surface through its carboxylic acid groups. Further photoemission studies of biisonicotinic acid on evaporated layers of gold on TiO_2 also show that the molecule bonds through its carboxylic acid group by studying the O $1s$ core level spectra for a monolayer.

STM studies of biisonicotinic acid adsorbed on Ag:Si(111)$\sqrt{3} \times \sqrt{3}$R30° in the submonolayer regime are also presented, and on the Au(111) $22\times\sqrt{3}$ surface as a comparison to the photoemission experiments. Biisonicotinic acid forms irregular close packed islands on Ag:Si(111), possibly as the molecules can adopt up to six different structural isomers when confined to a plane. Biisonicotinic acid cannot be easily imaged on Au(111), which may be because it is bonded upright (as isonicotinic acid does on rutile TiO_2(110) [111], or it is highly mobile.

6.3 Sample preparation

For the experiments in this chapter, the following preparation was used for cleaning the samples and for molecule depositions.

6.3.1 TiO_2 preparation

The rutile TiO_2(110) single crystal substrates were obtained from Pi-Kem, UK and were prepared by first annealing to ~ 700°C in 1×10^{-6} Torr O_2, in a process which creates bulk defects and induces N-type semiconduction. The surface was then cleaned by sputtering with Ar^+ ions for 10 minutes followed by annealing in 1×10^{-6} Torr oxygen gas (99.99% pure) for 10 minutes at 600°C to minimise the defects at the surface. The crystal is left

to cool in 1×10^{-6} Torr oxygen. The surface of rutile TiO_2, though well characterised, requires careful preparation in order to avoid the formation of patterned surface structures - see Section 4.3.

6.3.2 Molecule preparation

All molecules were deposited using a home built retractable thermal evaporator, or Knudsen cell. The evaporator was separated from the analysis (beamline 4.1, Daresbury laboratories) or preparation (Beamline I3.11, MaxLab) chamber by a gate valve when molecules were not being deposited. All molecules were thoroughly degassed before evaporation by heating to close to their sublimation temperatures for $\sim$ 30 minutes, then by heating at their sublimation temperatures for $\sim$ 10 minutes. This removes any water and other solvents which may be present. For isonicotinic acid, a monolayer was typically deposited by heating the molecule to 100°C and depositing for 10 minutes during which the sample was held at 200°C so that no multilayer adsorption would take place. Multilayers were prepared by depositing the molecules onto a monolayer sample cooled to -100°C and which was maintained at this temperature for the duration of the experiment. The deposition rate for the multilayers was controlled by varying the temperature of the evaporator from 65°C for a slow evaporation to 130°C for a rapid evaporation.

Biisonicotinic acid was acquired through collaboration with the School of Chemistry [2]. For synchrotron based experiments it was deposited at 280°C, onto a sample held at 200°C for 30 minutes for monolayer growth for the photoemission experiments. Heating the substrate prevents the formation of a multilayer film as with isonicotinic acid. For multilayer growth, the substrate was kept at room temperature during deposition, again with the molecule heated to 280°C. No substrate cooling is required for biisonicotinic acid multilayer growth. In STM experiments biisonicotinic acid was deposited at 210°C for 20 minutes in order to obtain a submonolayer coverage of molecules, which was monitored using a quartz crystal microbalance (QCM).

6.4 TiO_2 characterisation

In the valence band studies of isonicotinic and biisonicotinic monolayers, the substrate provides a significant contribution to the overall spectrum obtained. Thus a comprehensive

[2] by David Ring, School of Chemistry, University of Nottingham

study of the substrate valence band at different positions is useful. The crystal was initially aligned with its crystal planes horizontally and vertically to the **E**-vector of the incoming synchrotron light using Low Energy Electron Diffraction (LEED)(Section 6.4.1).

6.4.1 Low energy electron diffraction (LEED)

Low energy electron diffraction, or LEED, is a surface science technique which maps the crystal surface of a sample in reciprocal space. In these studies it was used as a method of checking the surface reconstruction of the sample and to align the crystallographic directions of the surface precisely with respect to the polarisation of the incoming synchrotron light. The quality of the surface can also be checked using photoemission spectroscopy, where defect surface states can be detected if present (Figure 3.14). Experiments performed on beamline 4.1 at Daresbury Laboratories require surfaces to be checked by LEED as the beamline cannot provide the photon energies required to probe the core levels of the substrate atoms (the binding energy of Ti $2p$ electrons is 458eV).

A low energy electron beam (in the range 20 - 200 eV) from a filament is incident normally on the sample, which must be crystallographically well ordered to reflect the diffracted electrons to form the LEED pattern on a fluorescent screen. Only elastically scattered electrons are collected, as secondary scattered electrons are prevented from reaching the screen by a retardation grid. Electrons are Bragg scattered from the crystal substrate and detected on the screen, plotting out a crystal structure of the substrate in reciprocal space. The diffraction spot pattern may be rotated on the screen by rotating the sample azimuthally. This is done in order to line up a crystal plane with the horizontal polarisation of the beam.

The diffraction pattern for the (110) surface is a rectangular grid; thus the crystal was azimuthally rotated until the grid of diffraction spots showed horizontal and vertical arrays of spots. This was taken to be the zero degree azimuthal angle. The surface was characterised using a photon energy of 40eV, which is the energy most commonly used to study the valence bands of samples in this chapter since it allows us to access the valence electrons of the sample with a high surface sensitivity. Figure 6.9 shows the changes in the valence band of clean rutile TiO_2 with changing tilt and azimuthal angles. All spectra have been normalised to the dip at 10eV for comparison. It can be seen that the spectra vary significantly with changes in both the tilt angle and azimuthal angle. A characterisation of

the valence band of TiO_2 can also be found in Ref [113].

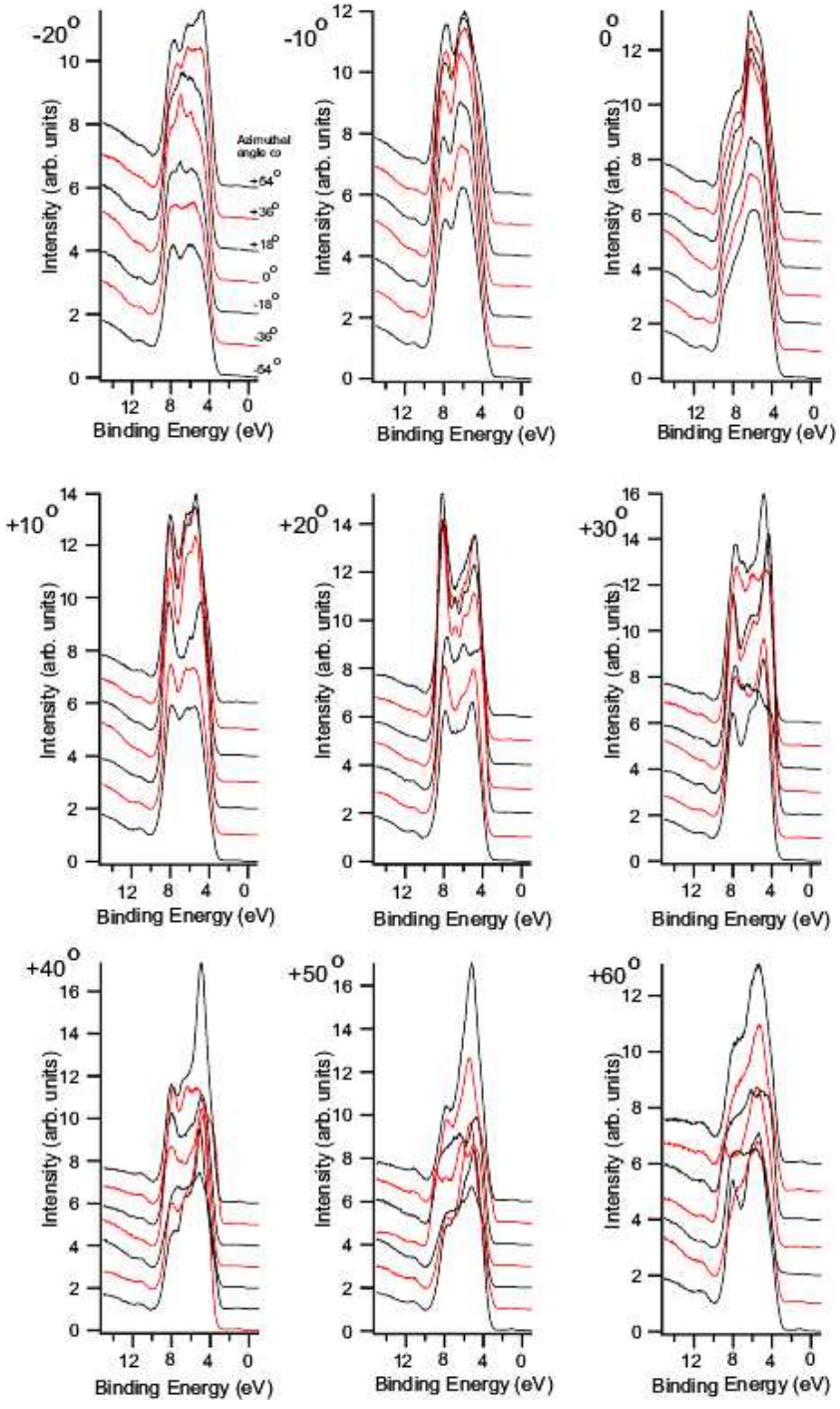

FIGURE 6.9: Valence bands at 40eV of a clean rutile TiO_2 substrate taken at different tilt and azimuthal angles. Each plot shows spectra taken at one tilt angle (from -20° to +60° in 10° steps) over a range of azimuthal angles, as labelled.

6.5 Isonicotinic acid valence band studies

The primary investigation of isonicotinic acid is based on changing the tilt angle of a sample with respect to the incoming synchrotron radiation, to study both multilayers and monolayer characteristics on rutile TiO_2(110). No extensive valence band studies of isonicotinic acid have previously been reported. As the tilt angle of an ordered molecular film is altered there are large changes in the valence band spectra as different molecular orbitals are probed. Conversely, if the molecules are disordered on the sample, then changing the tilt angle has little effect on the valence band obtained.

Further experiments were performed using valence band spectroscopy with well ordered multilayer samples of isonicotinic acid on TiO_2, by altering both the tilt and the azimuthal orientation of the sample (see Figure 3.6 for the definition of the possible angular motion). There are not such strong trends apparent when the azimuthal angle is changed, in that an ordered multilayer shows significant differences in the valence band on changing the tilt angle, but not when the azimuthal angle is altered. Possible reasons for this are discussed.

6.5.1 Overview of isonicotinic acid valence band spectra

Figure 6.10 shows an overview of the valence band characteristics of isonicotinic acid on TiO_2. The valence band spectra were all taken at normal emission (the surface is perpendicular to the direction of the analyser) for clean TiO_2, a monolayer of isonicotinic acid, and a multilayer film. Also shown is an estimate of the valence band spectrum for an isolated monolayer of isonicotinic acid obtained by subtracting the contribution of the underlying TiO_2 surface from the monolayer spectrum (b). Spectra were normalised to the intensity of the main (most intense) peak. All the spectra were calibrated to the Fermi level of the sample, which could be measured in these studies.

The valence band spectrum of the multilayer is shifted to higher binding energy, which is most likely due to steady-state charging in the thick film. The difference spectrum compared with the spectrum from a monolayer shows that the electronic structure of the molecule is not significantly modified upon chemisorbing to the surface, since they are very similar. The lower intensity of the peak at 8.5 eV (peak 2) compared with the multilayer may be due to the presence of the surface state peak (see ref. [114]) in the spectrum of clean TiO_2 at the same energy, used for the subtraction (which is not expected to remain for the

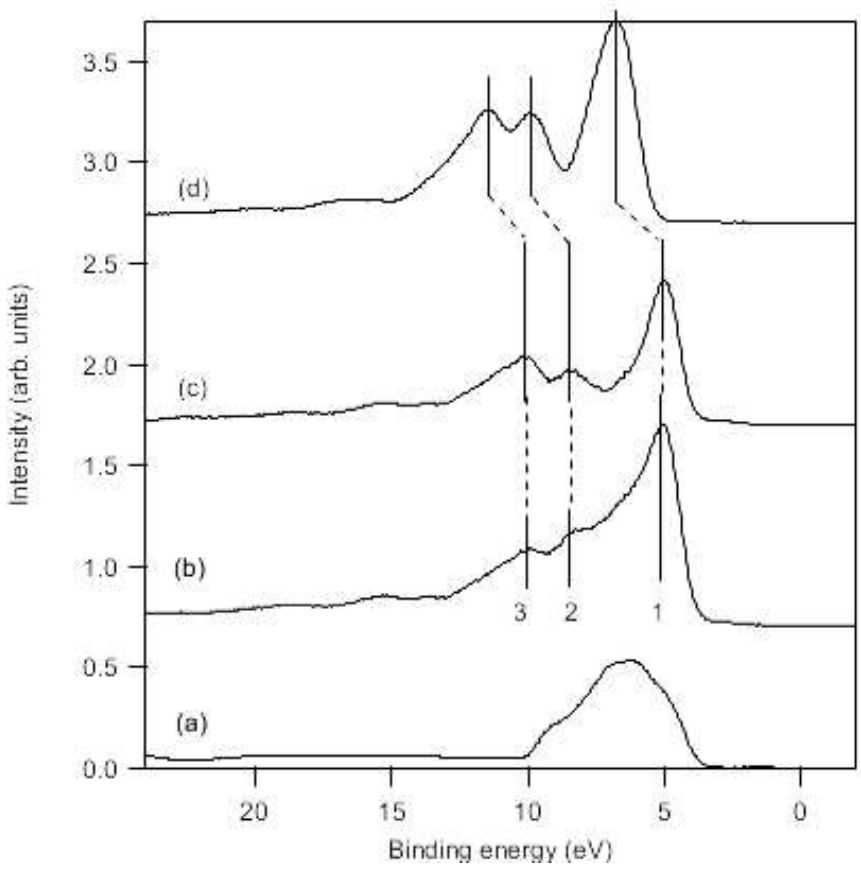

FIGURE 6.10: Valence bands at 40eV at normal emission of isonicotinic acid on TiO_2 showing a) Clean TiO_2, b) Monolayer of isonicotinic acid, c) A difference spectrum of b)-a) showing the effect of the molecular monolayer only, and d) a multilayer spectrum. The features labelled 1,2,3 are all at the same separation for each spectrum within experimental error, as shown.

monolayer). The relative energy separations of the molecular orbital peaks in the monolayer and the multilayer, labelled 1,2,3 in Figure 6.10 are the same within experimental error.

6.5.2 Isonicotinic acid multilayers

As previously discussed, both slow and fast depositions of isonicotinic acid multilayers can be performed to achieve ordered and disordered films. Figure 6.11 shows the valence band spectra ($h\nu$ = 40eV) measured over the full range of available incidence/emission angles for a multilayer film of isonicotinic acid adsorbed on the TiO_2(110) surface. In this case a slow multilayer was prepared using a substrate temperature of $-100°C$, and by evaporating

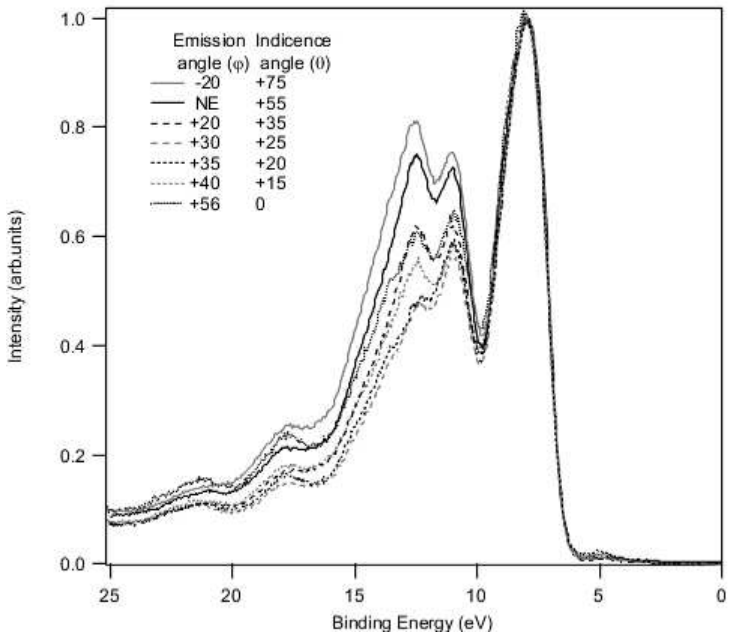

FIGURE 6.11: Valence bands taken using $h\nu$ = 40eV of a slowly grown multilayer of isonicotinic acid on TiO_2 taken at different tilt angles. Angular differences demonstrate the growth of an ordered film under these slow deposition conditions

isonicotinic acid at 65°C onto a chemisorbed monolayer (formed using a molecule evaporation temperature of 200°C). The spectra have been normalised to the intensity of the main lowest binding energy peak in order to illustrate the angular dependence of the spectra. The intensities of the peaks in the energy range from 10-25 eV relative to the intensity of the peak at 7.5eV show a clear angular dependence. The effect is most pronounced for the two peaks at 12 eV and 13.5 eV. Furthermore, it is evident that it is the incidence angle and not the emission angle which plays the most important role in this dependence. If the emission angle, and consequently surface sensitivity, was the key factor, then we would expect to observe very similar spectra for $+20°$ and $-20°$ emission, in contrast to the observed spectra. Therefore it is proposed that the valence band spectra are strongly dependent in this case on the angle of incidence and consequently the interaction of the electric field vector of the incoming radiation with the molecules on the surface. It follows then that there must be a high degree of molecular ordering in the multilayer for such an effect to be observed. Such ordering might arise due to the formation of head-to-tail intermolecular hydrogen bonds giving upright arrays of molecules (see Figure 6.8).

The formation of an ordered film is strongly dependent on the preparation conditions. The valence band spectra shown in Figure 6.12 were measured after a fast deposition of isonicotinic acid to form a disordered multilayer. In this case the fast multilayer was prepared with the sample held at -100°C by evaporating isonicotinic acid at the hotter temperature of 130°C onto a chemisorbed monolayer. The spectra have again been normalised to the intensity of the first peak at 7.5eV for direct comparison with Figure 6.11. The angular dependence of the film is suppressed in this case, with the intensity ratios of the peaks at 7.5 eV, 12.0 eV and 13.5 eV remaining essentially unchanged with varying incidence/emission angle. This suggests a significantly more disordered film than that shown in Figure 6.11, most likely due to the suppression of hydrogen-bond formation between the molecules due to the rapid molecule deposition rate. The features of varying intensity at energies $>$ 15eV change intensity as they are resting on a background count, which changes depending on the position of the manipulator which is different at different tilt angle positions.

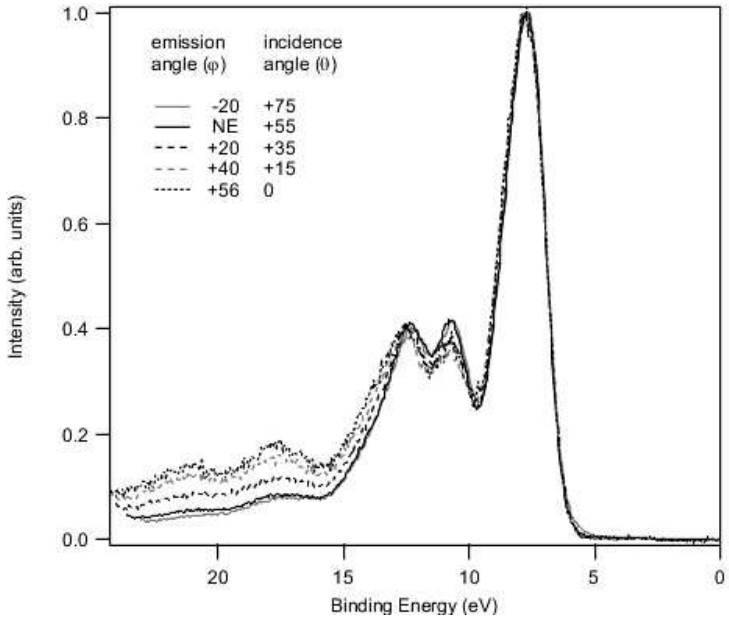

FIGURE 6.12: Valence band spectra taken using $h\nu = 40$eV of a rapidly grown multilayer of isonicotinic acid on TiO_2 taken at different tilt angles. There are no angular differences, demonstrating the growth of a disordered film under the fast deposition conditions

6.5.3 Isonicotinic acid monolayers

A tilt angle dependence is also observed for monolayers of isonicotinic acid chemisorbed to the surface of rutile $TiO_2(110)$, formed by depositing the molecule at $\sim 100°C$ with the substrate held at a temperature of 200°C. At this substrate temperature, growth is limited to a single chemisorbed monolayer as shown previously [110]. Figure 6.13 shows the valence band spectra measured for an isonicotinic acid monolayer at $-20°$, $0°$ (normal emission), $+20°$, $+40°$ and $+56°$ emission angles. All of the spectra have again been normalised to the intensity of the highest energy peak at 5eV and exhibit an angular dependence with respect to the incoming light. Although the spectra now contain a significant contribution from the underlying titanium dioxide substrate, the observed angular dependence is not dominated by changes in the surface sensitivity of the measurement, since the spectra obtained at $-20°$ and $+20°$ emission are very different. This suggests, as in the case of the multilayer, that there is significant molecular ordering in the monolayer and the angular dependence is related to the interaction of the electric-field vector of the polarised light with the molecular orbitals involved.

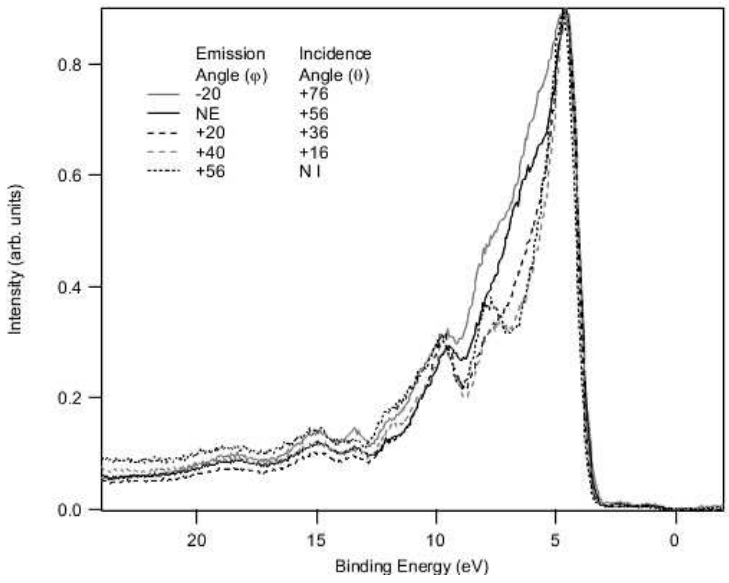

FIGURE 6.13: Valence bands taken using $h\nu = 40$eV of a monolayer of isonicotinic acid on TiO_2 taken at different tilt angles. Angular differences demonstrate the growth of an ordered film, which is expected for a monolayer.

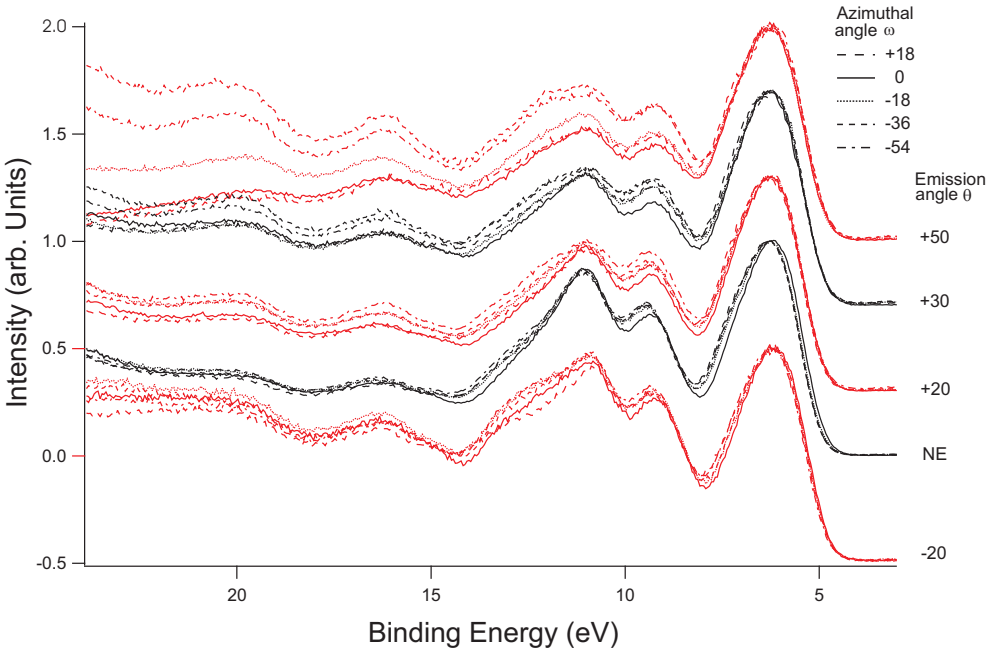

FIGURE 6.14: Valence bands at 40eV of a multilayer of isonicotinic acid on TiO_2 taken at different tilt (emission) and azimuthal angles. Away from normal emission there may be a dependence on azimuthal angle, but the background counts at angles far away from normal emission mean the data are hard to interpret.

6.5.4 Azimuthal angle studies of isonicotinic acid films.

As the tilt angle studies of isonicotinic acid on TiO_2 yielded interesting results, a similar experiment was performed involving changing both the tilt and azimuthal angle of an ordered multilayer of isonicotinic acid. One might expect that if a tilt angle dependence is observed in the valence band of an ordered multilayer film then the valence band spectra will also show an azimuthal angle dependence. The definition of the angular movements are shown previously in Figure 3.6. Thus a full range of valence band spectra were obtained from an ordered film over a range of tilt and azimuthal angles. Figure 6.14 shows valence band spectra taken using 40eV photons for an ordered film, at tilt angles of -20°, normal emission, +20°, +30° and +50°, and at azimuthal angles of -18°, 0°, +18°, +36° and +54°.

To ensure that the sample did not degrade due to prolonged exposure to the synchrotron light (suffer "beam damage") the first few spectra taken were repeated at the end of the data collection, and the scans were compared. No obvious beam damage had taken place, as the spectra had not changed over time. From the evidence obtained,

there does not clearly appear to be a dependence on the azimuthal angular orientation, as changing the azimuthal angle does not alter the valence band spectra significantly, and any changes that may be present are difficult to resolve clearly from the spectra taken.

It is worth noting that there appears to be the smallest measured deviations due to azimuthal angle changes at normal emission, and as the tilt angle is moved increasingly further away from normal emission, so the changes in the spectra taken at different azimuthal angles becomes larger. Careful analysis is required, since it is not obvious if these changes are due to ordering in the sample or due to a fluctuating background count at higher binding energies. It is clear that the data set taken at a tilt angle of $+50^{\circ}$ has a very variable background count. The background changes at grazing emission angles are due to the physical presence of the manipulator and other objects in the chamber close to the photoelectrons' path to the detector. Stray electric and magnetic fields are believed to be present at grazing emission angles which affects the spectra obtained at these angles. Particularly when the azimuthal angle changes, it is actually the sample holder which rotates, which has dimensions $\sim$ 15mm$\times$ $\sim$ 50mm and which also houses an electron beam heating filament. This large object can affect the path of the ejected photoelectrons travelling to the detector. Thus the data obtained is possibly affected by too many unavoidable variables to draw convincing conclusions from.

The lack of any obvious angular dependence may also be due to the substrate preparation, which if performed incorrectly can cause the surface to have row and rosette features and thus affect the ordering of any adsorbate atoms. Section 4.3 explains different surface structures which can form under less than ideal preparation conditions. The molecules may be bonded in chains through head to tail hydrogen bonding, and these chains may be oriented in an upright geometry as expected. However, the orientation of individual molecules in these chains may be random, and furthermore the ordered chains may exist in domains over the surface, with any azimuthal angular dependence in individual domains cancelled out over the relatively large area probed by the light spot on beamline 4.1 (which with white light is an arc $\sim$ 1mm high and $\sim$ 3mm wide).

6.5.5 Density functional calculations

The computational chemistry package Spartan'02 was used in this thesis for chemical calculations, to determine the geometry and molecular orbital energies of an isolated isonicotinic

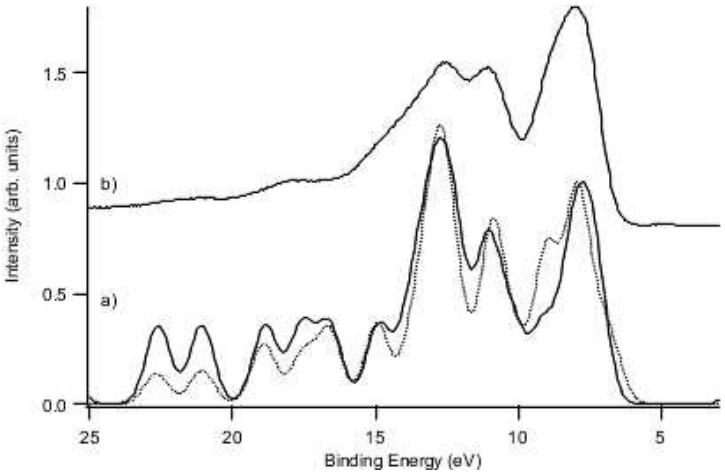

FIGURE 6.15: a) The valence band spectra calculated for an isolated isonicotinic acid molecule using (solid line) a DFT calculation in Spartan'02 and (dotted line) the more complex DFT calculation by Brena and Luo. b) Shows the valence band for a multilayer of isonicotinic acid. Peak positions between experiment and theory agree reasonably well.

acid molecule. Density functional theory (DFT) is used here within the B3LYP model, and is a standard choice for relatively simple organic molecules and gives reasonable values for molecular orbital energies. DFT models allow the electron-electron interactions to be incorporated into the model and give a more accurate result generally than molecular mechanics models like those used for the PTCDA work (Chapter 5). DFT methods involve the minimal energy of a group of electrons influenced by an external field as a functional of the electron density. There are different basis sets which may be used to give reliable results for specific systems. Here the hybrid density functional theory (DFT) B3LYP model was used, with a 6-31G* basis set, to compare theoretical molecular energy level data with experimental data.

The theoretical data here will be compared only to experimental results from a sample at fixed azimuthal angle as the results concerning a change in tilt angle only are the clearest. A theoretical spectrum is formed by taking the energy levels calculated in Spartan'02 for the molecular orbitals of the molecule, and plotting a Gaussian function of unit height and with a FWHM of 1eV at that energy. The combination of Gaussian peaks forms the theoretical valence band. Figure 6.15 shows the calculated valence band spectrum for an isolated gaseous molecule compared with experimental data for isonicotinic acid multilayers. It should also be noted that these calculations are based on a free gaseous

isonicotinic acid molecule, and therefore do not take into account the interaction with the $TiO_2(110)$ surface or with other molecules. The calculated valence band is compared to a multilayer film as the majority of molecules are not interacting with the substrate and no substrate is included in these calculations.

Also presented are the valence band spectra calculated using a more complicated model, by Brena and Luo[3]. Molecular geometries used for these calculations of the valence band spectra and molecular orbital shapes were again optimised at the hybrid DFT method B3LYP, with the standard 6-31G** basis set, using the GAUSSIAN 98 program [50]. The valence molecular orbital energies used for the valence band spectra were determined by Koopman's theorem at the DFT/B3LYP level with a 6-31G basis set. The valence band spectral intensities are obtained according to the Gelius intensity model [115] and the experimental relative photoionisation cross sections for the different orbitals at 40 eV excitation energy are used. The molecular orbital energies obtained were convoluted with Gaussian peaks of 1eV at FWHM to again create the theoretical valence band spectra. These calculations include the spectrum components from electron excitation in the three orthogonal coordinates x, y and z across a molecule. Also calculated are the theoretical valence band spectra for molecules in three different hydrogen bonding environments; these being a molecule hydrogen bonded on the nitrogen side (which is not thought to exist in these experiments), a molecule hydrogen bonded on the carboxylic acid side, and a molecule hydrogen bonded on both sides (a molecule in the bulk of a multilayer film). All the calculated spectra by Brena and Luo are presented in Figure 6.16.

In Figure 6.15 the theoretical spectrum calculated by Brena and Luo is a combination in equal proportions of the x,y and z components of a molecule hydrogen bonded on both sides to mimic a molecule in the bulk of a multilayer. The other theoretical spectrum is one from DFT calculations performed in Spartan'02. These two calculated spectra are compared to an experimental valence band for an disordered multilayer at normal emission and zero azimuth. A disordered film spectrum was used to cancel out any directional features in the valence band. It can be noted that the peak positions agree within experimental error, and the intensities, though not exact, are in reasonable agreement. This serves as an indicator that the models used are suitable for these molecular films.

Spectra calculated to mimic the effects of different sample orientations of a free

[3]B. Brena and Y. Luo, KTH, Stockholm

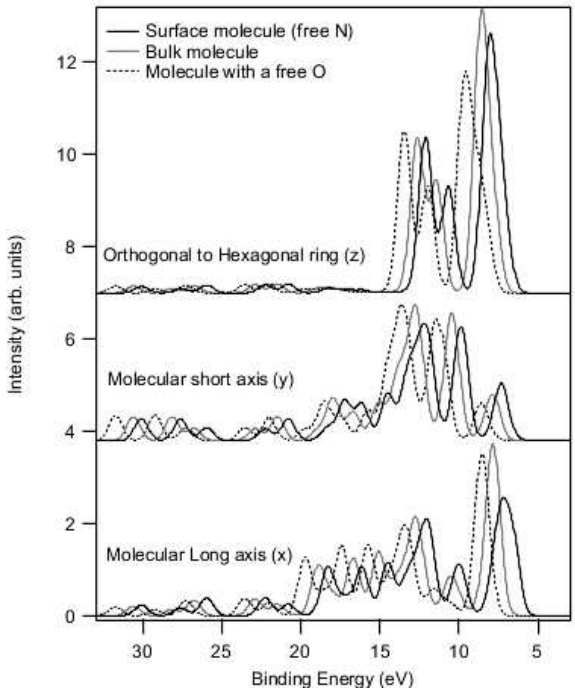

FIGURE 6.16: DFT calculated spectra for the x, y, and z components of the valence band. These are shown for molecules in three different chemical environments: H-bonded only on the carboxylic side; H-bonded at both sides; and H-bonded only on the pyridine ring side of the molecule

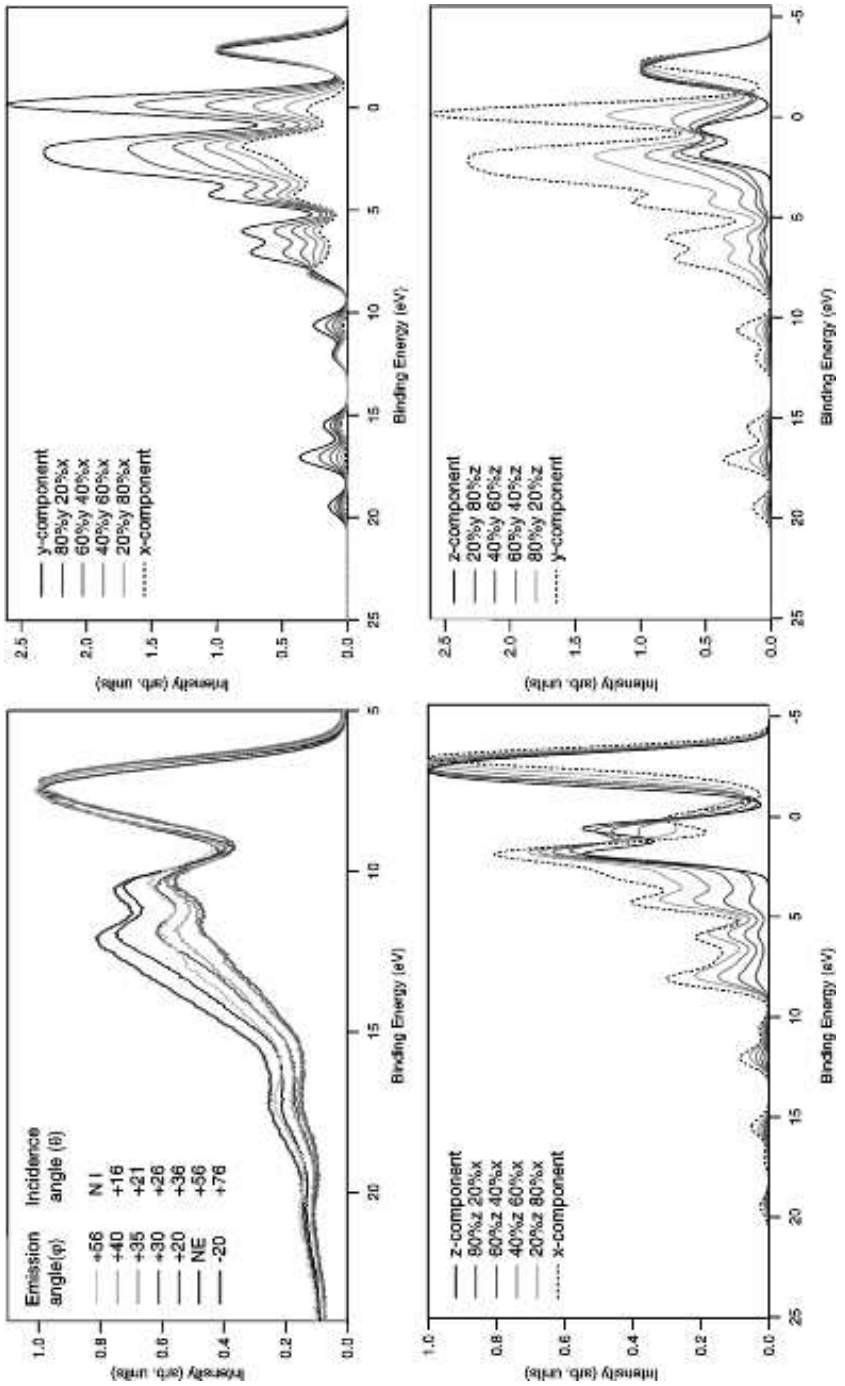

FIGURE 6.17: This shows a) the experimental data for an ordered multilayer with b) - d) the calculated valence band spectra for a hydrogen bonded molecule (from models by Brena and Luo). Peak positions between experiment and theory agree well and it can be seen that the theoretical curves may be used to determine the precise position of the molecules with a full set of experimental angular data.

molecule are shown in Figure 6.17, which demonstrate the possibility of using this model as a way of calculating the actual orientation of the molecules studied. The combinations of the three geometric contributions in varying proportions are presented to give an overall valence band spectrum for a molecule in different geometric orientations with respect to the electric field vector of the linearly polarised excitation radiation. Differences between the DFT calculated valence band spectra and the experimental data in Figure 6.17 may be due in part to the unknown azimuthal rotation of the molecules in the film, and also that the actual molecules will have contributions from the x, y and z components.

6.6 Isonicotinic acid summary

In this chapter so far, studies of ordered and disordered multilayers, and a monolayer, of isonicotinic acid have been investigated using valence band photoemission. An ordered film has valence band characteristics which are dependent on the tilt angle of the sample, whereas a disordered film shows no angular dependence. This is due to the molecular orbitals being probed to different degrees as the angle of the sample is changed with respect to the direction of the incoming polarised light. DFT calculations of an isolated isonicotinic acid molecule show peak position agreement with experimental data of a multilayer sample. More detailed DFT calculations by Brena and Luo, accounting for possible hydrogen bonding interactions and geometric components of the valence band, show that an angular dependence in valence band spectra can be theoretically modelled. Changes in the azimuthal angular orientation of an ordered multilayer show negligible changes in the valence band, which may not be expected, and reasons for this include ordered domain formation and stray field effects from the movement of the manipulator.

6.7 Biisonicotinic acid valence band studies

As the angular studies of isonicotinic acid on TiO_2 yielded interesting results, some preliminary studies were performed using biisonicotinic acid. As with isonicotinic acid, no extensive valence band studies of biisonicotinic acid have previously been reported. The valence band experiments described in this brief section were again performed on Beamline 4.1 at Daresbury laboratories.

After characterising the clean rutile TiO_2 substrate (Section 6.4), biisonicotinic acid was deposited from a Knudsen cell at 280°C onto the clean sample held at 200°C for

30 minutes, for a monolayer coverage. The elevated substrate temperature prevents the formation of any multilayers. Valence band spectra taken using 40eV photons with the sample positioned at normal emission are shown in Figure 6.18, and have been calibrated to the Fermi level of the tantalum sample holder. All spectra have been normalised to the lowest binding energy feature at 4.6eV for direct comparison. A difference spectrum has been calculated from the valence band of a chemisorbed monolayer minus the valence band of the clean substrate to simulate the valence band spectrum of an isolated biisonicotinic acid monolayer, in a similar manner to that in Figure 6.10 for isonicotinic acid.

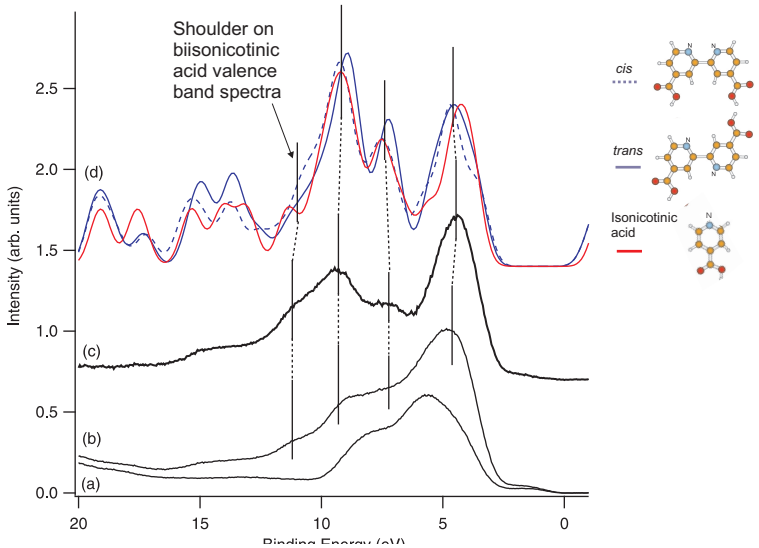

FIGURE 6.18: Valence band spectra at $h\nu$ = 40eV of a) TiO_2 substrate, b) monolayer of biisonicotinic acid and c) a difference spectrum, (b)-(a), to simulate free biisonicotinic acid molecules with no substrate influence. d) DFT calculated valence band spectra of an isolated biisonicotinic acid molecule in the (solid line) *trans* and (dashed line) *cis* configurations, and of an isolated isonicotinic acid molecule for comparison. Peak positions between the difference spectrum and the calculated spectra show a strong correlation. Note the calculated isonicotinic acid spectrum lacks the shoulder feature at $\sim$ 11eV.

Also included in Figure 6.18 are two calculated spectra. Using Spartan'02, the valence band spectra of a free biisonicotinic acid molecule in the *cis* and *trans* configurations are shown. The molecular energy levels were again calculated using DFT at the B3LYP level with a 6-31G* basis set using the Spartan'02 package, and the spectra are created by plotting a Gaussian function of unit height and with a FWHM of 1 at each calculated energy.

From Figure 6.18 it can be seen that the calculated spectra for an isolated molecule and the difference spectrum have similar peak positions. The peak intensities are not the same but are similar in that the three features at 4.6eV, 7.3eV and 9.2eV are the most intense. Also the peak at 9.2eV has a shoulder at higher binding energy, which is present in the difference spectrum and the calculated spectra; this feature is not as obviously present in the isonicotinic acid spectra. The spectra for both isonicotinic acid and biisonicotinic acid are very similar, which is perhaps to be expected as one biisonicotinic acid molecule is two isonicotinic acid molecules with a bond between them. It has been shown that when biisonicotinic acid is chemisorbed to the TiO_2 surface, an additional unoccupied molecular orbital gives rise to an extra feature in the NEXAFS spectrum. This feature does not appear in the NEXAFS spectrum of a multilayer of biisonicotinic acid [71]. It may be the equivalent occupied molecular orbital which is the source of the extra feature in the valence band shown in Figure 6.18 which does not appear in the calculated spectrum from an isolated isonicotinic acid molecule (shown in red in Figure 6.18).

A multilayer sample of biisonicotinic acid was not prepared, but this may be an interesting future experiment to see if the difference spectrum and the DFT calculated spectra are similar to a multilayer spectrum, as is observed with isonicotinic acid. It would also be of interest to prepare ordered and disordered multilayer films and examine how the valence band of these films varies with tilt angle.

6.8 Biisonicotinic acid on gold on TiO_2

Biisonicotinic acid was studied on rutile TiO_2 using core level photoemission at beamline I3.11 at MaxLab (see Section 3.2.3). The core levels of all elements of interest (C, N, O and Ti) can be accessed on this beamline. Gold was used in these studies as an intermediate layer between the TiO_2 surface and adsorbed biisonicotinic acid to determine the effects on the bonding of biisonicotinic acid to the surface using XPS. All spectra taken in these experiments were with the sample oriented at normal emission.

The study of biisonicotinic acid on gold on TiO_2 is of interest as a possible device for molecular solar cell fabrication without the use of a liquid electrolyte as with Grätzel cells. It may be possible to use an evaporated gold layer as a source of replenishment electrons for the excited dye molecules in the way an electrolytic solution does in a Grätzel cell. Of course many further studies are required to monitor molecular geometries and

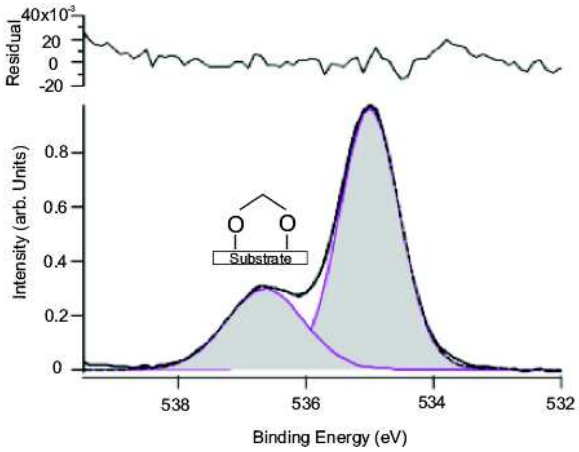

FIGURE 6.19: O 1*s* core level spectrum of a monolayer of biisonicotinic acid on TiO_2 taken using 598eV photons. The peak at 535eV originates from the substrate and the spectrum has been calibrated using this bulk substrate peak. The peak at 536.7eV is due to oxygen atoms in the molecule. Since there is only one molecular oxygen peak, thus one chemical environment, the molecules must bond in a bidentate fashion through the oxygen atoms, in agreement with previous work.

adsorption, charge transfer behaviour, and well calibrated deposition methods. The results presented here provide a small insight into the bonding characteristics of the solid state biisonicotinic acid-gold-TiO_2 device.

6.8.1 XPS of biisonicotinic acid on TiO_2

Monolayer regime

The TiO_2 substrate was cleaned and prepared in the usual way (Section 4.3). A monolayer coverage of biisonicotinic acid was deposited on TiO_2 by heating the molecule to 280°C while the substrate was held at 200°C to prevent multilayer formation. O 1*s* core level spectra were calibrated to the substrate oxygen signal at a well characterised value of 535 eV, and to the Fermi level of the sample. An O 1*s* spectrum obtained with 598eV photons is shown in Figure 6.19. 598eV was chosen as the excitation energy to provide a surface sensitive probe of the O 1*s* core level. The two peaks in the monolayer spectrum originate from the TiO_2 substrate at 535eV, and from the molecule at 536.7eV. Since there is a single molecular peak we can infer that all the oxygen atoms in the molecule are in the same chemical environment, and thus that the molecule is bonded through the carboxylic groups to the substrate, in agreement with previous studies [106]. The core level photoemission

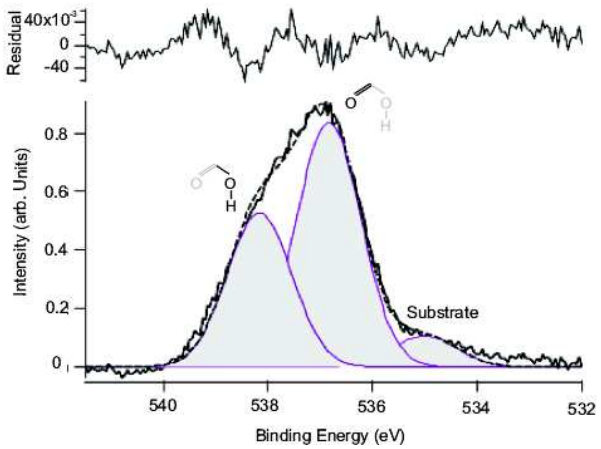

FIGURE 6.20: O 1*s* core level spectrum of a multilayer of biisonicotinic acid taken using 598eV photons. The peak at 535eV is due to substrate oxygen atoms and the spectrum has been calibrated using this peak. The peak at 536.7eV is due to carbonyl oxygen atoms and the peak at 538.1eV is due to hydroxyl oxygen atoms, perhaps involved in intermolecular hydrogen bonding. The contribution from molecular oxygen chemisorbed to the surface is too small to be observed.

peaks in this chapter have been fitted using a peak fitting algorithm developed in-house (Section 3.6.3).

Multilayer regime

A multilayer of biisonicotinic acid was prepared by depositing biisonicotinic acid for up to one hour on a room temperature TiO_2 substrate with a monolayer of biisonicotinic acid already present. After this deposition the core level photoemission spectrum changed significantly. In the O 1*s* spectrum shown in Figure 6.20, there are two oxygen molecular species and a highly attenuated substrate peak at 535eV. The molecular peaks are derived from carbonyl C=O and hydroxyl C—O-H oxygen species in biisonicotinic acid molecules (in agreement with Patthey *et al* [106]). O'Shea *et al* observe hydrogen bonding in ordered biisonicotinic acid molecular films [110]. The results presented here are such that in the multilayer film, both carbonyl and hydroxyl oxygen atoms are present. This suggests that hydrogen bonding may occur between hydroxyl oxygen atoms and neighbouring nitrogen ring atoms.

6.8.2 XPS of biisonicotinic acid on gold on TiO_2

Method

In the previous section, monolayer and multilayer biisonicotinic acid films adsorbed on $TiO_2(110)$ were studied, and agree with previous experiments. To take these experiments further, an intermediate gold layer was deposited between the TiO_2 and the molecules. Varying amounts of gold were deposited by varying the length of time taken for a single deposition before the deposition of a monolayer of biisonicotinic acid. "TiO_2-metal-dye ligand" systems are of interest from a molecular adsorption perspective but also for a consideration of charge transfer dynamics for possible solar cell applications. Here we will concentrate on the geometry and chemical bonding rather than any charge transfer properties.

To prepare the samples, the TiO_2 surface was prepared in the usual way (Section 4.3). Then to prepare the metal sandwich layer, gold metal was evaporated onto the TiO_2 substrate by heating a gold nugget held in a boronitride ceramic crucible in a Knudsen cell to 1400K. A ceramic crucible is required for deposition of metals in vacuum, as they tend to melt before they evaporate. A crucible is therefore required to hold the metal which will not allow any molten material to leak out. After taking core level photoemission spectra of the gold-TiO_2 sample for characterisation purposes, biisonicotinic acid was deposited in the same manner used for clean TiO_2 to form a monolayer, by heating the molecule to 280°C in a Knudsen cell while the substrate was held at 200°C to prevent multilayer formation.

Results

Figure 6.21 show the O $1s$ photoemission spectra from a monolayer of biisonicotinic acid on gold layers of different thicknesses on TiO_2 taken using a photon energy of 598eV. Gold was deposited for a different length of time before a biisonicotinic acid monolayer was deposited (10, 20, 40, 80 and 160 minute gold depositions were used). The gold-TiO_2 sample was heated to 200°C during biisonicotinic acid deposition to prevents multilayer formation; this did not cause any gold to be removed as the chamber pressure remained constant during sample heating. Since gold only sublimes at 1400K it is reasonable to assume that at a relatively low temperature such as 200°C there is a negligible effect on the gold layer. The effect of heating the gold-TO_2 samples was checked by taking an Au $4f$ spectrum and Ti $2p$ spectrum before and after a 30 minute anneal at 200°C with no molecule deposition, and the spectra did not change as a result of the heating.

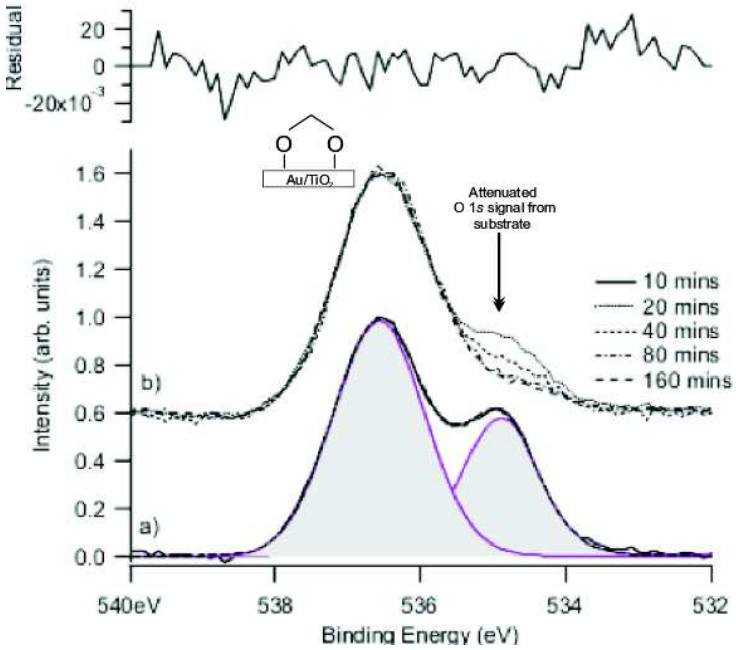

FIGURE 6.21: O 1*s* core level spectrum of a monolayer of biisonicotinic acid taken using 598eV photons on increasing amounts of gold on TiO_2. a) Spectrum taken from a monolayer of biisonicotinic acid deposited after a 10 minute gold deposition. The curve fit shows there to be only two components, from the substrate and the molecule. b) The substrate peak is gradually attenuated after longer gold depositions but the molecule feature remains a single peak, suggesting only one chemical state of the oxygen in the molecules.

Figure 6.21 shows a steady attenuation of the oxygen signal at 535eV from the TiO_2 substrate as the gold coverage increases, which is expected. Of interest is the presence of only one molecular oxygen species at 536.7eV, which is present in all of the spectra regardless of the thickness of the gold sandwich layer. That it is a single peak is demonstrated by the theoretical curve fit. This single molecular peak suggests that all oxygen atoms in the molecules again are in an equivalent chemical environment. This indicates that the molecules have a deprotonated carboxylic acid group and bond in a bidentate fashion through the carboxylic acid group on gold as on TiO_2. There is no change in the chemical shift between the substrate oxygen peak and the molecular oxygen peak in any of the spectra obtained from a TiO_2 surface, thick gold sample surface, or on intermediate gold coverages. This also suggests the same chemical environment for all of these systems; a chemisorption bonding configuration through the carboxylic acid group.

A similar study of a pyridinecarboxylic acid derivative on a metallic surface has been performed by Xu *et al* [116] who investigate acridine-9-carboxylic acid monolayers on Ag(111). Two different phases are observed dependent on the density of steps on the silver surface. They find hydrogen bonding between the central ring nitrogen and a neighbouring carboxylic acid group, or a carboxylic acid-carboxylic acid interaction forming molecular pairs. The molecules are thought to sit at a 45° tilt angle to the surface.

6.9 STM investigation of biisonicotinic acid

An STM investigation of biisonicotinic acid was performed based on two different surfaces. One study focusses on the deposition of biisonicotinic acid on gold. A substrate was used which was composed of a 150nm thick gold layer on a mica substrate, which can be prepared as described in Section 4.4 to produce the Au(111) $22 \times \sqrt{3}$ reconstruction. This surface was used as a model gold surface to compare with the synchrotron studies in Section 6.8 of biisonicotinic acid on gold on TiO_2.

The second study involves the deposition of biisonicotinic acid on the Ag-Si(111)$\sqrt{3}\times\sqrt{3}$R30° surface, for similar reasons to those outlined in Chapter 5 concerning PTCDA. Ag-Si(111) is a relatively passive substrate over which the molecules are expected to diffuse, and any ordered molecular regions tend to be stabilised by molecule-molecule interactions rather than molecule-substrate bonding. The preparation of the Ag-Si(111)$\sqrt{3} \times \sqrt{3}$R30° surface is described in Section 4.2.

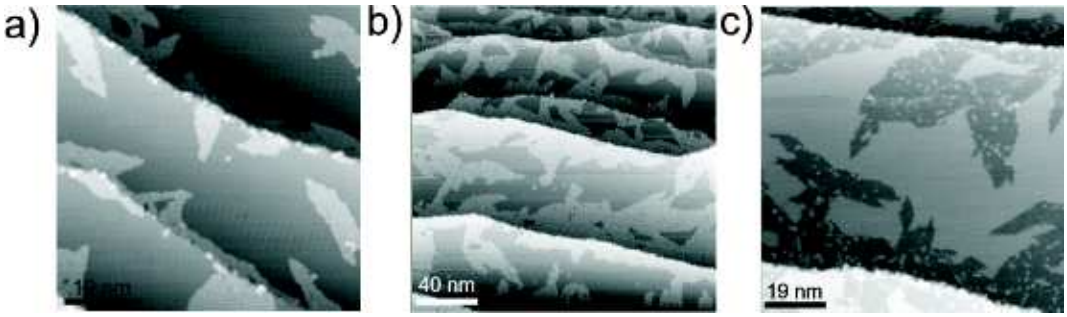

FIGURE 6.22: Biisonicotinic acid island formation on the Ag-Si(111)$\sqrt{3} \times \sqrt{3}$R30° surface. a) 2 min. deposition at 210°C; b) a further 2 min. deposition at 210°C onto sample (a); c) another region on sample (b). All images are taken at -2V bias, 0.05naA tunnel current. It can be seen that the islands are irregularly shaped and the smaller islands nucleate at step edges.

6.9.1 Method

Biisonicotinic acid was thoroughly degassed prior to deposition and was found to sublime from a Knudsen cell at 210°C from chamber B (Section 2.5) as measured using a quartz microbalance in the STM system. The lower deposition temperature in these studies compared to that used in the synchrotron experiments is chosen to ensure only submonolayer coverages are obtained. Depositions were also only performed for 120 seconds at a time to keep the coverage at a submonolayer level.

6.9.2 Biisonicotinic acid on Ag-Si(111)$\sqrt{3} \times \sqrt{3}$R30°

Figure 6.22 is an overview of the long range morphology of samples prepared by depositing biisonicotinic acid onto Ag-Si(111)$\sqrt{3} \times \sqrt{3}$R30° for 120 and 240 seconds. The molecular islands which are present appear to initially nucleate at step edges and form rather irregular regions with neat island borders. The larger island in Figure 6.22c) appears stable in the middle of a step; perhaps this formed by originally nucleating at a defect site on a terrace. The irregular island shapes suggest at first that the molecules are perhaps not well ordered, but are held in place in the island strongly enough such that edge molecules are not easily displaced by the STM tip. Loosely bound molecules at the edge of an island may appear in an STM image as a fuzzy island outline [116].

Closer inspection of these islands reveals rather disordered molecular packing with small locally ordered regions. Figure 6.23 shows one such island typical of those imaged.

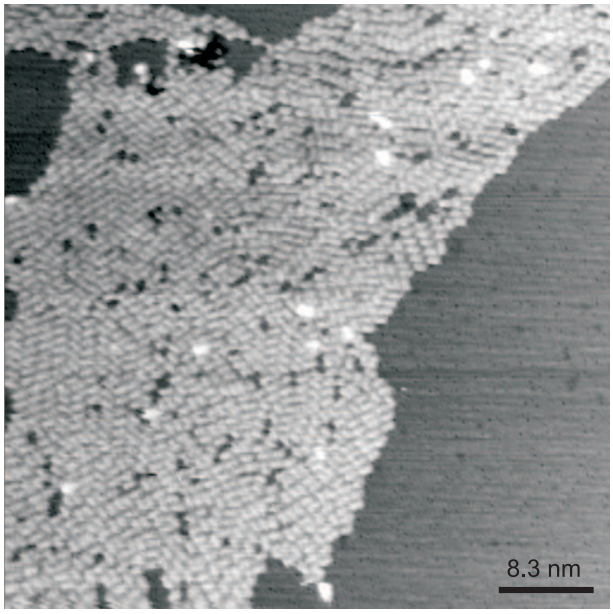

FIGURE 6.23: High resolution image of biisonicotinic acid island on the Ag-Si(111)$\sqrt{3} \times \sqrt{3}$R30° surface taken at -2.0 V bias, 0.05nA tunnel current. There are small regions of local ordering in an irregular region. This island is typical of those imaged.

It can be seen that there are regions of about 15 molecules which are well ordered, but the island overall is rather disordered, with small defects and no real overall direction of preference along which the molecules or ordered groups of molecules align. From measurements of the size of individual bright features it is thought that each bright feature is a single biisonicotinic acid molecule. Molecules with extended π-orbitals such as biisonicotinic acid and larger examples such as PTCDA (Chapter 5) tend to lie flat on surfaces, maximising π-electron donation into the unoccupied states of the surface and allowing maximum back donation from the surface occupied states to the π^* molecular orbitals.

The molecules can be individually resolved, but no details can be determined as to the geometry of each individual molecule. Calculations used to determine a theoretical valence band for an isolated biisonicotinic acid molecule (see Section 6.7) were expanded to model the geometry of the HOMO of an individual molecule. The calculated HOMOs of a biisonicotinic acid molecule in the *cis* and *trans* configurations are shown in Figure 6.24. From these calculations, it is thought that in the STM images, the lozenge shaped feature corresponding to one molecule is a low resolution image of the HOMO, thus the long axis of each bright feature is in the direction across the two pyridine rings of one molecule, as

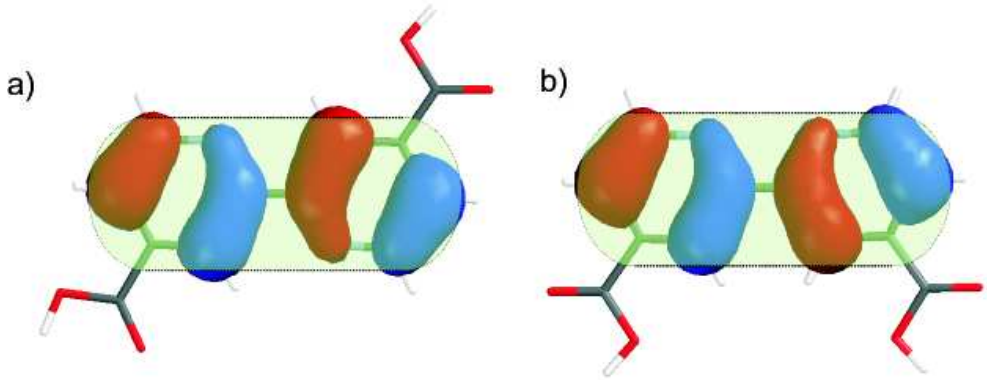

FIGURE 6.24: Biisonicotinic acid calculated using DFT at the B3LYP level using a 6-31G* basis set in the a) *trans* and b) *cis* configurations. The green overlay represents how a molecule appears in an STM image. The long axis of bright features in the STM images corresponds to the axis across both pyridine rings in one molecule, and each molecule appears as a lower resolution representation of the calculated HOMO. The configuration of a single molecule, either *cis* or *trans*, cannot be determined from the HOMO in STM images

indicated in the figure. Additionally it appears that the geometry of a molecule, whether *cis* or *trans*, cannot be determined from the shape of a molecule in the images.

Of the ordered regions, higher magnification images are shown in Figure 6.25. There appears to be what can be termed a herringbone arrangement, a brickwork pattern, a trellis arrangement and a close packed phase. Figure 6.25a) shows a regular herringbone phase, with the herringbone row direction, from bottom right to top left, apparently following the direction of one of the principal axes of the surface reconstruction. Overall it was difficult to clearly image both the details of the molecular islands and the surface reconstruction. Figure 6.25b) shows a trellis scheme which was readily observed in these islands. The ordering is not, however, regular, but the molecules appear to form a "criss cross" pattern with groups of one, two or three molecules stacked in line before a molecule lies across the row direction. Figure 6.25c) shows a brickwork phase where the molecules appear to have their long axis (in this case this is the direction across both pyridine rings) aligned and molecules sit either next to one or between two molecules in the next row. Figure 6.25 d) shows molecules which are close packed, in an elongated hexagonal structure.

One reason for the variety of molecular arrangement may be that one biisonicotinic acid molecule can adopt one of six different geometries on the surface, as there is the

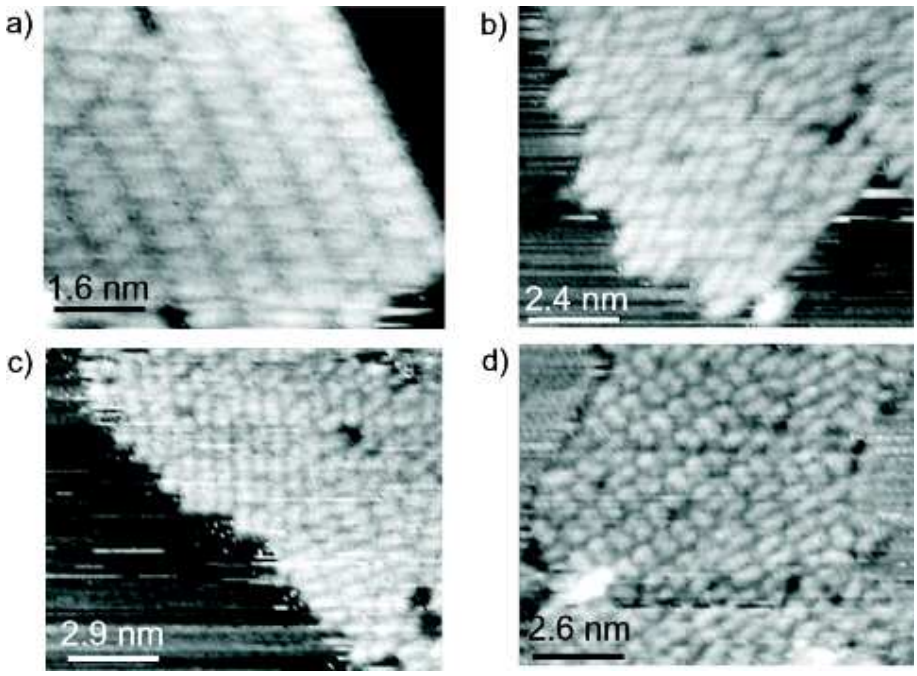

FIGURE 6.25: Ordered phase regions of biisonicotinic acid on the Ag-Si(111)$\sqrt{3} \times \sqrt{3}$R30° surface. a) herringbone phase; b) trellis phase; c) a brickwork phase in two directions; d) an interlocked close packed phase.

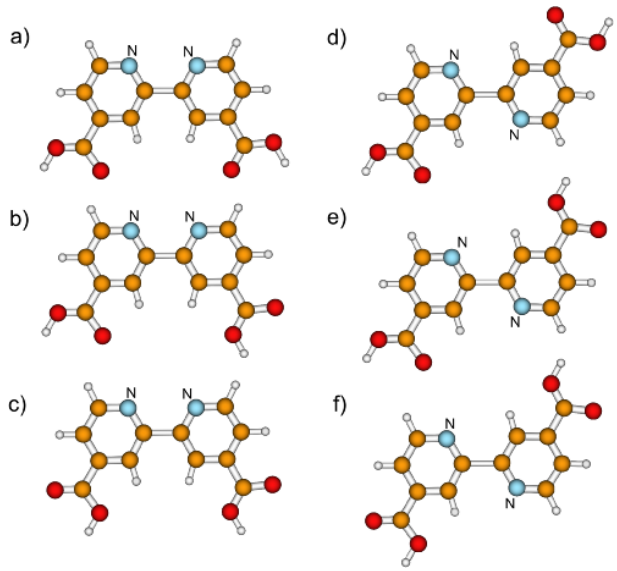

FIGURE 6.26: The six possible isomers of biisonicotinic acid adsorbed on a surface such that the plane of the pyridine rings is in the plane of the surface. Rotation can occur about the C—C bond between the two pyridine rings, and also about each C—C bond between a ring and the attached carboxylic acid group. a)-c) *cis* configurations and d)-f) *trans* configurations.

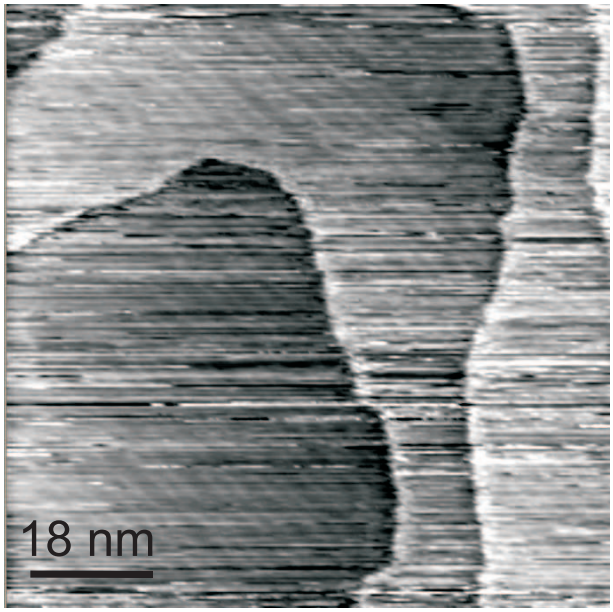

FIGURE 6.27: Biisonicotinic acid on Au(111) taken at -2V bias, 0.05nA tunnel current. No molecules can be clearly observed in this image. The image is streaky as if any adsorbate molecules are being dragged by the STM tip due to being mobile or loosely bound. The $22 \times \sqrt{3}$ reconstruction of the gold surface is resolved.

possibility for functional groups to rotate about single bonds in three places in a molecule. DFT calculations in Spartan'02 within the B3LYP model with a 6-31G* basis set show the two main isomers (*cis* and *trans*) to be very similar in energy (both are -871.7 ± 0.1 eV) and both are stable. Once adsorbed onto a surface each biisonicotinic acid molecule can essentially exist as one of six possible isomers as shown in Figure 6.26. Rotation is possible about the C—C bond joining the two pyridine rings, and about the two C—C bonds between the pyridine rings and the carboxylic acid groups. Thus a single ordered phase cannot readily form.

6.9.3 STM of biisonicotinic acid on Au(111)

Biisonicotinic acid was deposited for 2 minutes at 210°C onto a 150nm gold layer on mica. The samples prepared were all very difficult to obtain a clear image from. A range of both positive and negative biases were employed and the most stable imaging was found to be when using -1.0 to -2.0 V bias. Typical images obtained are shown in Figures 6.27 and 6.28. Figure 6.27 shows streaking in the direction of the tip raster motion. The sample may have

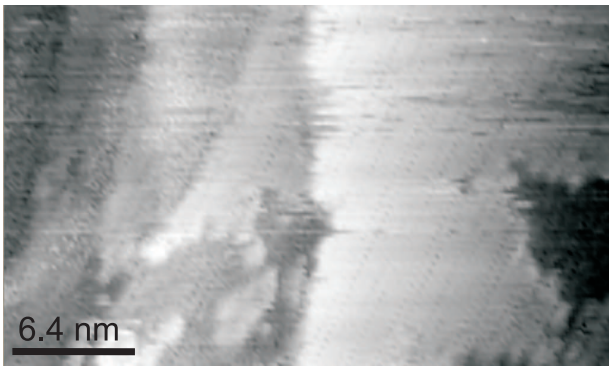

FIGURE 6.28: Possible biisonicotinic acid islands on the Au(111) surface taken at -2V bias, 0.05nA tunnel current. This image may be evidence that biisonicotinic acid can form stable islands on the gold surface though images like this were the exception rather than the rule. It may be that the molecules are bound upright on the surface and are thus difficult to image.

been difficult to image clearly because the biisonicotinic acid molecules are bonded upright on the surface, which agrees with the core level photoemission data presented in Section 6.8. Figure 6.28 is an example of an image apparently showing a molecular island, though images like this were not routinely obtained and Figure 6.27 shows a more typical image. Schnadt *et al* attempted to image isonicotinic acid on TiO_2 and found it very difficult to image clearly because the molecules were bonded upright through the carboxylic acid group [73].

6.10 Conclusions

Isonicotinic acid may be deposited onto TiO_2 to form an ordered monolayer. Depending on the growth conditions, both ordered and disordered multilayers may be grown. Slow growth conditions, at temperatures of 65°C over 30 minutes produce ordered multilayers. Fast growth conditions with a molecular deposition temperature of 130°C give disordered multilayers. Valence band spectra can be used to check for order in films by changing the tilt of the sample with respect to the incoming linearly polarised synchrotron radiation. Changing the angle of the sample changes the extent to which different molecular orbitals are probed, and in an ordered sample this gives rise to pronounced differences in the valence band spectra measured. In a disordered film no changes are observed with changing tilt angle.

Azimuthal rotation of an ordered isonicotinic acid multilayer film does not give rise to any obvious change in the valence band, even in ordered samples where tilt angle changes give different spectra. This may be due to the molecules forming small ordered domains which give a significant tilt angle dependence but not an azimuthal angle dependence. It may also indicate the preparation conditions of the substrate are not ideal and a patterned substrate allows the formation of a molecular film with little azimuthal angular order. It is also difficult to interpret spectra taken at different azimuthal angles due to stray electric and magnetic fields caused by the changes in position of the manipulator, which affects the ejected photoelectrons and a variable background count is measured.

DFT calculations can give theoretical valence band spectra in close agreement with those found experimentally. More complex theoretical studies may prove useful in determining the geometry of ordered molecular films on surfaces.

Preliminary valence band studies of biisonicotinic acid monolayers on rutile TiO_2 (110) show, as with isonicotinic acid, that the molecular orbitals of the molecules do not change significantly upon adsorption. A difference spectrum taken from a biisonicotinic acid monolayer valence band spectrum minus a clean substrate valence band spectrum is similar in peak position and intensity to the valence band calculated in Spartan'02 for an isolated molecule. Further investigations could include a tilt angle dependence study and a multilayer study in a similar vein to those performed for isonicotinic acid.

Biisonicotinic acid is known from previous work to bond to TiO_2 in a 2-M bidentate fashion through the deprotonated carboxylic acid groups. The core level photoemission results presented in Section 6.7 confirm this. From studies of biisonicotinic acid on gold on TiO_2, is can be seen that the molecules bond to the gold through the carboxylic group as on the TiO_2, as both carboxylic acid oxygen atoms are in the same chemical environment. The molecular oxygen core level photoemission peak for biisonicotinic acid bonded to either TiO_2 or any coverage of gold is found at the same binding energy of 536.7eV with the same lineshape.

STM investigations of biisonicotinic acid show on the Ag-Si(111)$\sqrt{3} \times \sqrt{3}$R30° surface that limited local ordering in overall disordered islands is present. This may be due to the many different geometries and hydrogen bonding configurations which a biisonicotinic acid molecule may adopt upon adsorption. Biisonicotinic acid on Au(111) could not be imaged clearly, suggesting it is either highly mobile, or in a geometry which is not easy to image, e.g. bonded upright as on TiO_2, which is in agreement with photoemission studies.

Chapter 7

Electrospray deposition

It is currently a great challenge in surface science and vacuum science to deposit particularly fragile or large molecules in vacuum without causing any damage to them. Molecules are usually deposited in vacuum by sublimation from a heated crucible. However, some molecules fragment or become otherwise corrupted upon heating.

The Nottingham Nanoscience group has established research programs which would benefit from a vacuum solution deposition method, including the study of dye sensitised solar cells with synchrotron radiation investigations such as those discussed in Chapter 6. In particular the deposition of large dye molecules, such as the so-called N3 dye [117], onto clean TiO_2 surfaces in vacuum would allow new experiments to be performed which could give information about the charge transfer dynamics and physics of molecular solar cells [101]. Other research interests include ordered non volatile designer molecules on surfaces, such as PTCDI derivatives with functional side chains for use in constructing functionalised molecular networks [25], and nanoparticle arrays [118], amongst other research programmes.

It can also prove difficult to deposit molecules from solution onto a sample which is to be analysed by a vacuum technique without sample contamination. For example, silicon readily oxidises in air and it is not therefore trivial to deposit molecules from solution onto clean silicon.

This chapter provides an overview of the processes which occur during electrospray ionisation, and reports how this established technique has been used here in developing a portable electrospray deposition system which can deposit, *in vacuo*, dissolved or suspended non volatile molecules onto a sample which may then be analysed by UHV techniques. The electrospray technique is widely used for research in mass spectrometry of proteins and

other macromolecules [119]. The system designed in this project is fundamentally different to commercially available apparatus, in that the chamber into which the molecules are sprayed is held at $< 1 \times 10^{-2}$ Torr during spray. The spray of molecules can then be directed through a lens system or onto a sample directly.

As an initial test of the system silicon samples with a native oxide surface were used. An electrosprayed layer of poly(ethylene) oxide (PEO) from a solution of water and methanol was formed. Also, double walled carbon nanotubes were deposited by electrospray from a suspension in ethanol. All the sample surfaces were analysed using atomic force microscopy (AFM). The electrospray system is currently in its developmental stage and should ultimately be able to deposit any molecule. We hope to use the system to deposit other materials of interest such as nanoparticles, and large dye molecules for developing molecular dye sensitised solar cells. This instrumentation development project has provided many experimental challenges, which are discussed in this chapter.

7.1 Electrospray principles

The electrospray ionisation technique was developed by John B. Fenn and co-workers [119], first presented in 1988 [120], and is now widely used in mass spectrometry. His early results showed the mass spectrum of proteins up to 40000 units molecular weight; until this point no-one had produced highly charged ions as large as this without fragmentation. It is notable that Fenn was awarded the Nobel prize for Chemistry in 2002 [121] for his work on electrospray ionisation of macromolecules (proteins). Electrospray has become a widespread technique in mass spectrometry with over 17000[1] papers published using the technique. Electrospray was patented as a chemical analysis tool using spray under low pressure, in 2001 by Sheehan *et al* [122]. There are currently no electrospray experiments reported involving the entire process from spray to deposition, which occurs in vacuum conditions, though there are systems reported in which the spray occurs in air and is drawn into a vacuum system [123, 124].

The electrospray ionisation process involves a solution with the molecule to be investigated dissolved in it. This solution passes along a capillary held at high potential, and is then drawn out into a cone (see Section 7.1.1) at the end of the capillary. A competition of forces exists between the repulsion of charged molecules in the solution and the surface

[1] Web of Science search, August 2006

tension holding the liquid together in a droplet. At a critical point (close to the Rayleigh limit) the cone of solution explodes in what is termed a "Coulomb explosion". These resultant droplets of solution move away from the emitter along the potential gradient of the system whilst fragmenting and desolvating (see Section 7.1.2), to finally leave the molecule of interest, for analysis or deposition. Several excellent and extensive review articles have been published on the subject, by example by Gaskell [125] and Vestal [120]; a textbook by de Hoffmann and Stroobant is also available [126]. In this thesis the aim is to just outline the essential points describing the entire electrospray process.

7.1.1 Taylor cone and spray formation

A solution of molecules is prepared and one end of a long capillary tube is placed in the reservoir. The other end of the capillary has an electrospray tip, or emitter, attached. Solution moves along the capillary to the end of the electrospray tip and is drawn out, ideally into a Taylor cone shape, before a jet of solution forms. The Taylor cone is so called after G. Taylor who reported the phenomenon in 1964 [127], long after it had been noted by Zeleny in the 1930's [128]. The Taylor cone has an active tip from which solution can be ejected into a jet under the necessary conditions. The different modes of spray which can be ejected from a Taylor cone have been systematically studied by Cloupeau *et al* [129–131]. The spray mode adopted is dependent on many factors including the solvent volatility and viscosity, solution flow rate, and tip potential. Other phenomena can also affect the spray. It has been reported [120] that a coronal discharge can be observed at lower negative potentials, which is a problem with the electrospray/atomisation of liquid metals. Usually in air electrospray a sheath gas flow is used around the tip to prevent this. In vacuum electrospray the electric field is not limited by the appearance of these coronal discharges [129].

The magnitude of the potential applied to the electrospray tip directly affects the shape of the liquid cone formed at the end of the tip. At the lowest voltages several dripping modes are observed; the study of these phenomena are usually carried out with the tip pointing downwards rather than using a horizontal geometry to prevent the tip becoming excessively wet. At higher, but still relatively low voltages, a spherical drop forms at the end of the tip. Increasing the potential further elongates the drop due to an increased charge being held there. At the critical onset voltage the Taylor cone forms, then as the surface

tension cannot hold the like charges together in the liquid any longer, a spray forms as a cone-jet emitted from the end of the cone. The point at which the surface tension of the droplet is balanced exactly by the charges in the droplet is the Rayleigh limit [132], given in Equation 7.1.

$$q^2 = 8\pi^2\epsilon_0\gamma D^3 \tag{7.1}$$

q is the total charge held in the droplet, ϵ_0 is the permittivity of air, γ is the liquid surface tension, and D is the droplet diameter.

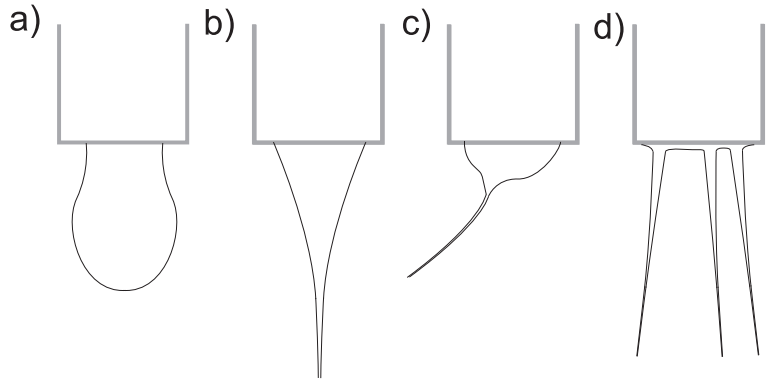

FIGURE 7.1: Cone formations (adapted from [129]) a) a dripping tip at low voltage, b) a Taylor cone with jet, c) an asymmetrical cone and d) multiple jet formations.

A single emitted jet can vary in length, diameter and direction. Further increasing the potential applied to the electrospray tip can facilitate the formation of both primary and satellite sprays (forming outside the radius of standard spray), unstable kinked and branched jets, and at the highest potentials where spray is still permitted, several cone jets can exist at the end of one tip in a multi jet mode, though this mode is unstable. Some cone formations are shown in Figure 7.1. It is clear that many different spray modes may be achieved in these electrospray systems and much effort has been employed in understanding the physics, both experimental and theoretical, of these phenomena.

The resultant jet of fluid breaks up into a series of droplets. Gomez and Tang [133] investigated electrostatic sprays of heptane before electrospray mass spectrometry became a popular technique. They photographed Coulomb fission of heptane droplets from "conical protrusions" on the droplet surface which produced a stream of equisized smaller offspring droplets. Figure 7.2 shows one such droplet in the process of exploding. The droplets

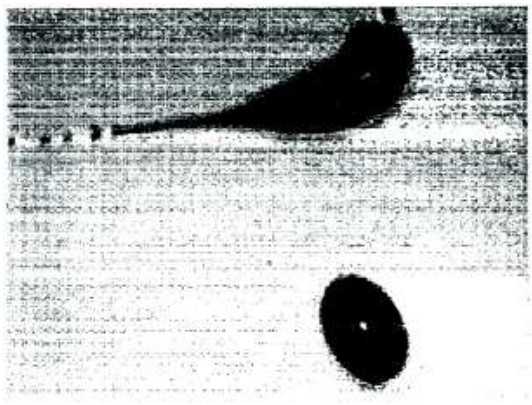

FIGURE 7.2: A Coulomb explosion from a droplet resulting in a series of droplets from a conical protrusion on the droplets surface (after Gomez and Tang [133])

were produced during electrospray in the "cone jet" regime, from a Taylor cone similar to that shown in Figure 7.1b), which is believed to be the most stable cone-jet mode for electrospray. They noted that the electrosprayed cloud of droplets existed in two regions, a primary inner cloud and an outer shroud of satellite droplets which dispersed readily due to Coulomb repulsion. They also noted that droplet rupture can form at only 70 - 80% of the Rayleigh limit. This work was the first of its kind involving photography of droplet formation events.

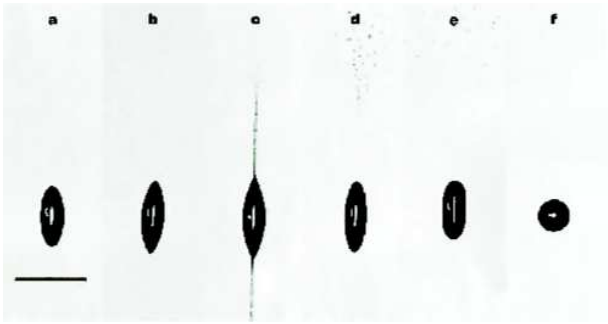

FIGURE 7.3: Evolution of a droplet. In the third image (c) the jets have formed, and in (d) they explode into microdroplets (after Duft *et al* [134]). The scale bar is $100\mu m$.

Taylor cones, and 'jet spray' phenomena have been investigated by Duft *et al* [134, 135]. They photographed an isolated droplet of ethylene glycol (using high speed microscopy) evolving as it becomes charged beyond the Rayleigh limit, shown in Figure 7.3. The droplet gradually becomes unstable as neutral molecules evaporate, and jets form and

explode into a cloud of droplets. They find that about 100 daughter droplets form from each jet, carrying about one third of the total charge of the system and are about 0.3% the mass of the initial droplet.

7.1.2 Desolvation of ions

After the Coulomb explosion, the cloud of droplets continues to explode and break up due to Rayleigh instabilities, and the droplets become smaller as loosely bound solvent molecules evaporate from the droplet surface. Along the path from the electrospray tip to the sample, the molecule of interest is protected by solution, so it can ultimately be deposited without becoming damaged [136]. The exact nature of the desolvation process is still debated to some extent. The initial studies of desolvation in electrospray were performed by Iribarne and Thompson, who studied desolvation and the electrospray process from both a theoretical [137], and from the mass spectrometrist's view [138]. They describe an ion evaporation model (IEM) which states that the surface of a charged droplet has an electric field such that an individual molecular ion can be lifted from the droplet surface and ejected into the gas phase. This is thought to occur for droplets smaller than 10nm in diameter, and droplets with a higher proportion of charged species are more likely to desolvate by this method. This theory takes account of droplets formed by atomisation rather than electrospray, so any external field is not accounted for. The other model commonly used for explaining the desolvation of a droplet into individual charged species is the Charge Residue Model (CRM). This model, first proposed by Dole *et al* [139] for neutral macromolecules and later published by Röllgen *et al* [140], explains the production of gaseous species from electrospray by repeated Coulomb fission. They believe that a sequence of Rayleigh instabilities leads to subsequent Coulomb fission events, and these smaller droplets repel each other and split further, ultimately leaving a spray of fine droplets containing only one molecule. The generation of ions in electrospray is still debated and the actual desolvation mechanism could well involve processes described by both of these models.

7.2 Current applications

This section gives examples of electrospray used as a deposition technique for novel applications, particularly with large biological molecules rather than detailing any of the extensive mass spectrometry research performed using the technique.

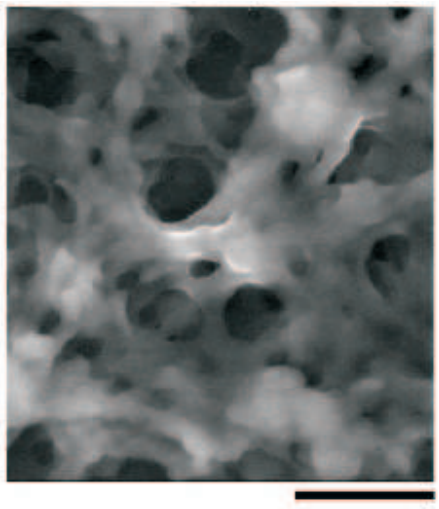

FIGURE 7.4: Electrosprayed α lactalbumin cross linked with glutaraldehyde. A porous structure is seen, and biological activity is retained. Scale bar = 0.75μm (after Uematsu *et al* [141]).

Uematsu *et al* [141] deposited the protein α-lactalbumin using a commercial electrospray deposition system in dry air (see Figure 7.4). The protein thin films were then cross linked with glutaraldehyde vapour. SEM and AFM images of the resulting structures reveal a porous film morphology. Different film structures were observed depending on solution concentration, with decreasing pore size as the concentration of the spray solution increases. The films were tested mechanochemically using Ca^{2+} ions, and responded as expected, demonstrating the biological activity is preserved during the electrospray process. This research has applications in biomaterials and demonstrates the applicability of electrospray as a deposition tool for proteins.

In a similar biological experiment Morozov *et al* [143, 144] used the electrospray deposition technique to create biologically active arrays. By electrospraying proteins labelled with different radioactive isotopes from solution through a dielectric mesh onto a slightly charged substrate, a bioarray was formed. The protein dots were stabilised by cross-linking with glutaraldehyde vapour, and the biological functionality of the molecules was retained. Further investigations include studying different electrosprayed polymers and DNA on mica, and imaging of the morphology of these samples using AFM [142]. They found they could observe globular and fibrillar structures by changing the concentration, solvent, or ion charge. Increasing solution concentration allows for the observation of glob-

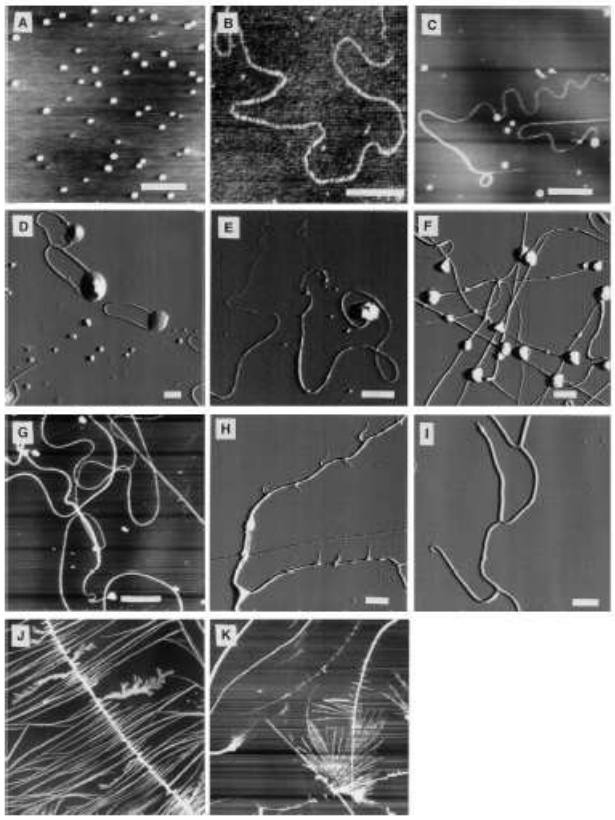

FIGURE 7.5: Structures observed by AFM from electrosprayed polymers. A - PEO globules; B - part of a PAM strand; C - l-DNA fibres; D - pins of l-DNA from image C; E - Pins of PVP; F -"beads on a string" from PEO; G - electrospun PAM fibres; H - branched PAM fibres; I - branched PVA structures; J - large dentritic structures from PEO on mica; K - Whisks and fibres of PEO on mica. PEO - poly (ethylene) oxide, PAM - polyacrylamide, PVP - polyvinylpyrrolidone, DNA - deoxyribonucleic acid, PVA - polyvinylalcohol. A, B, D, E scale bars are 0.5μm, other scale bars are 1μm (for full details see [142].)

ules, larger globules, and extended structures. Further increasing the concentration produced complex fan shapes and "beads on a string" structures. This research demonstrates how surface morphology depends on the experimental variables such as solvent type, tip potential and solution concentration. Some of the structures observed are from very concentrated solutions where the polymers are not strictly electrosprayed but are deposited by "electrospinning". See Figure 7.5 for details of the many morphologies observed.

Ku and Kim [123] have used electrospray in vacuum with glycerol solution to investigate droplet size distribution with a freezing method. They find the spray current depends on the applied tip voltage and the flow rate of the liquid, and that the Taylor cone

has a cusp shaped tip, allowing a thinner jet emission and thus smaller droplet formation. The pressure range is below 1×10^{-3} Torr, in a single chamber system. They found spraying in vacuum to be more stable than in air as determined by the onset of corona formation with tip voltage. They chose to spray in vacuum to reduce coronal effects and note that not all liquids can be sprayed in vacuum due to their volatility, and that those with a high surface tension, such as viscous glycerol, are the most suitable. They use a backing pressure to push the glycerol solution through the tubing to the tip. They also explain that the surrounding density of air and thus the mean free path affect the spray considerably, through a consideration of coronal onset.

Rauschenbach *et al* have developed an electrospray system for the deposition of molecules and clusters in vacuum [124]. They create an ion beam by injecting the solution into a chamber in ambient conditions which makes use of a gas flow and a high potential counter electrode to produce the ion beam. This beam then travels through various pumping stages, two quadrupoles and two lens systems before deposition. They use this method of creating the spray of solution as it ensures the ions do not reach the target with too high a kinetic energy, because if their energy is too great then the molecules can fragment on impact. They demonstrate their technique by depositing gold clusters onto graphite where they are observed to adsorb onto step edges. They also deposit bovine albumin serum, which forms a fractal structure.

7.3 Our electrospray system

The electrospray deposition system developed in this project aims to overcome the problem of fragmentation or corruption of large or fragile molecules during vacuum deposition, and facilitate the vacuum deposition of molecules which are usually held in solution (such as nanoparticles). The system is also designed so that the entire electrospray process occurs in vacuum. The vacuum system has been developed with portability in mind; the whole system is modular with chambers of inner diameter $\sim$ 60mm which can easily be transported. This enables it to be taken easily to other vacuum facilities such as synchrotrons or STM chambers. Since the apparatus is in its developmental stage, the chambers are designed such that any changes to the system are relatively easy to make. Figure 7.6 shows a schematic of the nanospray system.

A 3m length of polyetheretherketone (PEEK, a vacuum-compatible flexible plastic)

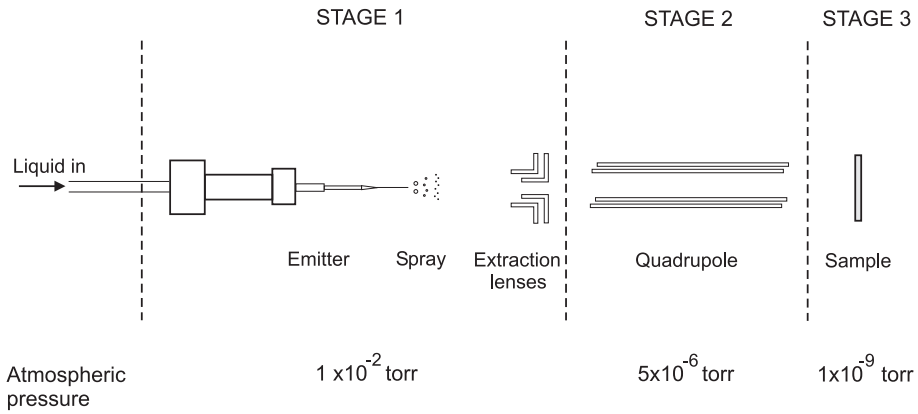

FIGURE 7.6: Schematic of the vacuum nanospray deposition system. The tip is held horizontally and spray is directed along a potential/pressure gradient through a set of electrostatic lenses. A mass quadrupole is available but not yet commissioned. The sample can be placed at various points along the system. Differential pumping allows the pressure in the different chambers to reach the values noted.

tubing (0.005"ID, 1/16" OD, Supelco) connects a reservoir of nanospray solution to a 20cm stainless steel capillary (0.005"ID, 1/16" OD) through a custom-made vacuum flange into Stage 1. The PEEK tubing has a 2μm filter on the air side so that dust particles cannot enter the tubing and cause a blockage. The reservoir can be pressurised using dry nitrogen gas to help push the solution through the tubing. The solution consists of either 25% pure water and 75% methanol, or 50% pure water and 50% methanol, and the molecule of interest to be sprayed. Stage 1 is maintained at a pressure of 1×10^{-2} torr during spray and lower than 1×10^{-3} torr without spray by a $70Ls^{-1}$ turbomolecular pump backed by a scroll pump.

The steel capillary inside the first vacuum chamber has an electrospray needle (tip) mounted on the end using a microtight PEEK fitting (Upchurch Scientific) to connect the two. In commercial systems the capillary and emitter have a sheath gas flow at low flow rate around them to limit the dispersion of the spray [125, 126] and prevent coronal discharge. The gas flow is not present in this system as the electrospray process occurs in vacuum and coronal discharges are therefore suppressed at a low enough pressure. The custom-made feedthrough flange also has an electrical feedthrough connection for a high voltage wire to be connected to the tip. The capillary and tip are mounted on a 3-way manipulator for accurate tip positioning.

The electrospray process itself occurs at the end of the emitter which is held at a

high potential (2-3 kV). Due to the intense electric field formed here, the solution becomes charged as it reaches the tip. The fine electrospray droplet plume produced at the end of the tip is thus also charged, and is attracted to the grounded sample, while the droplets continue to desolvate. The spray can pass through an electrostatic lens system, the purpose of which is to focus the ions into a narrow beam before reaching the sample, and also to act as a small aperture between the two separately pumped vacuum chambers to maintain a low pressure in Chamber 2. Currently the lenses are not used to focus the ions as the potentials required for the lenses to be effective are difficult to determine. This may be because the ions are travelling too fast to be focussed effectively and the spray is sensitive to potential changes nearby. For the experiments described later in this chapter (Section 7.5) the sample is usually either positioned in front of the lenses for deposition, or just behind them for a lower pressure environment. Differential pumping can allow a pressure of $\sim 1 \times 10^{-2}$ Torr during spray in the initial chamber and in the second chamber the pressure can reach $\sim 1 \times 10^{-5}$ Torr.

The sample can be mounted on a linear drive, in front of or behind the lenses, to change the tip-sample distance. To check a spray is being formed, the sample (or other target used for measuring the incident ion current) is attached via an electrical feedthrough to a Keithley picoammeter. A LabVIEW program has been developed to plot the current from ions hitting the target against time (Section 7.4). The ion current can actually be accurately measured and plotted in real time from many points along the nanospray system, including the extraction lenses and quadrupole rods, allowing the spray current to be tracked. We can use this information to optimise the potentials applied to the tip and lenses and the tip position for a reliable spray.

Stage 2 also has a $70Ls^{-1}$ turbomolecular pump, can house a mass quadrupole (ABB Extrel) and is separated from Stage 1 by the electrostatic lens system. The lenses have a 3mm diameter orifice for focussing the ion beam (a lens system with a 6mm diameter hole is available too but using this results in a higher overall pressure in Stage 2 due to the larger aperture). During spray the pressure in Stage 2 is below 5×10^{-6} Torr due to differential pumping. The differential pumping allows the whole nanospray system to be attached to a UHV chamber such as a synchrotron end station, which forms Stage 3, and a pressure of $< 1 \times 10^{-9}$ Torr is maintained in this final stage during spray.

7.3.1 Choice of emitter

There are many types of emitter available commercially for electrospray use. Usually borosilicate glass or fused silica glass tips are used [145,146] as these are cheap and relatively robust. We have used this type in our system, which have an aluminium coating on the outside of the emitter (apart from the sharp end of the tapered tip) to allow them to have a high potential applied. These have an inner diameter of $30\mu m$ and flow rate of 300-1000 nL/min (SilicaTips are obtained from New Objective [147]). A new type of stainless steel emitter developed by Ishihama *et al* [148] has also been used which gives a reliable performance over 1000 hours use, gives a wide flow range of between 50 and 1500 nL/min, may be cleaned using sonication, and have a low risk of blockage [149]. These have been used in electrospray under vacuum conditions by Ku *et al* [123] and used in this project also. Both emitters have been successfully used here, but the stainless steel ones are favoured for vacuum work as the inner diameter ($\sim 20\mu$m) is much smaller than other emitters, allowing for a lower pressure to be maintained whilst spraying. The flow rate of $100\mathrm{n}L\mathrm{min}^{-1}$ allows for a small spray to be produced, thus allowing the chamber pressures to remain sufficiently low to allow UHV conditions in Stage 3. A voltage of 2.5kV applied to a stainless steel tip was found to produce a steady ion current. The stainless steel tips are too small to easily see a spray forming through a vacuum chamber window, thus it is not trivial to observe the Taylor cone or spray mode at the end of the tip. The spray mode and reliability were monitored using the measured ion current and the LabVIEW control program.

7.4 Computer control

A LabVIEW program was developed to measure the electrospray ion current, and is summarised in the flow diagram in Figure 7.7. It allows the simultaneous measurement of ion currents to allow the real time monitoring of the vacuum electrospray performance, and also allow the Keithley picoammeter/source to act as a voltage source if required (for the mass quadrupole). The program follows the following procedure.

To take current readings, the Keithley is initialised for measurement. The program continuously reads the current measured by the Keithley (which corresponds to a reading every $\sim$ 1s), and also measures the time elapsed since the start of current measurement, by measuring the start time, then adding on the times taken for each subsequent loop of the `for` loop. This loop runs until the `on/off` selection is made (i.e. measurement is stopped).

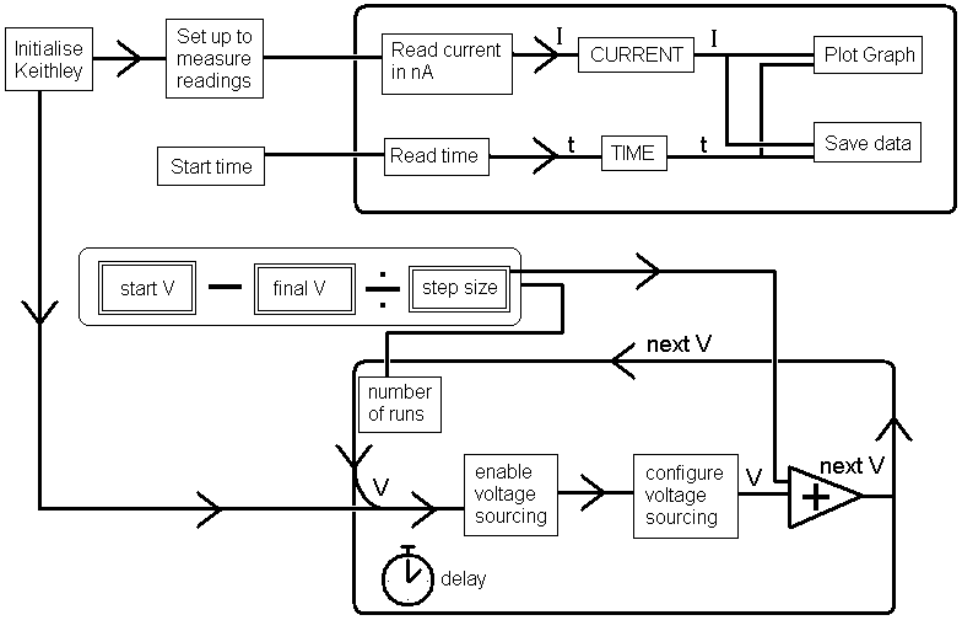

FIGURE 7.7: This schematic shows the main sections of the LabVIEW VI used to control the mass quadrupole of the electrospray. The top section reads in the current, and the bottom controls the voltage sourcing.

The current against time graph is plotted in real time, and the data is saved to a file also as the program is running. This program makes it easy to measure the spray detected on the sample whilst parameters are changed in the electrospray system.

To send out voltages (which can be used to control the mass quadrupole at a later stage), the program first enables the Keithley for voltage sourcing. The user, prior to measurement/sourcing, must enter the required start and end voltages, and a voltage step size. The program uses these to send out a voltage for a preset time (set in the `delay`). As the loop repeats, the voltage is increased by a step size (shown by the `add` node.) The number of times the voltage `while` loop runs is calculated from (`startV` − `finalV`) ÷ `step size`. This lower part of the program was tested by attaching the output to a digital multimeter to check the voltage outputs and can be disabled if no voltage control is required. Also, all sections of the program have error handlers associated which show if the program is running correctly.

An example current reading is shown in Figure 7.8. The current was detected on

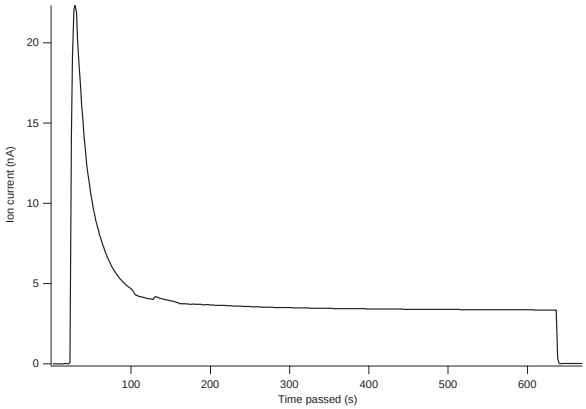

FIGURE 7.8: Spray current from water/methanol solution with 1% acetic acid. The spray starts at 25s and ends at 645s when the potential is removed from the emitter.

a target in front of the lenses using a water/methanol spray solution with 1% (by volume) acetic acid added. The target was in air, rather than vacuum, with a tip potential of 2.8kV. After 25s, the electrospray process begins and the ion current rises to 23nA. The current then falls exponentially to a steady current of 3.5nA before the potential is removed from the tip at 645s and the current falls to zero immediately.

7.5 Electrospray deposition of PEO

7.5.1 Blank solution

Initial test sprays were performed using methanol/water mixtures containing acetic acid, to determine the parameters required for a steady ion current. During spray the tip position could be changed using a manipulator and the potential applied to the tip could be altered to obtain a steady high current. These tests with "blank" solution are useful indicators of the performance of the system, i.e. that liquid is passing through from the reservoir to the sample, and that ions can pass through the lenses. In order to try and maximise the ion current detected during early development, a salt solution of copper sulphate in water/methanol solution was prepared and sprayed. However, salt solutions such as this are not suitable for electrospray in this system. The salt tends to accumulate at the end of the tip and blocks it up. It was often the case that a visible salt crust had built up at the end of the tip preventing further fluid flow. After determining how to obtain a steady spray current, the experiments were repeated using a solution of polyethylene oxide (PEO)

Table 3: Summary of PEO samples

Sample	Emitter voltage (kV)	Time (mins)	Conc^n (μ M)	Tip-sample sep^n (cm)
I	2.5	15	2.4	4
II	2.5	15	2.4	7
III	4	15	2.4	4
IV	2.5	5	25	4

The table summarises the different conditions used for PEO on silicon samples. Sample I is an example of optimal spray conditions, Sample II has a larger tip-sample separation, Sample III uses a high emitter potential and Sample IV uses a high concentration solution.

and using silicon as a deposition target.

7.5.2 PEO electrospray - Method

Tests using polymer solutions were performed in order to ensure that the solution containing a large molecule of interest (the polymer) was passing through the electrospray emitter and adsorbing onto a sample positioned in front of the lenses. A polymer was chosen as the "marker" molecule as polymers are easily prepared macromolecules, and can be observed under AFM. It was thought that changing the spray parameters may change the morphology of deposited films (see Ref. [142]). Solutions of 100,000 amu poly(ethylene) oxide (PEO) in methanol/water blank solutions were electrosprayed onto silicon substrates (prepared by ultrasonic cleaning in propan-1-ol). Two concentrations of PEO were used, a weaker one of 2.4μM and a more concentrated solution of 25μM. Blank solutions were made of either 25% pure water and 75% methanol, or 50% pure water and 50% methanol. The voltage applied to the electrospray tip was either 2kV or 4kV. Table 3 summarises the different conditions under which each sample was prepared in vacuum. Two PEO samples were prepared in air as well as under vacuum conditions for comparison (Figure 7.9). A drop-deposited sample was prepared by pipetting a drop of 2.4μM PEO solution onto a clean silicon sample. AFM images reveal amorphous blobs of polymer, quite different to any of the nanosprayed samples.

7.5.3 PEO sprayed in air

On samples prepared in air, only beads of polymer are present. A potential of 2kV was applied to the stainless steel emitter and the samples were observed to be covered with polymer beads $\sim 20\mu m$ in diameter, as imaged with an optical microscope, shown in Figures

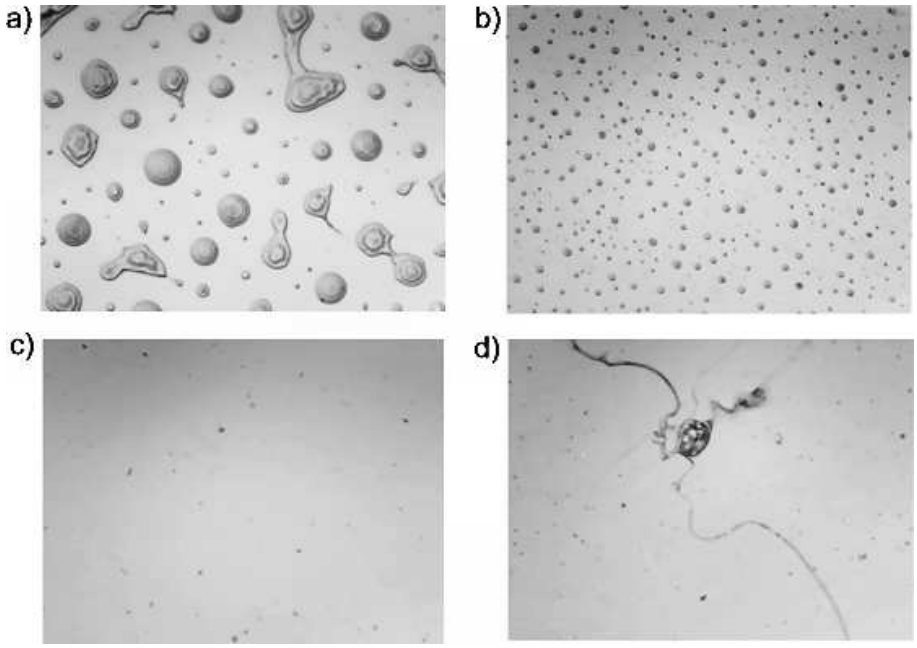

FIGURE 7.9: Optical microscope images taken under 100x magnification. All images are the same scale. a) Sample prepared in air for 2h with 2.4μM solution; b) Prepared in air for 15 mins with 2.4μM solution; c) Prepared in vacuum with 2.4μM solution for 15 mins; d) Prepared in vacuum with 25μ M solution for 15 mins; extruded polymer is visible.

7.9a) and b). One sample was lightly scratched and studied again, and the area showed dragged polymer-like marks, indicating that the beads observed were indeed PEO and not solution or contaminants. Also of interest is the size of beads in the 2 hour and 15 minute depositions in air. The increased size of beads in the 2 hour sample, as opposed to the increased uniform coverage of the sample, indicates that the polymer aggregates into beads after reaching the surface. Also, some of the larger beads in Figure 7.9a) have begun to merge together. We believe the droplets have formed during a de-wetting process on the surface, indicating perhaps the molecules are not fully desolvated. In these tests however the sample is held such that the spray moves directly from tip to sample without passing through the lenses/aperture. The studies described in this chapter are intended to show that material can be electrosprayed at a low pressure and that changing the electrospray tip potential can change the morphology of the resultant samples.

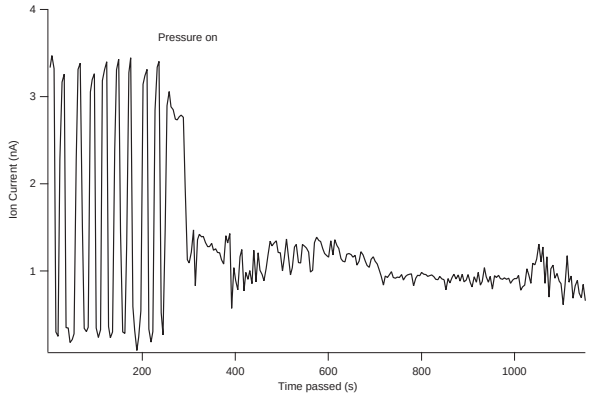

FIGURE 7.10: Spray current from water/methanol solution with PEO. The spray is not a steady value but is consistently non zero, thus material is being deposited. At 270s, the backing pressure is applied to the solution reservoir and the spray is much more stable (a steadier current is maintained around 1A).

7.5.4 PEO sprayed in vacuum

Under vacuum conditions (1×10^{-2} Torr), nanosprayed beads are too small to be observed under an optical microscope (Figure 7.9c)), and the largest are $\sim 0.6 \mu m$ in diameter as measured from AFM images. The beads are present alongside many other structures, formed under various spray conditions, as illustrated in Figures 7.11, 7.12 and 7.13. The spray conditions used to produce these different samples are summarised in Table 3. A current plot for Sample I is included in Figure 7.10. It is rather erratic, but this is typical of the ion current plots obtained when spraying solutions containing molecules. It was found in these tests that the application of a backing pressure to the solution reservoir often gave a steadier spray current. Ku *et al* [150] also use a backing pressure in their vacuum deposition experiments.

For Sample IV long polymer fibres were seen under an optical microscope with $100\times$ magnification. The formation of these extruded polymer fibres is attributed to the high solution concentration giving rise to a form of electrospinning phenomenon, in agreement with Morozov *et al* [144]. The fibres may form in the emitter and capillary because the solution evaporates in the vacuum chamber faster than it can be sprayed. Large fibres are formed inside the tubing and are expelled in a burst from the emitter (Figure 7.9d)). This is also evident by examining the plot of current with time for this sample; rather than a steady ion current, an unstable current is measured with time, with some periods

of steady current but other times with no measurable spray. The emitter perhaps becomes temporarily blocked with polymer when the fibres form, thus no current can be measured on the sample when there is no spray being produced.

Beads

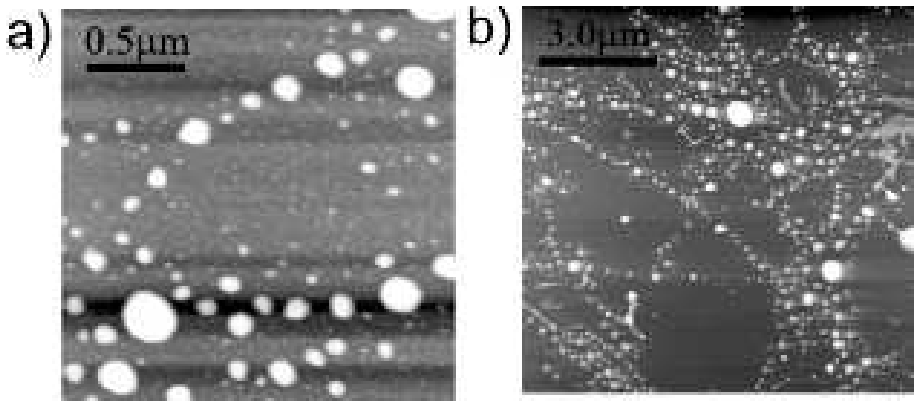

FIGURE 7.11: Bead formations on vacuum electrosprayed samples. a) Disperse beads from Sample I, b) Beads were observed to form lines on the surface, and bare patches can be observed next to covered areas (from sample IV).

Beads of polymer observed on vacuum deposited samples exist as illustrated in Figure 7.11. Bead distributions were either quite random, as in Figure 7.11a), or they appeared to follow some lines on the surface, shown in Figure 7.11b). The beads were also of different sizes, and some areas on the sample show no polymer beads at all. One cannot observe a uniform coverage of beads as in the air-prepared samples. Lines of beads may form from droplets adhering to an area of the sample which has been marked in some way, during cleaning or mounting. The lines may also be formed from beads being joined together by polymer fibres too thin to be resolved with AFM. Also beads may adhere to areas of higher defect density, and the silicon will have localised areas of different hydrophobicity. Lines may also appear if a droplet bursts on the surface, creating 'splash' lines marked by PEO beads. The top of Figure 7.11b) looks similar to a cellular network [118]. This may be due to a de-wetting mechanism of droplets of solution drying on the surface, perhaps indicating that the molecules of interest are not fully desolvated before contacting the sample.

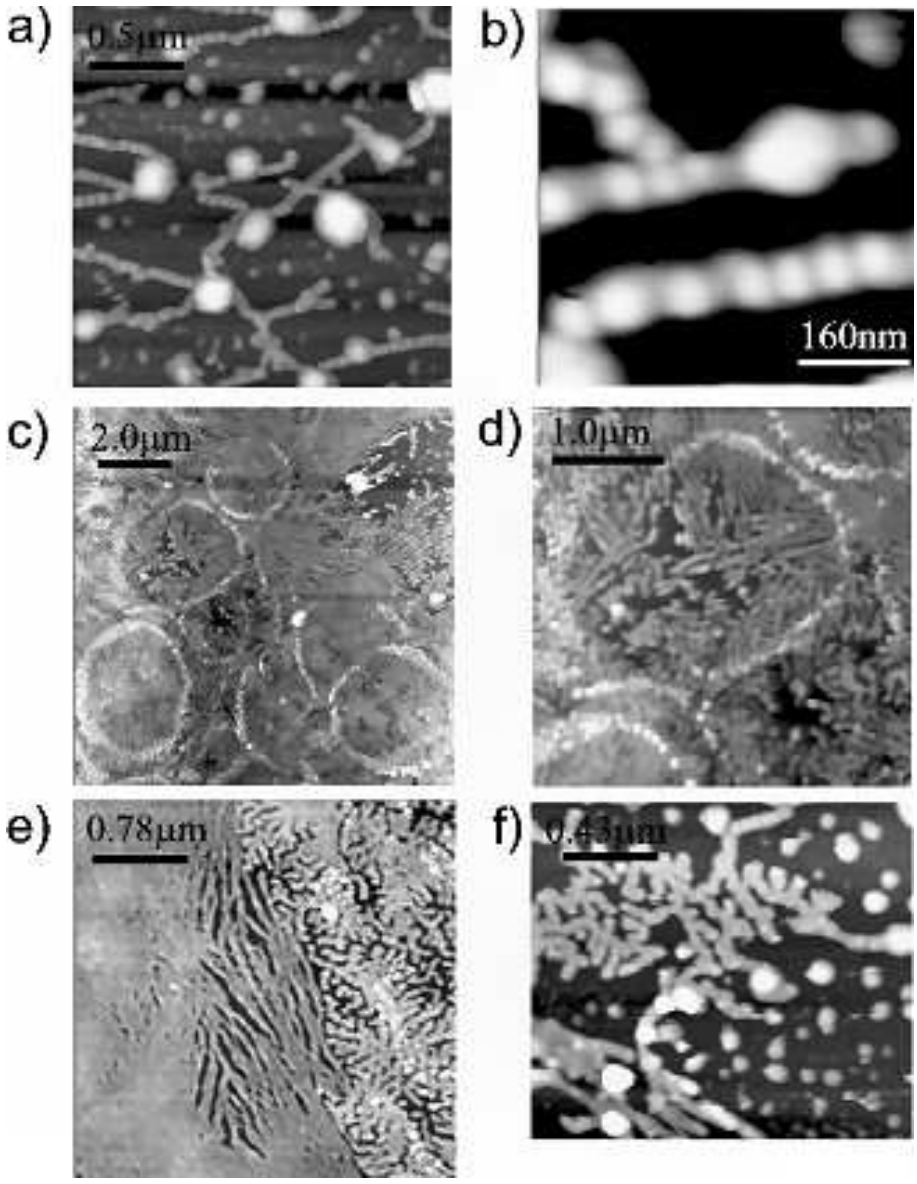

FIGURE 7.12: Varied morphologies of polymer strings a) Open strings with beads (sample III), b) PEO row formed from joined up beads, c) Strings radiating from points give star-like structures (sample II). The circular forms on top are discussed in the text, d) Close up on c) showing the star-like formations and the circular marks on top, e) Complete coverage on the left, with linear rows and closely spaced irregular rows on the right (sample III), f) Close up on irregular rows made from beads as in b)(sample III).

Strings

Figure 7.12 shows string-like formations of polymer on the surface, all of different morphologies but with a characteristic width of $\sim$ 80nm. Figure 7.12a) shows isolated strings with

beads of polymer on top. These strings appear to be composed of many beads of polymer (Figure 7.12b)) which have joined together to form a line, and these strings are joined at vertices marked by larger beads of polymer. In contrast, the strings in Figures 7.12c) and d) are linear, and they spread out from a central point to make star shapes. These rows also appear to be formed from small beads which have combined to form linear structures. Figure 7.12e) shows straight strings all lying in the same direction closer to an area of total coverage. The right of this image shows irregular short strings, shown in Figure 7.12f). Here, the strings are much more closely packed than in Figure 7.12b) but neither seem to lie along any preferential direction, and again they are comprised of many joined up beads. None of these structures appear to have formed from any well-known de-wetting process on the surface, and so perhaps they form before reaching the sample due to the electrospray process.

The circular features in Figure 7.12c) and d) appear to sit on top of the strings of polymer. They may form when droplets of electrospray solution, which are not fully desolvated, reach the sample and explode, leaving a polymer "residue" appearing as circular marks.

Dendrites

Figure 7.13a) shows a large area scan of Sample IV made using 25μM solution, and has areas which are shown in more detail in Figures 7.13b) and c). Figure 7.13b) shows an area of sample with a high coverage of polymer giving a rough appearance with features up to 25nm high. Figure 7.13c) shows areas with a lower coverage giving the polymers a dendritic appearance on the surface, quite different to the string features described above, as there is no characteristic width to the rows and the polymer is flatter (15nm high) than the bead-like string features. Figure 7.13a) shows how these two features, the dendrites and the rough coverage, probably form from the same mechanism but appear differently depending on the coverage. It is important to consider that the coverage was inhomogeneous across all samples. Figure 7.13d) is rather different; this shows a dendritic area of PEO with no surrounding material, unlike the other images. This appears to have formed from a diffusion limited aggregation mechanism after the solution has reached the sample. This sample was made at high voltage (4kV). Note we cannot rule out that this type of feature has not formed on samples prepared at a lower emitter voltage, but images of this were not

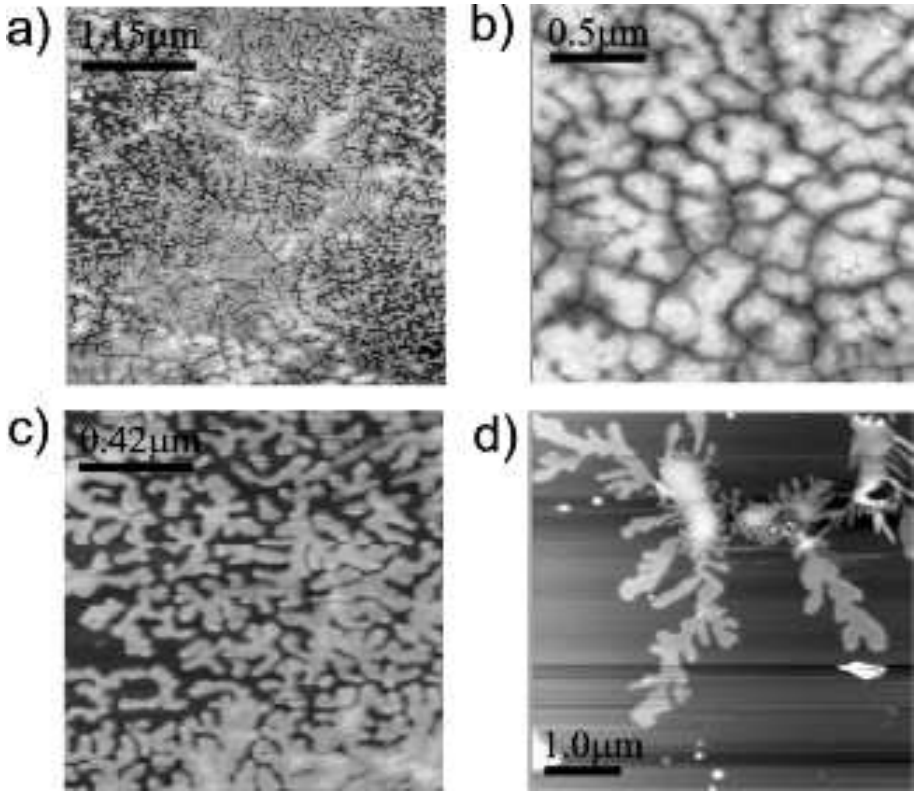

FIGURE 7.13: Dendritic structures formation. a) Large area image showing rough covered areas (bottom) next to curvy dendritic structures and bare silicon (sample IV) b) Close up on rough coverage, c) Close up on curvy dendritic structures, d) Isolated dendrite, of different appearance to those in c) (sample III).

obtained.

7.6 Electrospray of carbon nanotubes

Carbon nanotubes are an allotrope of carbon recently discovered by S. Iijima [152], which were discovered using an arc-discharge evaporation method similar to that used for fullerene synthesis. They essentially consist of a graphene sheet rolled up to form a tube, with carbon caps at either end much like a half-fullerene molecule. Figure 7.14 shows how the way in which the graphene sheet is rolled affects the arrangement of carbon atoms in different types of nanotube, which have different properties. Nanotubes can exist as single walled (a single layer), or multi-walled, with several coaxial nanotube layers nested together. They have many unique mechanical, chemical and electronic properties, and have been widely

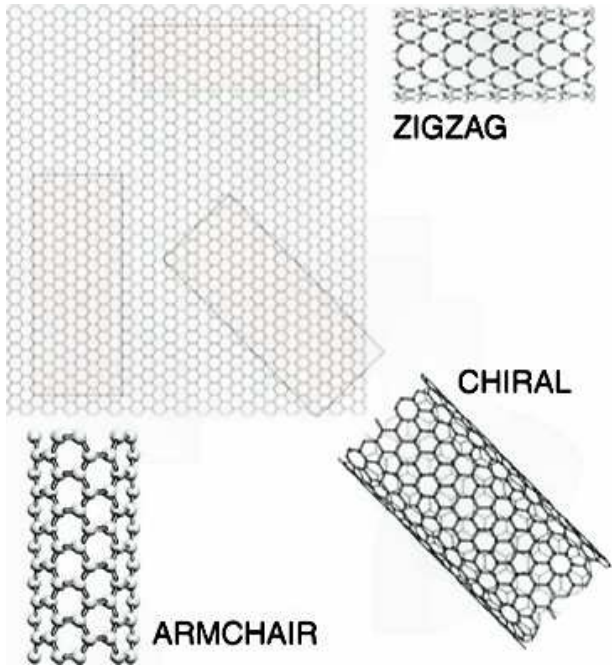

FIGURE 7.14: Schematic of different types of carbon nanotube (from [151]).

studied [153]. They were used in this electrospray project as an example of a large molecule for electrospray deposition, and we were interested to see if nanotubes could survive and be deposited using the electrospray process in the apparatus built here.

Double walled carbon nanotubes (DWNTs) were made available in a solution of ethanol for electrospray. DWNTs are not usually held in aqueous solution but in strongly non-polar solvents such as toluene. In this case the DWNTs were "suspended" in this ethanol solution by sonicating the beaker of solution every 15 minutes to keep the DWNTs floating in the suspension. This suspension was electrosprayed onto a silicon sample with a native oxide coating, for a period of two hours of spray, with breaks to sonicate the liquid and re-suspend the nanotubes. In this case the spray passed through the lens system, which was acting as an aperture, as no voltage was applied to the lenses. The emitter was held at 2.6eV with the sample 15cm away from the tip. Figure 7.15 shows two AFM images of bundles of DWNTs on the sample. In a 10μm $\times$ 10μm scan, one bundle like those shown was usually seen. The tubes are $\sim 1 - 2\mu$m long.

This experiment demonstrates that the nanotubes pass through the 2 μm filters and electrospray system, and adsorb onto the substrate in a relatively intact manner. They

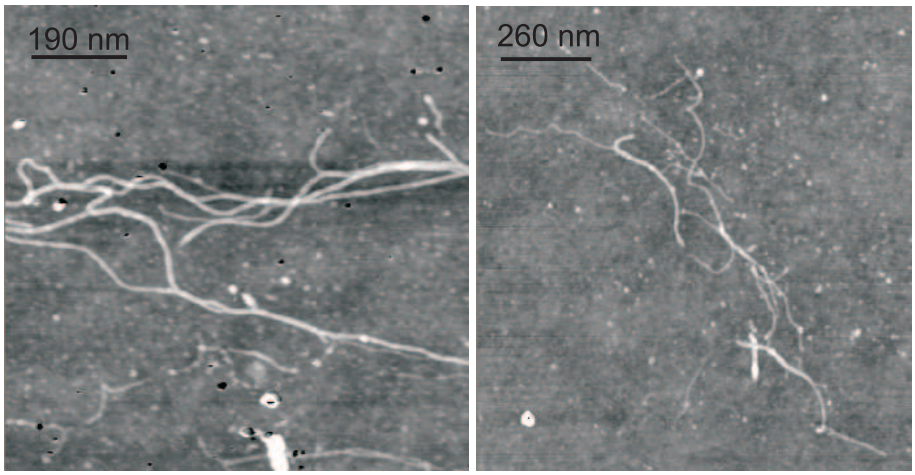

FIGURE 7.15: AFM images of SWNTs electrosprayed for 2 hours onto SiO_2 from a water/methanol suspension. The nanotubes appear in small bunches and intact.

do not appear as single isolated nanotubes which is desirable for some further experiments, but neither do they appear aggregated into large amorphous bundles which can happen with other deposition methods, such as drop deposition. Most importantly the nanotubes are not broken up into fragments on impact. It may be the case that the nanotubes imaged arrived at the sample still suspended in solution, which subsequently evaporated leaving just the nanotubes. Though we believe the electrospray travels from tip to sample very quickly (as the electrostatic focussing lenses are not yet in operation as it is difficult to have an effect on the spray), the nanotubes have not been destroyed during the deposition process. If the molecules are indeed travelling at high energy, they appear to be deposited intact. This may be perhaps that they are protected by the solution through the process.

This electrospray method of depositing carbon nanotubes is a promising technique for several reasons. Firstly, carbon nanotubes do not readily dissolve in either polar or non-polar solvents without adding some chemical functionality [154], which changes the properties of the nanotubes. Therefore it is desirable to have a method of depositing nanotubes in pristine form without any chemical changes. It is experimentally challenging to deposit carbon nanotubes in vacuum, and wet methods such as spin coating or a Langmuir-Blodgett deposition technique [155] are usually used. It is also difficult to obtain a disperse carbon nanotube film, as the molecules bunch together into large amorphous aggregates in solution. The electrospray technique described in this section allows the deposition in vacuum, from solution, carbon nanotubes onto a surface to form relatively disperse open

bunches of nanotubes. Further work in this area could concentrate on fine tuning the parameters available to form optimum molecular films, for example by changing the tip-sample distance, solution concentration, type of nanotube (single, double, or multi walled), emitter voltage, the application of a pressure on the solution reservoir, and the sonication treatment of the suspension.

7.7 Discussion

This chapter describes an electrospray system which has been developed, capable of spraying in both air and vacuum environments. In vacuum, the spray is more difficult to control but several successful depositions have been carried out. After several investigations of spraying PEO solutions and also blank solution (water and methanol only), several factors for a successful spray in vacuum were determined. For a maximum ion current to be measured, the tip-sample separation should be kept to a minimum. However, there is evidence (see Figure 7.12c and d)) that perhaps if the distance is not large enough, the molecules reaching the sample have not had enough opportunity to become completely desolvated, and ring-like features were observed which indicate droplets or bubbles reaching the surface and bursting. Also, using a more concentrated solution would suggest the sample preparation time can be shorter for a required coverage; however, if the solution is too concentrated, as with PEO electrosprayed onto Sample IV, then the tip can become blocked with accumulated molecule. The ion current detected with this more concentrated solution was not steady when preparing this sample and large polymer extrusions were observed under optical microscopy. A higher voltage applied to the tip also gives a higher current and a different sample morphology but it is more difficult to achieve a steady current/spray away from the optimal voltage of about 2.5kV.

Carbon nanotubes have been electrosprayed in vacuum and imaged using AFM. They appear relatively intact after the spray process and appear in elongated open bundles up to $1\mu m$ long.

7.7.1 Future considerations

Though the current is not a steady value in typical traces such as that shown in Figure 7.10, the best spray conditions are not necessarily the conditions under which the steadiest current is obtained, but those which allow for a constant non-zero current. One of the

biggest problems with electrospray in vacuum is that it can be difficult to maintain an ion current for long enough that a significant number of molecules are deposited and analysed. The lack of current can occur for a number of reasons. The tip may become blocked by dirt, though this is minimised by the inclusion of filters on either side of the capillary. The tip can also become blocked by the molecules which are to be deposited, such as salts or polymers from a concentrated solution. Air bubbles can also cause an intermittent spray, and these can become trapped if the capillary line isn't flushed through effectively with dry air prior to spray. This can sometimes be remedied by the application of a 'back pressure' of nitrogen to the reservoir of solution which forces the solution and air through the system (Figure 7.10).

The tips can become blocked with various materials, but they can be cleaned. Borosilicate glass tips can sometimes be cleaned out by blowing a high pressure of dry nitrogen through them, but they are unsuitable for sonication because they are too fragile. The sharpened glass tips become blunted when sonicated, which seems to affect the Taylor cone formation and make the spray of solution difficult to direct. Stainless steel tips are much narrower in diameter and can become blocked more easily, but can be cleaned numerous times by sonication and are far more robust and allow for a lower pressure in the spray chamber.

The direction of the spray jet can move during electrospray ionisation. As shown in Figure 7.1 c), at a certain voltage the jet direction can be rather far off centre. This makes it difficult to direct the spray at the sample through the lenses. In theory, the direction of the spray should be able to be directed through then lens system, but in practice this has so far been difficult to achieve. This may be because the ions are moving too quickly for the potentials applied to the lenses to have any deviating effect on the droplets. Applying a voltage higher than about 2kV to the lenses causes them to arc. A desolvation chamber employing a sheath gas flow prior to the lenses would perhaps slow the charged droplets down as well as causing further desolvation, which is desirable for clean sample preparation. However using an extra gas flow would increase the pressure in the first chamber and hence throughout the electrospray system. If the ions are slowed down then the mass quadrupole may be included in Chamber 2. This would provide a longer path for the ions to travel along before reaching the substrate, allowing more complete desolvation and an extra pumping chamber which would allow the pressure in the deposition chamber to be lower than it is currently. The mass quadrupole could be used to mass select required ions from the spray

by using their mass/charge ratio. The LabVIEW software used to measure and plot the ion current also has the ability to program the Keithley unit to provide a voltage, which is used to control the mass quadrupole. Also, there is an extra mass selection electronics unit available to control the quadrupole. This all requires commissioning in future developments

Overall this project has provided several interesting results and with further developments should provide a novel surface science tool for the deposition of many molecules.

Chapter 8

Summary

My PhD studies have focused primarily on the importance of hydrogen bonding interactions between molecules on surfaces, and how these interactions mediate ordered phase formation.

I have used scanning tunnelling microscopy (STM) to investigate the perylene derivative molecule PTCDA on the Ag-Si(111) $\sqrt{3} \times \sqrt{3}$R30° surface, alone and with C_{60}, and melamine. These studies show how hydrogen bonding interactions determine the morphology of flat molecular arrangements on a passive surface. Square, herringbone and hexagonal ordered phases of PTCDA were imaged in high resolution. The square PTCDA phase is particularly interesting and is a result of near commensurability of the molecular phase with the underlying hexagonal substrate. Its presence also demonstrates that ordered film growth may occur for crystal layers with different symmetries; in this case a square overlayer on a hexagonal substrate. The herringbone phase was observed, as in many other studies of PTCDA on different surfaces, and the hexagonal phase, which exists in two chiralities, is believed to be a combination of the square and herringbone phases. PTCDA and C_{60} were codeposited leading to isolated island formation of the two species. The codeposition of PTCDA and melamine yielded a hydrogen bonded hexagonal network and a double row phase, alongside small rosette arrangements. The hexagonal lattice is stabilised by two hydrogen bonding interactions which flank a potentially repulsive interaction between a PTCDA and a melamine molecule. The double row phase is complicated, but appears in greater abundance than the hexagonal phase. The rosette features only formed immediately after melamine deposition and were not observed after a short time ($\sim$ 2 hours).

Hydrogen bonding molecular systems of pyridinecarboxylic acids on rutile TiO_2 have been studied using photoemission spectroscopy to investigate the geometry of ordered films. Isonicotinic acid and biisonicotinic acid commonly feature as bonding ligands in many

molecular species, including the dye molecules used in molecular photovoltaic devices. Ordered multilayers and monolayers of isonicotinic acid were prepared and investigated using valence band photoemission. Ordered films show a tilt angular dependence of the valence band spectrum on the angle of the incoming linearly polarised synchrotron light as the molecular orbitals are probes to different extents. Biisonicotinic acid was also investigated in preliminary studies using valence band photoemission and DFT calculations may be used to model the measured valence band. Biisonicotinic acid was studied using core level photoemission, to bond in a monolayer in an upright geometry on rutile $TiO_2(110)$ through the carboxylic acid groups. Biisonicotinic acid was also found to bond to different coverages of gold on TiO_2 in an upright fashion through the carboxylic acid groups, as determined from O $1s$ photoemission data. STM studies were also performed to compare to the photoemission data. Clear STM images of biisonicotinic acid on gold were difficult to obtain, possibly because the molecules are upright or loosely bound. On the Ag-Si(111) $\sqrt{3} \times \sqrt{3}$R30° surface biisonicotinic acid was found to arrange in partially ordered islands, but no long range order was observed, due to the different geometric isomers possible when the molecule is confined to a place.

Large or fragile molecules cannot be sublimed in vacuum as they fragment upon heating. To facilitate the deposition of fragile molecules, and in fact any molecules which dissolve in a suitable solvent, an electrospray deposition system has been developed for the deposition of molecules in vacuum from solution. The polymer poly(ethylene) oxide (PEO) and single walled carbon nanotubes were both successfully deposited onto SiO_2 using electrospray deposition, and the surfaces were imaged using AFM. PEO forms many different structures on the SiO_2 surface using different deposition conditions, and carbon nanotubes were observed to adsorb in small bundles up to $1\mu m$. Further scope for this developmental deposition system are discussed and include the incorporation of a mass quadrupole for molecular selection.

8.1 List of publications

O'Shea, J. N. Swarbrick, J. C., Nilson, K., Puglia, C., Brena, B., Luo, Y., Dhanak, V. R., "Molecular ordering in isonicotinic acid on rutile $TiO_2(110)$ investigated with valence band photoemission" *Journal of Chemical Physics* **2004,** *121* (20), 10203-10208.

Swarbrick, J. C., Ma, J., Theobald, J. A., Oxtoby, N. S., O'Shea, J. N., Champness, N. R., Beton, P. H.
"Square, Hexagonal, and Row Phases of PTCDA and PTCDI on Ag-Si(111)$\sqrt{3} \times \sqrt{3}R30°$" *Journal of Physical Chemistry B* **2005,** *109* (24), 12167 - 12174.

Swarbrick, J. C., Taylor, J. B., O'Shea, J. N.
"Electrospray deposition in Vacuum" *Applied Surface Science* **2006,** (15), *252,* 5622-5626.

Swarbrick, J. C., Rogers, B. L., Champness, N. R., Beton, P. H.
"Hydrogen bonded PTCDA-melamine networks and mixed phases" *Journal of Physical Chemistry B* **2006,** *110* (12), 6110-6114.

O'Shea, J. N., Taylor, J. B., Swarbrick, J. C., Magnano, G., Schulte, K. H. G.
"Electrospray deposition of carbon nanotubes in vacuum" *Submitted to NanoLetters* **2006**.

8.2 Common acronyms

AFM - Atomic force microscopy

DNA - Deoxyribonucleic acid

DFT - Density functional theory

DWNT - Double walled (carbon) nanotube

E and B - Electric and magnetic fields

FWHM - Full width at half maximum

HOMO - Highest occupied molecular orbital

HOPG - Highly ordered pyrolytic graphite

IR - Infra red

LEED - Low energy electron diffraction

LUMO - Lowest unoccupied molecular orbital

NEXAFS - Near-edge x-ray absorption fine structure

NTCDA - Naphthalene tetracarboxylic dianhydride

Pc - Phthalocyanine

PEEK - Polyetherether ketone

PEO - Polyethylene oxide

PTCDA - Perylene tetracarboxylic dianhydride

STM - Scanning tunnelling microscopy

UHV - Ultra high vacuum

UPS - Ultraviolet photoemission spectroscopy

UV - Ultra violet

XAS - X-ray absorption spectroscopy

XPS - X-ray photoemission spectroscopy

List of Figures

References

[1] S. de Feyter and F. C. de Schryver. Two-dimensional supramolecular self-assembly probed by scanning tunneling microscopy. *Chemical Society Review*, 32(6):139–150, 2003.

[2] J. V. Barth, G. Costantini, and K. Kern. Engineering atomic and molecular nanostructures at surfaces. *Nature*, 437(7059):671–679, 2005.

[3] F. Bartha, O. Kapuy, C. Kozmutza, and C. Van Alsenoy. Analysis of weakly bound structures: hydrogen bond and the electron density in a water dimer. *Journal of Molecular Structure-TheoChem*, 666:117–122, 2003.

[4] J. D. Watson and F. H. C. Crick. Molecular structure of nucleic acids - a structure for deoxyribose nucleic acid. *Nature*, 171(4356):737–738, 1953.

[5] D. Wang, L. J. Wan, Q. M. Xu, C. Wang, and C. L. Bai. Adlayer structures of pyrene and perylene on Cu(111): an *in situ* STM study. *Surface Science*, 478(1-2):L320–L326, 2001.

[6] J. V. Barth, J. Weckesser, G. Trimarchi, M. Vladimirova, A. de Vita, C. Cai, H. Brune, P. Günter, and K. Kern. Stereochemical effects in supramolecular self-assembly at surfaces: 1-D versus 2-D enantiomorphic ordering for PVBA and PEBA on Ag(111). *Journal of the American Chemical Society*, 124(27):7991–8000, 2002.

[7] J. V. Barth, J. Weckesser, C. Cai, P. Günter, L. Bürgi, O. Jeandupeux, and K. Kern. Building supramolecular nanostructures at surfaces by hydrogen bonding. *Angewandte Chemie-International Edition*, 39(7):1230–1234, 2000.

[8] J. Weckesser, A. de Vita, J. V. Barth, C. Cai, and K. Kern. Mesoscopic correlation

of supramolecular chirality in one-dimensional hydrogen-bonded assemblies. *Physical Review Letters*, 87(9):096101, 2001.

[9] R. Otero, M. Schock nd L. M. Molina, E. Laegsgaard, I Stensgaard, B Hammer, and F. Besenbacher. Guanine quartet networks stabilized by cooperative hydrogen bonds. *Angewandte Chemie-International Edition*, 44(15):2270–2275, 2005.

[10] H. Tanaka, T. Nakagawa, and T. Kawai. Two-dimensional self-assembly of DNA base molecules on Cu(111) surfaces. *Surface Science*, 364(2):L575–L579, 1996.

[11] M. Furukawa, H. Tanaka, K. Sugiura, Y. Sakata, and T. Kawai. Fabrication of molecular alignment at the specific sites on Cu(111) surfaces using self-assembly phenomena. *Surface Science*, 445(1):L58 – L63, 2000.

[12] M. Bohringer, K. Morgenstern, W.-D. Schneider, and R. Berndt. Separation of a racemic mixture of two-dimensional molecular clusters by scanning tunneling microscopy. *Angewande Chemie-International Edition*, 38(6):821–823, 1999.

[13] M. Bohringer, K. Morgenstern, W-D Schneider, R. Berndt, F. Mauri, A. de Vita, and R. Car. Two dimensional self assembly of supramolecular clusters and chains. *Physical Review Letters*, 83(2):324–327, 1999.

[14] M. Bohringer, W.-D. Schneider, and R. Berndt. Two-dimensional self-assembly of supramolecular structures. *Surface Review and Letters*, 7(5-6):661–666, 2000.

[15] D. L. Keeling, N. S. Oxtoby, C. Wilson, M. J. Humphry, N. R. Champness, and P. H. Beton. Assembly and processing of hydrogen bond induced supramolecular nanostructures. *Nano Letters*, 3(1):9–12, 2003.

[16] S. Griessl, M. Lackinger, M. Edelwirth, M. Hietschold, and W.M. Heckl. Self-assembled two-dimensional molecular host-guest architectures from trimesic acid. *Single Molecules*, 3(1):25–31, 2002.

[17] A. Dmitriev, N. Lin, J. Weckesser, J. V. Barth, and K. J. Kern. Supramolecular assemblies of trimesic acid on a Cu(100) surface. *Journal of Physical Chemistry B*, 106(27):6907–6912, 2002.

[18] M. Lackinger, S. Griessl, W. A. Heckl, M. Hietschold, and G. W. Flynn. Self-assembly of trimesic acid at the liquid-solid interface - a study of solvent-induced polymorphism. *Langmuir*, 21(11):4984–4988, 2004.

[19] S. de Feyter, M. Larsson, N. Schuurmans, B. Verkuijl, G. Zoriniants, A. Gesquire, M. M. Abdel-Mottaleb, J. van Esch, B. L. Feringa, J. van Stam, and F. de Schryver. Supramolecular control of two-dimensional phase behavior. *Chemistry - A European Journal*, 9(5):1198 – 1206, 2003.

[20] S. de Feyter, A. Gesquiere, M. Klapper, K. Mullen, and F. C. de Schryver. Toward two-dimensional supramolecular control of hydrogen-bonded arrays: The case of isophthalic acids. *Nano Letters*, 3(11):1485–1488, 2003.

[21] L. M. A. Perdig ao, N. R. Champness, and P. H. Beton. Surface self-assembly of the cyanuric acid-melamine hydrogen bonded network. *Chemical Communications*, 5:538–540, 2006.

[22] G. M. Whitesides, J. P. Mathias, and C. T. Seto. Molecular self-assembly and nanochemistry - a chemical strategy for the synthesis of nanostructures. *Science*, 254(5036):1312–1319, 1991.

[23] C. T. Seto and G. M. Whitesides. Molecular self-assembly through hydrogen-bonding - supramolecular aggregates based on the cyanuric acid: melamine lattice. *Journal of the Americal Chemical Society*, 115(3):905–916, 1993.

[24] J. Lu, S. B. Lei, Q. D. Zeng, S. Z. Kang, C. Wang, L. J. Wan, and C. L. Bai. Template-induced inclusion structures with copper(II) phthalocyanine and coronene as guests in two-dimensional hydrogen-bonded host networks. *Journal of Physical Chemistry B*, 108(17):5161–5165, 2004.

[25] J. A. Theobald, N. S. Oxtoby, M. A. Phillips, N. R. Champness, and P. H. Beton. Controlling molecular deposition and layer structure with supramolecular surface assemblies. *Nature*, 424(6952):1029–1031, 2003.

[26] J. A. Theobald, N. S. Oxtoby, N. R. Champness, P. H. Beton, and T. J. S. Dennis. Growth induced reordering of fullerene clusters trapped in a two-dimensional supramolecular network. *Langmuir*, 21(5):2038–2041, 2005.

[27] D. L. Keeling, M. J. Humphry, R. H. J. Fawcett, P. H. Beton, C. Hobbs, and K. Kantorovich. Bond breaking coupled with translation in rolling of covalently bound molecules. *Physical Review Letters*, 94(14):146104, 2005.

[28] L. M. A. Perdigao, E. W. Perkins, J. Ma, P. A. Staniec, B. L. Rogers, N. R. Champness, and P. H. Beton. Bimolecular networks and supramolecular traps on Au(111). *Journal of Physical Chemistry*, 110(25):12539–12542, 2006.

[29] C. Bobisch, Th. Wagner, A. Bannani, and R. Möller. Ordered binary monolayer composed of two organic molecules: Copper-phthalocyanine and 3,4,9,10- perylene-tetra-carboxylic-dianhydride on Cu(111). *Journal of Chemical Physics*, 119(18):9804–9408, 2003.

[30] M. de Wild, S. Berner, H. Suzuki, H. Yanagi, D. Schlettwein, S. Ivan, A. Baratoff, H.-J. Güntherodt, and T. A. Jung. A novel route to molecular self-assembly: Self-intermixed monolayer phases. *ChemPhysChem*, 3(10):881–885, 2002.

[31] G. Binnig and H. Rohrer. Scanning tunneling microscopy. *IBM Journal of Research and Development*, 30(4):355–369, 1986.

[32] R. Wiesendanger. *Scanning Probe Microscopy and Spectroscopy: Methods and Applications*. Cambridge University Press, 1 edition, 1994.

[33] B. Das and J. Mahanty. Spatial distribution of tunnel current and application to scanning tunnelling microscopy - a semiclassical treatment. *Physical Review*, 36(2):898–903, 1987.

[34] Editors: J. A. Stroscio and W. J. Kaiser. *Scanning Tunneling Microscopy*. Academic Press, Inc., 1st edition, 1993.

[35] J. Bardeen. Tunnelling from a many-particle point of view. *Physical Review Letters*, 6(2):57–59, 1961.

[36] D. A. Bonnell. *Scanning Tunneling Microscopy and Spectroscopy- Theory, Techniques and Applications*. Wiley VCH Publishing, 2 edition, 2001.

[37] Website by J. Gebauer, Weber Group Research, The University of California, Berkeley. Cross sectional STM of III-V semiconductor surfaces, accessed 10/05/2006. http://www.mse.berkeley.edu/groups/weber/research/x-stm.html.

[38] M. Eremtchenko, J. A. Schaefer, and F. S. Tautz. Understanding and tuning the epitaxy of large aromatic adsorbates by molecular design. *Nature*, 425(6958):602–605, 2003.

[39] Website: AFM (Atomic Force Microscopy) by Heiko Ahrens. from Ernst-Moritz-Arndt-Universität Greifswald Institut für Physik - Applied Physics, accessed 28/07/2006. http://www3.physik.uni-greifswald.de/method/afm/eafm.htm.

[40] G. Margaritondo. *Elements of Synchrotron Light for Biology, Chemistry and Medical Research*. Oxford University Press, 1st edition, 2002.

[41] D. Attwood. *Soft X-rays and Extreme Ultraviolet Radiation - Principles and Applications*. Cambridge University Press, 1st edition, 2000.

[42] C. W. Hsu, M. Evans, C. Y. Ng, and P. Heimann. High resolution threshold and pulsed field ionization photoelectron spectroscopy using multi-bunch synchrotron radiation. *Review of Scientific Instuments*, 68(4):1694–1702, 1997.

[43] L. X. Chen. Probing transient molecular structures in photochemical processes using laser-initiated time-resolved x-ray absorption spectroscopy. *Annual Review of Physical Chemistry*, 56:221–254, 2005.

[44] V. R. Dhanak, A. W. Robinson, G. van der Laan, and G. Thornton. Beamline 4.1 - A dedicated surface science facility at Daresbury Laboratory. *Review of Scientific Instruments 2B*, 63(1):1342–1345, 1992.

[45] V. R. Dhanak. Website: Station 4.1 of the SRS Daresbury Laboratory. http://srs.dl.ac.uk/station/4.1/, 1999.

[46] R. Nyholm, J.N. Andersen, U. Johansson, B.N. Jensen, and I. Lindau. Beamline I311 at MAX-lab: A VUV/Soft X-ray undulator beamline for high resolution electron spectroscopy. *Nuclear Instruments and Methods in Physics Research A: Accelerators, Spectrometers, Detectors and Associated Equipment*, 467:520–524, 2001.

[47] R. Denecke, P. Vaterlein, M. Bässler, N. Wassdahl, S. Butorin, A. Nilsson, J.E. Rubensson, J. Nordgren, N. Mårtensson, and R. Nyholm. Beamline I511 at MAX II, capabilities and performance. *Journal of Electron Spectroscopy and Related Phenomena*, 103:971–979, 1999.

[48] A. Einstein. Generation and conversion of light with regard to a heuristic point of view. *Annalen der Physik*, 17(6):132–148, 1905.

[49] Spartan '02 Computational Chemistry package. by Wavefunction, Inc., 2002. http://www.wavefun.com/.

[50] M.J. Frisch, G.W. Trucks, H.B. Schlegel, G.E. Scuseria, M.A. Robb, J.R. Cheeseman, V.G. Zakrzewski, J.A. Montgomery Jr., R.E. Stratmann, J.C. Burant, S. Dapprich, J.M. Millan, A.D. Daniels, K.N. Kudin, M.C. Strain, O. Farkas, J. Tomasi, V. Barone, M. Cossi, R. Cammi, B. Mennucci, C. Pomelli, C. Adamo, S. Clifford, J. Ochterski, G.A. Petersson, P.Y. Ayala, Q. Cui, K. Morokuma, D.K. Malick, A.D. Rabuck, K. Raghavachari, J.B. Foresman, J. Cioslowski, J.V. Ortiz, B.B. Stefanov, G. Liu, A. Liashenko, P. Piskorz, I. Komaromi, R. Gomperts, R.L. Martin, D.J. Fox, T. Keith, M.A. Al-Laham, C.Y. Peng, A. Nanayakkara, C. Gonzalez, M. Challacombe, P.M.W. Gill, B. Johnson, W. Chen, M.W. Wong, J.L. Andres, M. Head-Gordon, E.S. Replogle, and J.A. Pople. Gaussian98. Computational Chemistry Program, 1998.

[51] J. M. Soler, E. Artacho, J. D. Gale, A. García, J. Junquera, P. Ordejón, and D. Sánchez-Portal. The SIESTA method for ab initio order-N materials simulation. *Journal Of Physics: Condensed Matter*, 14(11):2745–2779, 2002.

[52] Website by A. Wucher, Fachbereich Physik, Universität Kaiserslautern, D-67653 Kaiserslautern. Surface and Thin Film Analysis with Electron and Mass Spectrometric Techniques, accessed 20/08/2006. http://www.ilp.physik.uni-essen.de/wucher/tatf98/tatf98.html.

[53] M. P. Seah and W. A. Dench. Quantitative electron spectroscopy of surfaces: A standard data base for electron inelastic mean free paths in solids. *Surface and Interface Analysis*, 1(2), 1979.

[54] Website: H. Arnolds, Girton College and the Nanoscience Centre, Cambridge University. Surface Science and Heterogeneous Catalysis, accessed 16/05/2006. http://www-dak.ch.cam.ac.uk/laser/SurfaceScience.ppt.

[55] A. Proctor and P. M. A. Sherwood. Data analysis techniques in x-ray photoelectron spectroscopy. *Analytical Chemistry*, 54(1):13–19, 1982.

[56] S. Tougaard. Background removal in x-ray photoemission spectroscopy - relative importance of intrinsic and extrinsic processes. *Physical Review B*, 34(10):6779–6783, 1986.

[57] J. Schnadt, J. N. O'Shea, L. Patthey, J. Schiessling, J. Krempaský, M. Shi, N. Mårtensson, and P. A. Brühwiler. Alignment of valence photoemission, x-ray. absorption and substrate density of states for an adsorbate on a semiconductor surface. *Physical Review B*, 67:235420–235420, 2003.

[58] K. Takayanagi, Y. Tanishiro, S. Takahashi, and M. Takahashi. Structure analysis of Si(111)(7×7) reconstructed surface by transmission electron diffraction. *Surface Science*, 164(2-3):367–392, 1985.

[59] G. Binnig, H. Rohrer, C. Gerber, and E. Weibel. 7 x 7 reconstruction on Si(111) resolved in real space. *Physical Review Letters*, 50(2):120–123, 1983.

[60] M. J. Butcher, J. W. Nolan, M. R. C. Hunt, P. H. Beton, L. Dunsch, P. Kuran, P. Georgi, and T. J. S. Dennis. Orientationally ordered island growth of higher fullerenes on Ag/Si(111)$\sqrt{3} \times \sqrt{3}$R30°. *Physical Review B*, 64(19):195401, 2001.

[61] K. J. Wan, X. F. Lin, and J. Nogami. Surface reconstructions in the Ag/Si(111) system. *Physical Review B*, 47(20):13700–13723, 1993.

[62] T. Takahashi, S. Nakatani, N. Okamoto, T. Ishikawa, and S. Kikuta. A study of the Si(111)-square root 3 x square root 3 - Ag surface by transmission x-ray diffraction and x-ray diffraction topography. *Surface Science*, 242(1-3):54–58, 1991.

[63] U. Diebold. The surface science of TiO_2. *Surface Science Reports*, 48(5-8):53–229, 2003.

[64] B. O'Regan and M. Grätzel. A low-cost, high-efficiency solar cell based on dye-sensitized colloidal TiO_2 films. *Nature*, 353(6346):737–740, 1991.

[65] A. Hagfeldt and M. Grätzel. Molecular photovoltaics. *Accounts of Chemical Research*, 33(5):269–277, 2000.

[66] A. Hagfeldt and M. Grätzel. Light-induced redox reactions in nanocrystalline systems. *Chemical Review*, 95(1):49–68, 1995.

[67] M. Grätzel. Photoelectrochemical cells. *Nature*, 414(6861):338–344, 2001.

[68] M. K. Nazeeruddin and A. Kay and I. Rodicio and R. Humphry-Baker and E. Müller and P. Liska and N. Vlachopoulos and M. Grätzel. Conversion of light to electricity by *cis*-$x_2$bis(2,2-bipyridyl-4,4-dicarboxylate)ruthenium(ii) charge-transfer sensitizers (x = $c1^-$, br^-, i^-, cn^-, and scn^-) on nanocrystalline tio_2 electrodes. *Journal of the Americal Chemical Society*, 115:6382–6390, 1993.

[69] J. Schnadt, P. A. Brühwiler, L. Patthey, J. N. O'Shea, S. Södergren, M. Odelius, R. Ahuja, O Karis, M. Bässler, P. Persson, H. Siegbahn, S. Lunell, and N. Mårtensson. Experimental evidence for a sub-3-fs charge transfer from an aromatic adsorbate to a semiconductor. *Nature*, 418(6898):620–623, 2002.

[70] Website by K. Hermann, Theory Department, Fritz-Haber-Institut, Berlin. Gallery of BALSAC (and other) pictures, accessed 13/04/2006. http://www.fhi-berlin.mpg.de/th/personal/hermann/pictures.html.

[71] P. Persson, S. Lunell, P. A. Brühwiler, J. Schnadt, S. Södergren, J. N. O'Shea, O. Karis, H. Siegbahn, N. Märtensson, M. Bässler, and L. Patthey. N1s x-ray absorption study of the bonding interaction of bi-isonicotinic acid adsorbed on rutile TiO_2. *Chemical Physics*, 112(9):3945–3948, 2000.

[72] U. Diebold, J. Lehman, T. Mahmoud, M. Kuhn, G. Leonardelli, W. Hebenstreit, M. Schmid, and P. Vargad. Intrinsic defects on a $TiO_2(110)$ (1×1) surface and their reaction with oxygen: a scanning tunneling microscopy study. *Surface Science*, 411(1-2):137–153, 1998.

[73] J. Schnadt, J. Schiessling, J. N. O'Shea, S. M. Gray, L. Patthey, M. K-J. Johansson, M. Shi, J. Krempaský, J. Åhlund, P. G. Karlsson, P. Persson, N. Mårtensson, and P. A. Brühwiler. Structural study of adsorption of isonicotinic acid and related molecules on rutile TiO_2 I: XAS and STM. *Surface Science*, 540(1):39–54, 2003.

[74] H. Onishi and Y. Iwasawa. Reconstruction of $TiO_2(110)$ surface: STM study with atomic-scale resolution. *Surface Science*, 313(1-2):L783–L789, 1994.

[75] M. Li, W. Hebenstreit, L. Gross, U. Diebold, M. A. Henderson, D. R. Jennison, P. A.

Schultz, and M. P. Sears. Oxygen-induced restructuring of the TiO_2(110) surface: A comprehensive study. *Surface Science*, 437(1-2):173, 1999.

[76] J. V. Barth, H. Brune, G. Ertl, and R. J. Behm. Scanning tunnelling microscopy observations on the reconstructed Au(111) surface - atomic structure, long-range superstructure, rotational domains and surface defects. *Physical Review B*, 42(15):9307–9318, 1990.

[77] R. Strohmaier, J. Petersen, B. Gompf, and W. Eisenmenger. A systematic STM study of planar aromatic molecules on inorganic substrates I. Submolecular image contrast. *Surface Science*, 418:91104, 1998.

[78] K. Glöckler, C. Seidel, A. Soukopp, M. Sokolowski, E. Umbach, M. Bohringer, R. Berndt, and W-D. Schneider. Highly ordered structures and submolecular scanning microscopy contrast of PTCDA and DM-PBCDI monolayers on Ag(111) and Ag(110). *Surface Science*, 405(1):1–20, 1998.

[79] T. Schmitz-Hübsch, T. Fritz, T. Staub, A. Back, N. R. Armstrong, and K. Leo. Structure of 3,4,9,10-perylene-tetracarboxylic-dianhydride grown on reconstructed and unreconstructed Au(100). *Surface Science*, 437(1-2):163–172, 1999.

[80] I. Chizhov, A. Kahn, and G. Scoles. Initial growth of 3,4,9,10-perylenetetracarboxylic-dianhydride (PTCDA) on Au(111): a scanning tunneling microscopy study. *Journal of Crystal Growth*, 208(1-4):449–458, 2000.

[81] M.V. Tiba, O. Kurnosikov, C.F.J. Flipse, B. Koopmans, H.J.M. Swagten, J.T. Kohlhepp, and W.J.M. de Jonge. Ordering of organic molecules on passivated reactive substrates: PTCDA on O-p(2×2)Ni(111). *Surface Science*, 498(1-2):161–167, 2002.

[82] G. Sazaki, T. Fujino, J. T. Sadowski, N. Usami, T. Ujihara, K. Fujiwara, Y. Takahashi, E. Matsubara, T. Sakurai, and K. Nakajima. Epitaxial relation and island growth of perylene-3.4.9.10-tetracarboxylic dianhydride (PTCDA) thin film crystals on a hydrogen-terminated Si(111) substrate. *Journal of Crystal Growth*, 262(1-4):196–201, 2004.

[83] C. Kendrick, A. Kahn, and S. R. Forrest. STM study of the organic semiconductor PTCDA on highly-oriented pyrolytic graphite. *Applied Surface Science*, 104:586–594, 1996.

[84] R. Staub, M. Torker, T. Fritz, T. Schmitz-Hübsch, F. Sellam, and K. Leo. Scanning tunneling microscope investigations of organic heterostructures prepared by a combination of self-assembly and molecular beam epitaxy. *Surface Science*, 445(2-3):368–379, 2000.

[85] Q. Chen, T. Rada, Th. Bitzer, and N. V. Richardson. Growth of PTCDA crystals on H:Si(111) surfaces. *Surface Science*, 547(3):385–393, 2003.

[86] N. Nicoara, O. Custance, D. Granados, J. M. García, J. M. Gómez-Rodríguez, A. M. Baró, and J. Méndez. Scanning tunnelling microscopy and spectroscopy on organic PTCDA films deposited on sulfur passivated GaAs(001). *Journal of Physics: Condensed Matter*, 15(38):S2619 S2629, 2003.

[87] Th. Wagner, A. Bannani, C. Bobisch, H. Karacuban, M. Stohr, M. Gabriel, and R. Moller. Growth of 3,4,9,10-perylenetetracarboxylic-dianhydride crystallites on noble metal surfaces. *Organic Electronics*, 5(1-3):35–43, 2004.

[88] E. Umbach, M. Sokolowski, and R. Fink. Substrate-interaction, long-range order, and epitaxy of large organic adsorbates. *Applied Physics A-Materials Science and Processing*, 63(6):565–576, 1996.

[89] T. Schmitz-Hübsch, F. Sellam, R. Staub, M. Torker, T. Fritz, C. Kübel, K. Müllen, and K. Leo. Direct observation of organic-organic heteroepitaxy: perylene-tetracarboxylic-dianhydride on hexa-peri benzocoronene on highly ordered pyrolytic graphite. *Surface Science*, 445(2-3):358–367, 2000.

[90] T. Schmitz-Hübsch, T. Fritz, F. Sellam, R. Staub, and K. Leo. Epitaxial growth of 3,4,9,10-perylene-tetracarboxylic-dianhydride on Au(111): A STM and RHEED study. *Physical Review B*, 55(12):7972–7976, 1997.

[91] B. Krause, A. C. Dürr, K. A. Ritley, F. Schreiber, H. Dosch, and D. Smilgies. On the coexistence of different polymorphs in organic epitaxy: alpha and beta phase of PTCDA on Ag(111). *Applied Surface Science*, 175-176:332–336, 2001.

[92] U. Stahl, D. Gador, A. Soukopp, R. Fink, and E. Umbach. Coverage-dependent superstructures in chemisorbed NTCDA monolayers: a combined LEED and STM study. *Surface Science*, 414(3):423–434, 1998.

[93] H. W. Kroto. Buckminsterfullerene: The celestial sphere that fell to earth. *Angewandte Chemie-International Edition in English*, 31:111–129, 1992.

[94] W. Kratschmer, L. D. Lamb, K. Fostiropoulos, and D. R. Huffman. Solid C_{60} - a new form of carbon. *Nature*, 347(6291):354–358, 1990.

[95] K. Tsuchie, T. Nagao, and S. Hasegawa. Structure of C_{60} layers on the Si(111) – $\sqrt{3} \times \sqrt{3}$-Ag surface. *Physical Review B*, 60(15):11131–11136, 1999.

[96] M. D. Upward, P. Moriarty, and P. H. Beton. Double domain ordering and selective removal of C_{60} on Ag-Si(111)$\sqrt{3} \times \sqrt{3}$R30°. *Physical Review Letters*, 56(4):R1704–R1707, 1997.

[97] J. C. Swarbrick, J. Ma, J. A. Theobald, N. S. Oxtoby, J. N. O'Shea, N. R. Champness, and P. H. Beton. Square, hexagonal and row phases of PTCDA and PTCDI on Ag-Si(111)$\sqrt{3} \times \sqrt{3}$R30°. *Journal of Physical Chemistry B*, 109(25):12167–12174, 2005.

[98] F. Wurthner. Perylene bisimide dyes as versatile building blocks for functional supramolecular architectures. *Chemical Communications*, 14:1564–1579, 2004.

[99] P. Ordejon, E. Artacho, and J. M. Soler. Self-consistent order-N density-functional calculations for very large systems. *Physical Review B*, 53:10441–10444, 1996.

[100] J. C. Swarbrick, B. L. Rogers, N. R. Champness, and P. H. Beton. Hydrogen bonded PTCDA-melamine networks and mixed phases. *Journal of Physical Chemistry B*, 110(12):6110–6114, 2006.

[101] M. Grätzel. Molecular photovoltaics. *Accounts of Chemical Research*, 33(5):2000, 269-277.

[102] S. M. Grundy, H. Y. I. Mok, L. Zech, and M. Berman. Influence of nicotinic acid on metabolism of cholesterol and triglycerides in man. *Journal of Lipid Research*, 22(1):24–36, 1981.

[103] Y. Zhang, B. Heym, B. Allen, D. Young, and S. Cole. The catalase peroxidase gene and isoniazid resistance of mycobacterium-tuberculosis. *Nature*, 358(6387):591–593, 1992.

[104] K. S. Min and M. P. Suh. Construction of various supramolecules by $\pi-\pi$ interactions: Self-assembly of nickel(II) macrocyclic complexes containing pyridine pendant arms with bidentate ligands. *European Journal of Inorganic Chemistry*, (2001)(2):449–455, 2001.

[105] Michael Odelius, Petter Persson, and Sten Lunell. Bi-isonicotinic acid on rutile (1 1 0): calculated molecular and electronic structure. *Surface Science*, 529:4758, 2003.

[106] L. Patthey, H. Rensmo, P. Persson, K. Westermark, L. Vayssieres, A. Stashans, A. Petersson, P. A. Brühwiler H. Siegbahn, S. Lunell, and N. Mårtensson. Adsorption of bi-isonicotinic acid on rutile TiO_2(110). *Journal of Chemical Physics*, 110(12):5913–5918, 1999.

[107] A. G. Thomas, W. R. Flavell, C. Chatwin, S. Rayner, D. Tsoutsou, A. R. Kumarasinghe, D. Brete, T. K. Johal, S. Patel, and J. Purton. Adsorption of bi-isonicotinic acid on anatase TiO_2(101) and (001) studied by photoemission and NEXAFS spectroscopy. *Surface Science*, 592(1-3):159–168, 2005.

[108] P. Persson and S. Lunell. Binding of bi-isonicotinic acid to anatase TiO_2(101). *Solar Energy Materials and Solar Cells*, 63(2):139–148, 2000.

[109] R.E. Tanner, Y. Liang, and E.I. Altman. Structure and chemical reactivity of adsorbed carboxylic acids on anatase TiO_2(001). *Surface Science*, 506(3):251–271, 2002.

[110] J. N. O'Shea, Y. Luo, J. Schnadt, L. Patthey, H. Hillesheimer, J. Krempaský, D. Nordlund, M. Nagasono, P. A. Brühwiler, and N. Mårtensson. Hydrogen bond induced surface core level shift in pyridine carboxylic acids. *Surface Science*, 486:157–166, 2001.

[111] J. Schnadt, J. N. O'Shea, L. Patthey, J. Schiessling, J. Krempaský, M. Shi, N. Mårtensson, and P. A. Brühwiler. Structural study of adsorption of isonicotinic acid and related molecules on rutile TiO_2(110) II: XPS. *Surface Science*, 544(1):74–86, 2003.

[112] F. Takusagawa and A. Shimada. Isonicotinic acid. *Acta Crystallography Section B-Structural Science*, 32:1925–1927, 1976.

[113] P. J. Hardman, G. N. Raikar, C. A. Muryn, G. van der Laan, P. L. Wincott, G. Thornton, D. W Bullett, and P. A. D. M. A. Dale. Valence-band structure of TiO_2 along the $\Gamma - \Delta - X$ and $\Gamma - \Sigma - M$ directions. *Physical Review B*, 49(22):7170–7177, 1994.

[114] H. P. Steinruck. Angle-resolved photoemission studies of adsorbed hydrocarbons. *Journal of Physics - Condensed Matter*, 8(36):6465–6509, 1996.

[115] U. Gelius. Recent progress in ESCA studies of gases. *Journal of Electron Spectroscopy and Related Phenomena*, 5(NOV-D):985–1057, 1974.

[116] B. Xu, B. Varughese, D. Evans, and J. Reutt-Robey. Morphology selected molecular architechture: acridine carboxylic acid monolayers on Ag(111). *Journal of Physical Chemistry B*, 110(3):1271–1276, 2006.

[117] R. J. Ellingson, J. B. Asbury, S. Ferrere, N. H. Ghosh, J. R. Sprague, T. Q. Lian, and A. J. Nozik. Dynamics of electron injection in nanocrystalline titanium dioxide films sensitized with [Ru(4,4'-dicarboxy-2,2'-bipyridine)(2)(NCS)(2)] by infrared transient absorption. *Journal of Physical Chemistry B*, 102(34):6455–6458, 1998.

[118] P. J. Moriarty, M. R. D. Taylor, and M. Brust. Nanostructured cellular networks. *Physical Review Letters*, 89(24):248303, 2002.

[119] J. B. Fenn, M. Mann, C. K. Meng, F. S. Wong, and C. M. Whitehouse. Electrospray ionization for mass spectrometry of large biomolecules. *Science*, 246(4926):64–71, 1989.

[120] M. L. Vestal. Methods of ion generation. *Chemical Review*, 101(2):361–375, 2001.

[121] J. B. Fenn. Nobel lecture: Electrospray wings for molecular elephants, at http://www.nobel.se/chemistry/laureates/2002/fenn-lecture.pdf. 8/12/02, 2002.

[122] E. W. Sheehan, R. C. Willoughby, J. A. Jarrell, and D. M. Strand. Patent for electrospray for chemical analysis. Patent No.US 6,278,111 B, 2001.

[123] B. K. Ku and S. S. Kim. Electrohydrodynamic spraying characteristics of glycerol solutions in vacuum. *Journal of Electrostatics*, 57(2):109–128, 2003.

[124] S. Rauschenbach, F. L. Stadler, E. Lunedei, N. Malinowski, S. Koltsov, G. Costantini, and K. Kern. Electrospray ion beam deposition of clusters and biomolecules. *Small*, 2(4):540–547, 2006.

[125] S. J. Gaskell. Electrospray: Principles and practice. *Journal of Mass Spectrometry*, 32(7):677–688, 1997.

[126] E. de Hoffmann and V. Stroobant. *Mass Spectrometry Principles and Applications*. Wiley Publications, Chichester UK, 2001.

[127] G. I. Taylor. Disintegration of water drops in electric field. *Proceedings of the Royal Society of London series A - Mathematical and Physical Sciences*, A280(138):383–397, 1964.

[128] J. Zeleny. The electrical discharge from liquid points, and a hydrostatic method of measuring the electric intensity at their surfaces. *The Physical Review*, 3(2):69–91, 1914.

[129] M. Cloupeau and B. Prunetfoch. Electrohydrodynamic spraying functioning modes - a critical review. *Journal of Aerosol Science*, 25(6):1021–1036, 1994.

[130] M. Cloupeau and B. Prunetfoch. Electrostatic spraying of liquids in cone-jet mode. *Journal of Electrostatics*, 22(2):135–159, 1989.

[131] M. Cloupeau and B. Prunetfoch. Electrostatic spraying of liquids - main functioning modes. *Journal of Electrostatics*, 25(2):165–184, 1990.

[132] Lord Rayleigh. On the equilibrium of liquid conducting masses charged with electricity. *Philisophy Magazine*, 14(5):184–186, 1882.

[133] A. Gomez and K. Tang. Charge and fission of droplets in electrostatic sprays. *Physics of Fluids*, 6(1):404–414, 1994.

[134] D. Duft, T. Achtzehn, R. Muller, B. A. Huber, and T. Leisner. Rayleigh jets from levitated microdroplets. *Nature*, 421(6919):128, 2003.

[135] D. Duft, H. Lebius, and B. A. Huber. Shape oscillations and stability of charged microdroplets. *Physical Review Letters*, 89(8):084503, 2002.

[136] R. B. Cole. Some tenets pertaining to electrospray ionization mass spectrometry. *Journal of Mass Spectrometry*, 35(7):763–772, 2000.

[137] J. V. Iribarne and B. A. Thompson. On the evaporation of small ions from charged droplets. *The Journal of Chemical Physics*, 64(6):2287–2294, 1976.

[138] J. V. Iribarne and B. A. Thompson. Field induced ion evaporation from liquid surfaces at atmospheric pressure. *The Journal of Chemical Physics*, 71(11):4451–4463, 1979.

[139] M. Dole, L. L. Mack, R. L. Hines, R. C. Mobley, L. D. Ferguson, and M. B. Alice. Molecular beams of macroions. *Journal of Chemical Physics*, 49(5):2240–2249, 1968.

[140] G. Schmelzeisen-Redeker, L. Butfering, and F. W. Rollgen. Desolvation of ions and molecules in thermospray mass-spectrometry. *International Journal of Mass Spectrometry and Ion Processes*, 90(2):139–150, 1989.

[141] I. Uematsu, H. Matsumoto, K. Morota, M. Minagawa amd A. Tanioka, Y. Yamagata, and K. Inoue. Surface morphology and biological activity of protein thin films produced by electrospray deposition. *Journal of Colloid and Interface Science*, 269(2):336–340, 2004.

[142] V. N. Morozov, T. Y. Morozova, and N. R. Kallenbach. Atomic force microscopy of structures produced by electrospraying polymer solutions. *International Journal of Mass Spectrometry*, 178(3):143–159, 1998.

[143] V. N. Morozov, A. V. Gavryushkin, and A. A. Deev. Direct detection of isotopically labelled metabolites bound to a protein microarray using a charge-coupled device. *Journal of Biochemistry and Biophysical Methods*, 51(1):57–67, 2002.

[144] V. N. Morozov and T. Y. Morozova. Electrospray deposition as a method for mass fabrication of mono- and multicomponent microarrays of biological and biologically active substances. *Analytical Chemistry*, 71(15):3110–3117, 1999.

[145] B. B. Schneider, V. I. Baranov, H. Javaheri, and T. R. Covey. Particle discriminator interface for nanoflow ESI-MS. *American Society for Mass Spectrometry*, 14(11):1236–1246, 2003.

[146] D. R. Smith, G. Sagerman, and T. D. Wood. Design and development of an interchangeable nanomicroelectrospray source for a quadrupole mass spectrometer. *Review of Scientific Instruments*, 74(10):4474–4477, 2003.

[147] New Objective. Website for new objective online: Silicatips, at http://www.newobjective.com/products/silicatips.html. Website, 2002.

[148] Y. Ishihama, H. Katayama, N. Asakawa, and Y. Oda. Highly robust stainless steel tips as microelectrospray emitters. *Rapid Communications in Mass Spectrometry*, 16(10):913–918, 2002.

[149] Proxeon Biosystems. Nano-bore stainless steel emitters with unique characteristics website, at www.proxeon.com. Website, 2003.

[150] B. K. Ku and S. S. Kim. Electrospray characteristics of highly viscous liquids. *Journal of Aerosol Science*, 33:1361–1378, 2002.

[151] Website: University of Pennsylvania Carbon Nanotubes. Penn engineering: materials science and engineering, accessed 13/04/2006. http://www.seas.upenn.edu/mse/research/nanotubes.html.

[152] S. Iijima. Helical microtubules of graphitic carbon. *Nature*, 354(6348):56–58, 1991.

[153] P. M. Ajayan and T. W. Ebbesen. Nanometre-size tubes of carbon. *Reports on Progress in Physics*, 60(10):1025–1062, 1997.

[154] A. Hirsch. Functionalization of single-walled carbon nanotubes. *Angewandte Chemie-International Edition*, 41:1853–1859, 2002.

[155] V. Krstic, G. S. Duesberg, J. Muster, M. Burghard, and S. Roth. Langmuir-blodgett films of matrix-diluted single-walled carbon nanotubes. *Chemistry of Materials*, 10(9):2338–, 1998.